Symmetrical and Unsymmetrical Perylene Diimide Dyes for Photovoltaic Applications: Chiral, Amphiphilic and Electrochemical Properties

Hürmüs Refiker

Submitted to the
Institute of Graduate Studies and Research
in partial fulfillment of the requirements for the Degree of

Doctor of Philosophy
in
Chemistry

Eastern Mediterranean University
September 2011
Gazimağusa, North Cyprus

Approval of the Institute of Graduate Studies and Research

_____
Prof. Dr. Elvan Yılmaz
Director

I certify that this thesis satisfies the requirements as a thesis for the degree of Doctor of Philosophy in Chemistry.

_____
Prof. Dr. Mustafa Halilsoy
Chair, Department of Chemistry

We certify that we have read this thesis and that in our opinion it is fully adequate in scope and quality as a thesis for the degree of Doctor of Philosophy in Chemistry.

_____
Prof. Dr. Huriye İcil
Supervisor

Examining Committee
_____

1. Prof. Dr. Huriye İcil   _____

2. Prof. Dr. Okan Sirkecioğlu   _____

3. Assoc. Prof. Dr. Hamit Caner   _____

ABSTRACT

In this research, four novel perylene derivatives (BPDI, LPMI, LPDI and LPPDI) have been successfully synthesized. The synthesized compounds have been characterized and investigated in detail by NMR, IR, UV-vis, emission, DSC, TGA, elemental analysis, CV, SWV and CD.

The specific optical rotation values of LPMI, LPDI and LPPDI were measured as +1191.5, +201.7 and -1647.5, respectively at 20 ^{o}C. The compounds showed high thermal stabilities. The initial decomposition temperatures were calculated as 361 ^{o}C for BPDI, 387 ^{o}C for LPMI, 356 ^{o}C LPDI and 415 ^{o}C, for LPPDI. For LPPDI in NMP, two isosbestic points were observed at 533 and 611 nm which confirmed the presence of overlapped monomer and excimer emissions in the temperature range 10 ^{o}C to 80 ^{o}C. Fluorescence quenching of chiral dyes; LPMI, LPDI and LPPDI in m-cresol have been attributed to a charge transfer interaction. Moreover, the excited state of the four dyes can decay only by fluorescence in solid state mainly due to O-H$^{..}$N hydrogen bonds.

The novel photonic perylene dyes have a great potential in various fields such as solid state lightning technology, dye-sensitized solar cells and photomedicine.

Keywords: Amphiphilic, chiral, hydrogen-bonding, controlled self-assembly, perylene, DSSC.

ÖZ

Bu araştırmada 4 yeni madde (BPDI, LPMI, LPDI ve LPPDI) başarılı bir şekilde sentezlenmiştir. Sentezlenen maddeler NMR, IR, UV-vis, DSC, TGA, elemental analiz, dönüşümlü voltametri, kare dalga voltametrileri ve dairesel dikroizm (CD) yöntemleri ile karakterize edilip detaylı bir şekilde incelenmiştir.

LPMI, LPDI ve LPPDI'ın 20 ^{o}C'deki spesifik çevirme açıları sırası ile +1191.5, +201.7 ve -1647.5 olarak ölçülmüştür. Sentezlenen maddeler yüksek termal kararlılık gösterirken; bozulma sıcaklığı başlama noktaları BPDI için 361 ^{o}C, LPMI için 387 ^{o}C, LPDI için 356 ^{o}C ve LPPDI için 415 ^{o}C olarak hesaplanmıştır. Kiral asimetrik perilen diimide, LPPDI NMP çözgeni içinde sıcaklığa sıcaklığa bağlı emisyon çalışmasında 522 ve 611 nm de olmak üzere iki izobestik nokta sergilemiştir. Monomer ve ekzimer emisyonunun çakıştığını göstermektedir. LPMI, LPDI ve LPPDI maddelerinin m-kresol içinde flüoresans söndürmesi yük transferi etkileşimine bağlanmıştır. Ayrıca katı fazdaki 4 madde de uyarık durumda sadece O-H$^{..}$N hidrojen bağı yüzünden sadece flüoresans yapabiliyor.

Elde edilen sonuçlara göre; sentezlenenin maddeler ışık teknolojilerinde, boya ile duyarlaştırılmış güneş pillerinde ve ışıklı terapi anlanlarında kullanılmak üzere büyük potansiyel taşımaktadırlar.

Anahtar Kelimeler: Amfifil, kiral, hidrojen bağı, kontrollü kolayca kurululabilirlilik, perlilen, boya ile duyarlaştırılmış güneş pilleri.

Dedicated to my beloved parents;

Zerinç Refiker & M. İlker Refiker

ACKNOWLEDGMENTS

"For a successful technology, reality must take precedence over public relations,

for Nature cannot be fooled"

Richard Feynman

TABLE OF CONTENTS

LIST OF TABLES

LIST OF FIGURES

xiv

xv

xviii

xxiii

LIST OF SCHEMES

LIST OF ABBREVIATIONS

A	:	Absorbance
Å	:	Armstrong
Anal.	:	Analytical
AU	:	Arbitrary unit
Ave.	:	Average
c	:	Concentration
calcd.	:	Calculated
^{13}C NMR	:	Carbon- 13 nuclear magnetic resonance spectroscopy
CB	:	Conduction band
CT	:	Charge transfer
CD	:	Circular dichroism
CV	:	Cyclic voltammetry
D	:	Dye
DCM	:	Dichloromethane
DMAc	:	Dimethylacetamide
DMF	:	N,N'-dimethylformamide
DMSO	:	Dimethyl sulfoxide
DSC	:	Differential scanning calorimetry
DSSC	:	Dye sensitized solar cell
eV	:	Electron volt

E	:	Electric field
$E_{1/2}$	:	Half-wave potential
EA	:	Electron affinity
E_g	:	Band gap energy
EI	:	Electron ionization
E_{ox}	:	Oxidation potential
ΔE_p	:	Separation of peal potentials
E_{pa}	:	Anodic peak potential
E_{pc}	:	Cathodic peak potential
Eqn.	:	Equation
E_{red}	:	Reduction potential
E_s	:	Singlet energy (excited state energy of 0-0 electronic transition) in kcal/mol
ET	:	Energy transfer
f	:	Oscillator strength
ff	:	Fill-factor
Fc	:	Ferrocene
FT-IR	:	Fourier transform infrared spectroscopy
FU	:	Functional unit
GHG	:	Greenhouse gas
H	:	Magnetic field
hυ	:	Irradiation
^{1}H NMR	:	Proton nuclear magnetic resonance spectroscopy
HOMO	:	Highest occupied molecular orbital

Hz	:	Hertz
i_p	:	Peak current
i_{pa}	:	Anodic peak current
i_{pc}	:	Cathodic peak current
I_{sc}	:	Short circuit current
ITO	:	Indium tin oxide
J	:	Coupling constant
k_d	:	Rate of constant of radiationless deactivation
k_f	:	Fluorescence rate constant
k_q	:	Rate constant for bimolecular fluorescence quenching
l	:	Path length
LCPL	:	Left circularly polarized light
LED	:	Light emitting diode
LB	:	Langmuir-Blodgett
LUMO	:	Lowest unoccupied molecular orbital
mdeg	:	Millidegrees
min.	:	Minimum
MPP	:	Maximum power point
mV	:	Millivolt
M_w	:	Molecular weight
n	:	Refractive index
n	:	Number of electrons (in the reduction process)
N	:	Avogadro's number
NHE	:	Normal Hydrogen electrode

NMP	:	*N*-methylpyrrolidinone
ORD	:	Optical rotatory dispersion
P_{max}	:	Maximum power
PDA	:	Perylene-3,4,9,10-tetracarboxylic dianhydride
PDI	:	Perylene diimide
PIGE	:	Paraffin impregnated graphite electrode
PV	:	Photovoltaic
RCPL	:	Right circularly polarized light
Red.	:	Reduction
RT	:	Room temperature
Sat.	:	Saturated
$S_{(u/s)}$	:	Integral emission area of (unknown/standard)
SC	:	Solar cell
SCE	:	Saturated calomel electrode
SHE	:	Standard hydrogen electrode
s	:	Standard
S	:	Singlet state
SWV	:	Square wave voltammetry
T	:	Triplet state
$TBAPF_6$	:	Tetrabutylammoniumhexafluorophosphate
T_d	:	Decomposition temperature
TFAc	:	Trifluoroacetic acid
TGA	:	Thermogravimetric analysis
THF	:	Tetrahydrofuran

TWh/yr	:	Terawatt-hour per year
u	:	Unknown
UV-vis	:	Ultraviolet visible light absorption
V	:	Volt
vs.	:	Versus
VB	:	Valence band
V_{oc}	:	Open Circuit Voltage
δ	:	Chemical shift
ε	:	Extinction coefficient
ε_{max}	:	Maximum extinction coeffiecient/Molar absorptivity
Φ_f	:	Fluorescence quantum yield
Θ	:	Ellipticity
$[\Theta]$	:	Molar ellipticity
ν	:	Scan rate
υ	:	Wavenumber
$\Delta\bar{\nu}_{1/2}$	:	Half-width (of the selected absorption)
$\bar{\nu}_{max}$	:	Mean frequency (of the selected band)
τ_0	:	Theoretical radiative lifetime
τ_f	:	Fluorescence lifetime
λ	:	Wavelength
λ_{exc}	:	Excitation wavelength
λ_{em}	:	Emission wavelength

λ_{max}	:	Maximum wavelength
$[\alpha]_D^{20}$	:	Specific optical rotation

xxx

Chapter 1

INTRODUCTION

For a maintainable civilization, availability of clean, safe and affordable energy in adequate amounts for each citizen is precondition. The world energy supply should be sustainable in itself as well. In other words, renewable energy technologies should replace gradually the use of limited fossil resources so that greenhouse gas (GHG) emissions have to be diminished considerably [1]. Renewable energy sources include biomass, solar, wind, geothermal and hydropower energies. They use endemic resources which result in zero or almost zero emissions of air pollutants and greenhouse gases. Unfortunately, photovoltaic energy is the most expensive source referring to Table 1.1 which makes the further development in the field of less expensive materials and lower processing costs inevitable.

In literature, photovoltaics (PV) has the meaning of *light-electricity*; *photo* comes from the Greek word; *phos*, meaning *light* and *volt* from the scientist Alessandro *Volta* who first studying electricity [1]. In 1839, Becquerel discovered the photovoltaic effect by observing a photocurrent when platinum electrodes covered with silver halogen were irradiated in aqueous solution [2].

Table 1.1: Energy production and cost in the world [2].

	World energy production in 2003 (TWh)	Electricity costs in 2003 (€ cents / kWh)
Hydroelectricity	3000	2-8
Bio-energy	175	5-6
Wind energy	75	4-12
Geothermal	50	2-10
Marine energy	0.5	8-15
Solar thermal energy	0.8	12-18
Photovoltaic energy	2.5	26-65
Renewable energies	3300	-
Total electrical energy	15000	2-3.5

Arrays which can be formed by ranging from a few milliwatts up to a multi-megawatt installation is the unique property belonging to photovoltaics. It is recorded that the total amount of solar energy reaching earth's surface exhibits several thousand times the world total energy use. The renewable energy sources have a potential greater than 440,000 TWh / yr, i.e. almost 4 times the earth's total energy consumption. It is clear that PV could definitely compensate for the majority of future electrical needs (Figure 1.1) [1].
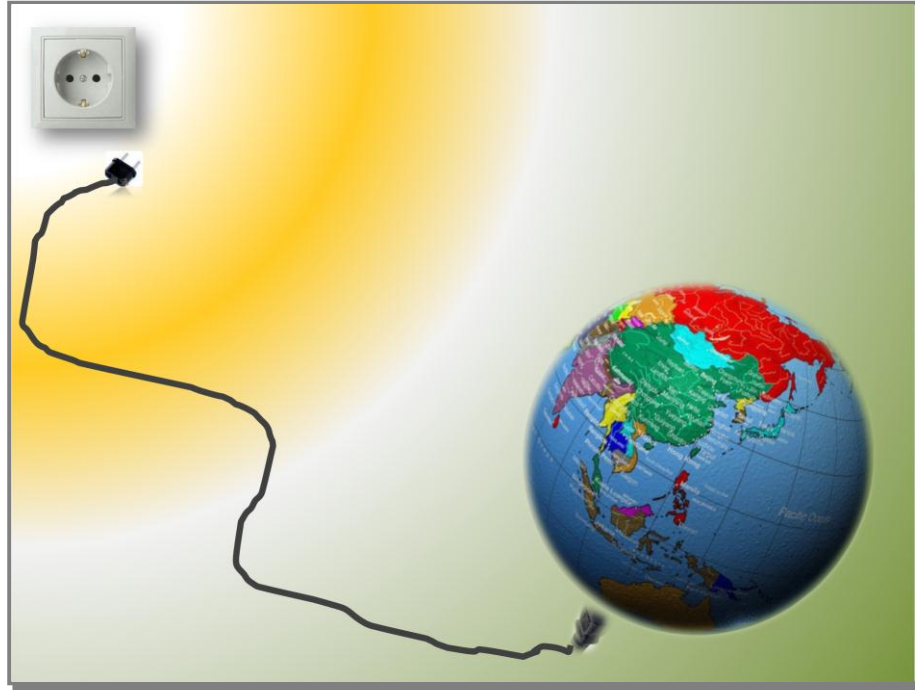
Figure 1.1: Earth supplying its all electricity demands by PV in the near future.

The solar cells, photovoltaic devices, directly utilize solar radiation to produce electricity [3]. Silicon-based solar cells have been developed very fast in the last decades and dominate the photovoltaic markets (70%) today. Although silicon-based solar cells exhibit excellent properties in efficiency (25% power conversion efficiency) and lifetime, the high cost of raw materials and complex processing techniques seem to outweigh their advantages. Therefore, it is needed to develop new materials and concepts in this field not only for reducing the overall production cost of PV technology but also for increasing their efficiency [4].

In literature, dye-sensitized solar cells (DSSCs,) have emerged as an inexpensive and environmentally friendly alternative for the conversion of solar energy into electricity based on a large band gap nanocrystalline semiconductor sensitized by a dye which is chemically linked to the semiconductor surface and exhibits considerable absorption in the visible range [5,6]. It was Grätzel who pioneered the

3

nanocrystalline DSSC technology in the early nineties and he published its best conversion efficiency to be over 10% in 2003 [7].

The fundamental photophysical and redox reactions involved in a DSSC are represented schematically below:

$$D + h\upsilon \rightarrow D^* \tag{1}$$

$$D^* + TiO_2 \rightarrow D^+ + e^-_{CB}(TiO_2) \tag{2}$$

$$D^* \rightarrow D \tag{3}$$

$$2D^+ + 3I^- \rightarrow 2D + I_3^- \tag{4}$$

$$D^+ + e^-_{CB}(TiO_2) \rightarrow D + TiO_2 \tag{5}$$

$$I_3^- + 2e^- \text{ (catalyst)} \rightarrow 3I^- \tag{6}$$

$$I_3^- + e^-_{CB}(TiO_2) \rightarrow 3I^- + TiO_2 \tag{7}$$

When the dye (D) is exposed to light ($h\upsilon$), it is excited to electronically excited state D^* (1). Intentionally the dye is selected in such a way that its electronic excited state lies energetically above the conduction band (CB) edge of the semiconductor nanoparticles. Under this condition, electron injects to the semiconductor (2) successfully, competing with the deactivation reaction (3). In order to obtain a high current generation, the oxidation of iodide (4) and reduction of iodine (6) have to compete effectively with the charged-separated recombination reactions (5) and (7). Generally, the mixture of I_3^-/I^- ions in organic solvents commonly is used as charge

4

carriers [8,6].

DSSC has three essential components for photocurrent generation:

1. A nanocrytsalline oxide semiconductor as an electrode responsible for photoelectron collection [5]. TiO_2, ZnO, SnO_2, Nb_2O_5 are some familiar semiconductor oxides which have been used in DSSC. Due to its low price, abundance in the market, nontoxicity, biocompatibility and wide applicability in health products as well as in paints, TiO_2 is the most preferable semiconductor till now [9].

There are a number of functional groups such as salicylate, carboxylic acid, sulphonic acid, phosphonic acid and acteylacetonate derivatives through which anchoring to TiO_2 could be achieved. The carboxylic acid and phosphonic acid functional groups are the most widely used and successful ones up to now [10]. In the literature, there is little information about the binding mode of phosphonic acid derivatives even though an ester type formation has been suggested. The carboxylic acid groups, while enabling efficient adsorption of the dye on the surface, can motivate electronic coupling between the donor levels of the excited dye and the acceptor levels of TiO_2 semiconductor [10]. It is noted that the adsorption of dyes onto TiO_2 surface is taking place through the formation of C-O-Ti ester linkage of carboxylic group with the TiOH group [11]. Accordingly, the most likely binding configurations of carboxylic group containing synthesized perylene dyes, onto TiO_2 surface have been proposed in Figures 1.2-1.5.
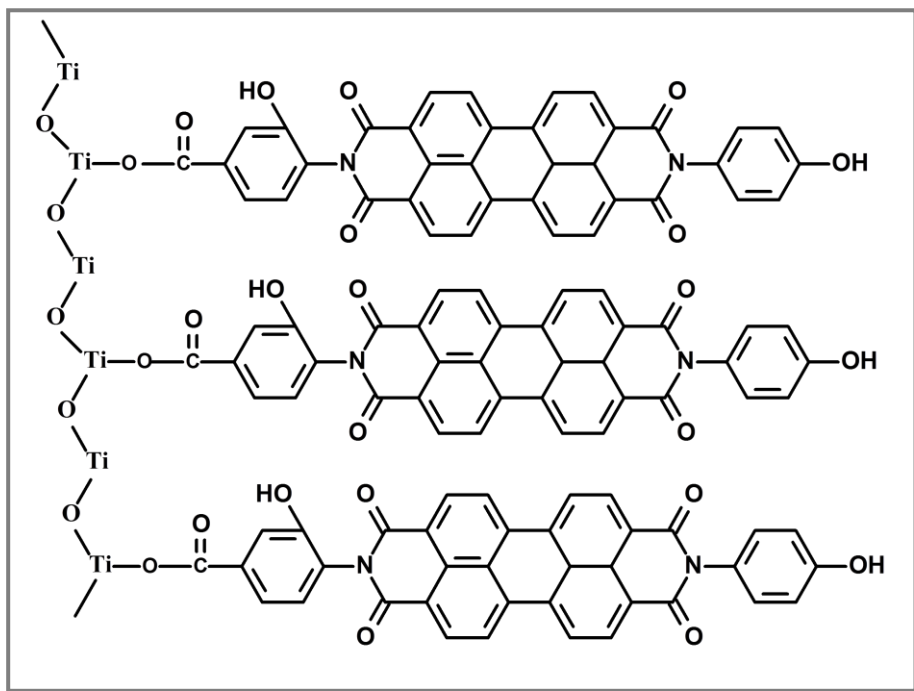
Figure 1.2: The most likely binding configuration of N-(2-hydroxy-4-benzoic acid)-N'-(4-hydroxyphenyl)-3,4,9,10 perylenebis(dicarboximide) (BPDI) onto TiO_2 surface.
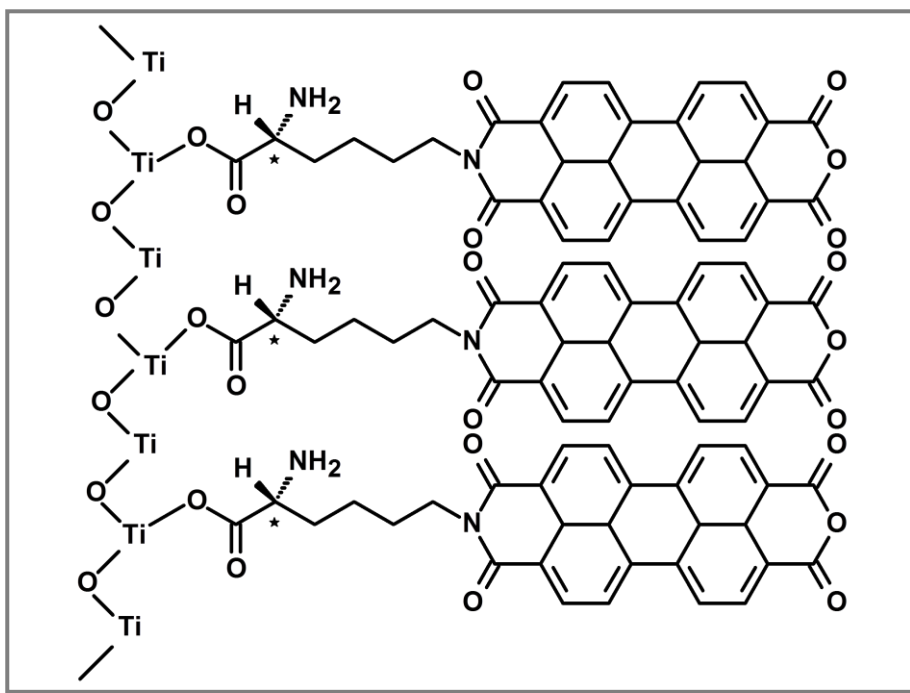
Figure 1.3: The most likely binding configuration of N-((2S)-2-aminohexanoic acid)-3,4,9,10 perylenetetracarboxylic-3,4 anydride-9,10 imide (LPMI) onto TiO_2 surface.
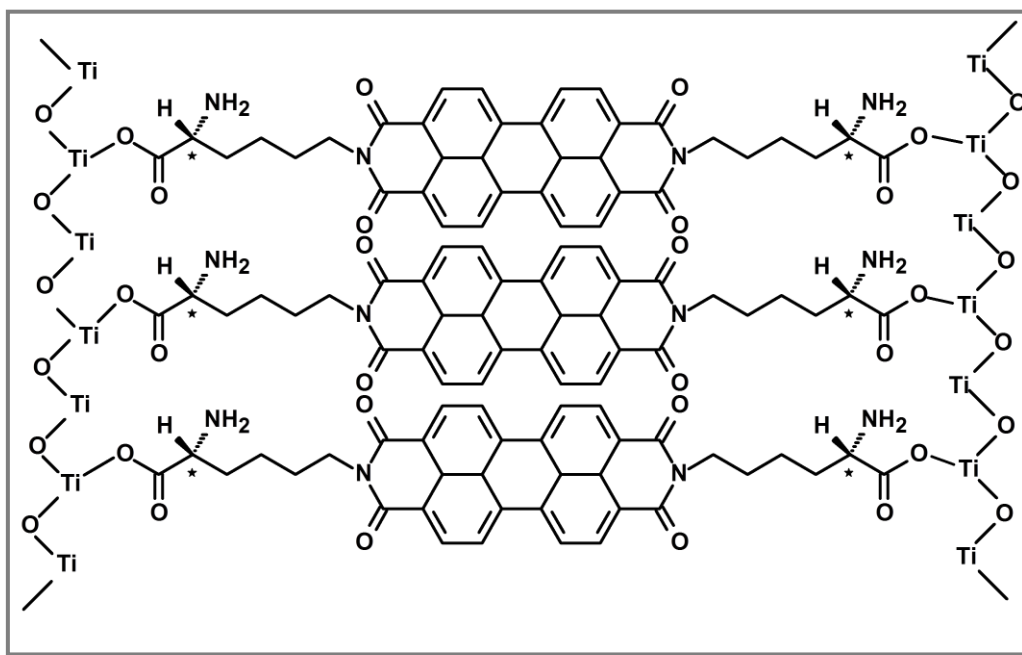
Figure 1.4: The most likely binding configuration of N,N'-bis((2S)-2-aminohexanoic acid)-3,4,9,10 perylenedicarboximide (LPDI) onto TiO_2 surface.
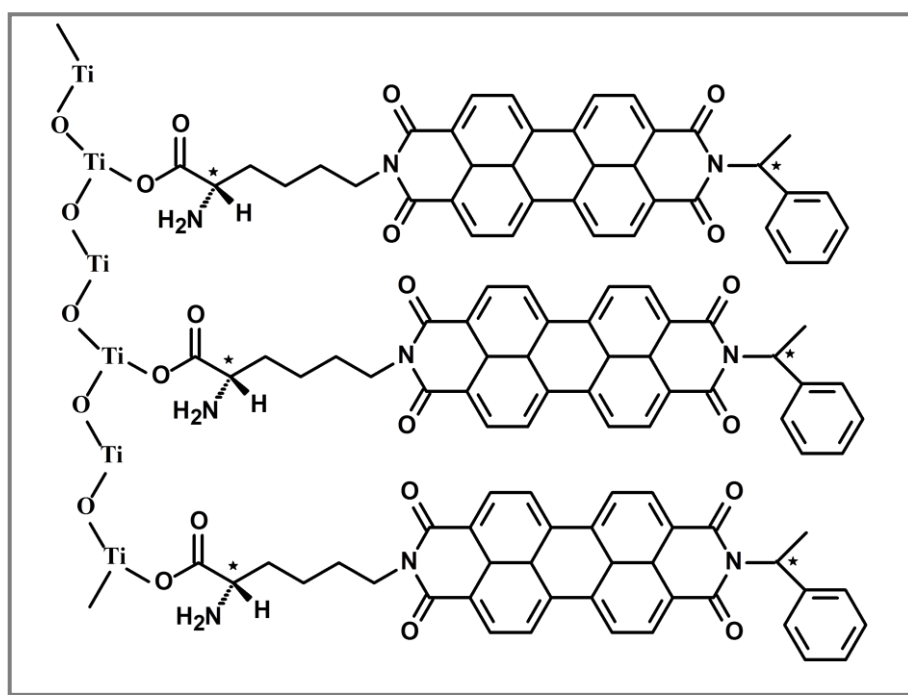
Figure 1.5: The most likely binding configuration of N-((2S)-2-aminohexanoic acid)-N'-((S)-1-phenylethyl)-3,4,9,10 perylenedicarboximide (LPPDI) onto TiO_2 surface.

2. Suitable dye molecules attached to TiO_2 surface for visible absorption [5]. A dye sensitizer is expected (which serves as the solar absorber in DSSC) to absorb all light below 920 nm. Moreover, it is necessary to be sustainable at least 10^8 redox turnovers under irradiation. This refers to 20 years of exposure to ambient light [9].

The sensitizers used in DSSC can be classified into two categories according to their structure; organic and inorganic dyes. Inorganic dyes consist of metal complexes like poylpyridylcomplexes of ruthenium and osmium, metal porphyrin, phthalocyanine and inorganic quantum dots. While organic dyes can be natural and synthetic organic dyes [9]. Due to high stability, outstanding redox properties and good response for natural visible, polypyridyl ruthenium dyes are widely applied and investigated as sensitizers [9]. Some Ru dyes reported in literature are presented in Figure 1.6 together with their conversion efficiencies. Organometallic dyes, N3, N719 and black dye developed by Grätzel showed more than 11% efficiency in DSSC. On the other hand, the increase in the demand for Ru raw materials seems to make ruthenium complexes increasingly more expensive. As a consequence, further research and development of a wide variety of dyes with different binding groups and linkers in DSSC have been inevitable [10].

Organic dyes, exhibiting the advantages of easy separation and purification, lower cost, higher molar absorption coefficients than Ru (II) complexes, easy molecular design (the introduction of substituent onto chromophore skeleton would enable the control of photophysical, electrochemical properties and stereochemical structures)

caused the development of DSSC based on organic dyes [9]. Figure 1.7 shows a summary of organic dyes used in literature with their conversion efficiencies.

Recently, Grätzel and co-workers have introduced a series of new π-conjugated organic dyes (abbreviated as HKK-BTZ1, HKK-BTZ2, HKK-BTZ3 and HKK-BTZ4) consisting of triphenyl amine (TPA) moieties as the electron donor and benzothiadiazole moieties as the acceptor/anchoring groups for the application in DSSCs [12]. They have reported 7.30% of maximum photo-to-electron conversion efficiency based on HKK-BTZ4 dyes. Somehow, it was 7.82% with Ru dye N719-sensitized DSSC. This implies the compatibility of organic sensitizers with Ru-based dyes. However, sharp and narrow absorption bands in the blue region of visible region of organic sensitizers are still their disadvantages which have to be improved and overcome.

3. An electrolyte conducting electrons from the counter-electrode for the regeneration of the excited dye cations [5].

There are 3 types of electrolytes that can be used in DSSC; liquid electrolytes, quasi-solid state electrolyte and solid electrolyte. The liquid electrolytes depending on the solvent used can be divided into two groups: Organic solvent electrolyte and inorganic liquid electrolyte. The commonly used redox couple in DSSC is I_3^- / I^-. More detailed explanations and discussions about the solar cells are presented in Chapter 2.
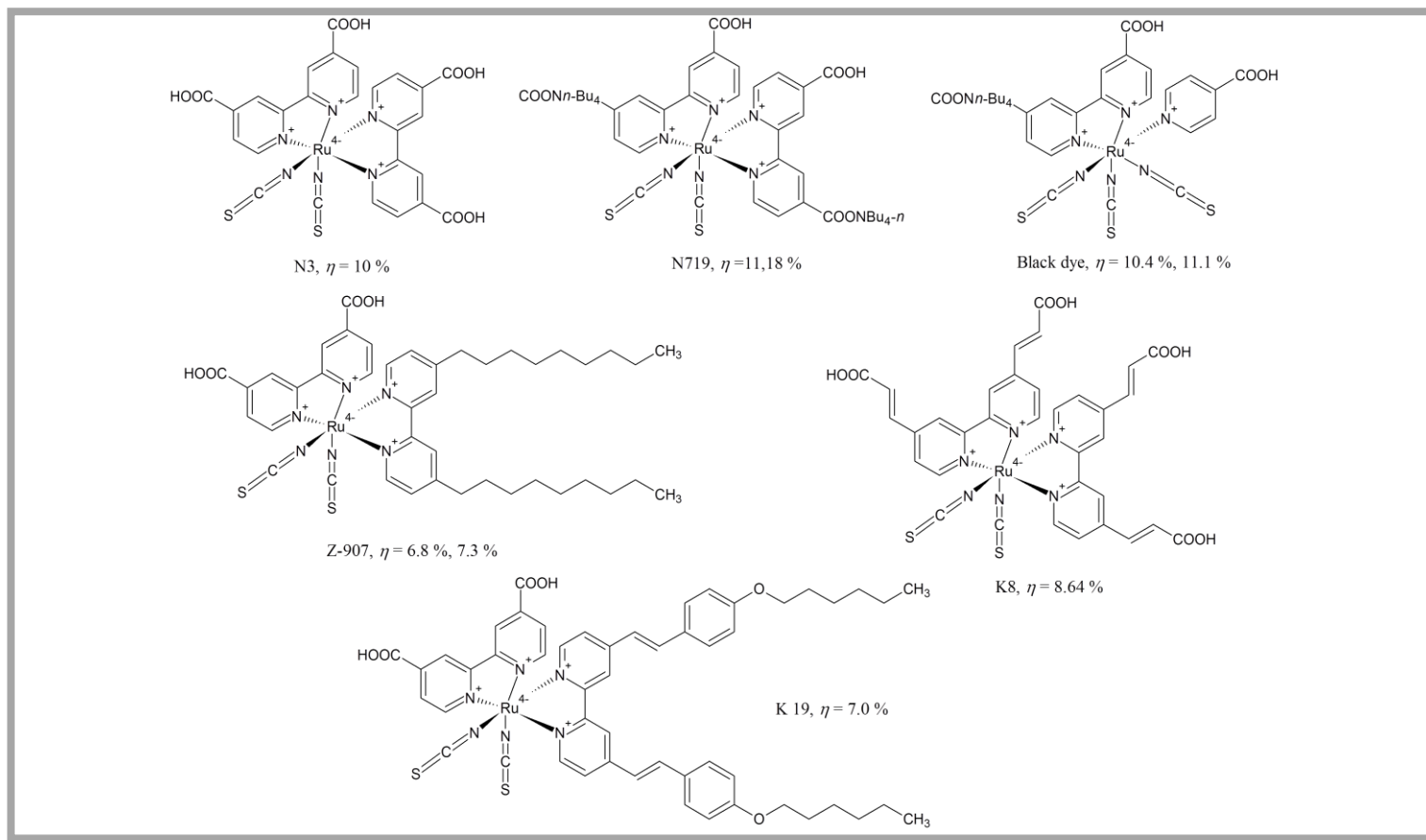
Figure 1.6: Molecular structures of some Ru-based dyes and their conversion efficiencies [9].
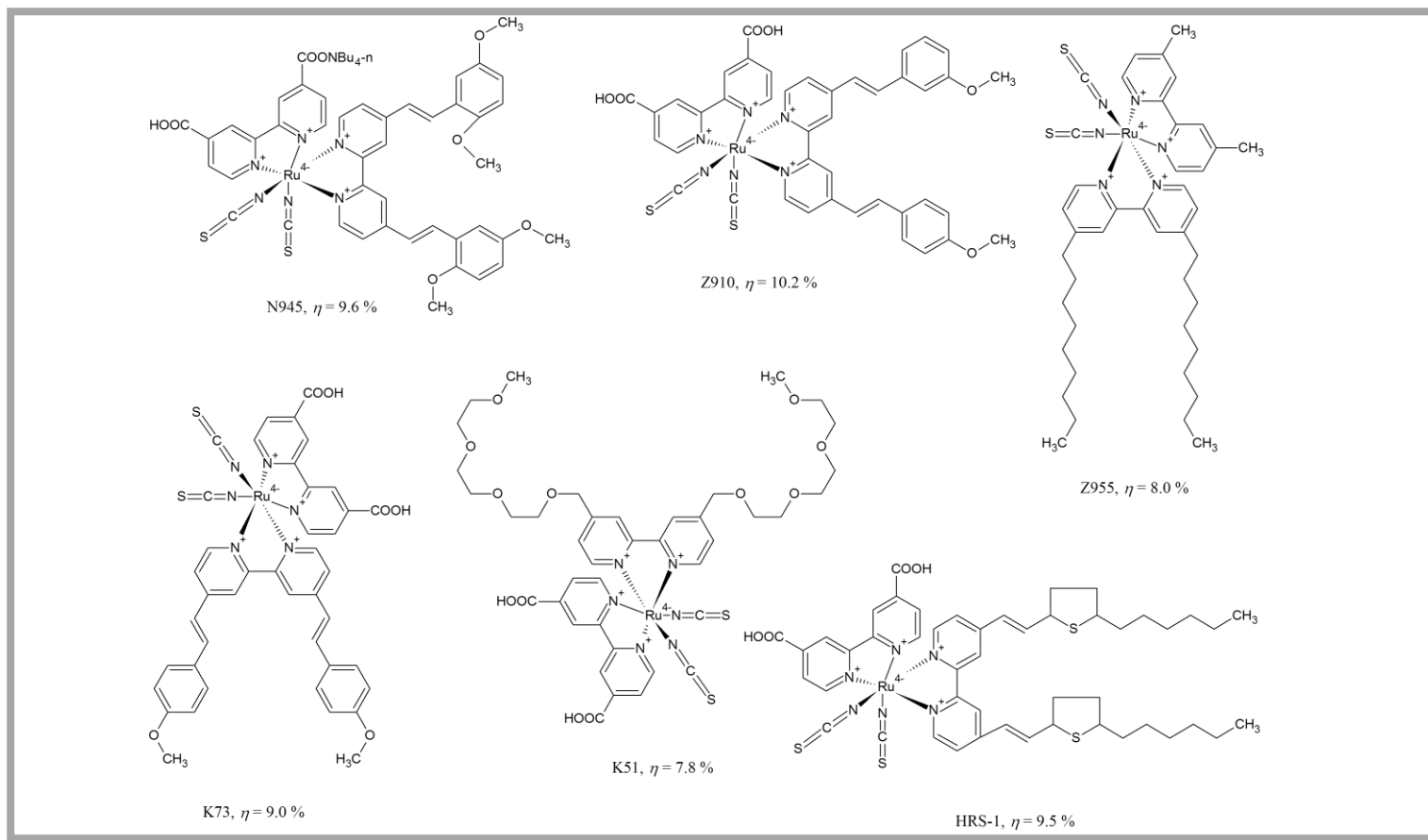
Figure 1.6: Molecular structures of some Ru-based dyes and their conversion efficiencies [9] (cont).
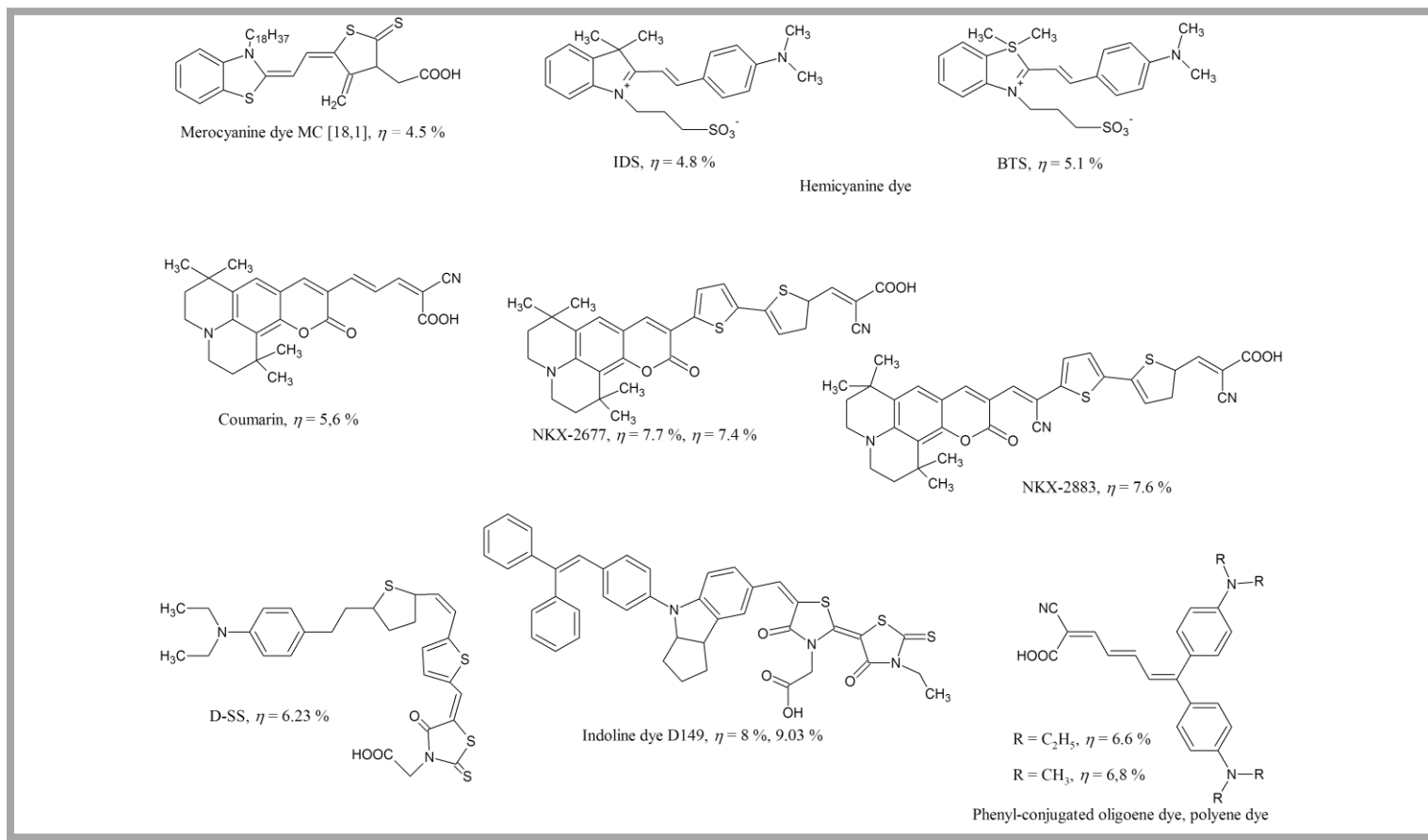
Figure 1.7: Molecular structures of some organic dyes and their conversion efficiencies [9].
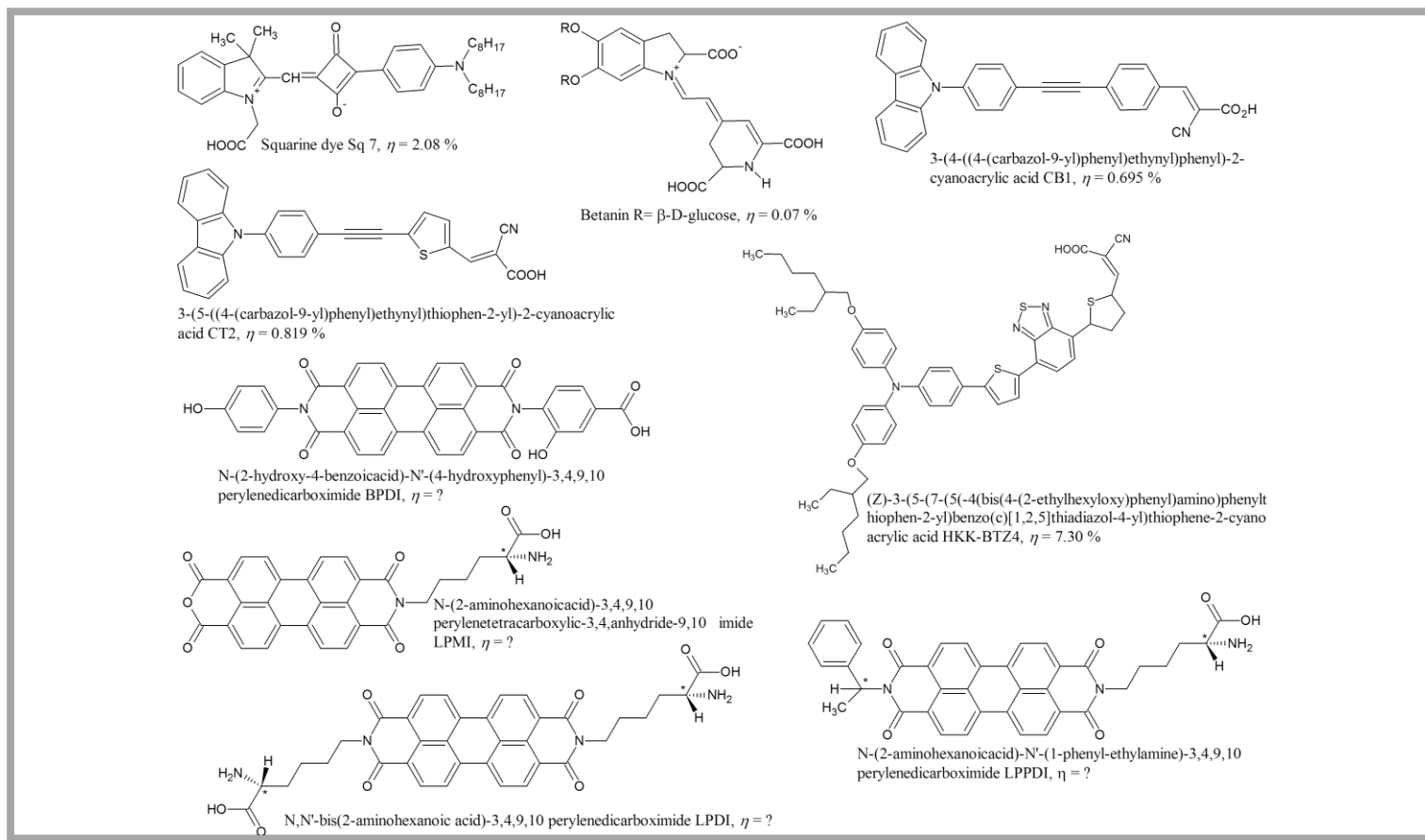
Figure 1.7: Molecular structures of some organic dyes and their conversion efficiencies [9] (cont).

In the present study, we have synthesized four special and novel perylene derivatives; N-((2S)-2-aminohexanoic acid)-3,4,9,10 perylenetetracarboxylic-3,4 anydride-9,10 imide (LPMI), N,N'-bis((2S)-2-aminohexanoic acid)-3,4,9,10 perylenedicarboximide (LPDI), N-((2S)-2-aminohexanoic acid)-N'-((S)-1-phenylethyl)-3,4,9,10 perylenedicarboximide (LPPDI) and N-(2-hydroxy-4-benzoic acid)-N'-(4-hydroxyphenyl)-3,4,9,10 perylenedicarboximide (BPDI). Their specialty arises from their synthetic routes and the features of the substituents.

In literature, planarity of aromatic systems is important for solar cell applications as it is expected to favor charge and energy (exciton) transport. The well-defined vibronic structure would give rise better contribution of external quantum efficiency to absorption features [13]. Perylene-3,4,9,10-tetracarboxylic dianhydride (PDA) has a rigid, planar π system which suffers from intrinsically low solubility due to its strong π-π interaction. Solubilizing substituents are required in order to improve the processibility of PDA. For the cases as in solar cells where the retaining planarity of PDA is important, terminal positions are the preferred sites for attaching the subsituents. All of the 4 novel dyes have been synthesized by nucleophilic attack at the terminal positions.

As it is discussed previously, carboxylic group containing dyes are highly preferable in the construction of DSSCs as adsorption of dyes onto TiO_2 surface is achieved through the formation of C-O-Ti ester linkage. Accordingly, all of the compounds have at least one carboxyl group in their structure providing a wide range of their applications.

LPMI, LPDI and LPPDI are chiral compounds having at least one α-amino acid, L-lysine as an amine source. Zhao and co-workes have reported steric and sterochemical control would be safely achieved by using an enantiomerically pure α-amino acid with a tunable side group as amine source. It is also mentioned that the configurational chirality may be expressed as helical aggregates of PDI chromophores in a defined fashion, which could result in an increased density of charge carrier mobilities [14]. Besides potential applications in DSSCs, the chiral property of these compounds suggests opportunities in biochemistry as DNA-binding and chirooptical switches.

These four novel synthesized compounds have been characterized and investigated in detail by NMR, IR, UV-vis, emission, DSC, TGA, elemental analysis, CV, SWV (both in solid and solution) and CD (except that of BPDI).

Chapter 2

THEORETICAL

2.1 Solar Cells (Photovoltaic Cells)

A solar cell or a photovoltaic (PV) cell is a tool that changes solar energy into electricity via photovoltaic effect [15]. Photovoltaic effect is based on photons absorption inducing the formation of electron hole pair formation (photoconductive effect) which is followed by charge separation by means of the junction. In 1839, Becquerel observed a photocurrent when platinum electrodes, covered with silver halogen were illuminated in aqueous solution (photoelectrochemical effect) [2]. Hence, he discovered the photovoltaic effect.

In general, junction devices are accepted as photovoltaic cells or solar cells and here it should be emphasized that it is the current not the voltage which is produced by the radiation of photons. The cell itself supplies the source of electromagnetic force (e.m.f.). In addition, photoelectric devices which are electrical current sources, are driven by a flux of radiation. Most of the photovoltaic cells are silicon semi-conductor junction devices.

Three generations of solar cells exist depending on the order of each became prominent.

1- First Generation:

First-generation cells are accepted as the cells having large surface area, high-quality and single junction devices. They are the most represented productions commercially. However, due to their high energy and labour input demand, any significant development in order to decrease production costs is limited. Single junction silicon devices are reaching the theoretical limiting efficiency of 33%.

2- Second Generation:

Development of second-generation materials is aimed to focus on energy needs and production costs of solar cells. Vapour deposition and electroplating are advantageous alternative manufacturing techniques so that they reduce high-temperature processing significantlyly. Second-generation technologies have been available in market place since 2008. The most successful second generation solar cells are cadmium telluride (CdTe), copper indium gallium selenide, amorphous silicon and micromorphous silicon.

3- Third Generation:

The main purpose of third-generation technologies is to increase the electrical performance of solar cells keeping comparatively less expensive production costs as well. Active research is forcing conversion efficiencies up to 30-60%. This generation includes dye-sensitized solar cells, polymers solar cells, and nanocrystalline solar cells. They differ from classical p-n heterojunction (consisting of bulk junctions where charge separation is achieved). This approach can be offered as an alternative way for producing less expensive solar cells [15].

2.2 Dye-sensitized Solar Cells (DSSC)

A dye-sensitized solar cell can be accepted as a hybrid of photogalvanic and solar cells based on semiconductor electrodes. The cell is made up of a dye coated semiconductor electrode and a counter electrode oriented in a sandwich arrangement and an electrolyte containing a redox mediator (A/A⁻) [16] (typically, dye-derived nanocrystalline titania films as photoanode, platinized counter electrode filled with electrolyte solution of I_3^-/I^- in organic solvents [9]).

2.2.1 Basic Principles of DSSC

The basic operating principles of DSSC have been given in Figure 2.1. When exposed to sunlight, the dye molecule becomes photo-excited and ultrafast injects an electron into the conduction band of the semiconductor electrode. Later the dye is subsequently restored to the original state by the electron given by the electrolyte, usually the solution of an organic solvent or ionic liquid solvent containing the I_3^-/I^- redox system. The recapture of the conduction band electron by oxidized dye regeneration is intercepted by the regeneration of sensitizer by iodide. While the iodide is regenerated, in turn, by reduction of triiodide at the counter electrode, the circuit is being completed through the external load [9]. The maximum photovoltage that could be achieved will be the difference between the Fermi level (conduction band) of the semiconductor under illumination and the redox potential of the mediating redox couple. As a result, electric power is generated without a permanent chemical transformation. Along with these processes, electrons in the conduction band of semiconductor may be recombined with the oxidized dye sensitizers or electron [16].
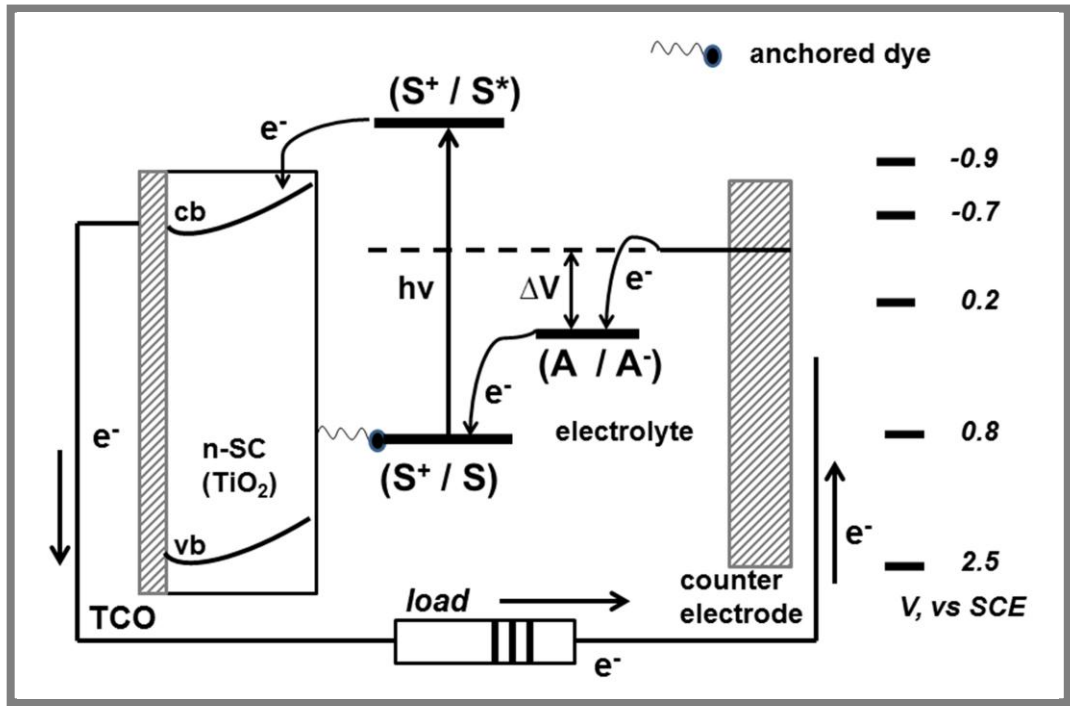
Figure 2. 1: Schematic presentation for operation principles of dye-sensitized solar cells [16].

The orders of magnitude for the rate constants of electron transfer steps involved in DSSC are schematized and summarized in Scheme 2.1. Electron injection into the conduction band is in the sub-ps to ps range. Rate constant for the back electron transfer is much smaller typically $\tau \sim 1$ μs. The electron passing through the nanocrystalline TiO_2 electrode to the back contact is highly slower than that of a single crystal TiO_2 decaying in the ms to s range. Reduction of the oxidized dye by iodide takes place on a timescale of 10^{-8} s [16].

$$D^* \rightarrow D \qquad\qquad\qquad \sim 30 \text{ ns}$$

$$D^* + TiO_2 \rightarrow D^+ + TiO_2(e^-) \qquad < 200 \text{ fs}$$

$$D^+ + TiO_2 \rightarrow D + TiO_2 \qquad\qquad \sim 500 \text{ ns}$$

$$D^+ + I^- + I^- \rightarrow D + I_2^{-\bullet} \qquad\qquad \sim 20 \text{ ns}$$

$$I_2^{-\bullet} + e^- \rightarrow 2\, I^- \qquad\qquad \sim 100 \text{ ns to ms order}$$

$$2I_2^{-\bullet} \rightarrow I^- + I_3^- \qquad\qquad \mu s$$

$$I_3^- + 2e^- \rightarrow 3\, I^- \qquad\qquad ms$$
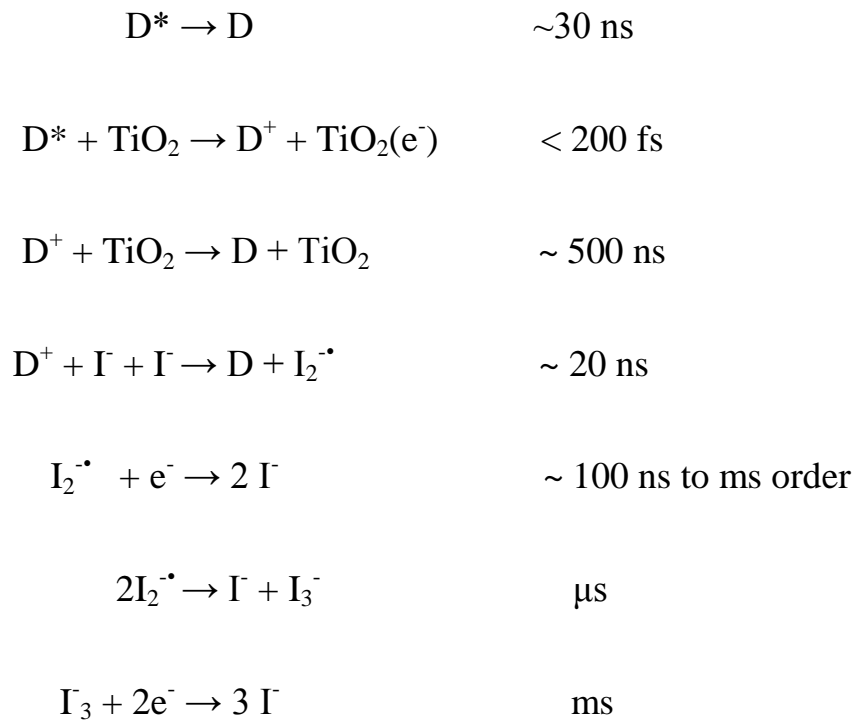
Scheme 2.1: Kinetics of electron transfer in DSSC.

2.2.2 Solid state dye-sensitized solar cells

Although liquid electrolyte based dye-sensitized solar cells are widely accepted as low cost and high-efficiency alternative to conventional inorganic photovoltaic solar cells, stability problems such as leakage, evaporation and contamination of the solvents hamper the progress of actual application [17]. To overcome this problem, solid-charge transport materials such as inorganic hole conductors, organic hole conductors or ionic polymer blends have been developed [18]. Mainly, small organic molecules as hole conductors are very promising for solid-state devices due to easy purification by standard methods, exact structure-property arrangements and high hole conductivity [19]. Bach et al presented the first dye-sensitized heterojunction of TiO_2 with the amorphous organic hole-transport material 2',2',7,7'-tetrakis(N,N di-

p-methoxyphenyl-amine)9,9'-spirobifluorene(OMeTAD) [20]. Recent studies and investigations have been in progress to increase the efficiency further to 4% [21].

2.3 Semiconductor

Solids can be classified as conductors, semi-conductors and insulators depending on their conductivity of electrons. In the case of insulators, the gap between the valence band and the conduction band (forbidden energy band) ($h\upsilon < E_g$), is very large. Thus there is no current conduction as it is not possible for the electrons in the valence band to reach the conduction band. For semi-conductors ($h\upsilon > E_g$), the gap is moderate hence the electrons in the valance band may acquire sufficient energy to cross the forbidden region. Finally, there is no forbidden gap existing for conductors ($E_g \sim 0$) and hence, electrons can easily move to the conduction band [15]. Semiconductors are special and essential for the construction of solar cells. In order to achieve electric power in a solar cell, generation of current and voltage are required. Generating current requires electron mobility and generating voltage needs a gap between electron energy states. Electron mobility and gaps between energy states are owned by metals and insulator, respectively, but it is only semiconductors which show both properties [22]. TiO_2, ZnO, SnO_2, and Nb_2O_5 are some of the semiconductor oxides used in dye-sensitized solar cells [9].

2.3.1 Titanium dioxide

Titanium dioxide (TiO_2), due to its low cost, abundance in the market, nontoxicity, thermal and photooxidative stabilities, is the most preferred metal oxide in the construction of nanostructured semiconductors as electrodes [9]. TiO_2 has mainly three crystalline structures; rutile, anatase and brookite. The most stable and extensively investigated form of the three structures is the rutile. However, anatase is

often used in electrodes in photovoltaic cells since anatase, thermodynamically has the most stable surface. The experimental bulk band gap is recorded as 3.0 and 3.2 eV for rutile and anatase, respectively [9,23].

2.3.1 Anchoring Groups

It is essential for the molecular components to be structurally modified so that they could be attached to the host matrix. Figure 2.2 exhibits some of the commonly used configurations of molecules binding to oxide and non-oxide surfaces. Silanyl, (–O–Si–), amide (–NH–(C-O)–), carboxyl (–O–(C-O)–), phosphonato (–O–(HPO$_2$)–) have proved to form stable linkages, Mostly, reactive elements (silanyl, carboxylic acid or phosphonic acid) react readily with surface hydroxyl groups of oxide surfaces to form stable linkages that show good stability.
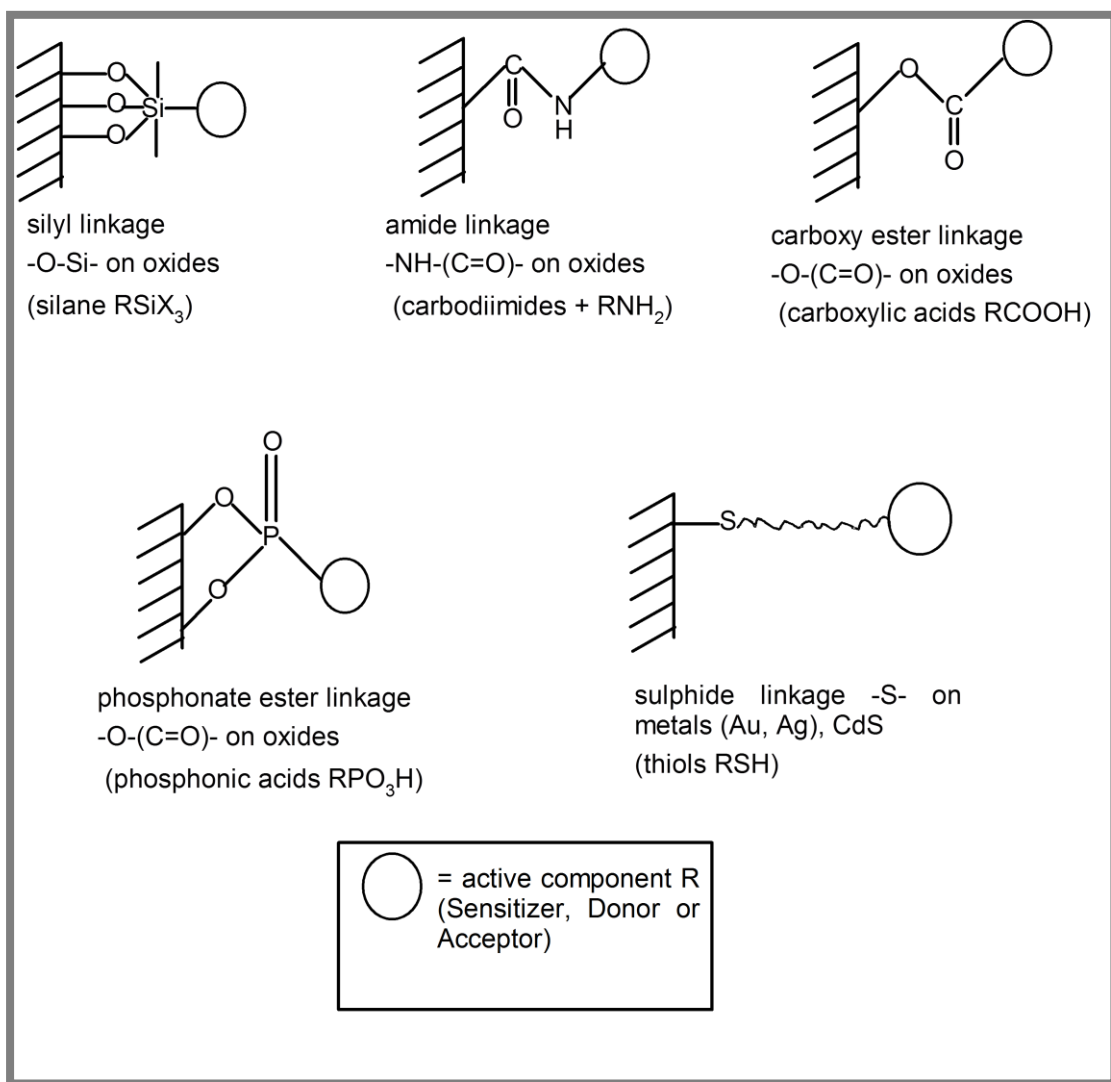
Figure 2.2: Some of the commonly used modes of attaching molecules on oxide and non-oxide surface [16].

2.4 Chromophores

As it was discussed earlier in Chapter 1, chromophores used in DDSC could be classified as ruthenium based chromophores and organic chromophores through which metal-free organic sensitizers has attracted great attention in recent years.

There are many reasons for using organic materials in the applications of photovoltaic solar cells:

1. They can be easily processed by spin coating or doctor blade techniques (wet-processing) or evaporation through a mask (dry-processing).

2. Organic materials are relatively small in amounts (100 nm thick films) and producing them in large scale is easier compared to that of inorganic materials (growth processes).

3. In order to adjust band gap, valance and conduction energies, charge transport together with solubility and several other structural properties, organic materials can be tuned chemically.

4. Many possible chemical structures and functionalities of organic materials (polmers, oligomers, dendrimers, organo-minerals, dyes, pigments, liguid crystals,...) give rise to an active research for competitive materials with the desired PV properties.

Polymers, oligomers, dendrimers, dyes, pigments, liquid crystals, organo-mineral hybrid materials, all organic semiconductors have in common part of their electronic structure which is based on conjugated π electrons. π electrons from conjugation are much more mobile than the σ electrons; that is they can jump from site to site between carbon atoms with a low potential energy barrier when compared to the ionization potential. Such a system shows all of the desired properties of organic materials like light absorption and emission, charge generation and transport [24].

2.4.1 Perylene Derivatives, Properties and Application Areas

Kardos in 1913 pioneered the investigation on chemistry of perylene and its derivatives [25] where he had explained the reaction of naphthalene-1,8-dicarboximide in molten alkali to perylene dimides. Since then, perylene colourants have been commercialized for red dyes and pigments.

Perylene dyes have unique properties such as strong absorption and emission, high fluorescence quantum yield near unity ($\Phi_F \approx 1$), nontoxicity and low cost [26]. They exhibit high thermal, chemical and photo stabilities as well as electrochemical performance [27]. They have high molar absorptivity and good n-type semiconductivity [28]. All these special features make perylene dyes extensively investigated active components in the fields of photovoltaic cells, chemical sensors, electroluminescent devices, organic field effect transistors (OFETs) [26], fluorescent solar collectors, laser dyes, light emitting diodes [29] and fluorescent labeling in biochemistry and medicine [30].

A main drawback of working with perylene dyes is their intrinsically low solubility due to strong π-π interaction. The solubility of the perylene bisimide strongly depends on the substitution (Figure 2.3) and two suggestions have been proposed to enhance the solubility in organic solvents. When the two N-substituents in the pery regions are two alkyl long chains or ortho-substituted phenyl groups, then these substituents will be forced out of the plane of the chromophore and thereby hamper the face-to-face π-π stacking of the perylene bisimides, which will improve the solubility of the molecules. Where the retaining planarity of PDI is important, pery positions could be the preferred sites for attaching the substituents [31]. Another suggestion for increasing the solubility of the perylene bisimide is the substitution to bay-positions (Figure 2.3). Bromination and subsequent imidization can lead to 1,6,7,12-tetrabromo-3,4:9,10-perylenedianhydride. It is possible to replace the bromines by bulky derivatives like piperidine. Because of their bulkiness, the substituents in the bay-region force the aromatic core to bend, which increases the solubility [32].

25
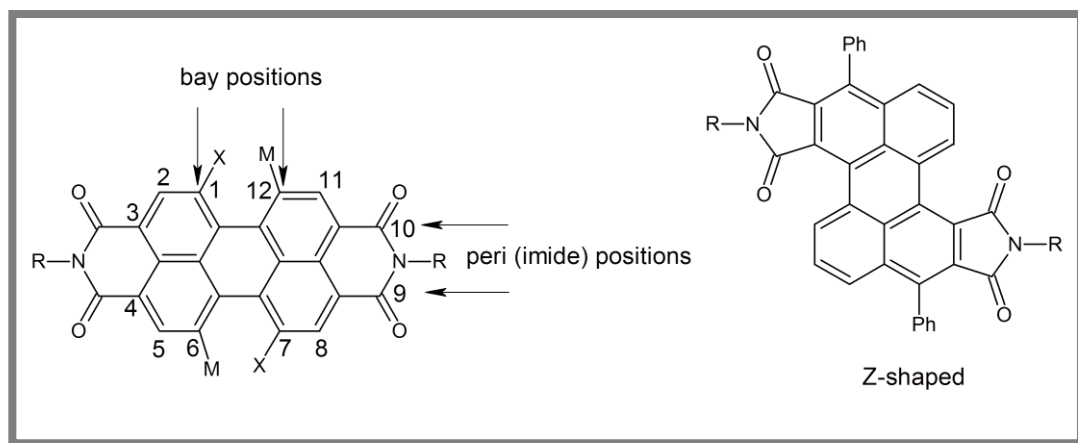
Figure 2.3: Synthetically feasible positions to tune electronic properties and enhance the solubility of PDI.

Ilhan and coworkers report the first and unique example of a nonlinear or Z-shaped perylene bisimide, N, N'-bis(octyl)-3,9-diphenylperylene-1,2,7,8-tetracarboxyl bisimide (18% yield) which differs from conventional linear systems in both the position and size of the imide rings (Figure 2.3). They observed that in spite of twisting of the perylene core, it exhibited similar absorption and emission behavior to conventional perylene bisimides [33].

2.4.2 Intermolecular interactions

The design and self-assembly of small functional molecule components into supramolecular aggregates are of great interest in comprehending intermolecular interactions as a main branch of supramolecular chemistry [34]. The supramolecular approach to the ordered PDI assembly based on many non-covalent interactions such as π-π interactions, static electronic interactions, and metal-ligand coordination have drawn attention a lot in the past decade [26].

Self-assembly, enabling an efficient control of highly mesoscopic order of molecules is a promising avenue for developing novel functional materials and enabling the tuning of macroscopic properties of optoelectronic devices such as solar cells, light emitting diodes, and field transistors [34]. Among the various methods to bring about

supramolecular self-organization, π-π interactions and hydrogen-bonding (directional and selective) are the most thoroughly studied interactions [35].

2.4.2.1 Types of aggregates

Van der Waals like attractive forces between the molecules are strong intermolecular forces which often cause self-association of dyes in solution or at the solid-liquid interface in dye chemistry. The aggregates show clear changes in the absorption band when compared to monomeric species. The molecular exciton coupling theory; coupling of transition moments of the constituents, express the bathochromically shifted J-bands (J for Jelly, who pioneered the investigation of these shifts) and hypsochromically shifted H bands (H for hypsochromic) of the aggregates. They are called J aggregates and H aggregates which exhibit J bands and H bands, respectively in their absorption spectrum.

The dye molecule is accepted as a point dipole and the excitonic state of the dye aggregate is separated into two levels via the interaction of transition dipoles according to exciton theory (Figure 2.4). The dye molecules either may aggregate in a parallel (//) manner (plane to plane stacking) to form a sandwich-type configuration (H-dimer) or in a head to tail configuration (end to end stacking) to form a J-dimer. While a transition to the higher state in a parallel configuration having parallel transition moments leads to hypsochromic (blue) shift, a transition to a lower state in head to tail configuration with 90° transition moments gives rise to a bathochromic (red) shifts.
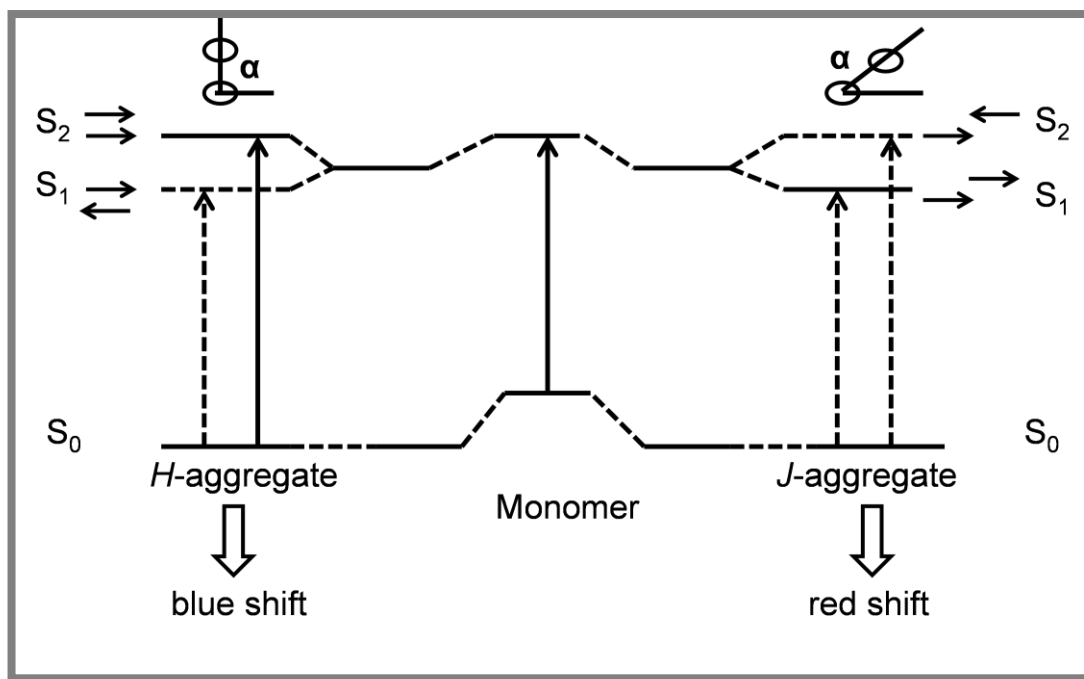
Figure 2.4: Presentation of the relationship between chromophore arrangement and spectral shift based on the molecular exciton coupling theory [36].

Parallel dye molecules stacked plane to plane and end to end give rise to H and J aggregates and form crystal molecule in two dimensions. Depending on their structural packing, H and J aggregates have different optical properties. It is the different slip angles of the stacked molecules which give rise to difference in structure. The slippage angle can be explained as the angle between long axis (line passing through the center of the aggregates or parallel to it) and one of the parallel molecule. According to exciton coupling theory (Figure 2.4), when chromophores are aligned in a parallel manner, two new excitonic bands, one with greater energy and the other with lower than the monomer energy level are generated. In H aggregates, it is the lower state more stabilized. As a result, the transition from the excited state to the ground state is very quick and generally occurs between the excitonic bands with diminishing dipole moments due to most of the nonradiative energy losses like thermal losses. Hence, H aggregates show large Stoke shifts with

28

low fluorescence yields. In case of J aggregates, transition only to low energy states is allowed. As a result, J aggregates have little Stoke shift with high fluoresence quantum yields which enable their detection by fluorescence microscopy as well.

Ghosh and coworkers investigated the influence of peripheral alkyl side chains on the self-assembly of perylene bisimide chromophores and reported that chromophores substituted with linear alkyl chain (least steric demand) formed sandwich-type H aggregates whereas perylene bisimide chromophores bearing branched alkyl groups (higher steric demand) formed slipped J aggregates or no aggregates at all [37].

Jancy et al. synthesized a series of highly fluorescent liquid-crystalline perylene diimide molecule having amide or ester linkage and end-capped by phenyl, monododecyloxy phenyl or tridodecyloxy phenyl units. The self-organized amide-functionalized series formed H-type aggregates in toluene etc., while only the monododecyloxy phenyl end-capped molecule in the ester series tended to self-organize with a typical J aggregate in toluene [38].

2.4.2.2 Hydrogen-bonding

Hydrogen-bonding has been recorded as the most important of all directional intermolecular interactions. It plays a key role in determining the molecular configuration and molecular aggregation. It was stated that the discovery of hydrogen bonding was almost 100 years ago and still is a vital topic in scientific researches including minerology, material science, general inorganic and organic chemistry, biochemistry, molecular medicine and supramolecular chemistry [39]. Due to directionality and specificity of hydrogen-bonding, much interest has been grown in various supramolecular systems such as urea-containing tetraphoxy-

substituted perylene bisimide synthesized by Wurthner et al. [40]. Moreover, the fascinating architecture and unique functionality have motivated Young and coworkers to prepare perylene bisimide derivatives bearing complementary hydrogen-bonding moieties (perylene derivative bearing two melamine blocks and 1,6,7,12-tetra(4-tert-butylphenoxy)-perylene-3,4,9,10-tetracarboxylic acid bisimide) with the final targeting of developing novel functional materials and optoelectronic devices [34].

2.4.3 Supramolecular Chirality and Amphiphilicity in Solution and in Solid-state

Self-assembling of organic molecules both in solution and solid state is a vital step in designing bottom-up electronic and optoelectronic devices [41]. Precise control of the morphology and properties is a main challenge in supramolecular self-assembly. As a result, the importance of precise modulations of the morphology and properties of PDI self-assembly via non covalent interactions such as π-π interaction, van der Waal forces, hydrogen bonding, static electronic interactions and metal ligand coordinations has previously mentioned in the above section [42,26]. Besides the tendency of PDIs to aggregate into n-type semi-conducting molecular stacks, in the presence of chiral units, helical PDI stacks with preferred handedness would be achieved which could lead to increased charge carrier mobilities [43]. In addition to these, introduction of amphiphilicity is expected to add one more dimension to the self-assembling of PDIs providing different morphologies like micelles, vesicles, planar bilayers and nanotubes. There morphologies are affected by environmental parameters such as nature of the solvent, the ratio of the good/poor solvent or temperature [44]. In literature, there are few reports on amphiphilic unsymmetric PDIs and nonracemic chiral amphiphilic unsymmetric PDIs so far may be due to the

difficulties on the synthesis of amphiphilic PDIs [26]. R. Sun and coworkers reported the first two nonracemic chiral amphiphilic PDI with enantiomerically α-amino acids [43]. Then C. Xeu and coworkers synthesized the first soluble nonracemic chiral perylene tetracarboxylic diimide polymers via acylic diene metathesis polymerization with the use of optically pure l-α amino acid as the starting materials [14]. Among some examples of the amphiphilic unsymmetric PDIs, N-decylperylene-3,4,9,10   tetracarboxylic,3,4-ethoxyethoxyethoxypropyl-9,10-imide synthesized by X. Yang et al, and 1,7-bis-pyridinoyl perylenediimide amphiphile reported by S. Xu and coworkers are available in literature [41,42]. Very recently sugar-based amphiphilic based perylenediimide derivative N-(l-hexylheptyl)-N'-((4-amino-phenyl)-α-D-glucopyranoside)-perylene-3,4,9,10-tetracarboxylbisimide   has been synthesized and reported by Y. Huang an coworkers [44].

2.4.4 Photoinduced Electron/Energy Transfer (PET)

Conversion of sunlight to chemical potential is a vital and attractive chemical reaction in nature and is based on the photoinduced electron transfer in the photosynthetic reaction center. This fascinating process has potential applications in many areas such as photomedicine, photovoltaic cells and molecular devices which serve as sensors and switches.

In photoinduced energy and electron transfers, upon photoexcitation energy of an electron is transferred from a donor to an acceptor resulting in a radical cation of the donor and a radical anion of the acceptor which recombine rapidly to the initial state of the system [27].
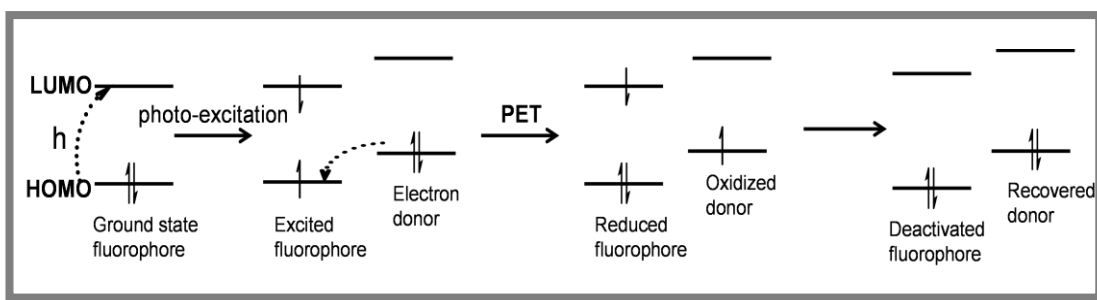
Figure 2.5: Schematic representation of photoinduced electron transfer [45].

Figure 2.5 shows schematically a photoinduced electron transfer taking place between an electron donor and a fluorophore (electron acceptor). Upon excitation, molecular orbital in higher energy is populated (HOMO is elevated) and electron transfer takes place.

Rybtchinski and coworkers studied the photoinduced electron transfer in self-assembled dimers of 3-fold symmetric donor-acceptor molecules based on peryelene-3,4,9,10-dicarboximide where N, N-diethylaniline and perylene dicarboximide made up donor-acceptor unit [46]. Recently, Aigner et al have prepared new fluorescent perylene diimide indicators which exhibited pH sensitivity by photoinduced electron transfer [45].

Chapter 3

EXPERIMENTAL

3.1 Materials

A Perylene-3,4,9,10-tetracarboxylic dianhydride, 4-aminophenol, 2-hydroxy-4-benzoic acid, potassium hydroxide, phosphoric acid and isoquinoline were supplied from Aldrich. 2,6-diaminohexanoic acid was purchased from Sigma. Sodium tetrafluoroborate ($NaBF_4$) and ferrocene were obtained from Fluka. All organic solvents used were of spectroscopic grade unless otherwise stated.

3.2 Instruments

Infrared spectra were obtained through KBr pellets using Mattson Satellite FT-IR spectrometer. UV/vis spectra of solutions were recorded with a Varian-Cary 100 spectrometer. UV/vis spectra of solid state were measured in thin films using a Perkin-Elmer UV/VIS/NIR Lambda 19 spectrometer, equipped with solid accessories. Optical rotations were measured with a Dr. Kernchen sucromat digital automatic polarimeter, 589 nm and 20 ^{0}C. CD spectra were measured on a JASCO 810 spectropolarimeter. Emission spectra of solutions and solid state were measured in thin films with a Cary Eclips spectrophotometer, equipped with solid state accessories. Solid-state emission spectra were recorded in the front-face mode with sample surface oriented at 35 ^{o} and 55 ^{o} with respect to the excitation and emission beams, respectively. The excitation was performed at 485 nm. Excitation and emission filters were used during the measurements of solid-state spectra in order to

minimize the signals from the scattered exciting light which is inherently greater when measuring opaque solid as compared to clear (non-scattering) liquids measured at the traditional light angle orientation. Elemental analyses were obtained from a Carlo-Erba-1106 C, H, N analyzer. TGA thermograms were recorded with a TG-MS: Simultane TG-TG-DTA/DSC apparatus STA 449 Jupiter from Netzsch, equipped with Balzers Quadstar 422 V. Samples were heated at 10 K/ min in oxygen. Thermal analyses were recorded using DSC 820 Mettler Toledo instrument. The samples were heated at 10 K/min nitrogen. ^{1}H and ^{13}C NMR spectra were recorded on Bruker AVANCE-400 spectrometer with tetramethylsilane (TMS) as internal reference. Cyclic and square-wave voltammetries in solutions were performed using a three-electrode cell with a glassy carbon as counter and 2 mm Pt as working electrode; solutions were 10^{-5} M in electroactive material and 0.05 M in supporting electrolyte, sodium tetrafluoroborate ($NaBF_4$). Ferrocene was used as an internal reference. The scan rate of 20–1000 mV^{-1} and the frequency 20–2000 Hz were employed for cyclic and square-wave voltammetries, respectively. Cyclic and square-wave voltammetries in solid state were performed using Ag/AgCl electrode as a reference electrode. Glassy carbon served as an auxiliary electrode. Carbon paste was used as the working electrode material which was obtained by pressing graphite powder (25 mg, Aldrich) and paraffin oil (10 µL, Fluka) mixture in a holed Teflon tip. The supporting electrolyte was 1 M HCl. The scan rate of 10–1000 mV^{-1} and the frequency 10–2000 Hz were employed for solid state cyclic and square-wave voltammetries, respectively. Fluorescence lifetime measurement was performed by time correlated single photon counting technique (FLS920, from Edinburgh Instruments).

3.3 Methods of Syntheses

In the previous chapter, in order to obtain a better processability, different types of synthetic approaches were mentioned for reducing perylene diimide (PDI) π-stacking interaction and render solubility. In this study, functionalization at the imide nitrogen atom is the preferred option. Thus the planarity of PDI core is retained. As far as charge transport is concerned, planarity of PDI rings is preferable in order to establish PDI π-stacks as efficient charge transport pathways [14].

Unsymmetrical perylene diimide, chiral perylene monoimide and its corresponding symmetrical and unsymmetrical perylene diimides were prepared according to the synthetic pathways shown in Scheme 3.1 and the procedures mentioned in the literature [47]. The most common procedure to synthesize symmetrical perylene diimide is the condensation of perylene-3,4,9,10 tetracarboxylic dianhydride (PDA) with a primary amine in m-cresol and isoquinoline. However, unsymmetrically N,N'-disubstituted PDIs are not accessible via a stepwise condensation of PDA with two different primary amines because of the differences in reactivity of the amines. A three step reaction mechanism reported by Tröster has been applied for the syntheses of unsymmetrically substituted perylene dyes [48]. First, perylene-3,4,9,10-tetracarboxylic acid monoanhydride monopotassium carboxylate was prepared. Second, N-alkyl(aryl)-3,4,9,10-perylene tetracarboxylic monoanhydride monoimide was synthesized as the key intermediate. Finally, the unsymmetrical perylene dyes were prepared via condensation of corresponding amines with N-alkyl(aryl)-3,4,9,10-perylene tetracarboxylic monoanhydride monoimide in the solvent mixture of m-cresol and isoquinoline.

All of the synthesized compounds were characterized by ^{1}HNMR, ^{13}CNMR, IR and elemental analyses. The optical, photochemical, thermal and electrochemical properties of the compounds both in solution and solid states have been investigated in detail. Besides, the chirooptical properties of chiral perylene monoimide and its corresponding diimides have been analyzed.
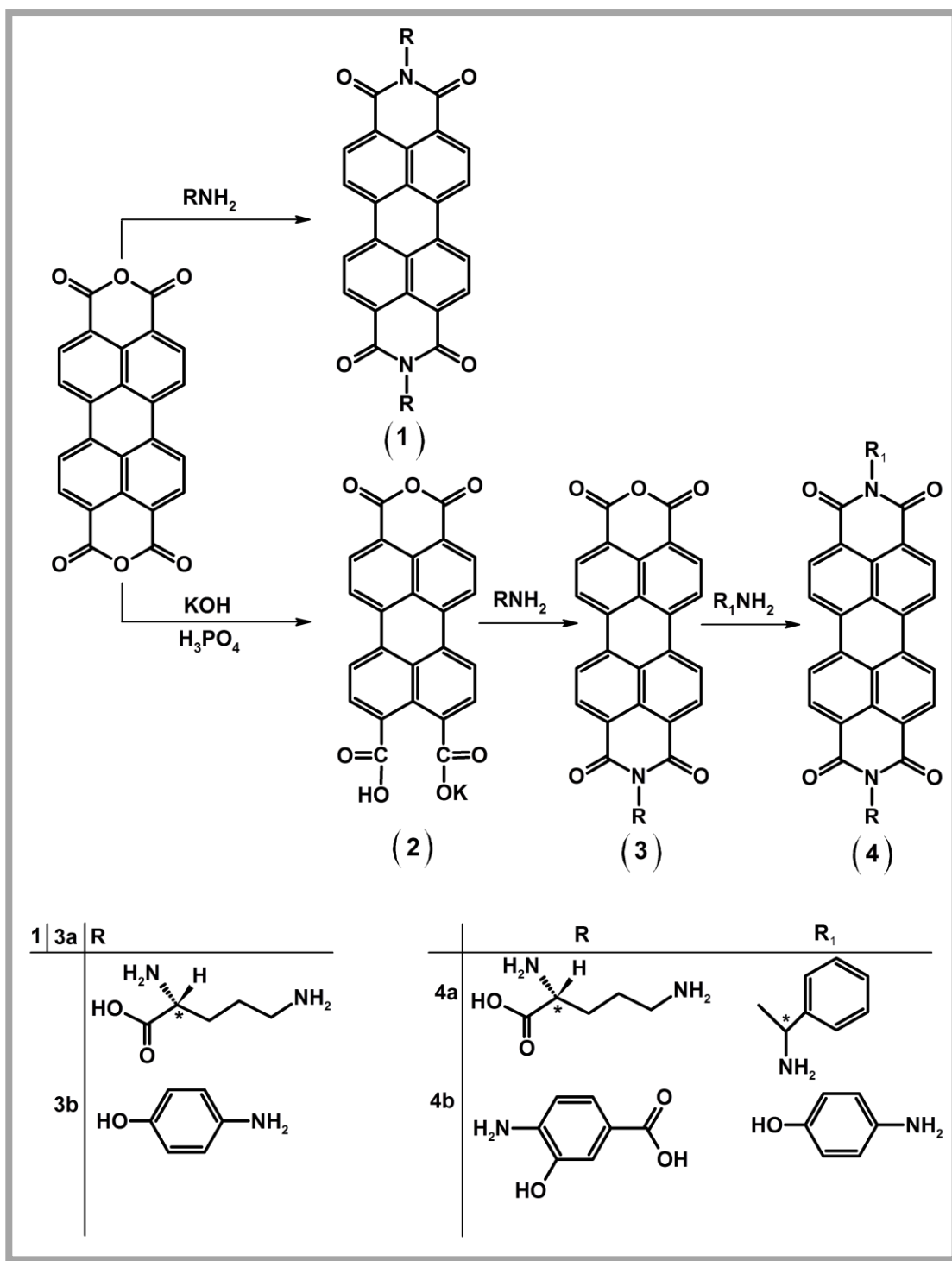
Scheme 3.1: Synthesis of perylene-3,4,9,10-tetracarboxylic acid monoanhydride monopotassium carboxylate, perylene monoimides and their corresponding diimides.

3.3.1 N-((2S)-2-aminohexanoic acid)-3,4,9,10 perylenetetracarboxylic-3,4 anydride-9,10 imide (3a; LPMI)
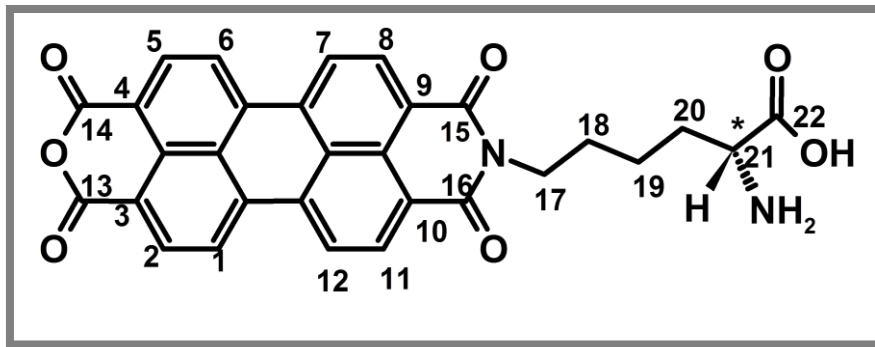
Perylene-3,4,9,10-tetracarboxylic monoanhydride monopotassium carboxylate (1.0 g, 2.2 mmol), N-2-aminohexanoic acid (1.6 g, 11 mmol) and water (50 mL) were stirred at 0-5 ^{o}C for 4 h. After stirring the mixture at 90 ^{o}C for 2 h, potassium carbonate (25% 12.5 mL) was added and stirred for another 1 h at 90 ^{o}C. The precipitate was collected by vacuum filtration and washed with potassium carbonate (2%). The precipitate was dissolved in KOH (3.5%, 100mL) heated to 90 ^{o}C, kept at this temperature for 5 min and filtered while it is hot. After acidification with hydrochloric acid (10%), the precipitate was collected by vacuum filtration and dried under vacuum at 100 ^{o}C. The crude product was purified with simple purification techniques. Yield (60 %); black powder with shiny goldish particles. $[\alpha]_D^{20}$: + 1191.5 (c = 0.0188, H_2SO_4), FT-IR (KBr, cm^{-1}): ν = 3442, 3097, 2925, 2850, 1766, 1725, 1690, 1655, 1593, 1556, 1444, 1400, 1320, 1244, 1125, 1015, 806, 731. ^{1}HNMR, δ_H(ppm) (400 MHz, $CDCl_3$ + CF_3COOH, TMS) = 8.85-8.53 (m, 8 Ar-H, H-C(1), H-C(2), H-C(5), H-C(6), H-C(7), H-C(8), H-C(11), H-C(12)), 4.38-4.34 (m, H-C(21)), 2.37-1.29 (m, 8 C-H_2, H_2C(17), H_2C(18), H_2C(19), H_2C(20)). UV/Vis (DMF): λ_{max} (nm) = 450, 485, 520. UV/Vis (solid state): λ_{max} (nm) = 491, 545. Fluorescence (DMF): λ_{max} (nm) = 533, 572, 619. Fluorescence (solid state): λ_{max} (nm) = 663.

Fluorescence quantum yield (DMF, reference N,N′-didodecyl-3,4,9,10-perylenebis(dicarboximide) with $\Phi_f = 100\%$, $\lambda_{exc.}= 485$ nm) = 30%. Anal. Calcd. for $C_{30}H_{20}N_2O_7$ (M_w, 520.5); C, 69.29; H, 3.87; N, 5.38. Found: C, 68.85; H, 3.72; N, 4.91.

3.3.2 N,N'-bis((2S)-2-aminohexanoic acid)-3,4,9,10 perylenedicarboximide (1; LPDI)
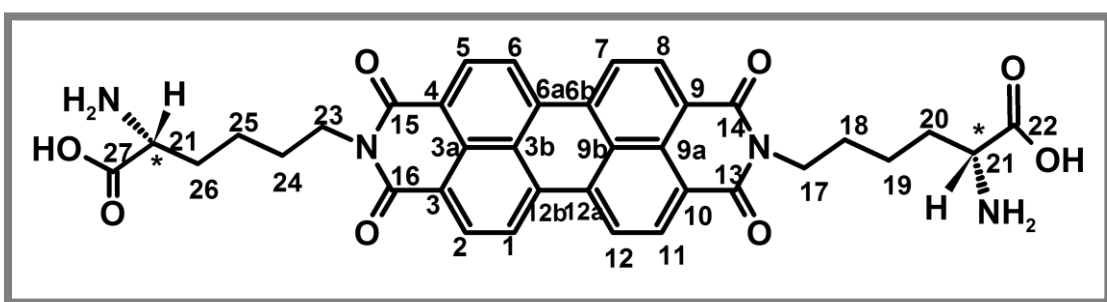
A mixture of perylene-3,4,9,10-tetracarboxylic dianhdride (1.0 g, 2.6 mmol), N-2-aminohexanoic acid (1.1 g, 7.5 mmol), m-cresol (40 mL) and isoquinoline (4 mL) were stirred under argon atmosphere at 80 °C for 1 h, 100 °C for 4 h, 120 °C for 4 h, up to 160 °C for 5 h, then at 180 °C for 7 h and finally at 200 °C for 7 h. The warm reaction mixture was poured into cooled acetone (300 mL). The precipitate was collected by vacuum filtration, washed with water and dried under vacuum at 100 °C. The crude product was extracted for 48 hours with methanol then chloroform in order to remove high boiling point solvents and excess reactants using Soxhlet apparatus. Yield (80%); bordeaux powder. $[\alpha]_D^{20}$: = + 201.7 (c = 0.0188, H_2SO_4). FT-IR (KBr, cm^{-1}): ν = 3346, 3064, 2930, 2853, 1696, 1654, 1598, 1577, 1442, 1406, 1342, 1242, 1160, 1123, 959, 850, 818 744. UV/Vis (DMF): λ_{max} (nm) = 457, 487,

523. UV/Vis (solid state): λ_{max} (nm) = 464, 502, 552. Fluorescence (DMF): λ_{max} (nm) = 533, 575, 624. Fluorescence (solid state): λ_{max} (nm) = 661. Fluorescence quantum yield (DMF, reference N,N′-didodecyl-3,4,9,10-perylenebis(dicarboximide) with Φ_f = 100%, $\lambda_{exc.}$ = 485 nm) = 42%. Anal. Calcd. for $C_{36}H_{32}N_4O_8$ (M_w, 648.7); C, 66.66; H, 4.97; N, 8.64. Found: C, 66.13; H, 4.44; N, 8.12.

3.3.3 N-((2S)-2-aminohexanoic acid)-N'-((S)-1-phenylethyl)-3,4,9,10 perylenedicarboximide (4a; LPPDI)
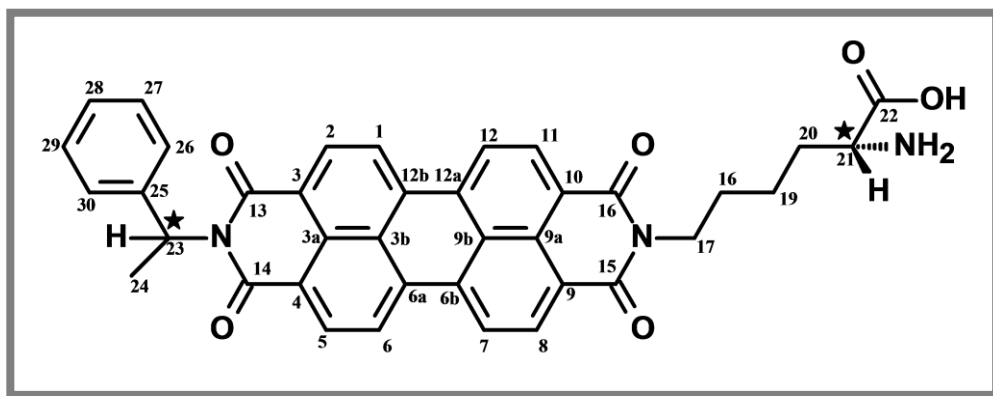
N-(2-aminohexanoic acid)-3,4,9,10 perylenetetracarboxylic-3,4 anhydride-9,10 imide (0.5 g, 0.96 mmol), (S)-(−)-1-phenylethylamine (0.366 mL, 2.88 mmol), m-cresol (40 mL) and isoquinoline (4 mL) were stirred at 80 °C for 4 h. Then the solution was heated at 100 °C for 4 h, at 120 °C for 2 h, 140 °C for 2 h, 160 °C for 3 h and finally at 200 °C for 6 h. The reaction was carried out under Argon atmosphere. The warm solution was poured into 250 mL of chloroform. The precipitates were collected by vacuum filtration and dried in vacuum oven at 100 °C. Finally methanol and chloroform soxhlets have been applied in order to remove high boiling and

excess reactants. Yield (85%); color dark brown-red. $[\alpha]_D^{20}$: = -1647.5 (c = 0.02, DMF), FT-IR (KBr, cm^{-1}): ν = 3516, 3369, 3069, 2919, 2853, 1696, 1654, 1593, 1577, 1443, 1407, 1341, 1251, 1174, 1121, 956, 852, 811, 743. UV/Vis (DMF): λ_{max} (nm) = 461, 490, 527. ^{1}HNMR, δ_H(ppm) (400 MHz, CDCl$_3$ + CF$_3$COOH, TMS) = 8.94-8.45 (m, 8 Ar-H, H-C(1), H-C(2), H-C(5), H-C(6), H-C(7), H-C(8), H-C(11), H-C(12)), 7.54-7.31 (m, 5 Ar-H, H-C(26), H-C(27), H-C(28), H-C(29), H-C(30), 6.63-6.59 (q, J=8 Hz, 1H-C(25), 4.34-4.08 (m, H-C(21), 2.60-1.30 (m, 8 CH$_2$, H$_2$-C(17), H$_2$-C(18), H$_2$-C(19), H$_2$-C(20). UV/Vis (solid state): λ_{max} (nm) = 471, 506, 555. Fluorescence (DMF): λ_{max} (nm) = 536, 577, 629. Fluorescence (solid state): λ_{max} (nm) = 658. Fluorescence quantum yield (DMF, reference N,N′-didodecyl-3,4,9,10-perylenebis(dicarboximide) with Φ_f = 100%, $\lambda_{exc.}$= 485 nm) = 75%. Anal. Calcd. for C$_{39}$H$_{34}$N$_3$O$_6$ (M_w, 640.4); C, 73.11; H, 5.35; N, 6.56. Found: C, 73.29; H, 5.44; N, 6.72.

3.3.4 Synthesis of N-(4-hydroxyphenyl)-3,4,9,10 perylenetetracarboxylic-3,4-anydride-9,10-imide (3b; OHPMI)
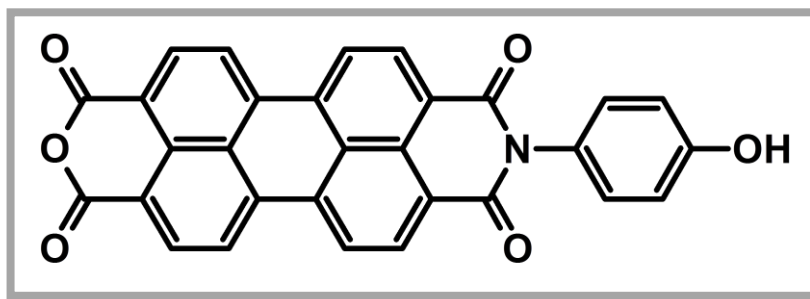
N-(4-hydroxyphenyl)-3,4,9,10   perylenetetracarboxylic-3,4-anhydride-9,10-imide was first prepared by Pasaogullari, N. [47]. Then it was synthesized and purified as a

key intermediate for the preparation of synthesis of N-(2-hydroxy-4-benzoic acid)-N'-(4-hydroxyphenyl)-3,4,9,10 perylenedicarboximide.

3.3.5 Synthesis of N-(2-hydroxy-4-benzoic acid)-N'-(4-hydroxyphenyl)-3,4,9,10 perylenedicarboximide (4b; BPDI)
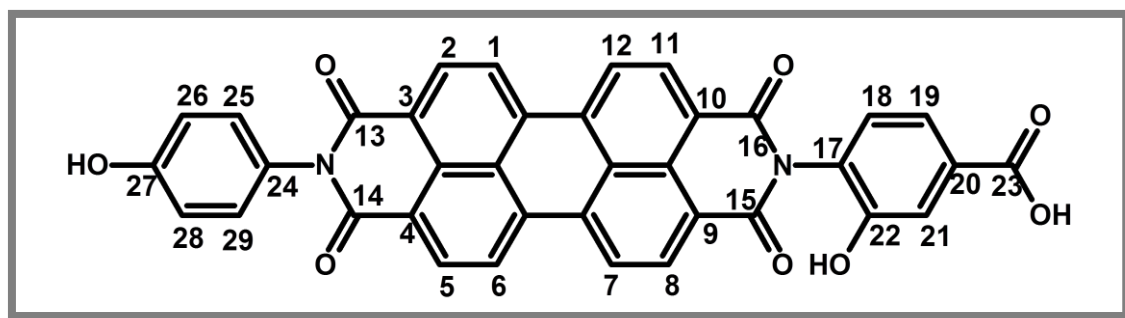
N-(4-hydroxyphenyl)-3,4,9,10 perylenetetracarboxylic-3,4-anhydride-9,10-imide (0.8 g, 1.82 mmol), 4-amino-3-hydroxybenzoic acid (0.542 g, 3.684 mmol), isoquinoline (4 mL) and m-cresol (40 mL) were stirred at 60 $^{\circ}$C for 6 hours, to 100 $^{\circ}$C for 3 hours, 120 $^{\circ}$C for 4 hours, 160 $^{\circ}$C for 8 hours then 180 $^{\circ}$C for 8 hours and finally at 200 $^{\circ}$C for 10 hours. The reaction has been carried out under Ar atmosphere. The warm solution was poured into 300 mL of methanol. Then the precipitates were filtered under vacuum and dried in vacuum oven at 100 $^{\circ}$C. Finally, methanol and chloroform soxhlets have been applied in order to remove high boiling solvents and unreacted reactants. Yield (80 %); black powder. FT-IR (KBr, cm^{-1}): υ = 3340, 3062, 1693, 1658, 1593, 1351, 1251, 1174, 1126, 966, 810, 743. UV/Vis (DMF): λ_{max} (nm) = 457, 490, 526. UV/Vis (solid state): λ_{max} (nm) = 476, 512, 556. Fluorescence (DMF): λ_{max} (nm) = 539, 579, 621. Fluorescence (solid state): λ_{max} (nm) = 558. Fluorescence quantum yield (DMSO, reference N,N′-didodecyl-

3,4,9,10-perylenebis(dicarboximide) with Φ_f = 100%, $\lambda_{exc.}$ = 485 nm) = 0.05%. Anal. Calcd. for $C_{37}H_{18}N_2O_8$ (M_w, 618.6); C, 71.85; H, 2.93; N, 4.53. Found: C, 68.2; H, 7.9; N, 4.3.

Chapter 4

DATA and CALCULATIONS

4.1 Optical Properties

4.1.1 Maximum Extinction Coefficients (ε_{max})

The maximum extinction coefficient, intrinsic property of the species, measures the intensity of light that a chemical species absorbs at given wavelength, where the actual absorbance, A of a sample is dependent on the path length (l) and the concentration (c) of the species applying the Beer Law,

$$A = \varepsilon_{max}cl$$

<div align="right">Eqn. (4.1)</div>

where,

A = absorbance

ε = molar extinction coeffients at the selected absorption wavelength (l mol^{-1} cm^{-1})

c = concentration (mol L^{-1})

l = pathlength (cm).

4.1.2 Fluorescent Quantum Yields (Φ_f)

Quantum yield is defined as the fraction of molecules of a particular compound that emits a photon when exposed to direct excitation. It is a measure of the proportion of de-excitation that occurs radiatively. Quantum yields give important information

about the excited electronic state, radiationless transitions and coupling of electronic to vibronic states [49]. All of these processes are indicated in the following Jablonski diagram (Figure 4.1).
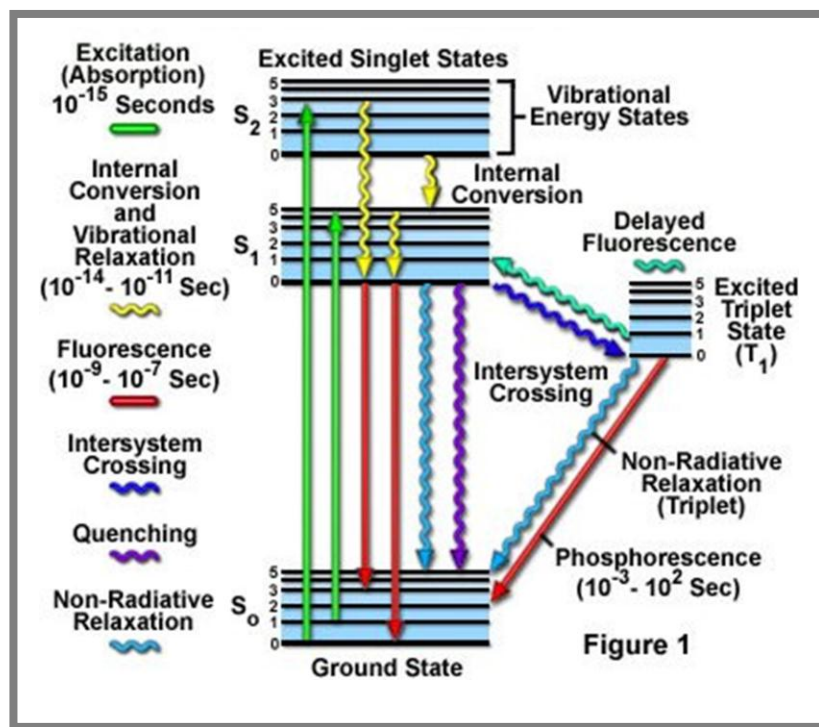
Figure 4.1: A general Jablonski diagram

Calculation of accurate quantum yield values for new compounds is important. For this reason, two methods have been recorded in literature; the comparative and absolute methods. Comparative method uses fluorescence standards with known fluorescence quantum yields for solution measurements, where absolute method is available for both solution and solid state measurements. Absolute method directly aims to find the number of photons emitted and number of photons absorbed. Hence the ratio can be calculated. For this process, a highly reflective sphere as the sample compartment in the fluorimeter is substituted so that all light entering the sphere is either absorbed by the sample or collected by fluorescence detector. In this way, total

number photons emitted by the sample and the photons absorbed can be obtained as the difference between the photon numbers at the excitation wavelength reaching the detector with the sample in or out of the substituted sphere. Correction for solvent refractive index is not necessary in this method [50].

In the current study, the comparative method of Williams and coworkers, as the most reliable method, has been used with standard sample of known Φ_f value. Accordingly the solutions of the standard and test samples with exactly same absorbance at the same excitation wavelength can be thought to be absorbing same number of photons. Hence, a simple ratio of the integrated fluorescence intensities of the two solutions will give the ratio of the quantum yield values [51]. Applying the equation given below, once the standard sample is known, Φ_f for the test sample can be calculated.

$$\Phi u = \frac{As}{Au} \times \frac{Su}{Ss} \times \left(\frac{nu}{ns}\right)^2 \times \Phi s$$

Eqn. (4.1)

Where;

Φ_u = quantum yield of the unknown

Φ_s = quantum yield of the standard

A_s = absorbance of the standard

A_u = absorbance of the unknown

S_u = integral emission area across the unknown band

S_s = integral emission area across the standard band

n_u = refractive index for the solvent of unknown

n_s = refractive index for the solvent of standard

N,N'-didodecyl-3,4,9,10-perylenebis(dicarboximide) with a Φ_f =100% in chloroform was used as a reference for the quantum yield measurements of perylene dyes. The emission spectra of the compounds and the reference were taken at the wavelength, λ_{exc} = 485 nm. Absorbances of sample and reference solutions were adjusted to be 0.1 at the excitation wavelength to minimize any effect originated from re-absorption of the fluorescence. Applying the equation 4.1, relative quantum yields were determined and presented in Table 4.1.

Table 4.1: Fluorescence quantum yield data of LPMI and LPDI

Fluorescence quantum yield, Φ_f

Solvents	LPMI	LPDI	LPPDI	BPDI
DMF	0.30	0.42	0.75	-
DMSO	0.13	0.08	-	0.05
Acetic acid	0.54	0.48	-	-

4.1.3 Singlet Energies (E_s)

Singlet energy is the minimum amount of energy needed for a chromophore to get excited from ground state to excited state and it can be calculated using the equation 4.2 given below [52].

$$E_s = \frac{2.86 \times 10^5}{\lambda_{max}}$$

<div align="right">Eqn. (4.2)</div>

where,

E_s = singlet energy (kcal mol^{-1})

λ_{max} = maximum absorption wavelength (Å)

4.1.4 Oscillator Strength (f)

Oscillator strength, the dimensionless quantity, is used as a measure of the relative strength of the electronic transitions within atomic and molecular systems and can be calculated applying the following equation (Turro 1965).

$$f = 4.32 \times 10^{-9} \, \Delta\bar{\nu}_{1/2} \, \varepsilon_{max}$$

<div align="right">Eqn. (4.3)</div>

where,

f = oscillator strength

$\Delta\bar{\nu}_{1/2}$ = the half-width of the selected absorption (cm^{-1})

ε_{max} = molar extinction coefficient at the selected absorption wavelength (L mol^{-1} cm^{-1}).
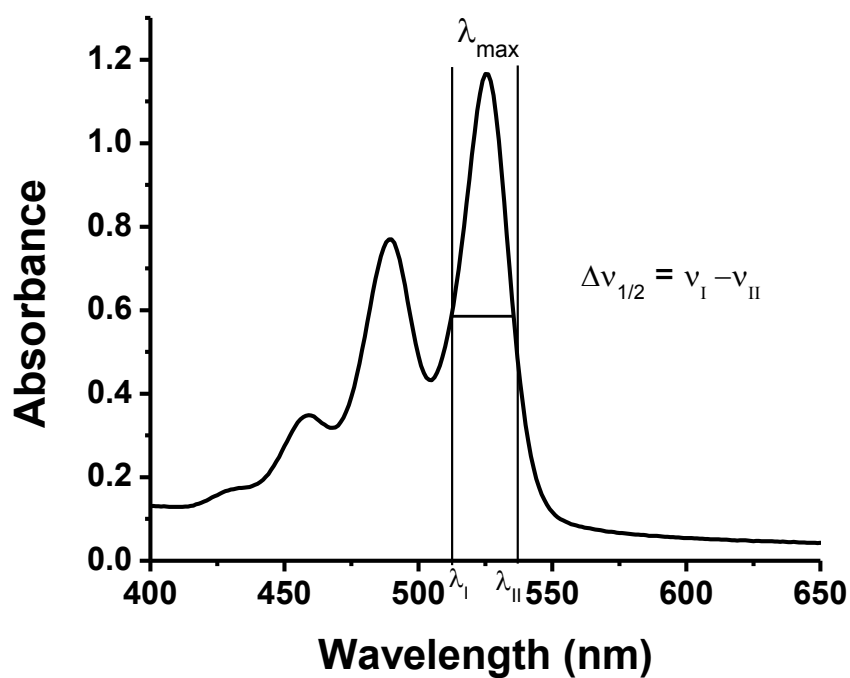
Figure 4.2: Representative graph for the half-width of the selected absorption

4.1.5 Theoretical Radiative Lifetimes (τ_0)

Theoretical radiative lifetimes were calculated by using the equation 4.4 given below (Turro, 1965).

$$\tau_0 = \frac{3.5 \times 10^8}{\overline{\nu}^2_{max} \times \varepsilon_{max} \times \Delta\overline{\nu}_{1/2}}$$

Eqn. (4.4)

where,

τ_0 = theoretical radiative lifetime (ns)

$\overline{\nu}_{max}$ = mean frequency of the maximum absorption band (cm^{-1})

49

ε_{max} = the maximum extinction coefficient at the maximum absorption wavelength ($L\ mol^{-1}\ cm^{-1}$)

$\Delta\bar{\nu}_{1/2}$ = the half-width of the selected absorption (cm^{-1})

4.1.6 Theoretical Fluorescence Lifetimes (τ_f)

Theoretical fluorescence lifetimes were calculated using the following equation (Turro, 1965).

$$\boldsymbol{\tau_f = \tau_0 \times \Phi_f}$$

Eqn. (4.5)

where,

τ_f = fluorescence lifetime (ns)

τ_0 = radiative lifetimes (ns)

Φ_f = fluorescence quantum yield

4.1.7 Fluorescence Rate Constants (k_f)

Fluorescence rate constants were calculated applying the equation shown below.

$$\boldsymbol{k_f = \frac{1}{\tau_0}}$$

Eqn. (4.6)

where,

k_f = fluorescence rate constant (s^{-1})

τ_0 = radiative lifetime (s)

4.1.8 Rate Constants of Radiationless Deactivation (k_d)

Rate constants of radiationless deactivation were calculated applying the following equation.

$$k_d = \frac{(k_f)}{(\Phi_f)} - k_f$$

<div align="right">Eqn. (4.7)</div>

where,

k_d = rate constant of radiationless deactivation (s^{-1})

k_f = fluorescence rate constant (s^{-1})

Φ_f = fluorescence quantum yield.

4.2 Chiroptical Properties

Chiroptical properties of the compound; LPMI, LPDI and LPPDI are investigated using circular dichroism spectroscopy. Circular dichroism is a type of light absorption spectroscopy. It measures the difference in absorbance of right- and left-circularly polarized light by a substance; RCPL and LCPL respectively. Historically, ellipticity, Θ, is the unit of circular dichroism which is defined as the tangent of the ratio of the minor to major elliptical axis. Axial ratios of 1:100 will result in an ellipticity of 0.57 degrees. Modern CD measurements can give a millidegree precision. In literature, circular dichroism is usually expressed as molar ellipticity [Θ]: [53].

$$[\Theta] = \frac{(\Theta \times M)}{(c \times l \times 10000)}$$

<div align="right">Eqn. (4.8)</div>

where,

Θ = ellipticity (mdeg)

M = molecular weight (g/mol)

c = concentration (g/mol)

l = the cell path (cm)

Table 4.2: Maximum absorption wavelengths λ_{max} (nm), extinction coefficients ε_{max} (l mol^{-1} cm^{-1}), oscillator strength f, fluorescence quantum yield Φ_f (λ_{exc} = 485 nm), radiative lifetimes τ_0 (ns), fluorescence lifetimes τ_f (ns), fluorescence rate constants k_f (10^8 s^{-1}), rate constants of radiationless deactivation k_d (10^8 s^{-1}), and optical activities $[\alpha]_D^{20}$ of LPMI and LPDI in DMF.

	λ_{max}	ε_{max}	f	Φ_f	τ_0	τ_f	k_f	k_d	$[\alpha]_D^{20}$
LPMI	520	-	-	0.3	-	-	-	-	+11191.5
						(2.9)[a]			
LPDI	523	120 000	0.6	0.4	6.7	2.8	1.5	2.1	+201.7
						(3.9)[a]			

[a] Experimental values are given in parenthesis.

4.3 Thermal Properties

The thermal behaviors of all compounds were studied by applying DSC and TGA at a heating rate of 10 K min^{-1} and 5 K min^{-1}, respectively.

4.4 Electrochemical Properties

The electrochemical parameters such as redox potentials, HOMO (highest occupied molecular orbital), LUMO (lowest unoccupied molecular orbital), band gap energies E_g, and electron transfer numbers of all compounds have been investigated in detail

using cyclic and square-wave voltammetries both in solutions and solid state using 0.05 M $NaBF_4$ and 1 M HCl as supporting electrolytes, respectively.

4.4.1 Redox Potentials ($E_{1/2}$)

For reversible processes where the cathodic and anodic waves are symmetric with respect to each other, the redox potential can be calculated by means of a cyclic voltammogram according to internal reference by applying the following equation [54]. At this point, the concentrations of reduced and oxidized species are equal.

$$E_{1/2} = \frac{E_{pc} + E_{pa}}{2}$$

Eqn. (4.9)

where,

$E_{1/2}$ = half-wave potential (V)

E_{pc} = cathodic peak potential (V)

E_{pa} = anodic peak potential (V)

The separation between the peak potentials (for a reversible couple) is given by equation 4.10 where n is the number of electrons.

$$\Delta E_p = E_{pa} - E_{pc} = \frac{0.059}{n} \ V$$

Eqn. (4.10)

Thus, the peak separation value can be used to calculate the number of electrons transferred. According to the equation 4.10, a fast one-electron process exhibits a peak potential separation (ΔE_p) of about 59 mV.

Table 4.3: Cyclic[a,b] voltammetry data of compounds, LPMI and LPDI in DMF.

Compound	E_{pc} / V	E_{pa} / V	ΔE_p / mV	$E_{1/2}$ / V vs. Ag/AgCl	E_{Fc} / V vs. Ag/AgCl	$E_{1/2}$ / V vs. Fc
LPMI	-0.166	-0.058	108	-0.112	0.700	-0.812
	-0.297	-0.242	55	-0.270	0.700	-0.969
	-0.441	-0.361	80	-0.401	0.700	-1.101
LPDI	-0.550	-0.478	72	-0.514	0.700	-1.214
	-0.778	-0.726	52	-0.752	0.700	-1.452

[a] Scan rate of 100 mV s^{-1}.
[b] Supporting electrolyte: 0.05M Sodium tetrafluorborate (NaBF$_4$).

Table 4.4: Cyclic[a,b] voltammetry data of compounds, LPMI, LPDI, LPPDI and BPDI in solid state.

Compound	E_{pc} / V	E_{pa} / V	ΔE_p / mV	$E_{1/2}$ / V vs. Ag/AgCl	E_{Fc} / V vs. Ag/AgCl	$E_{1/2}$ / V vs. Fc
LPMI	-0.37	-0.20	169	-0.29	0.27	-0.56
LPDI	-0.35	-0.22	126	-0.28	0.27	-0.55
LPPDI	-0.43	-0.22	215	-0.32	0.27	-0.59
BPDI	-0.38	-0.28	104	-0.33	0.27	-0.60

[a] Scan rate of 100 mV s^{-1}.
[b] Supporting electrolyte: 1 M HCl.

4.4.2 Lowest Unoccupied Molecular Orbital (LUMO)

The absolute energies of LUMO level have been calculated with respect to the vacuum level where the redox data are standardized to ferrocene/ferricenium couple which has a calculated absolute energy of – 4.8 eV [55, 56].

$$E_{LUMO} = -(4.8 + E_{1/2})$$

Eqn. (4.11)

where,

E_{LUMO} = energy of LUMO level (eV)

$E_{1/2}$ = half-wave potential (V)

Table 4.5: LUMO values of compounds, LPMI, LPDI, LPPDI and BPDI in solid state[a]

Compound	$E_{1/2}$ / V vs. Fc	LUMO / eV
LPMI*	-0.812	-3.988
LPMI	-0.558	-4.242
LPDI*	-1.214	-3.586
LPDI	-0.552	-4.248
LPPDI	-0.594	-4.206
BPDI	-0.597	-4.203

* in DMF
[a] at a scan rate of 100 mV s^{-1}.

4.4.3 Band Gap Energy (E_g)

The optical band gap energy values were calculated using absorption spectrum of the compound where the maximum absorption band is extrapolated to zero-absorbance and the following equation.

$$E_g = \frac{1240 \text{ eV nm}}{\lambda}$$

<div align="right">Eqn. (4.12)</div>

where,

E_g = band gap energy (eV)

λ = cut-off wavelength of the absorption band (nm)

Table 4.6: The optical band gap energy values of LPMI, LPDI, LPPDI and BPDI in solid state.

Compound	$\lambda_{0 \to 0}$ / nm	E_g / eV
LPMI*	520	2.246
LPMI	545	1.890
LPDI*	523	2.250
LPDI	552	1.737
LPPDI	554	1.696
BPDI	556	1.896

* in DMF

4.4.4 Highest Occupied Molecular Orbital (HOMO)

Highest occupied molecular orbital energy values were calculated using the equation given below.

$$\mathbf{E_{HOMO} = E_{LUMO} - E_g}$$

Eqn. (4.13)

where,

E_{HOMO} = energy of HOMO level (eV)

E_{LUMO} = energy of LUMO level (eV)

E_g = band gap energy (eV)

Table 4.7 HOMO values of compound LPMI, LPDI, LPPDI and BPDI in solid state[a].

Compound	LUMO / ev	E_g / eV	HOMO / eV
LPMI*	-3.988	2.385	-6.373
LPMI	-4.242	1.890	-6.133
LPDI*	-3.586	2.250	-5.836
LPDI	-4.248	1.737	-5.985
LPPDI	-4.206	1.696	-5.903
BPDI	-4.203	1.896	-6.099

* in DMF
[a] at a scan rate of 100 mV s^{-1}.

Table 4.8: Cyclic* voltammetry data of compound LPMI in DMF at different scan rates.

Scan rate $(m\,Vs^{-1})$	E_{pc} (V)	E_{pa} (V)	ΔE_p (mV)	i_{pc} (μA)	i_{pa} (μA)	i_{pa}/i_{pc}
20	-0.17	-0.06	113	0.18	0.08	0.44
	-0.31	-0.25	66			
	-0.44	-0.36	82			
50	-0.17	-0.06	102	0.26	0.13	0.50
	-0.29	-0.26	39			
	-0.45	-0.37	82			
100	-0.17	-0.06	108	0.39	0.24	0.61
	-0.30	-0.24	55			
	-0.44	-0.36	80			
200	-0.18	-0.06	118	0.74	0.22	0.30
	-0.30	-0.27	33			
	-0.45	-0.37	80			
300	-0.17	-0.06	101	0.93	0.32	0.34
	-0.31	-0.26	48			
	-0.45	-0.36	83			
400	-0.16	-0.06	99	0.36	0.74	0.49
	-0.30	-0.25	55			
	-0.45	-0.36	89			
500	-0.16	-0.06	102	0.71	0.26	0.37
	-0.30	-0.25	55			
	-0.45	-0.36	99			
750	-0.15	-0.06	91	1.03	0.61	0.59
	-0.29	-0.26	36			
	-0.46	-0.37	94			
1000	-0.15	-0.06	97	0.94	0.55	0.59
	-0.31	-0.25	61			
	-0.46	-0.36	100			

* supporting electrolyte: 0.05M $NaBF_4$

Table 4.9: Cyclic* voltammetry data of compound LPDI in DMF at different scan rates.

Scan rate (m Vs^{-1})	E_{pc} (V)	E_{pa} (V)	ΔE_p (mV)	i_{pc} (μA)	i_{pa} (μA)	i_{pa}/i_{pc}
50	-0.54	-0.48	66	0.33	0.08	0.24
	-0.77	-0.73	48			
100	-0.55	-0.48	72	0.47	0.16	0.34
	-0.78	-0.73	52			
200	-0.56	-0.50	61	0.63	0.27	0.43
	-0.78	-0.72	54			
300	-0.55	-0.49	55	0.94	0.5	0.53
	-0.80	-0.72	80			
400	-0.56	-0.49	66	1.37	0.65	0.47
	-0.80	-0.72	83			
500	-0.56	-0.49	69	1.43	0.79	0.55
	-0.81	-0.72	89			
750	-0.56	-0.50	64	1.68	1.22	0.73
	-0.81	-0.71	101			
1000	-0.56	-0.49	67	2.35	1.73	0.74
	-0.81	-0.71	104			

* supporting electrolyte: 0.05M NaBF$_4$

Table 4.10: Solid state cyclic* voltammetry data of compound LPMI at different scan rates.

Scan rate (m Vs^{-1})	E_{pc} (V)	E_{pa} (V)	ΔE_p (mV)	i_{pc} (μA)	i_{pa} (μA)	i_{pa}/i_{pc}
10	-0.39	-0.24	152	116.10	139.30	1.20
25	-0.38	-0.23	151	246.75	264.20	1.07
50	-0.38	-0.20	170	334.07	388.96	1.16
75	-0.38	-0.20	190	482.33	492.38	1.02
100	-0.37	-0.20	171	350.14	312.90	0.89
200	-0.39	-0.17	225	675.58	639.49	1.06
300	-0.40	-0.15	245	894.66	700.95	1.28
500	-0.42	-0.13	286	1129.41	758.25	1.49
750	-0.41	-0.14	264	805.45	627.89	1.28
1000	-0.43	-0.12	319	1183.76	766.94	1.54

* supporting electrolyte: 1 M HCl

Table 4.11: Solid state cyclic* voltammetry data of compound LPDI at different scan rates.

Scan rate (m Vs^{-1})	E_{pc} (V)	E_{pa} (V)	ΔE_p (mV)	i_{pc} (μA)	i_{pa} (μA)	i_{pa}/i_{pc}
10	-0.33	-0.26	79	15.83	13.54	0.86
25	-0.34	-0.25	92	25.60	25.90	1.01
50	-0.34	-0.24	99	31.66	32.04	1.01
100	-0.35	-0.22	126	24.46	23.28	0.95
200	-0.35	-0.22	124	56.39	54.49	0.97
300	-0.35	-0.22	128	71.28	70.60	0.99
500	-0.35	-0.21	142	79.69	80.40	1.01
750	-0.36	-0.20	158	68.97	64.94	0.94
1000	-0.36	-0.20	156	83.44	78.13	0.94

* supporting electrolyte: 1 M HCl

Table 4.12: Solid state cyclic* voltammetry data of compound LPPDI at different scan rates.

Scan rate (m Vs^{-1})	E_{pc} (V)	E_{pa} (V)	ΔE_p (mV)	i_{pc} (μA)	i_{pa} (μA)	i_{pa}/i_{pc}
10	-0.40	-0.27	135	1.67	1.89	1.13
25	-0.41	-0.25	157	3.10	3.09	1.00
50	-0.42	-0.24	178	3.35	3.33	0.99
100	-0.43	-0.22	210	4.57	4.50	0.98
200	-0.44	-0.21	230	6.52	6.00	0.92
300	-0.45	-0.20	249	8.24	7.39	0.90
500	-0.46	-0.20	255	9.97	7.14	0.72
750	-0.46	-0.17	295	6.19	7.23	1.17
1000	-0.48	-0.17	310	8.09	9.27	1.15

* supporting electrolyte: 1 M HCl

Table 4.13: Solid state cyclic* voltammetry data of compound BPDI at different scan rates.

Scan rate $(m Vs^{-1})$	E_{pc} (V)	E_{pa} (V)	ΔE_p (mV)	i_{pc} (μA)	i_{pa} (μA)	i_{pa}/i_{pc}
10	-0.37	-0.28	88	38.38	32.75	0.85
25	-0.37	-0.28	92	53.71	54.94	1.02
50	-0.37	-0.28	92	77.40	69.60	0.90
100	-0.38	-0.28	103	97.06	87.12	0.90
200	-0.38	-0.27	110	129.30	119.37	0.92
300	-0.38	-0.27	114	155.92	134.29	0.86
500	-0.38	-0.26	121	187.00	157.00	0.84
750	-0.39	-0.26	126	209.22	161.28	0.77
1000	-0.39	-0.26	128	228.73	191.92	0.84

* supporting electrolyte: HCl
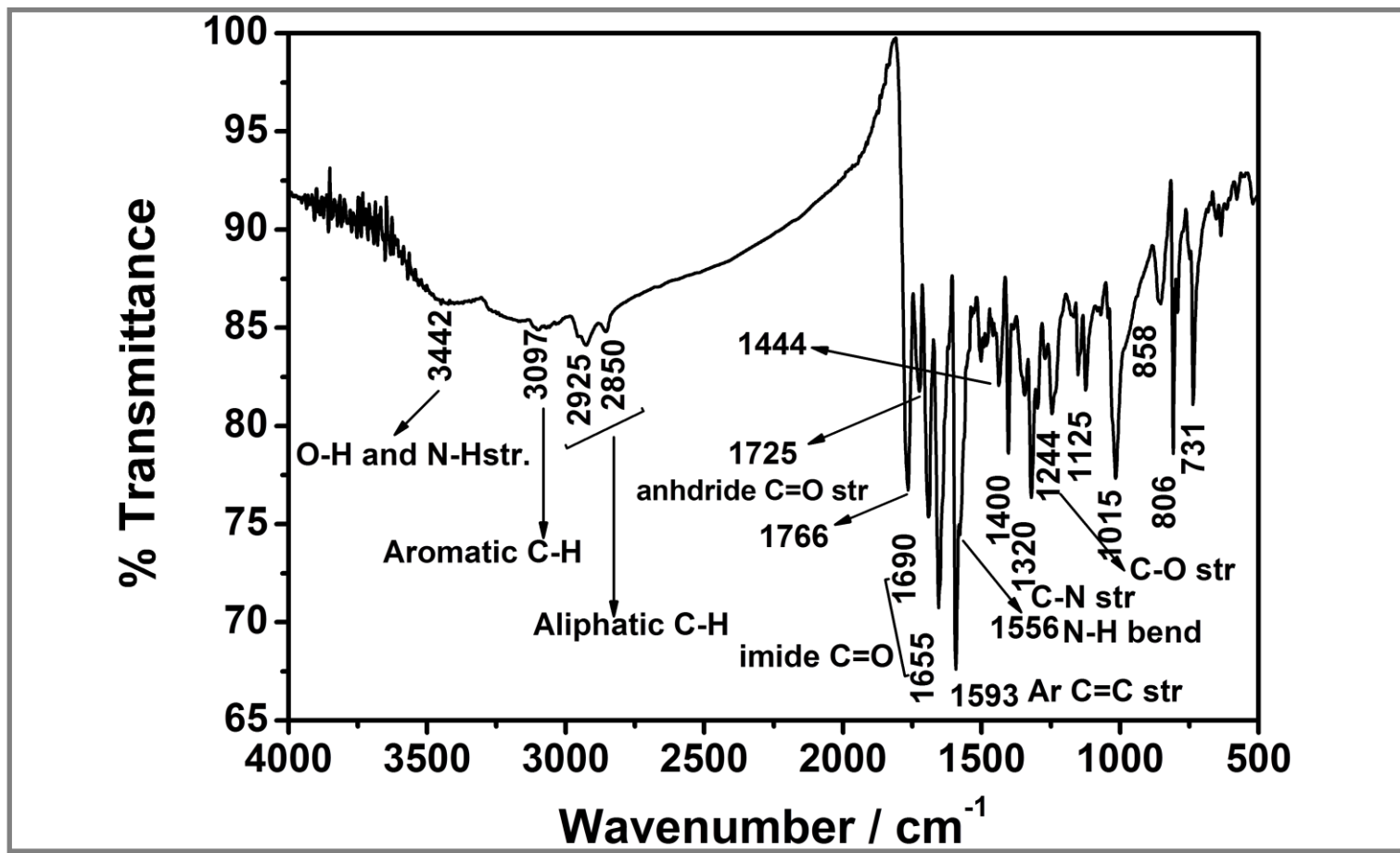
Figure 4.3: FT-IR spectrum of N-(2-aminohexanoic acid)-3,4,9,10 perylenetetracarboxylic-3,4-anhydride-9,10 imide (LPMI).
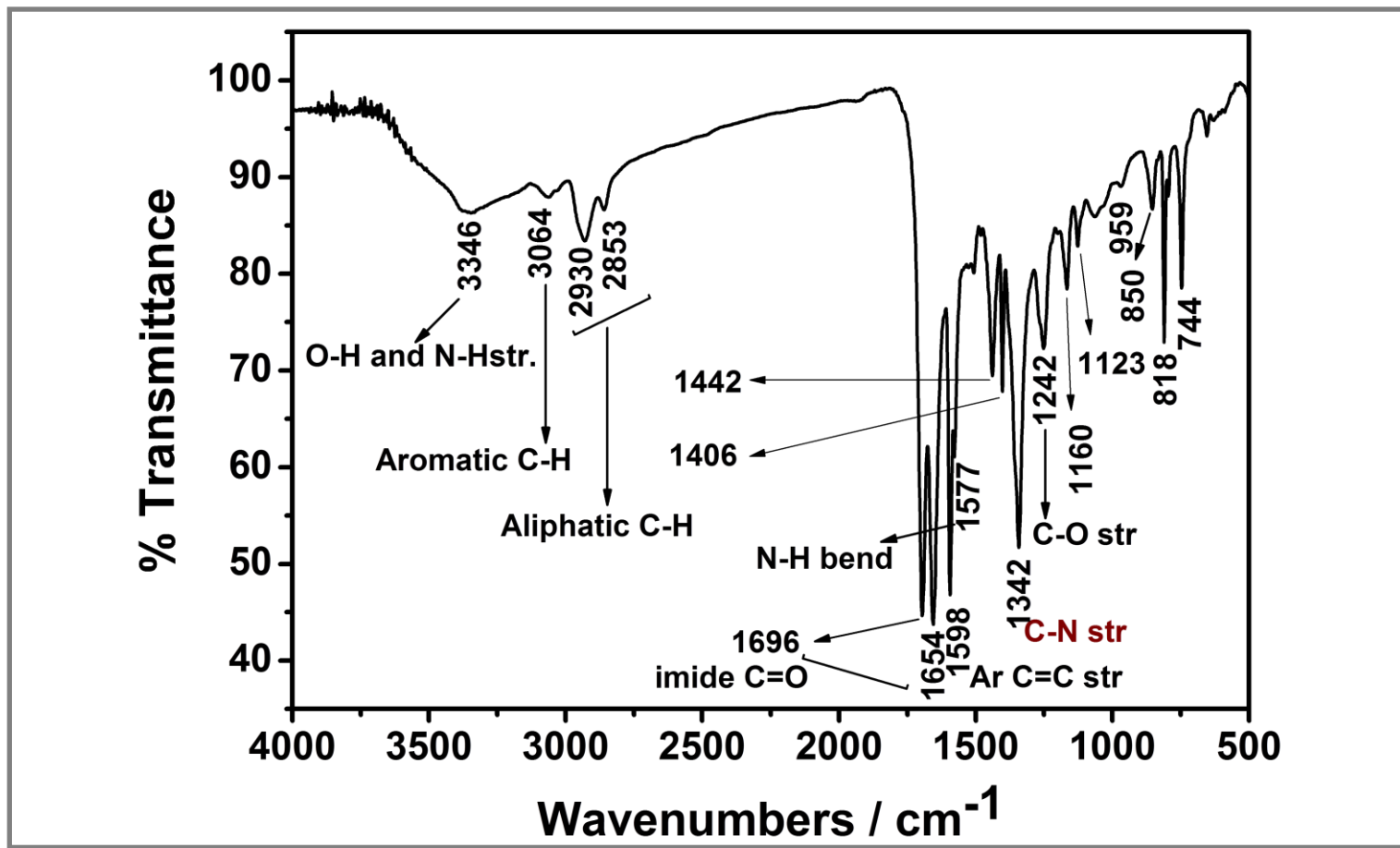
Figure 4.4: FT-IR spectrum of N, N'-bis(2-aminohexanoic acid)-3,4,9,10 perylenebis(dicarboximide) (LPDI).
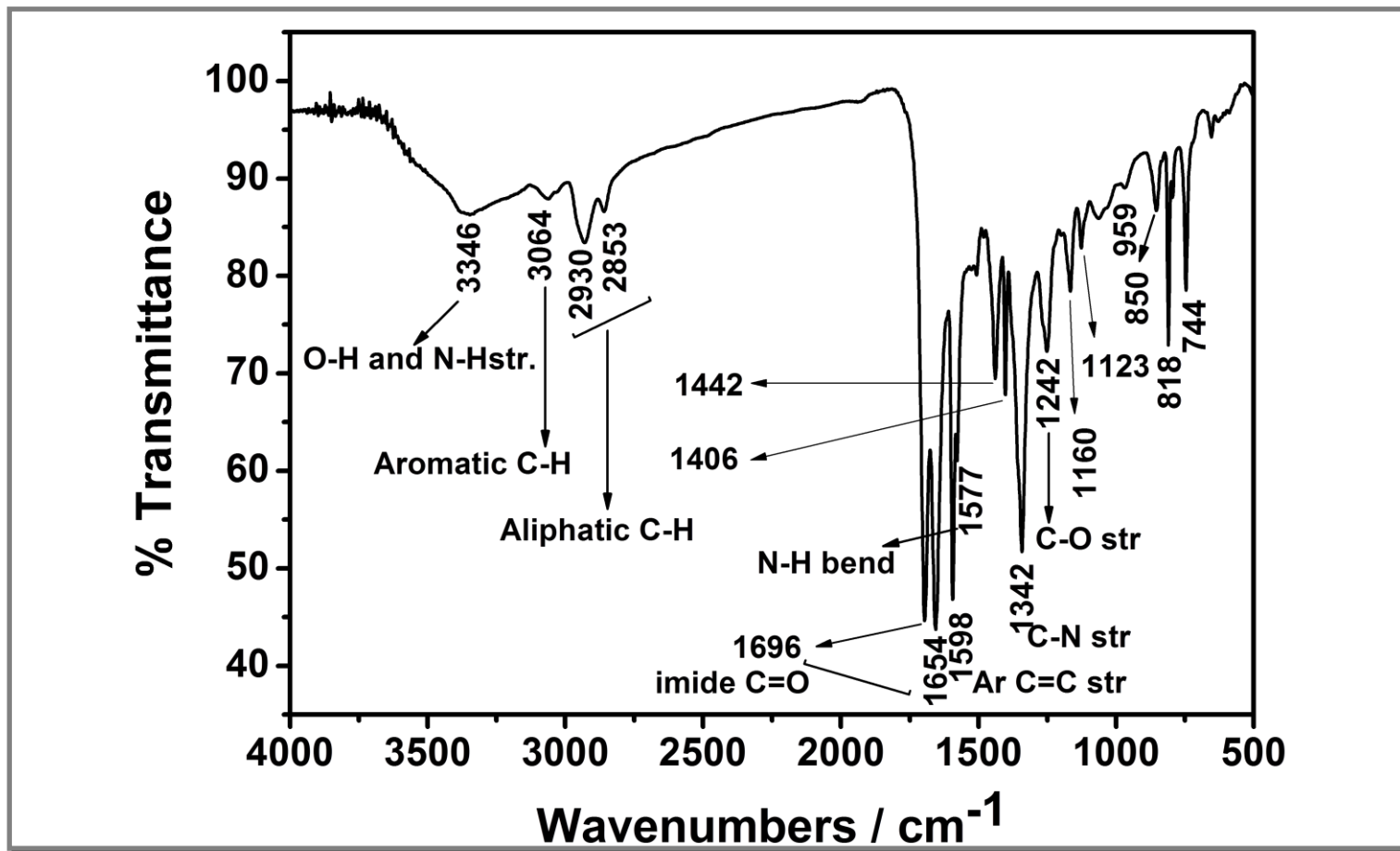
Figure 4.5: FT-IR spectrum of N-(2-aminohexanoic acid)-N'-(1-phenyl-ethylamine)-3,4,9,10 perylenebis(dicarboximide) (LPPDI).
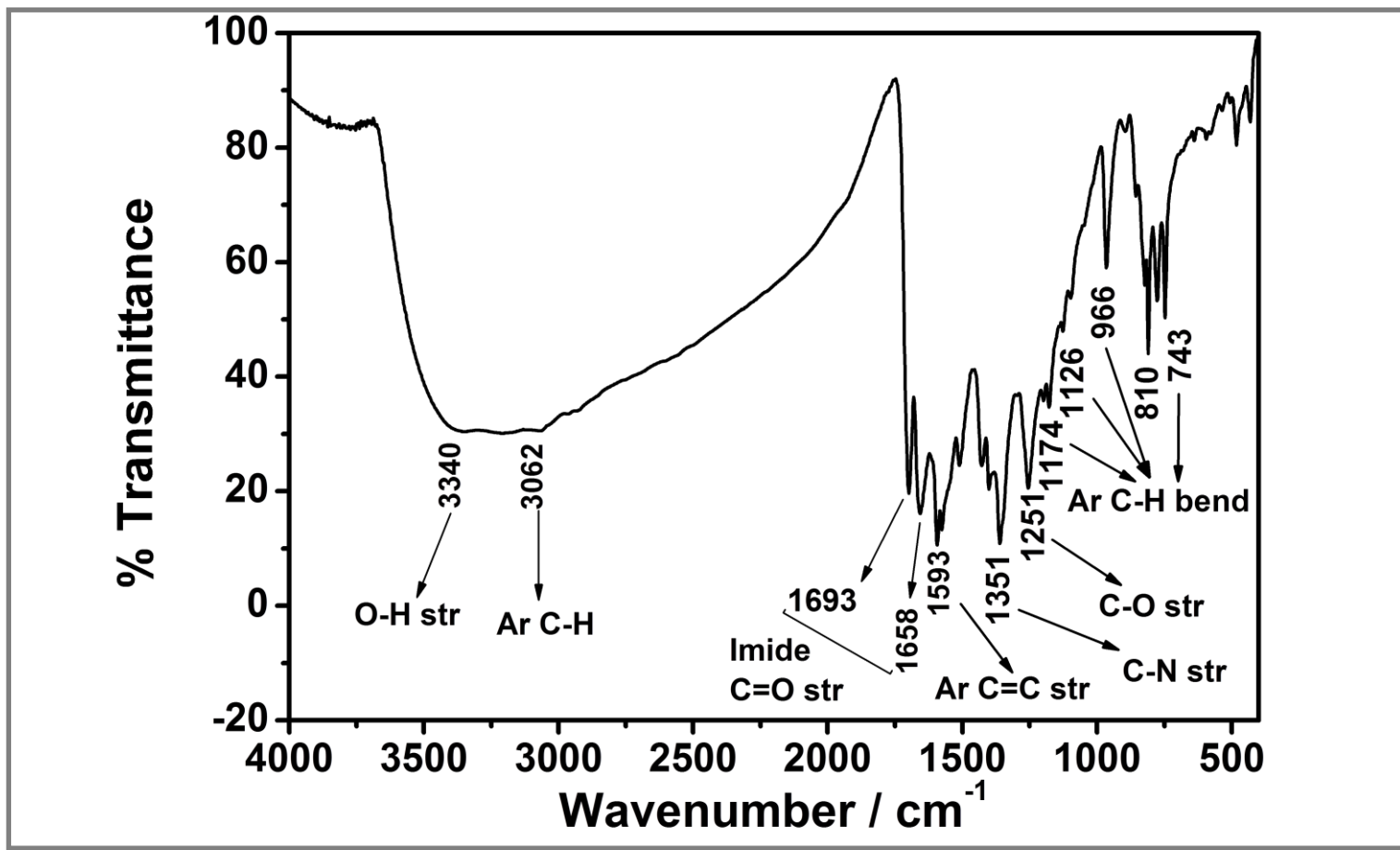
Figure 4.6: FT-IR spectrum of N-(2-hydroxy-4-benzoic acid)-N'-(4-hydroxyphenyl)-3,4,9,10 perylenebis (dicarboximide) (BPDI).
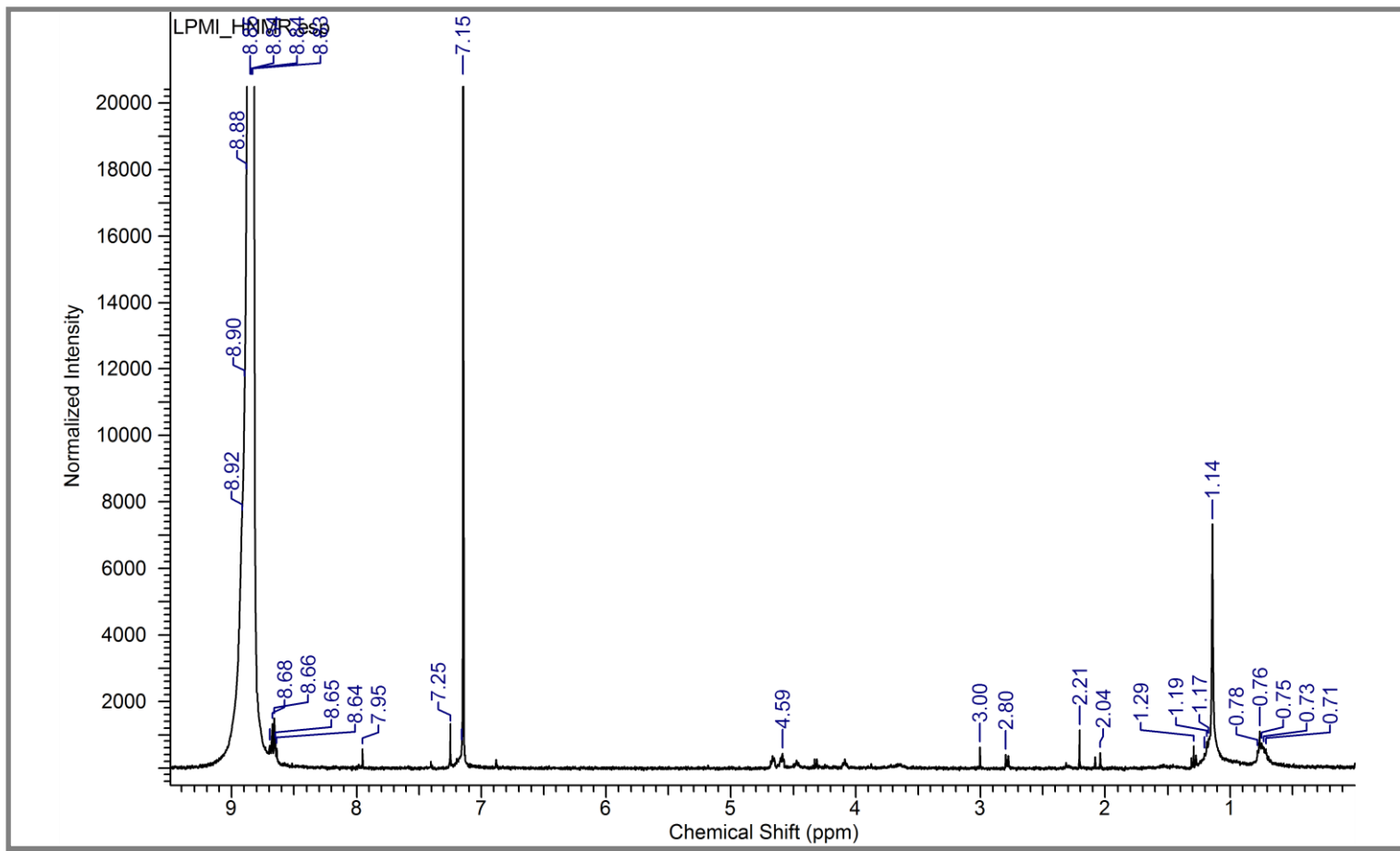
Figure 4.7: ^{1}H-NMR spectrum of N-(2-aminohexanoic acid)-3,4,9,10 perylenetetracarboxylic-3,4-anhydride-9,10 imide (LPMI) in $CDCl_3$ + CF_3COOH at 400 MHz.
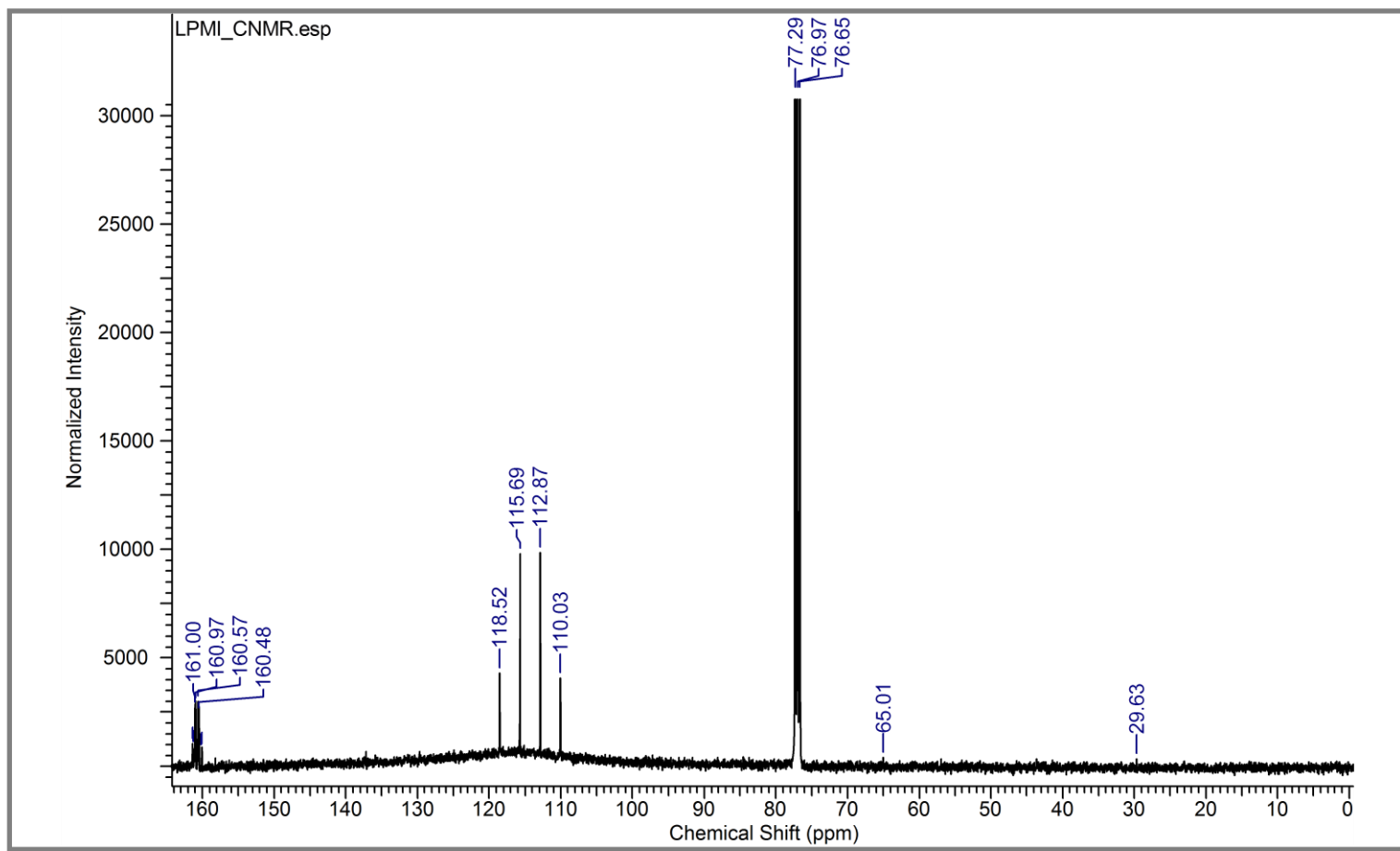
Figure 4.8: ^{1}C-NMR spectrum of N-(2-aminohexanoic acid)-3,4,9,10 perylenetetracarboxylic-3,4-anhydride-9,10 imide (LPMI) in CDCl$_3$ + CF$_3$COOH at 100 MHz.
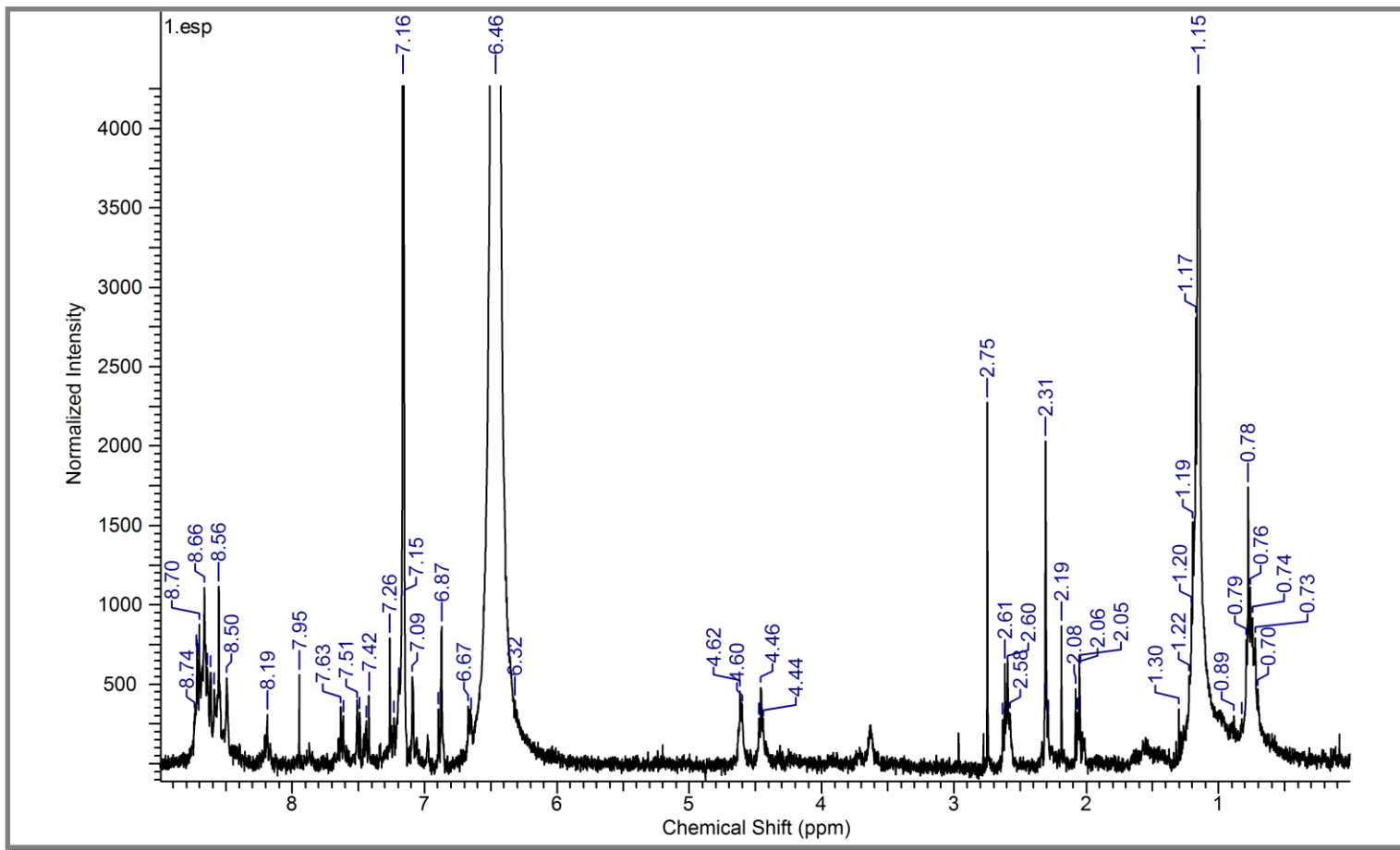
Figure 4.9: ^{1}H-NMR spectrum of N, N'-bis(2-aminohexanoic acid)-3,4,9,10 perylenebis(dicarboximide) (LPDI) in CDCl$_3$ + CF$_3$COOH at 400 MHz.
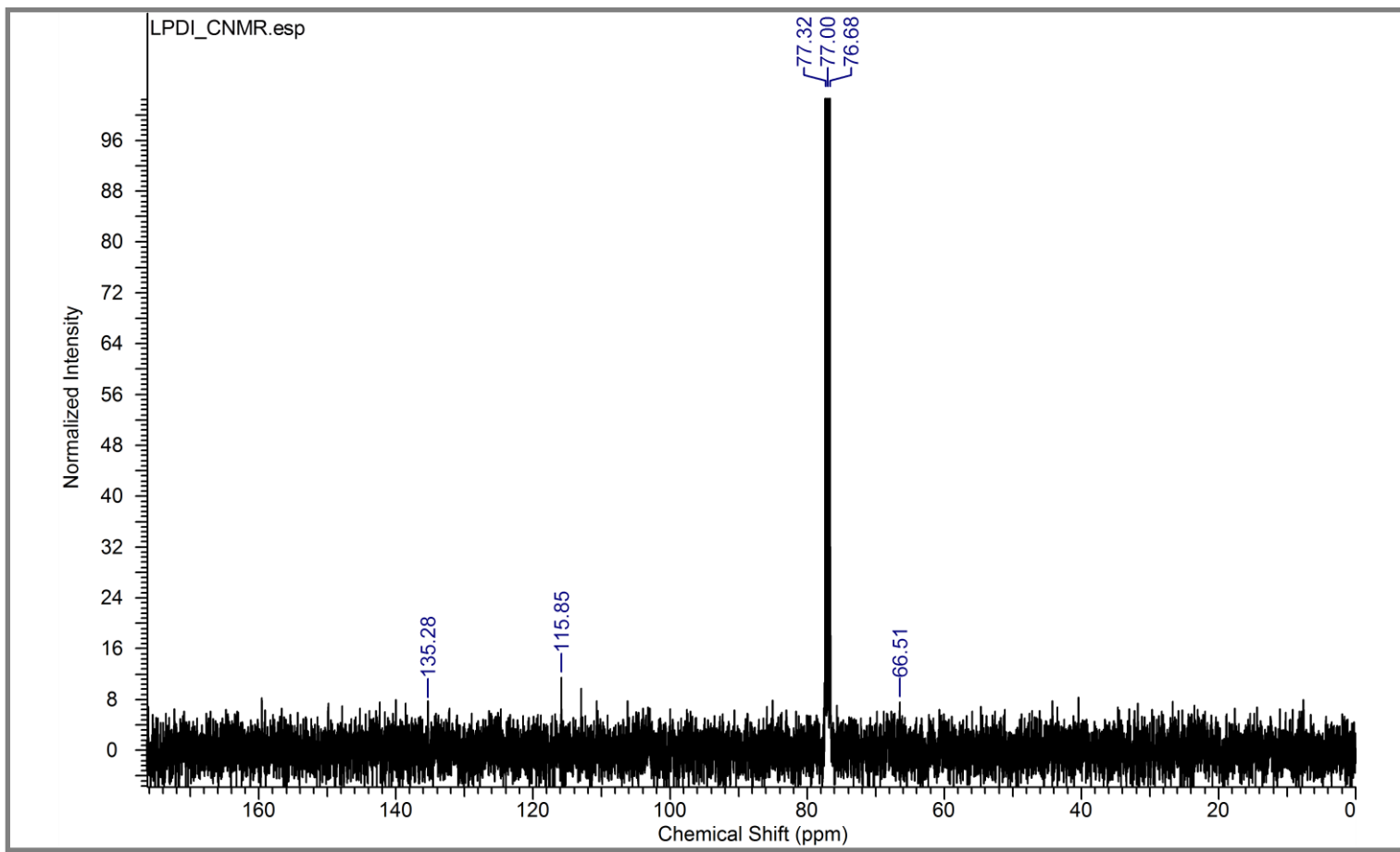
Figure 4.10: ^{1}C-NMR spectrum of N, N'-bis(2-aminohexanoic acid)-3,4,9,10 perylenebis(dicarboximide) (LPDI) in CDCl$_3$ + CF$_3$COOH at 100 MHz.
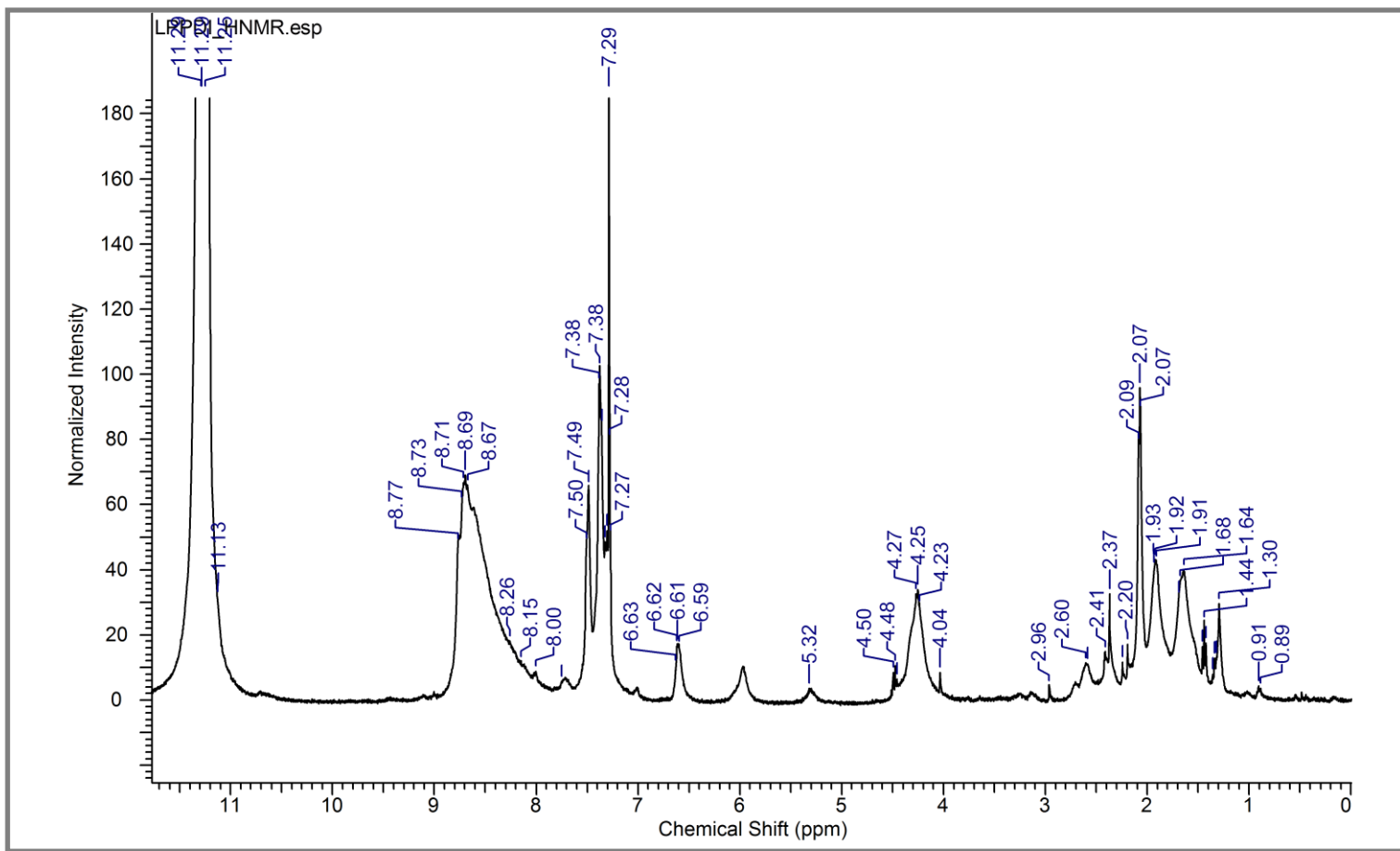
Figure 4.11: ^{1}H-NMR spectrum of N-(2-aminohexanoic acid)-N'-(1-phenyl-ethylamine)-3,4,9,10 perylenebis(dicarboximide) (LPPDI) in CDCl$_3$ + CF$_3$COOH at 400 MHz.
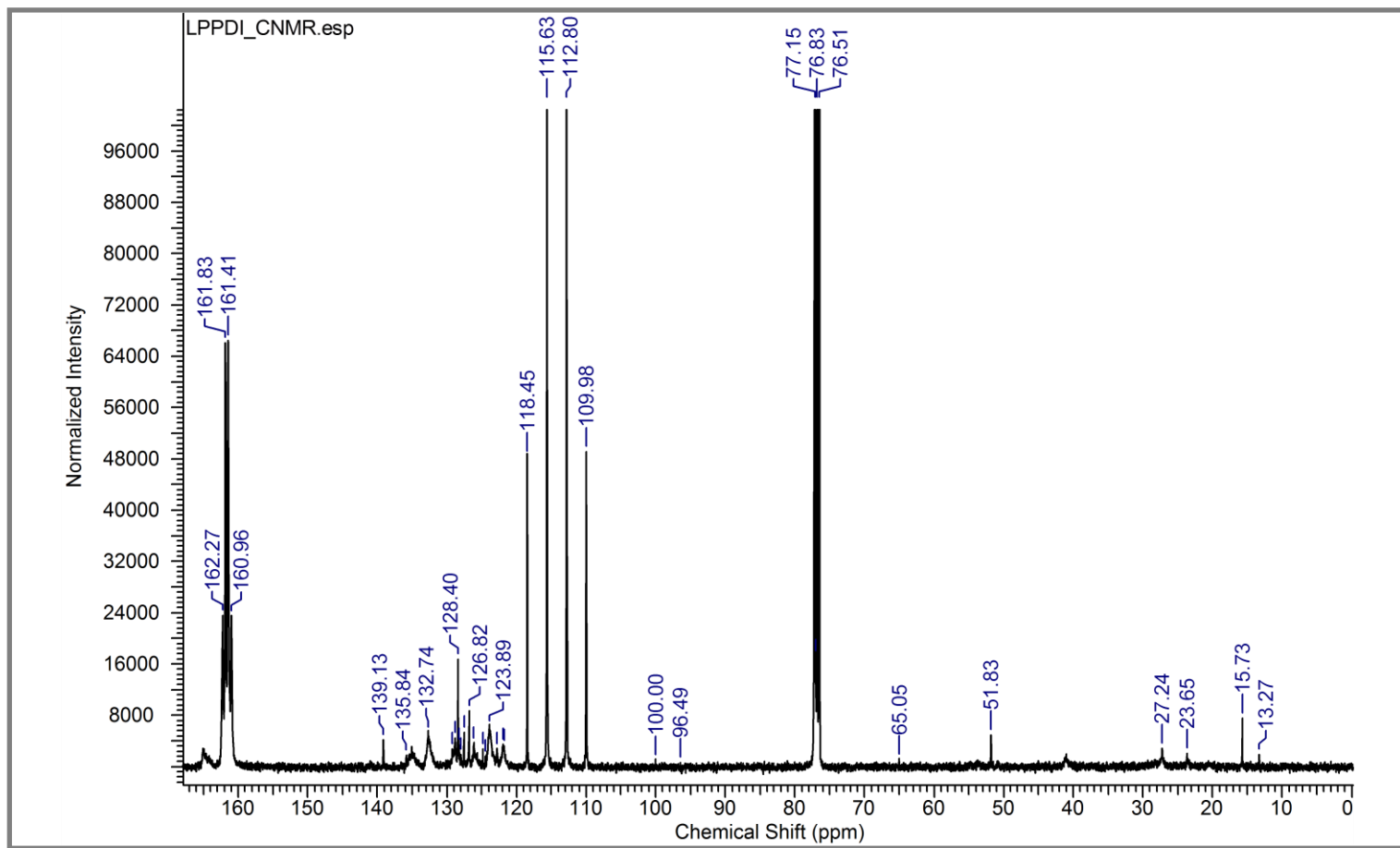
Figure 4.12: [1]C-NMR spectrum of N-(2-aminohexanoic acid)-N'-(1-phenyl-ethylamine)-3,4,9,10 perylenebis(dicarboximide) (LPPDI) in CDCl$_3$ + CF$_3$COOH at 100 MHz.
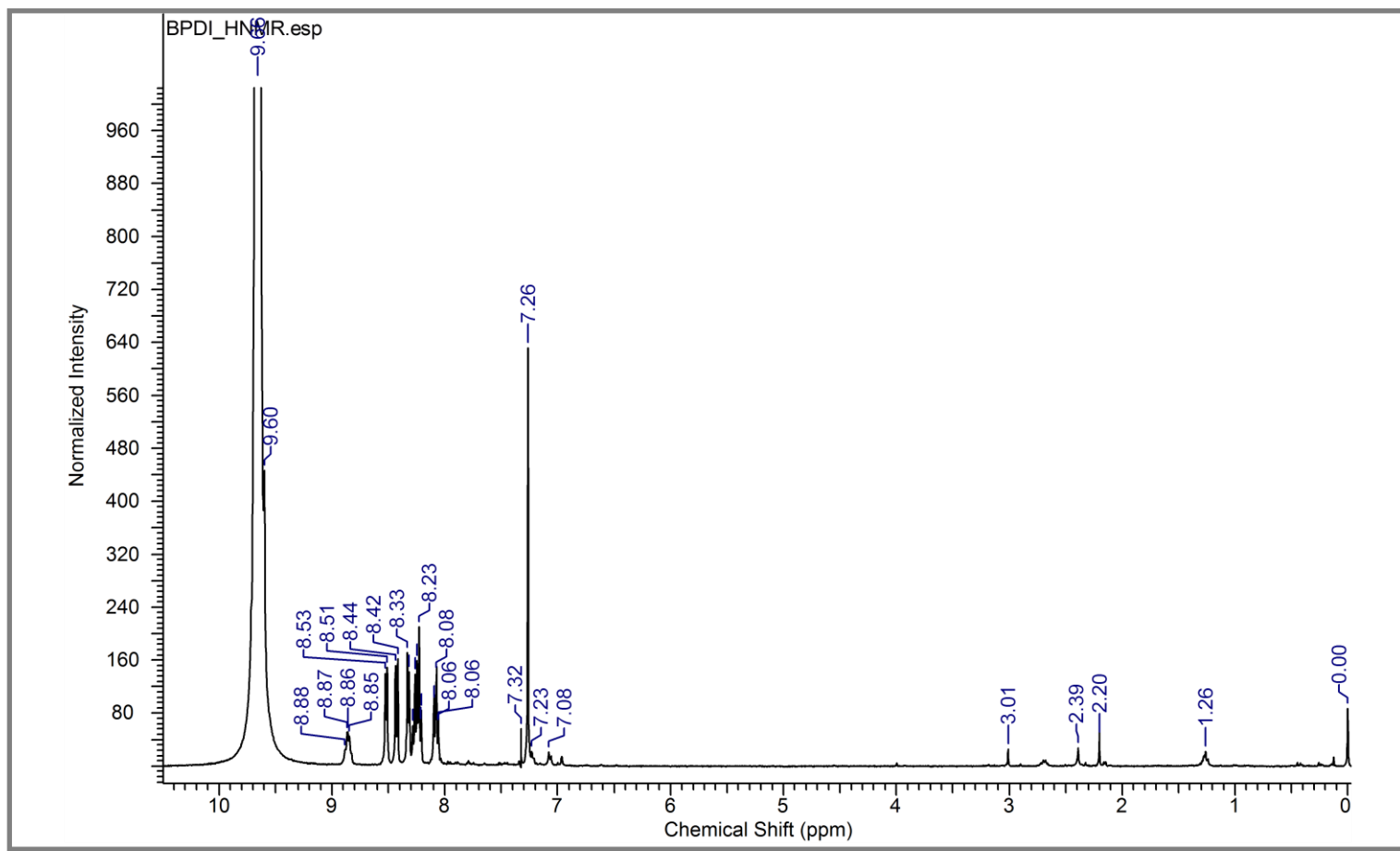
Figure 4.13: ¹H-NMR spectrum of N-(2-hydroxy-4-benzoic acid)-N'-(4-hydroxyphenyl)-3,4,9,10 perylenebis (dicarboximide) (BPDI) in CDCl$_3$ + CF$_3$COOH at 400 MHz.
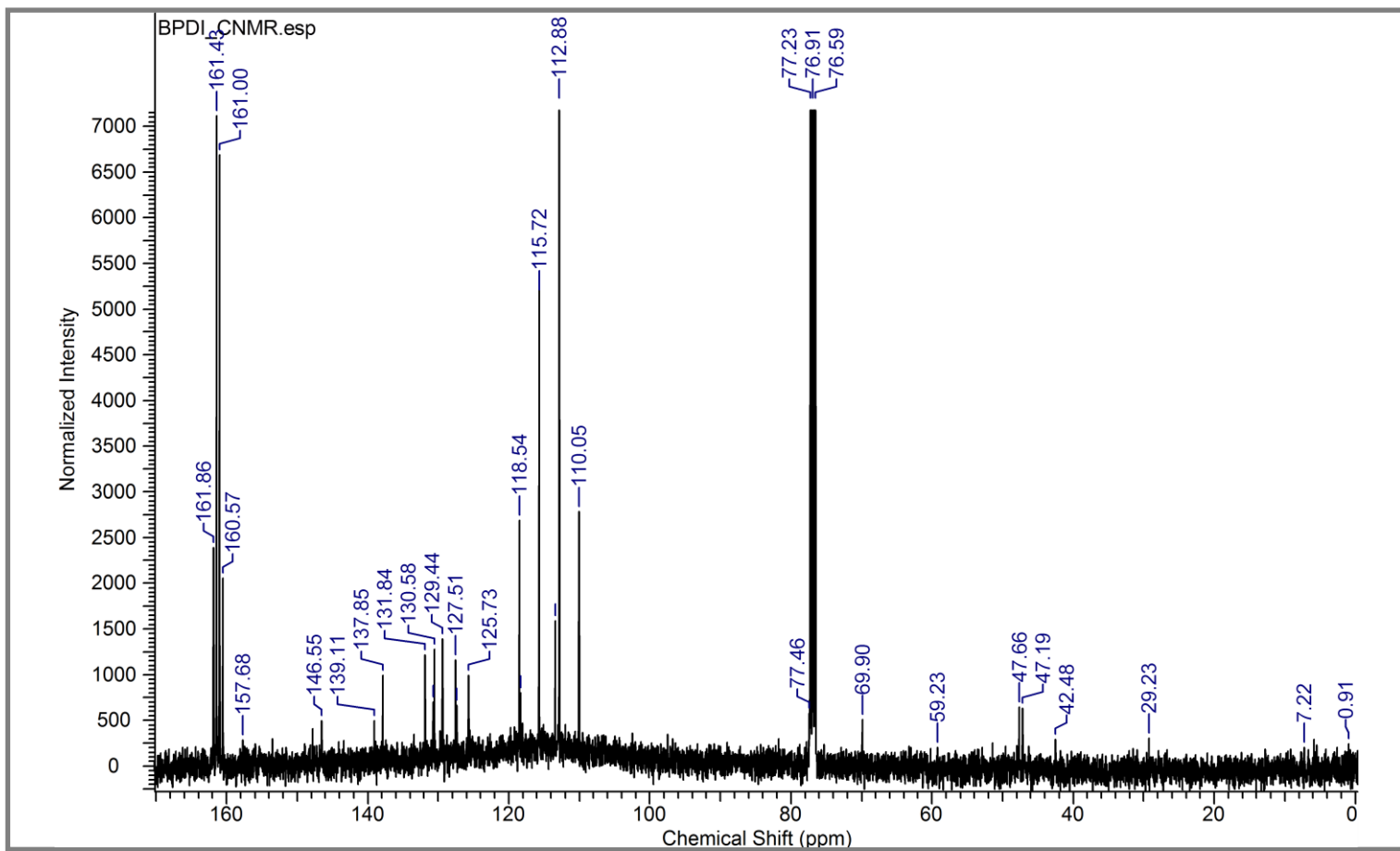
Figure 4.14: [1]C-NMR spectrum of N-(2-hydroxy-4-benzoic acid)-N'-(4-hydroxyphenyl)-3,4,9,10 perylenebis (dicarboximide) (BPDI) in CDCl$_3$ + CF$_3$COOH at 100 MHz.
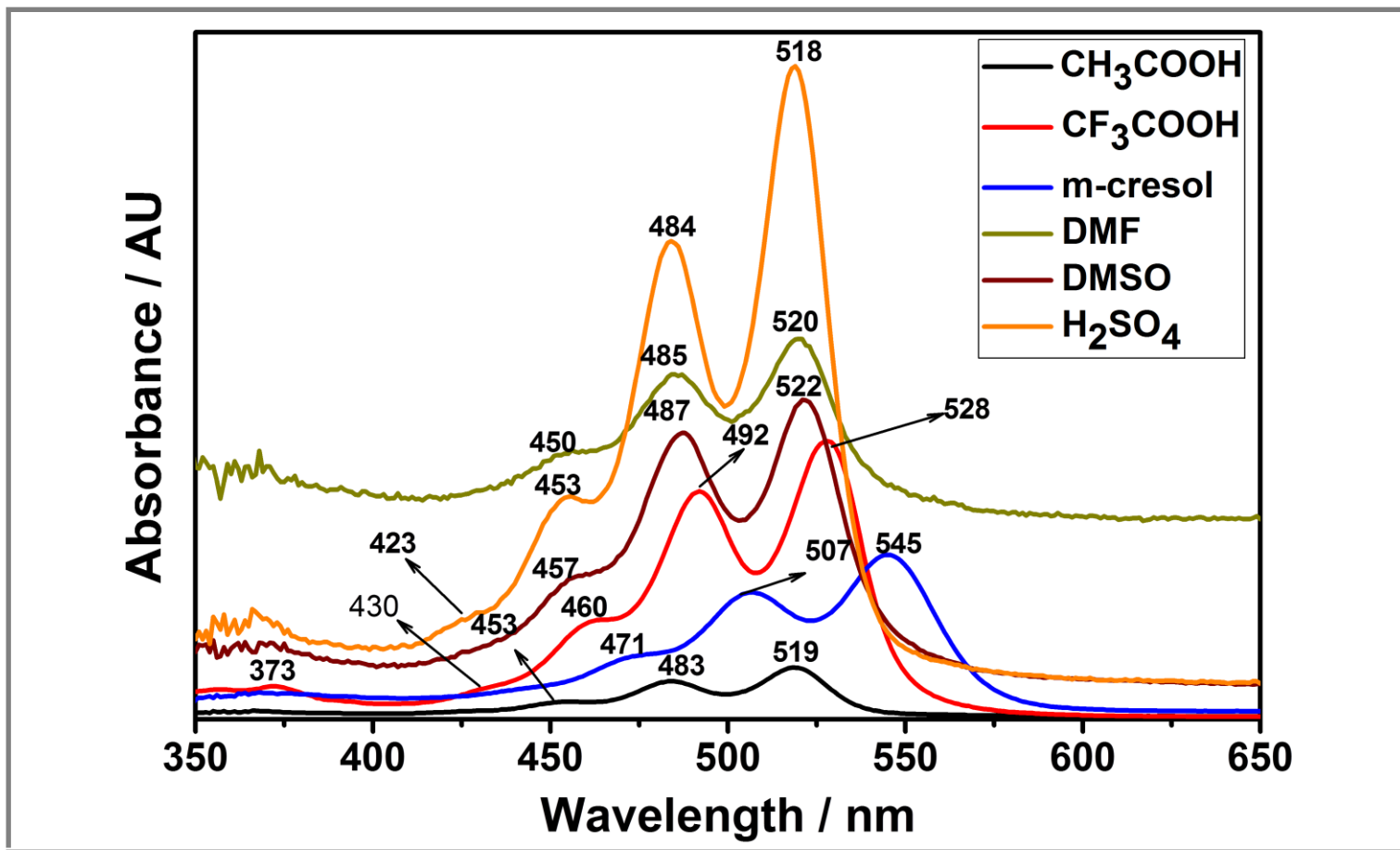
Figure 4.15: Absorption spectra of N-(2-aminohexanoic acid)-3,4,9,10 perylenetetracarboxylic-3,4-anhydride-9,10 imide (LPMI) in different solvents.
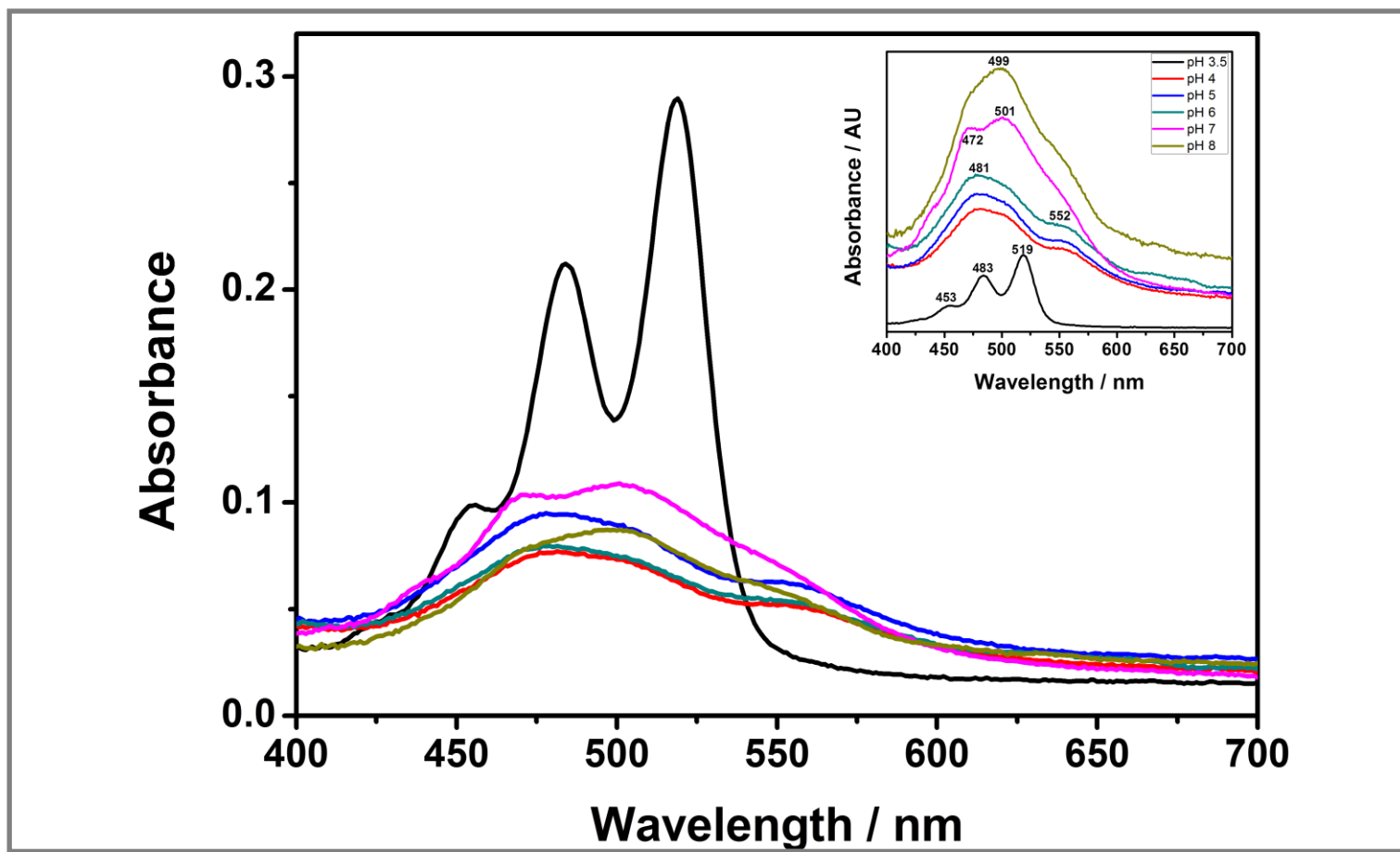
Figure 4.16: Absorption spectra of N-(2-aminohexanoic acid)-3,4,9,10 perylenetetracarboxylic-3,4-anhydride-9,10 imide (LPMI) in different pH values.
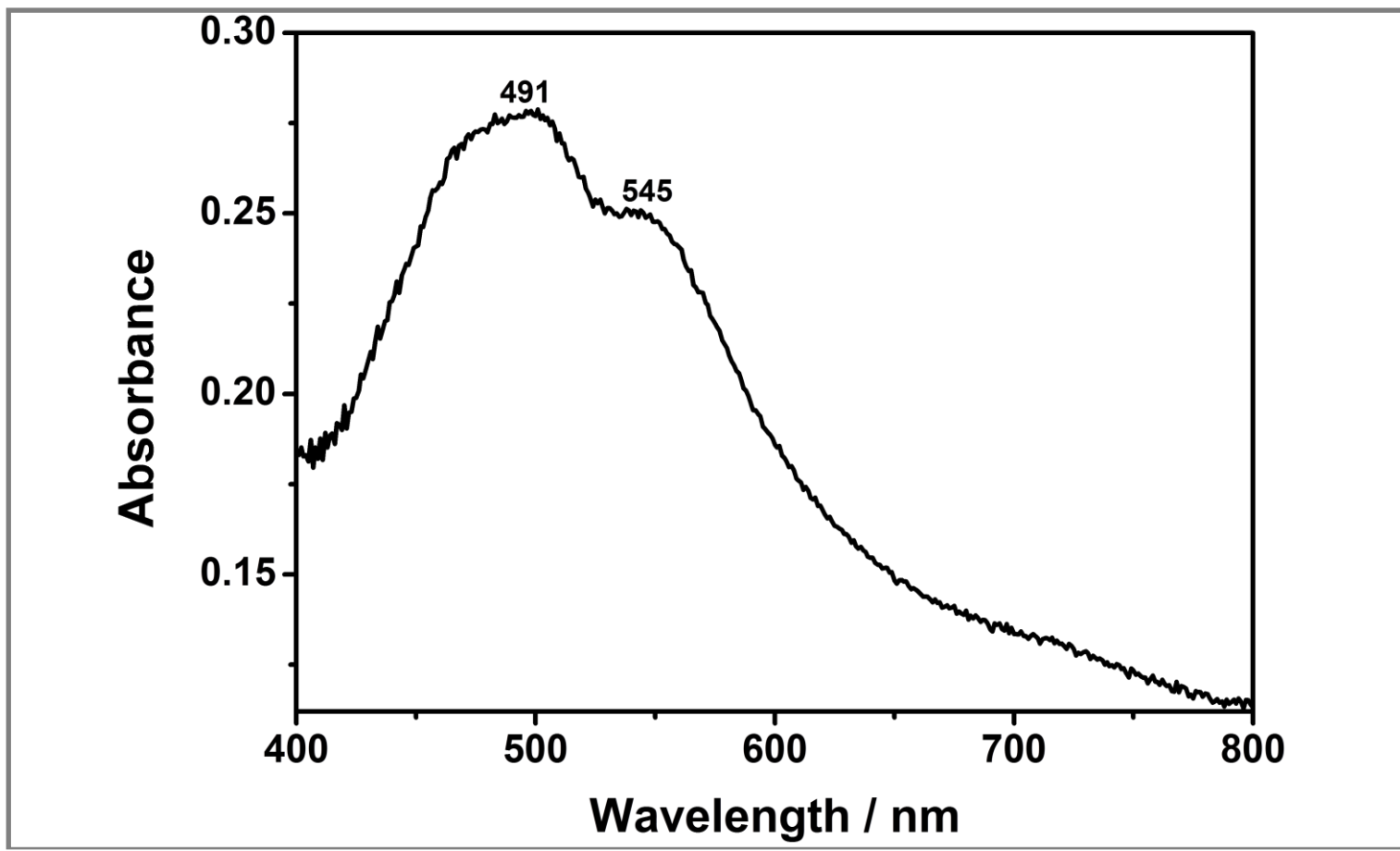
Figure 4.17: Solid-state absorption spectrum of N-(2-aminohexanoic acid)-3,4,9,10 perylenetetracarboxylic-3,4-anhydride-9,10 imide (LPMI).
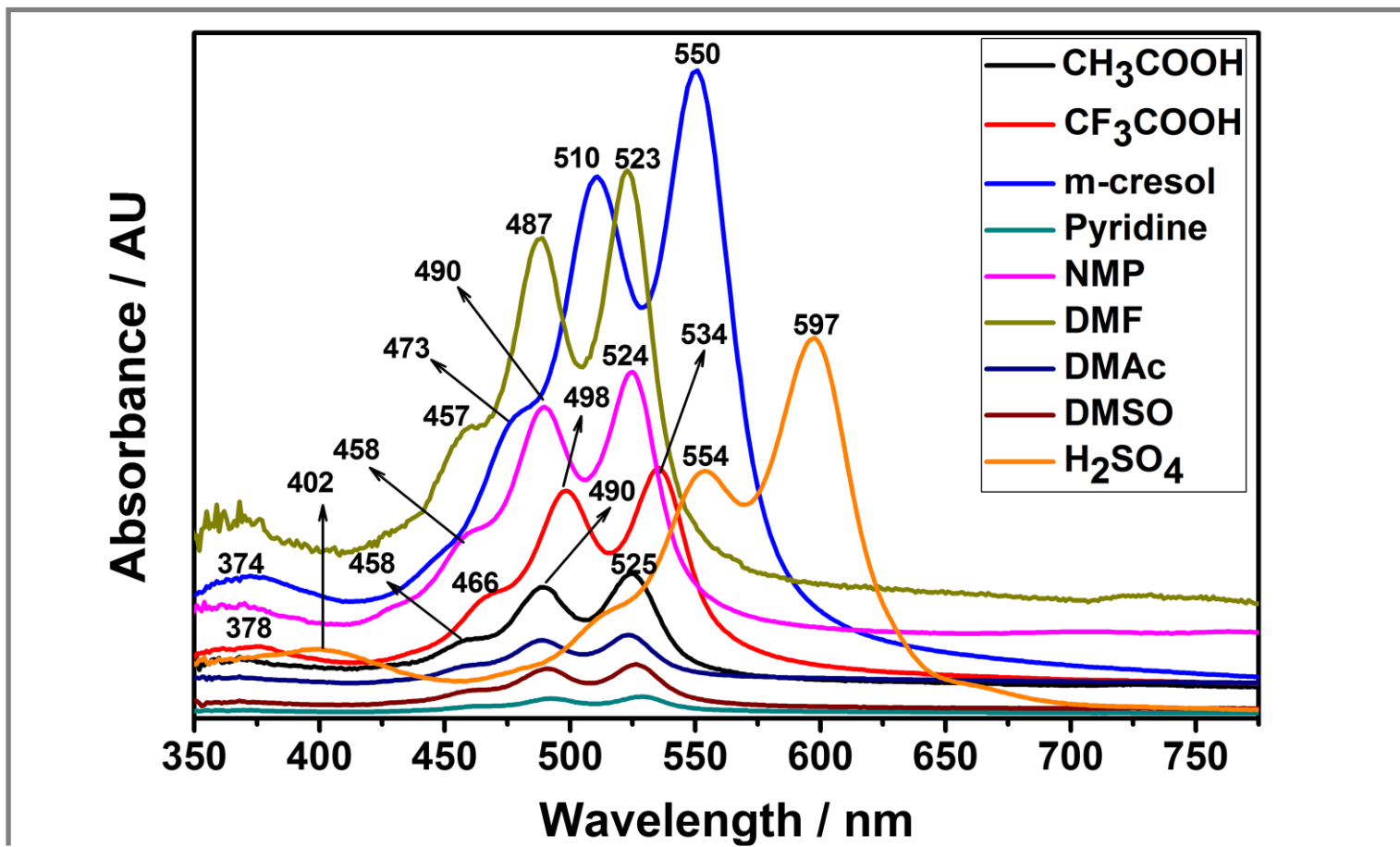
Figure 4.18: Absorption spectra of N, N'-bis(2-aminohexanoic acid)-3,4,9,10 perylenebis(dicarboximide) (LPDI) in different solvents.
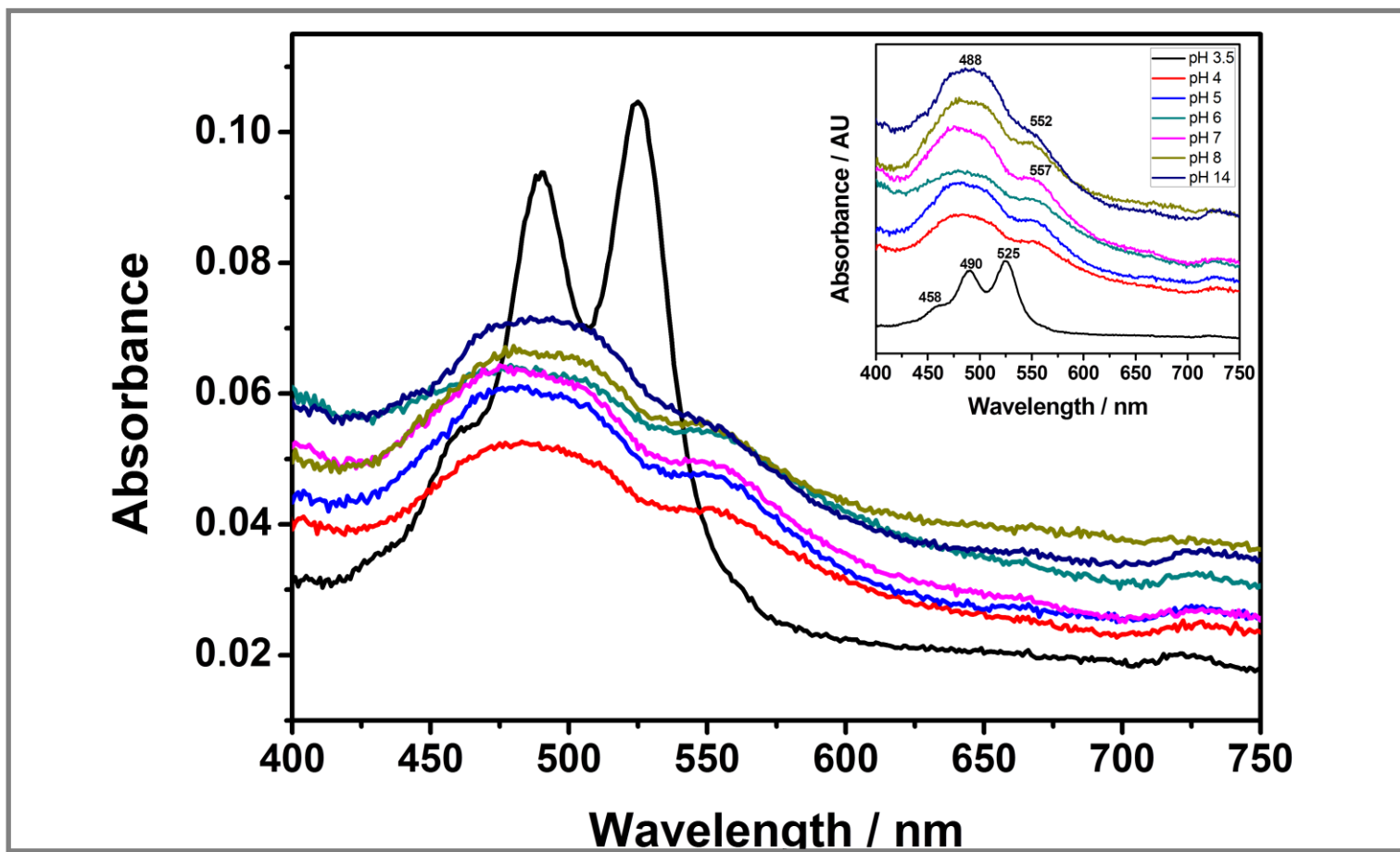
Figure 4.19: Absorption spectra of N, N'-bis(2-aminohexanoic acid)-3,4,9,10 perylenebis(dicarboximide) (LPDI) at different pH values.
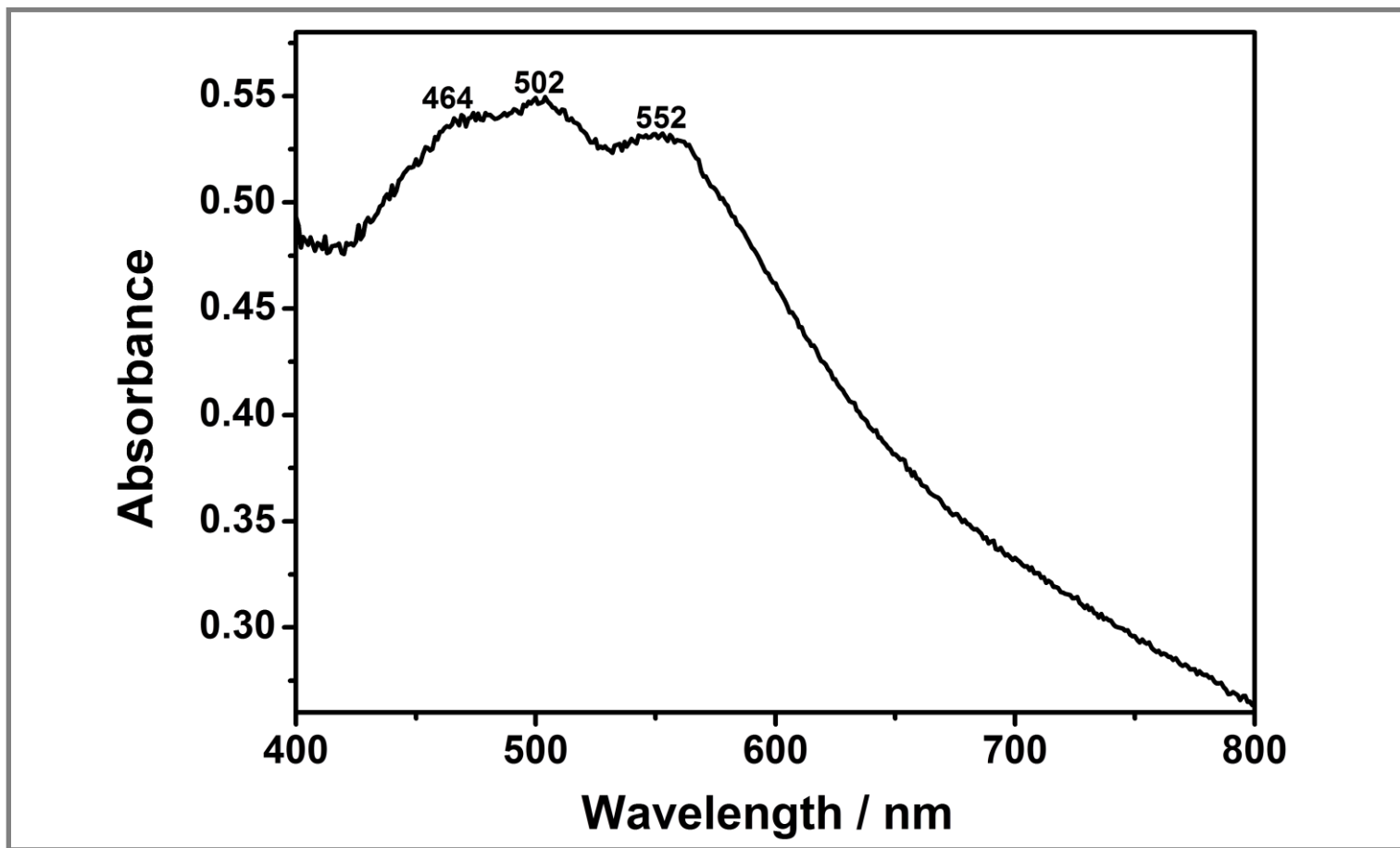
Figure 4.20: Solid-state absorption spectrum of N, N'-bis(2-aminohexanoic acid)-3,4,9,10 perylenebis(dicarboximide) (LPDI).
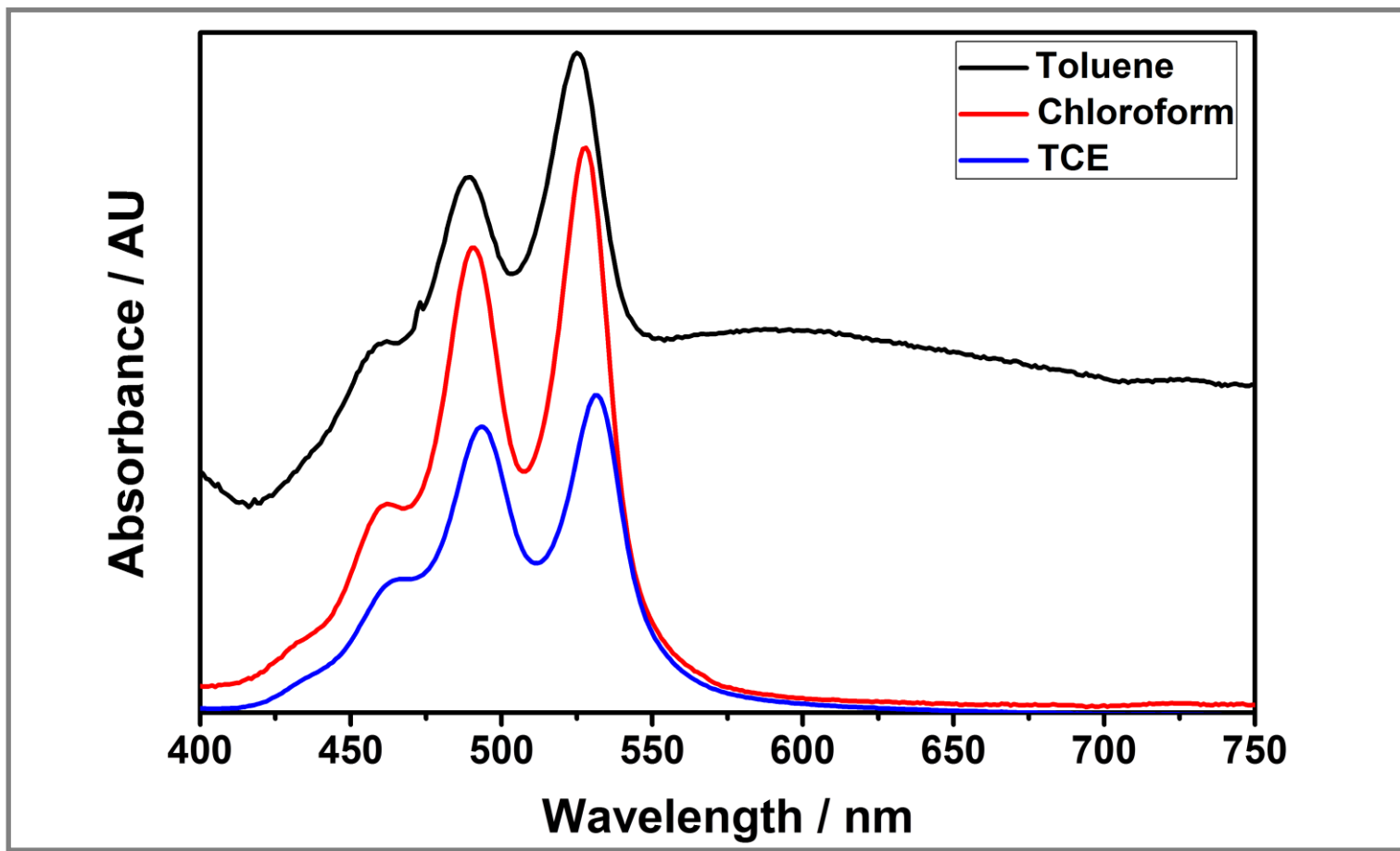
Figure 4.21: Absorption spectra of N-(2-aminohexanoic acid)-N'-(1-phenyl-ethylamine)-3,4,9,10 perylenebis (dicarboximide) (LPPDI) in non-polar solvents.
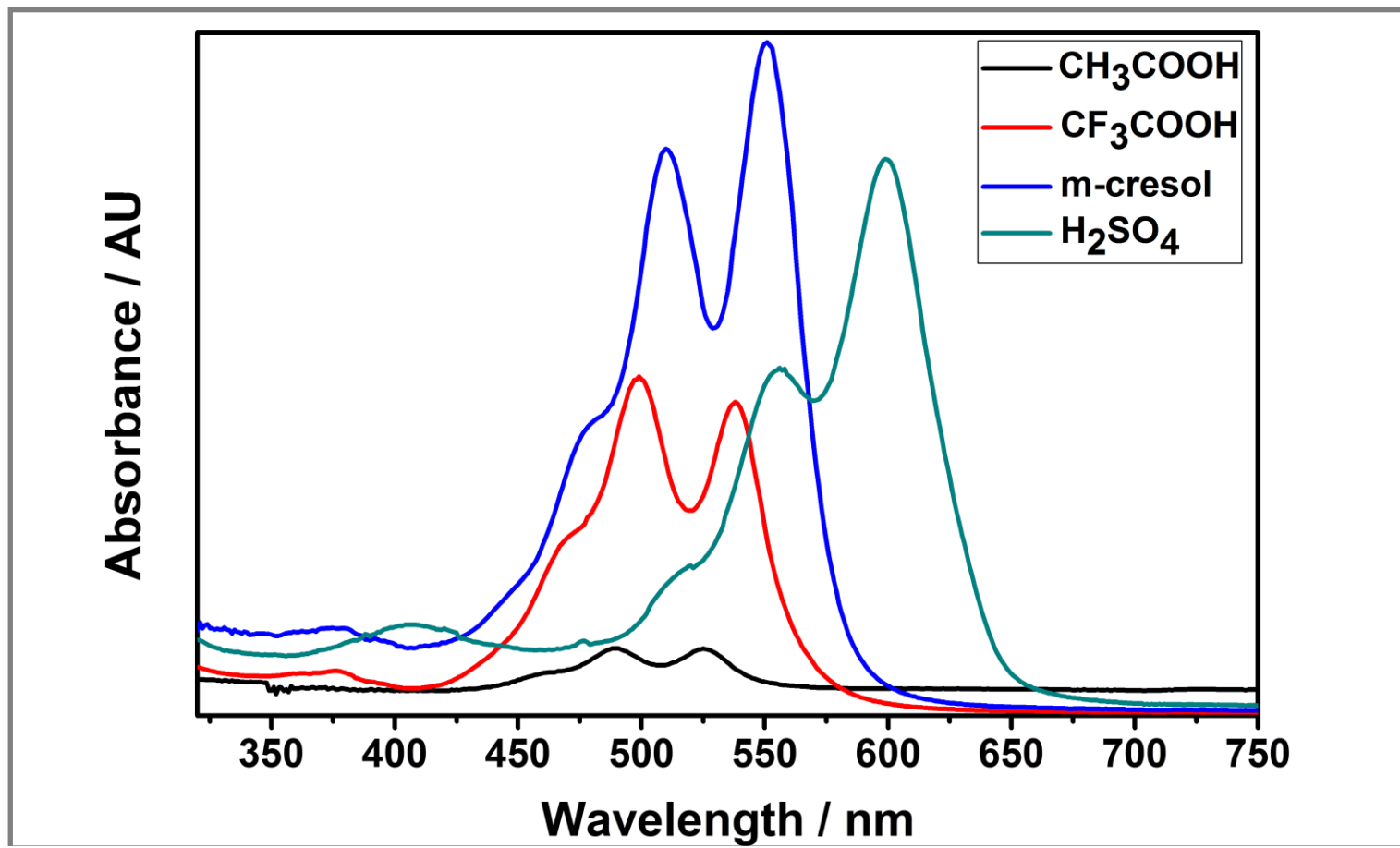
Figure 4.22: Absorption spectra of N-(2-aminohexanoic acid)-N'-(1-phenyl-ethylamine)-3,4,9,10 perylenebis (dicarboximide) (LPPDI) in polar protic solvents.
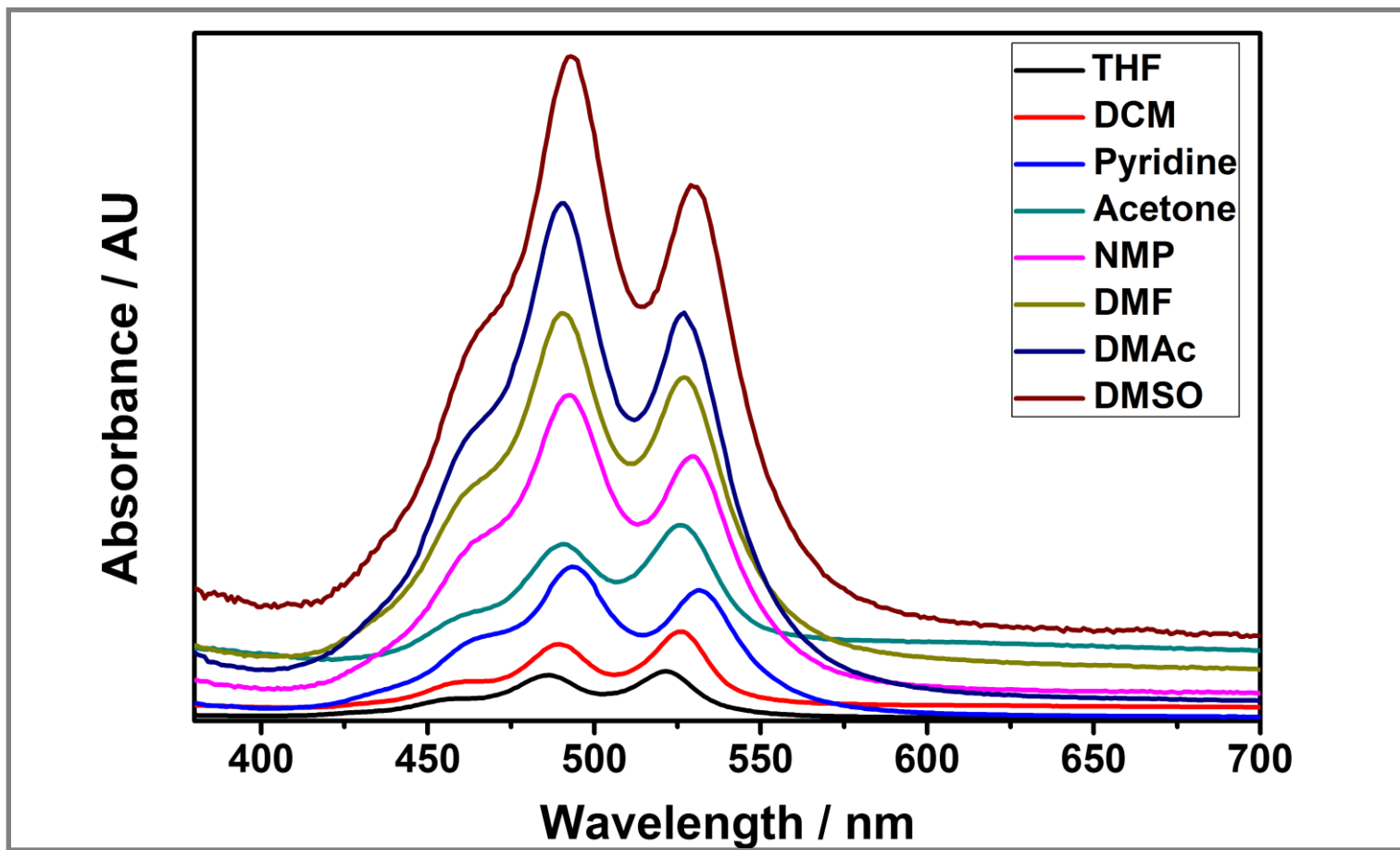
Figure 4.23: Absorption spectra of N-(2-aminohexanoic acid)-N'-(1-phenyl-ethylamine)-3,4,9,10 perylenebis (dicarboximide) (LPPDI) in dipolar aprotic solvents.

Figure 4.24: Solid-state absorption spectrum of N-(2-aminohexanoic acid)-N'-(1-phenyl-ethylamine)-3,4,9,10 perylenebis(dicarboximide) (LPPDI).
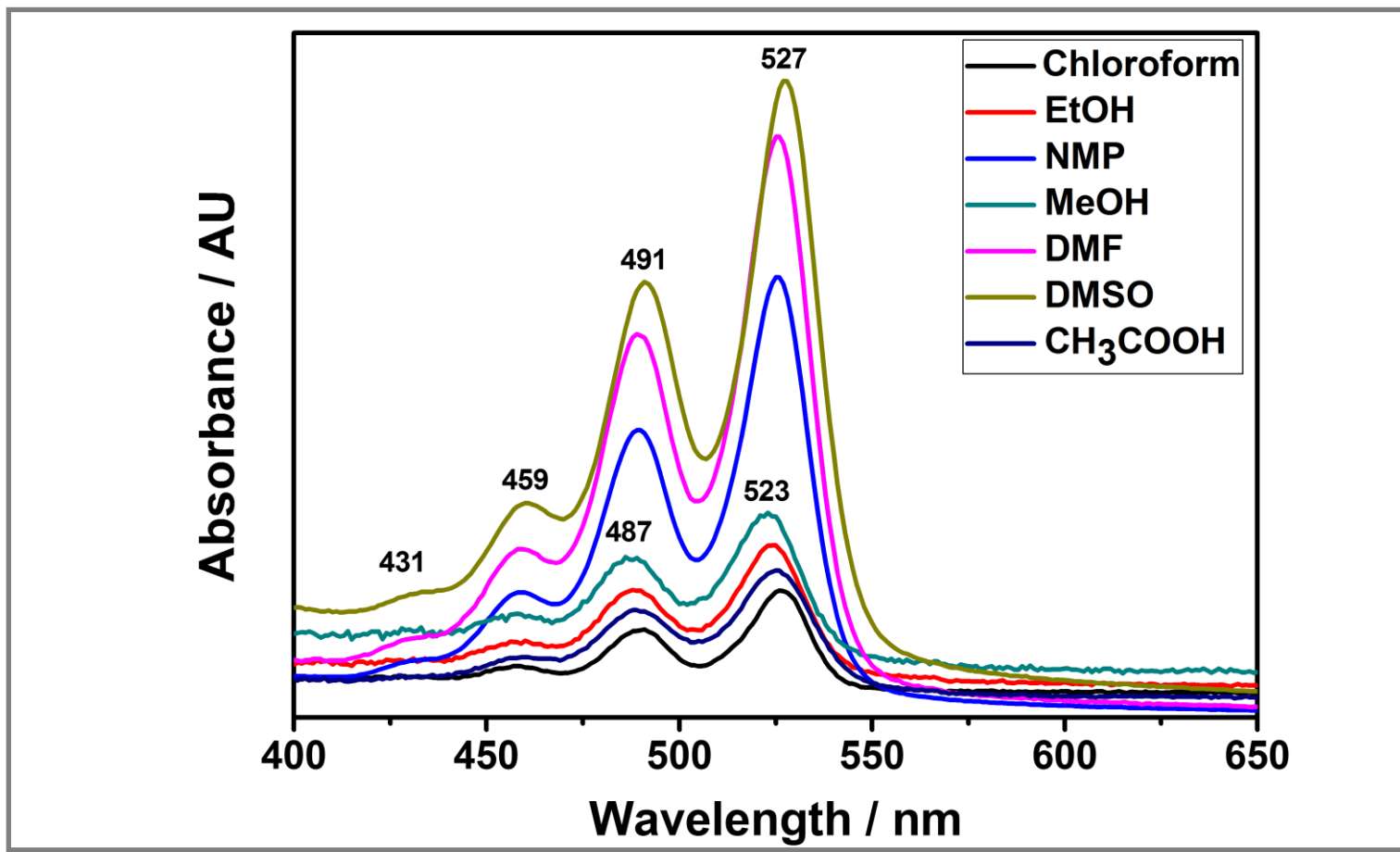
Figure 4.25: Absorption spectra of N-(2-hydroxy-4-benzoic acid)-N'-(4-hydroxyphenyl)-3,4,9,10 perylenebis (dicarboximide) (BPDI) in different solvents.

Figure 4.26: Absorption spectra of N-(2-hydroxy-4-benzoic acid)-N'-(4-hydroxyphenyl)-3,4,9,10 perylenebis (dicarboximide) (BPDI) at different pH values.

Figure 4.27: Absorption spectra of N-(2-hydroxy-4-benzoic acid)-N'-(4-hydroxyphenyl)-3,4,9,10 perylenebis (dicarboximide) (BPDI) at different pH values after filtration with 0.2 μm filter.
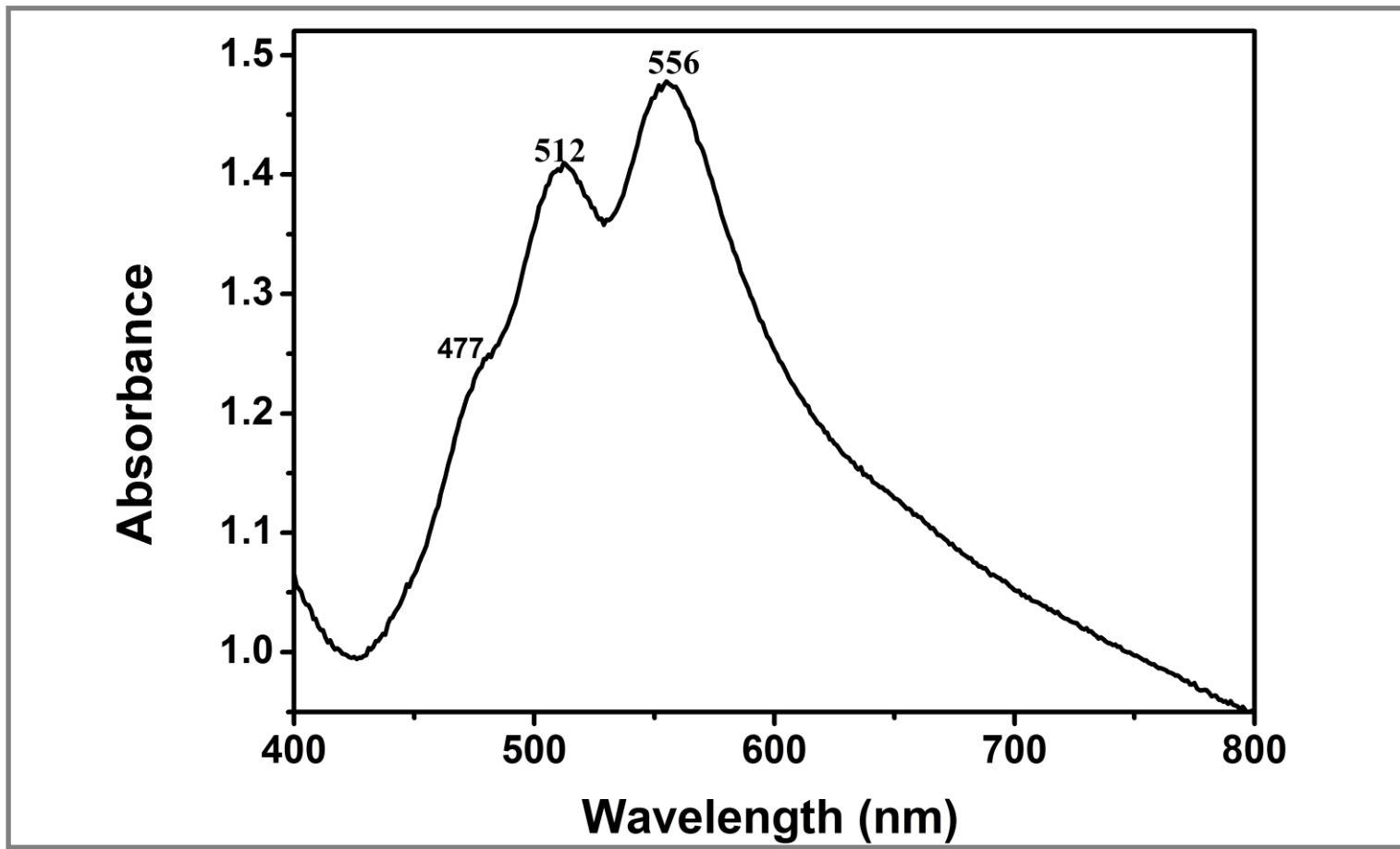
Figure 4.28: Solid-state absorption spectrum of N-(2-hydroxy-4-benzoic acid)-N'-(4-hydroxyphenyl)-3,4,9,10 perylenebis (dicarboximide) (BPDI).
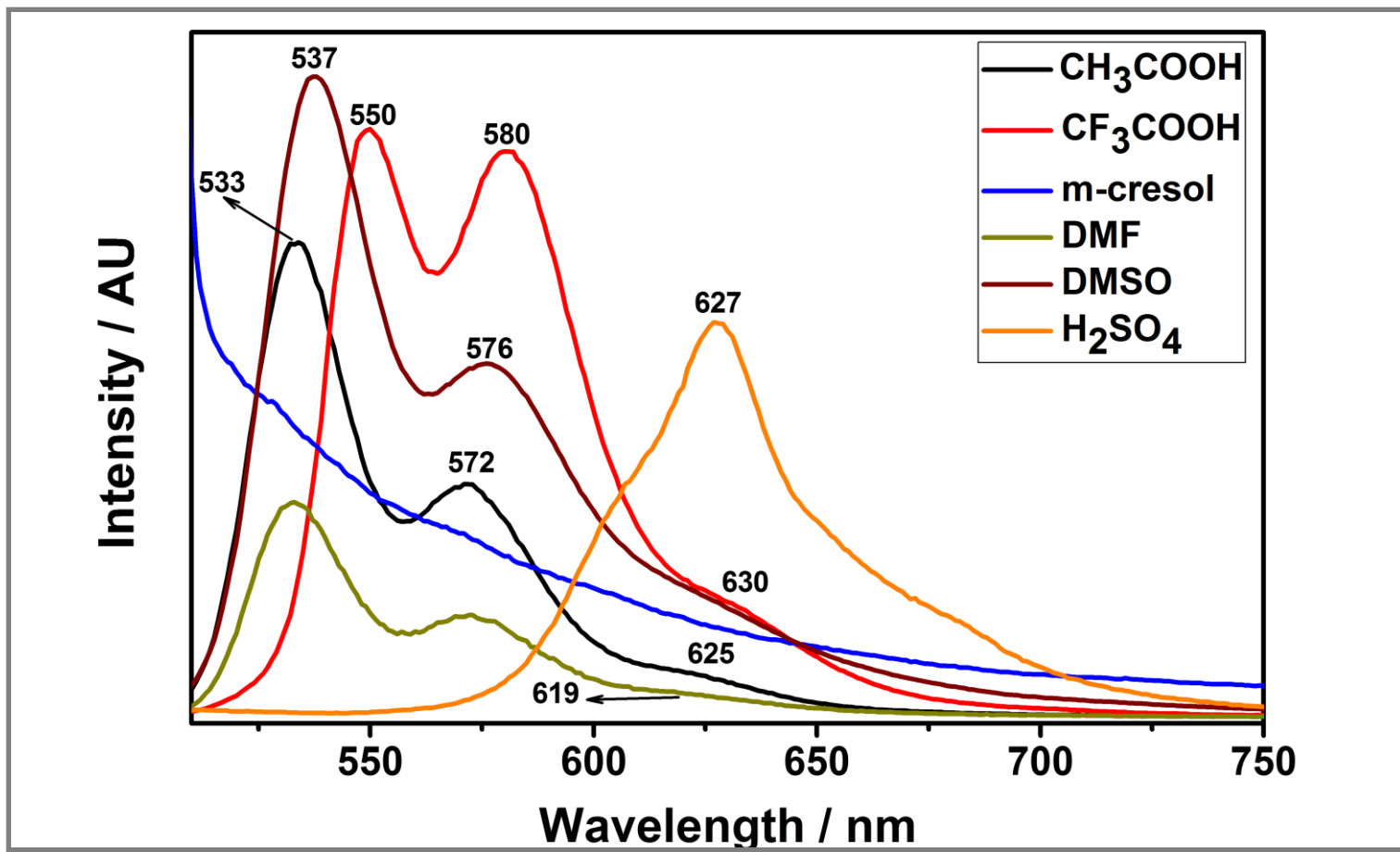
Figure 4.29: Emission spectra of N-(2-aminohexanoic acid)-3,4,9,10 perylenetetracarboxylic-3,4-anhydride-9,10 imide (LPMI) in different solvents.
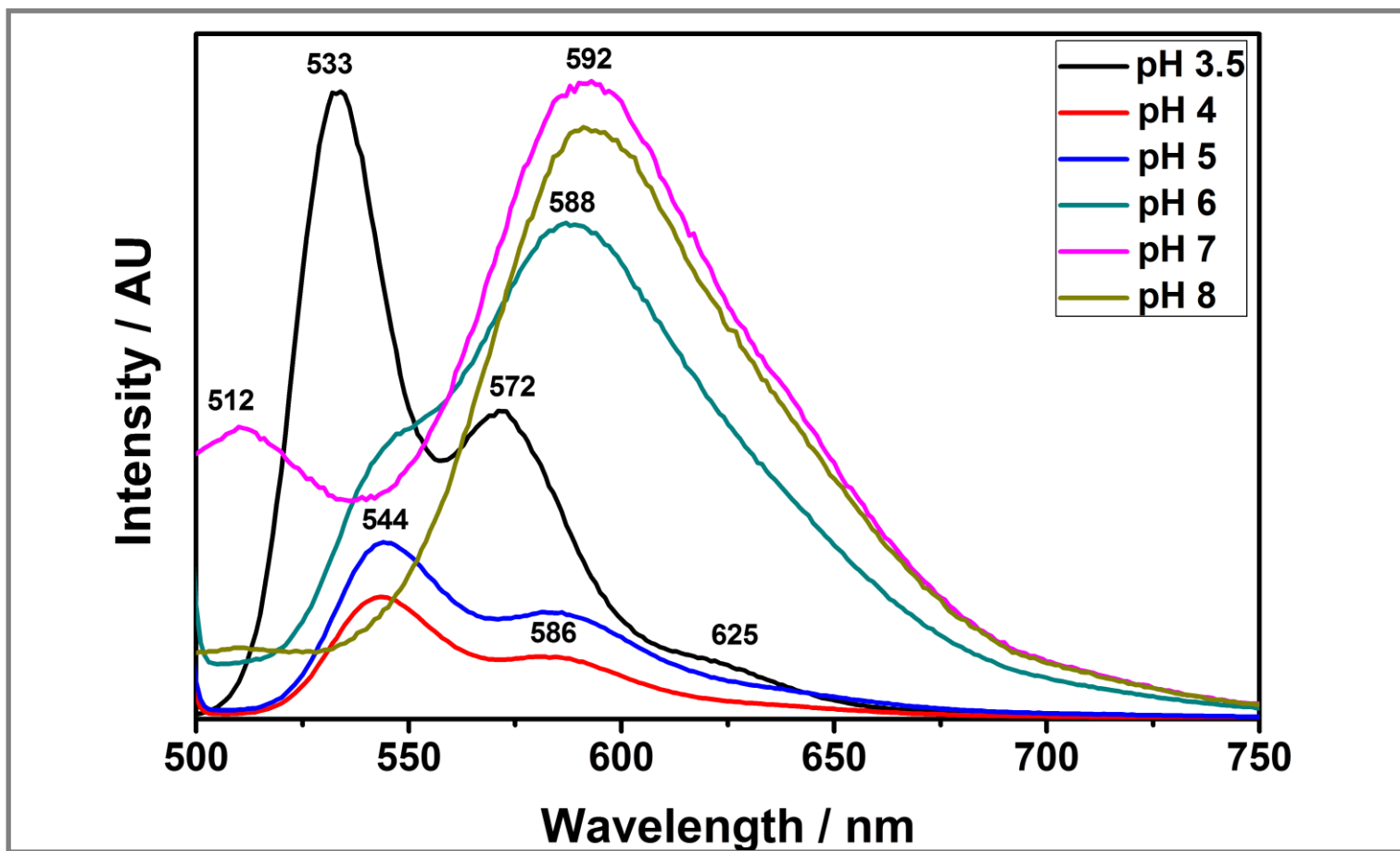
Figure 4.30: Emission spectra of N-(2-aminohexanoic acid)-3,4,9,10 perylenetetracarboxylic-3,4-anhydride-9,10 imide (LPMI) in different pH values.
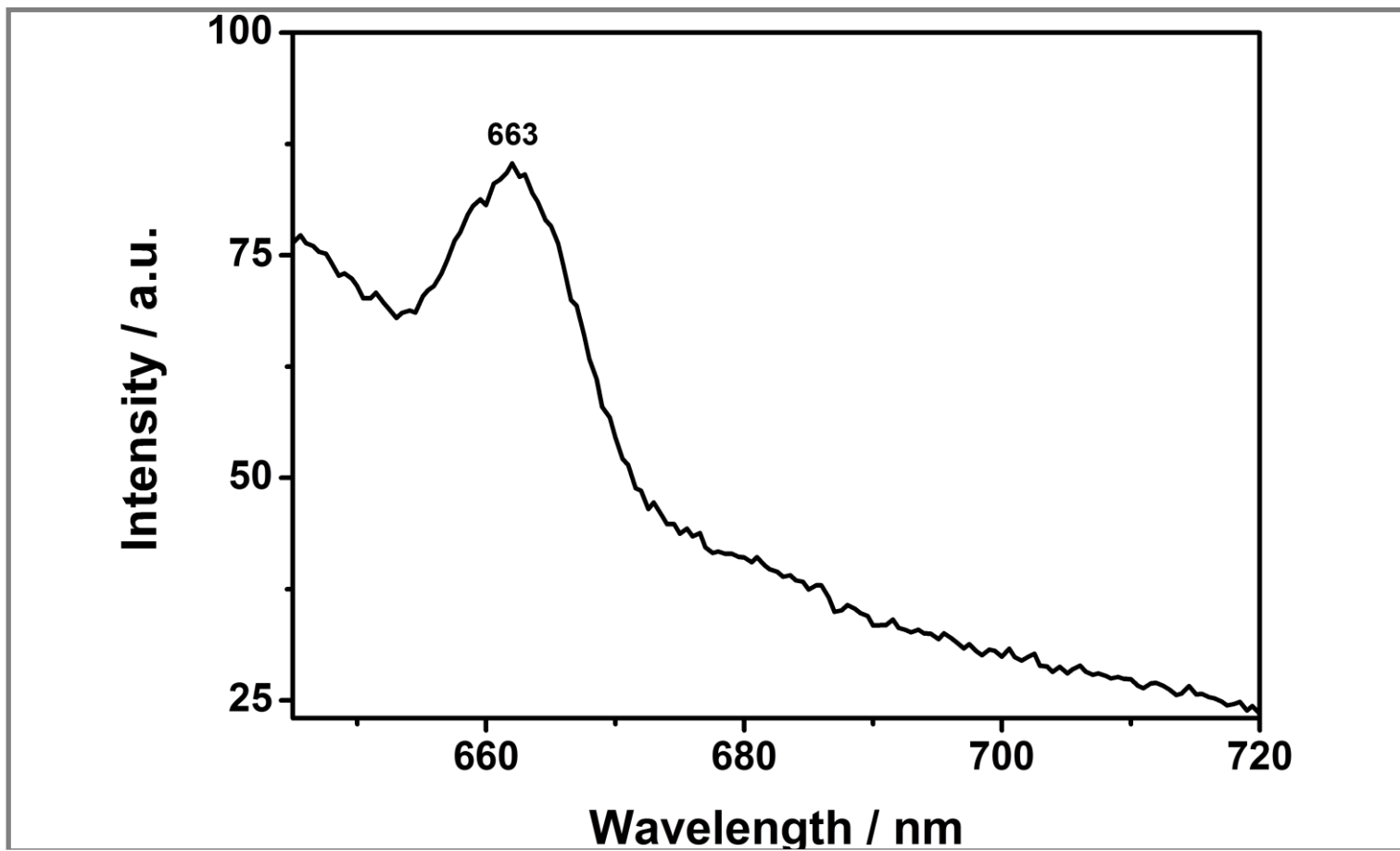
Figure 4.31: Solid-state emission spectrum of N-(2-aminohexanoic acid)-3,4,9,10 perylenetetracarboxylic-3,4-anhydride-9,10 imide (LPMI).
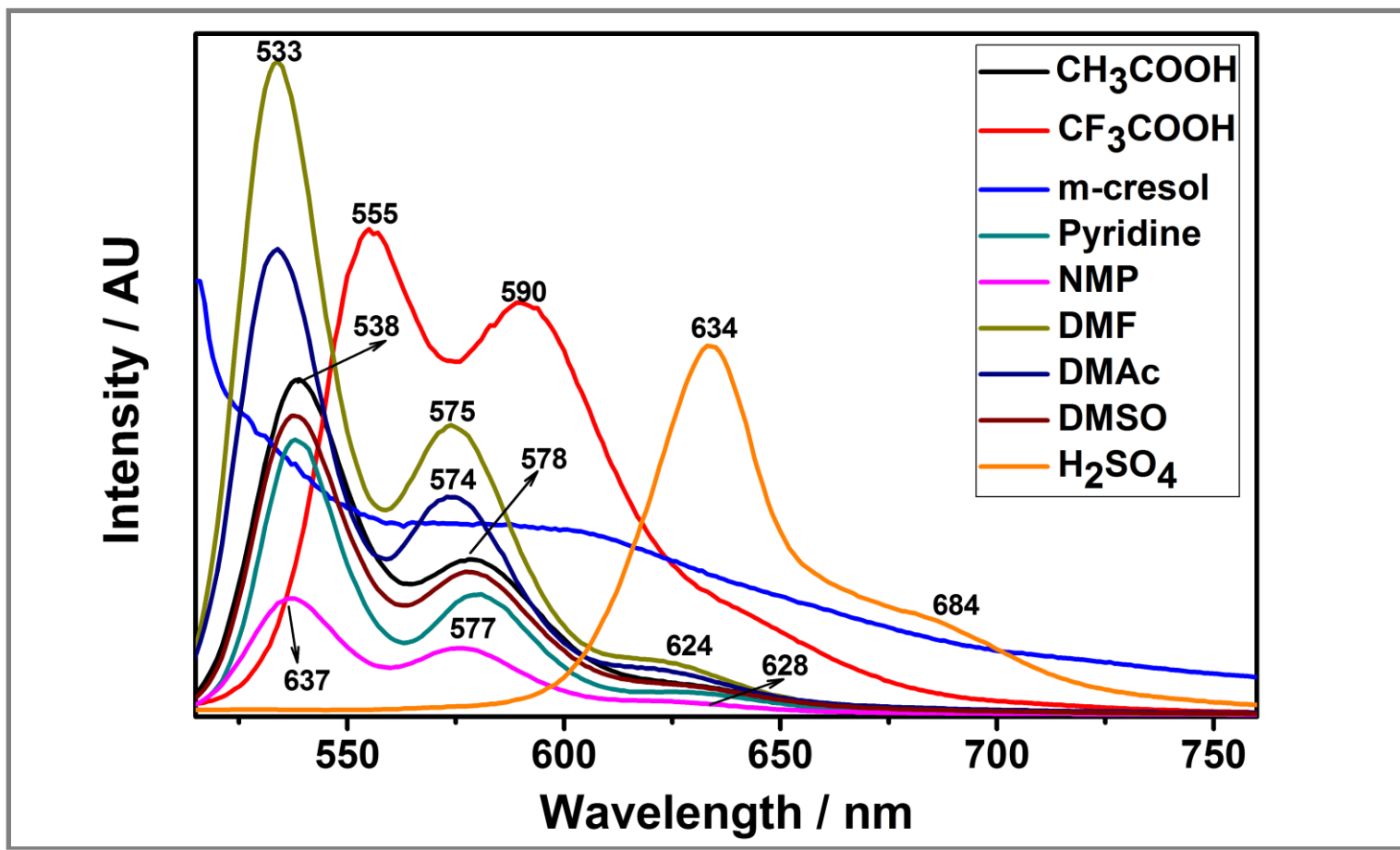
Figure 4.32: Emission spectra of N, N'-bis(2-aminohexanoic acid)-3,4,9,10 perylenebis(dicarboximide) (LPDI) in different solvents.
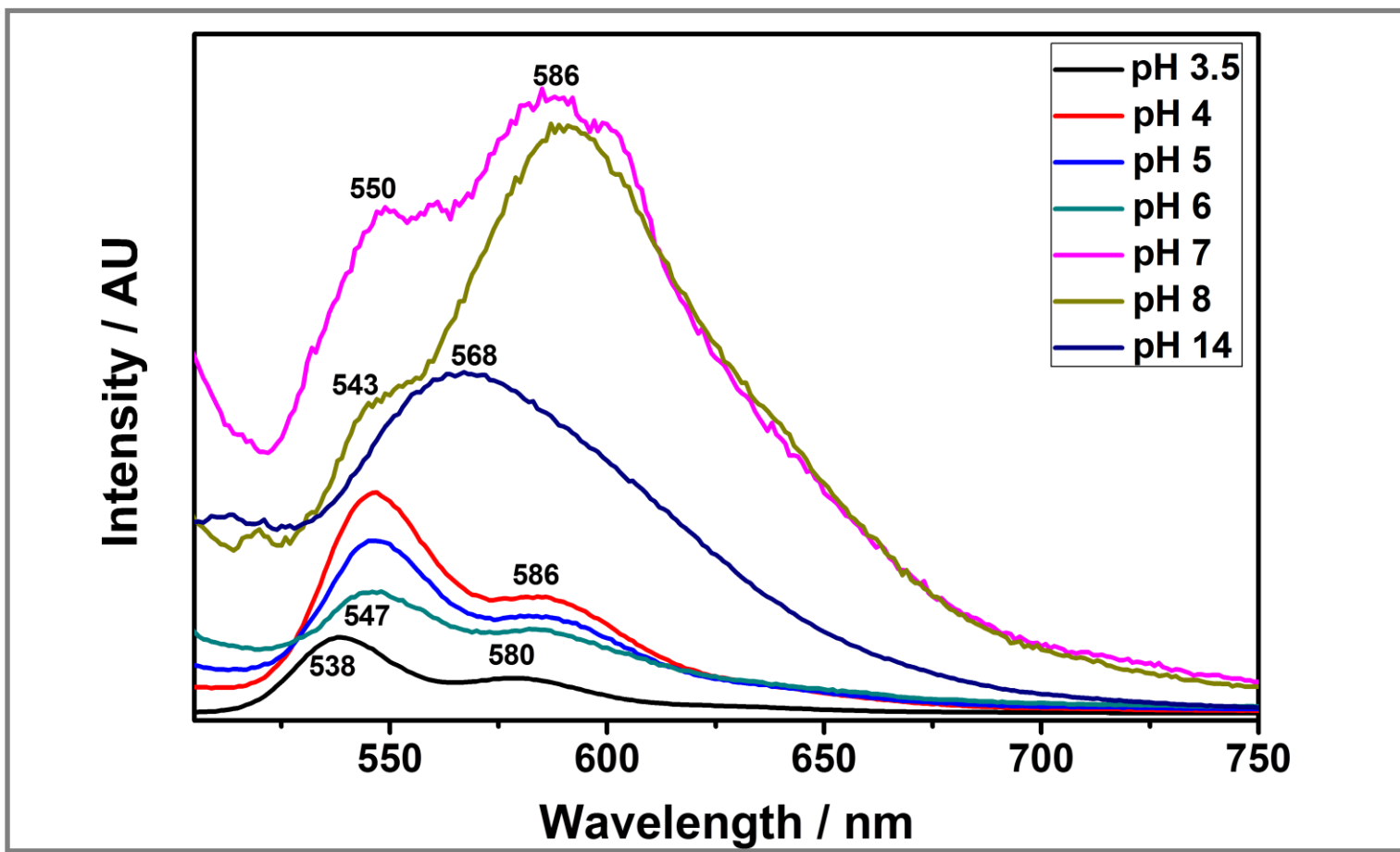
Figure 4.33: Emission spectra of N, N'-bis(2-aminohexanoic acid)-3,4,9,10 perylenebis(dicarboximide) (LPDI) at different pH values.
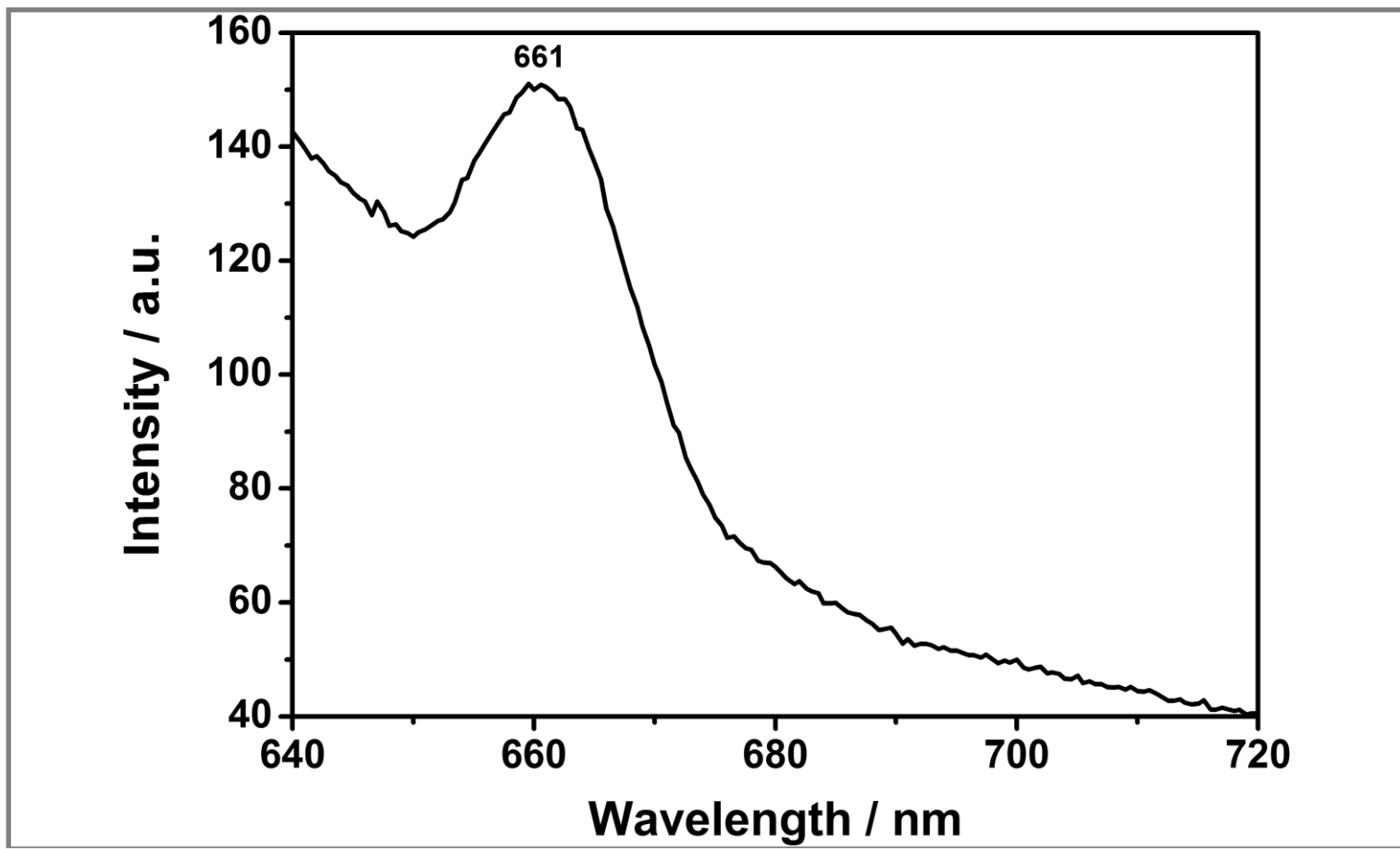
Figure 4.34: Solid-state emission spectrum of N, N'-bis(2-aminohexanoic acid)-3,4,9,10 perylenebis(dicarboximide) (LPDI).
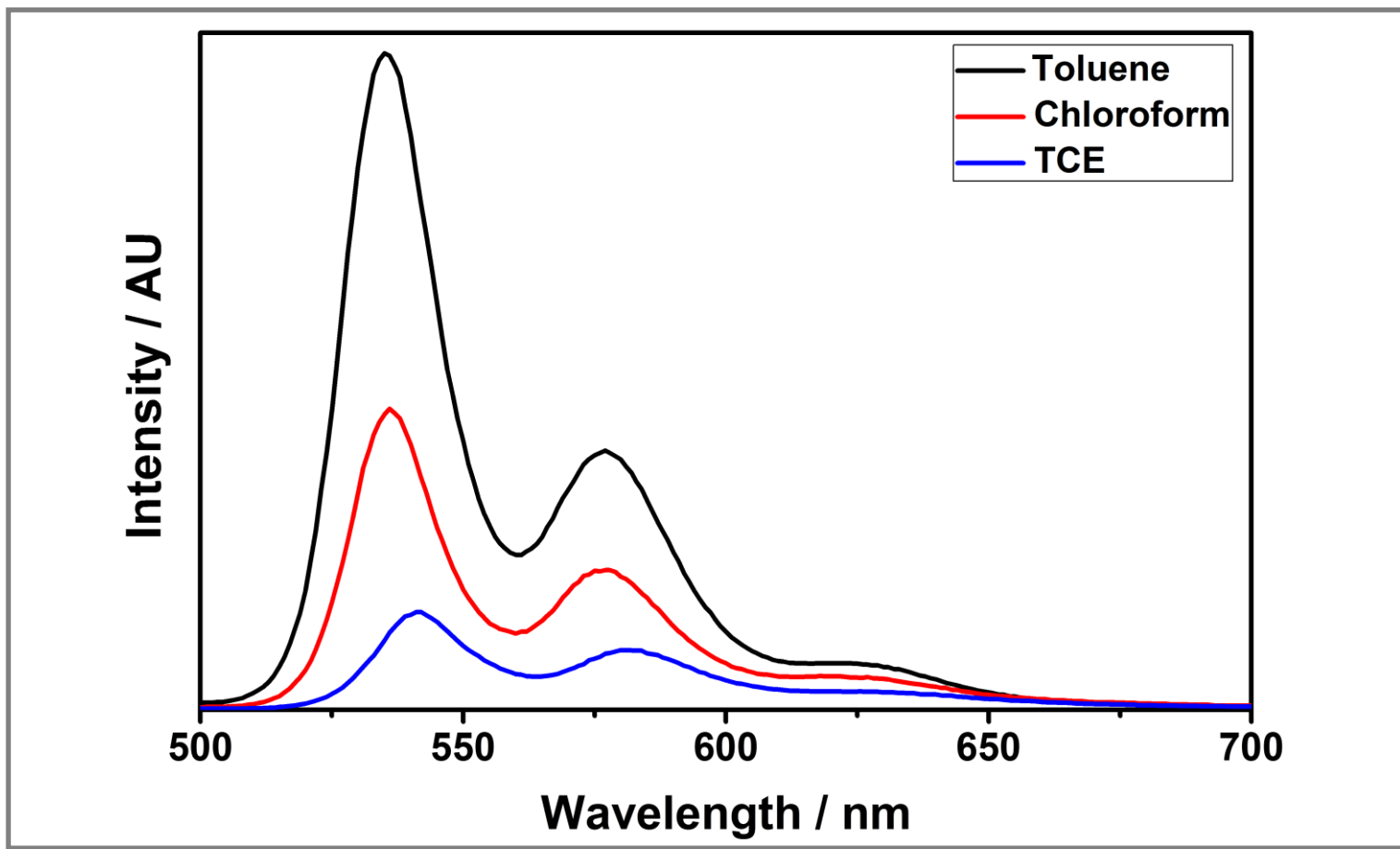
Figure 4.35: Emission spectra of N-(2-aminohexanoic acid)-N'-(1-phenyl-ethylamine)-3,4,9,10 perylenebis (dicarboximide) (LPPDI) in non-polar solvents.
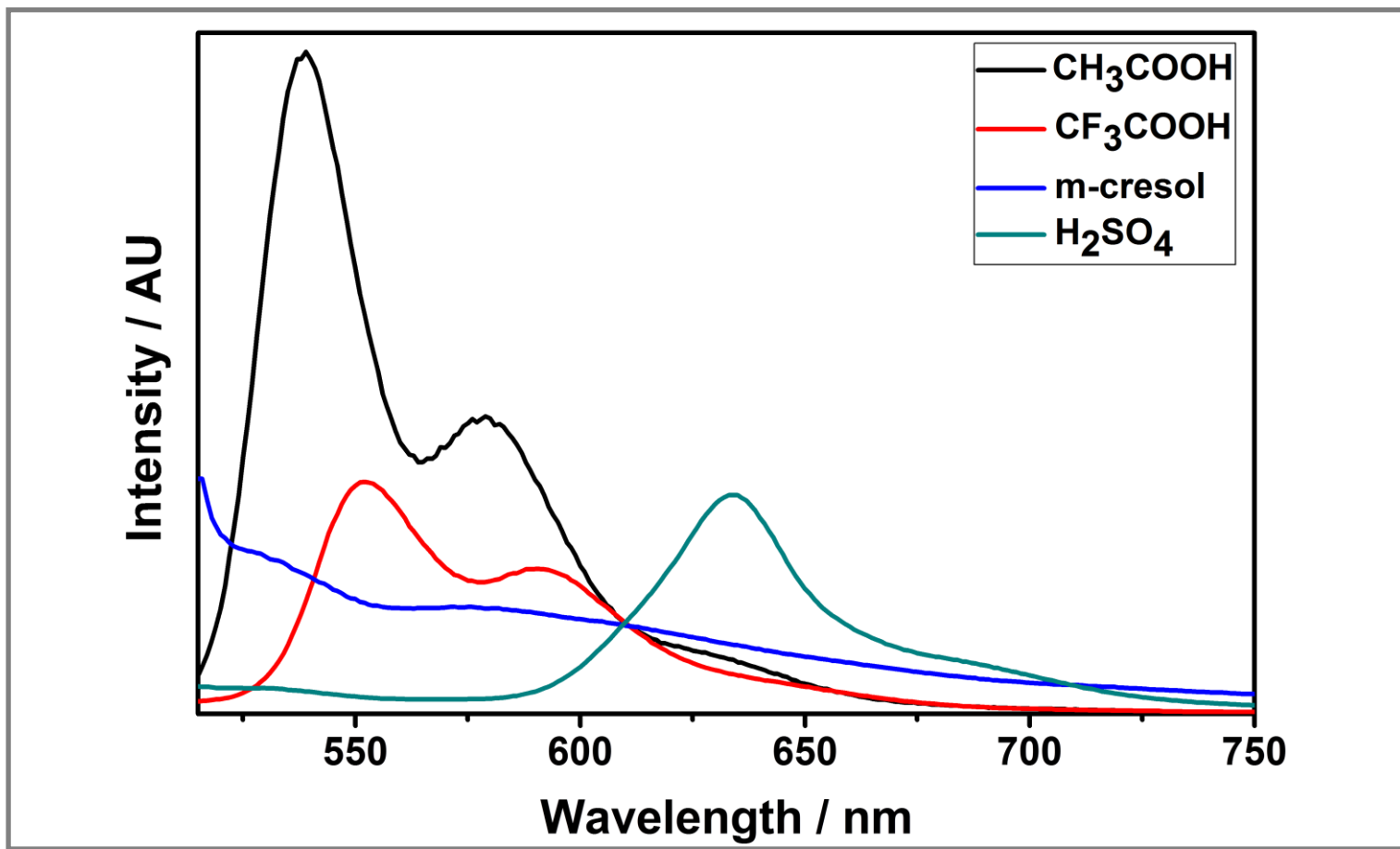
Figure 4.36: Emission spectra of N-(2-aminohexanoic acid)-N'-(1-phenyl-ethylamine)-3,4,9,10 perylenebis (dicarboximide) (LPPDI) in polar protic solvents.
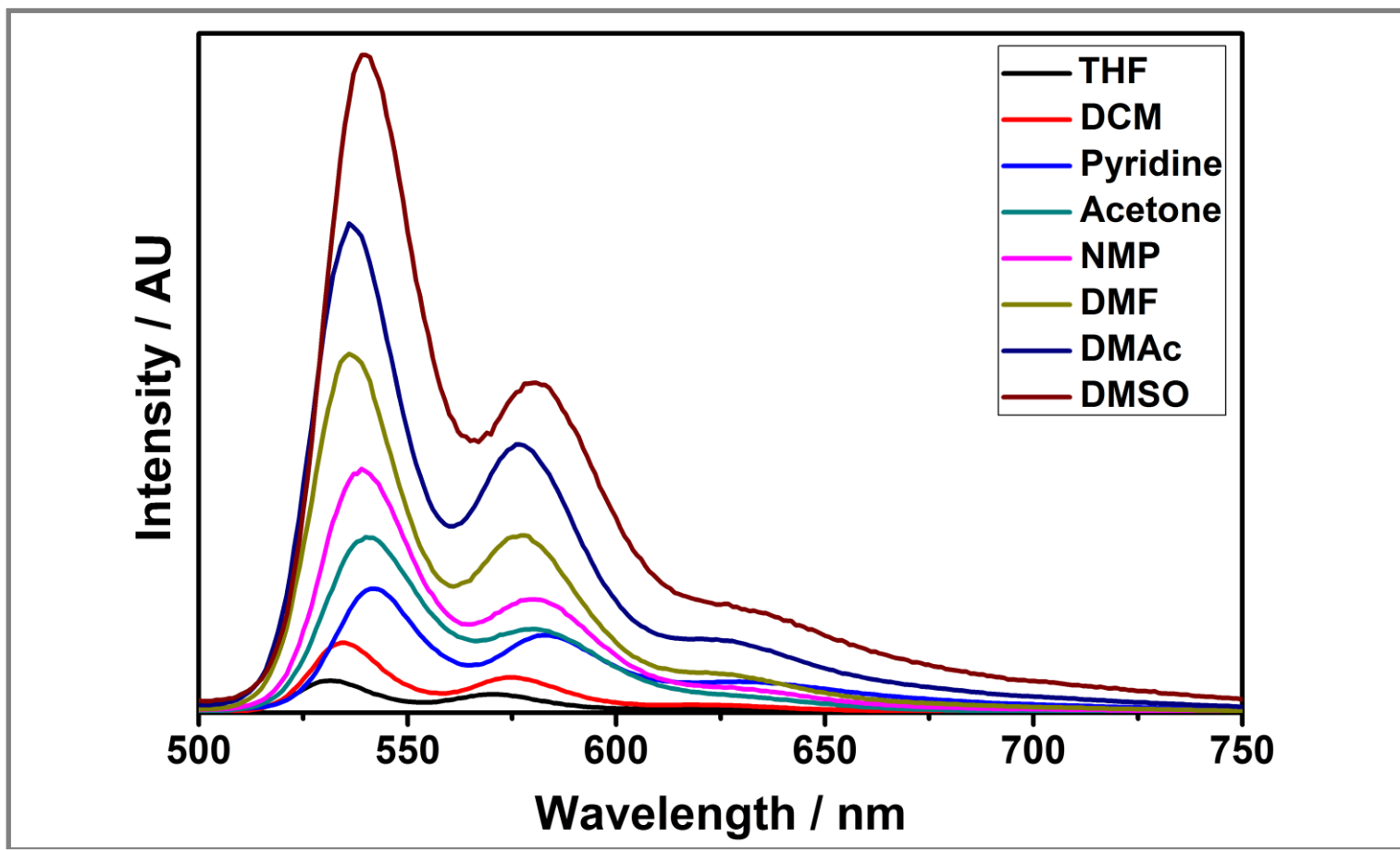
Figure 4.37: Emission spectra of N-(2-aminohexanoic acid)-N'-(1-phenyl-ethylamine)-3,4,9,10 perylenebis (dicarboximide) (LPPDI) in dipolar aprotic solvents.
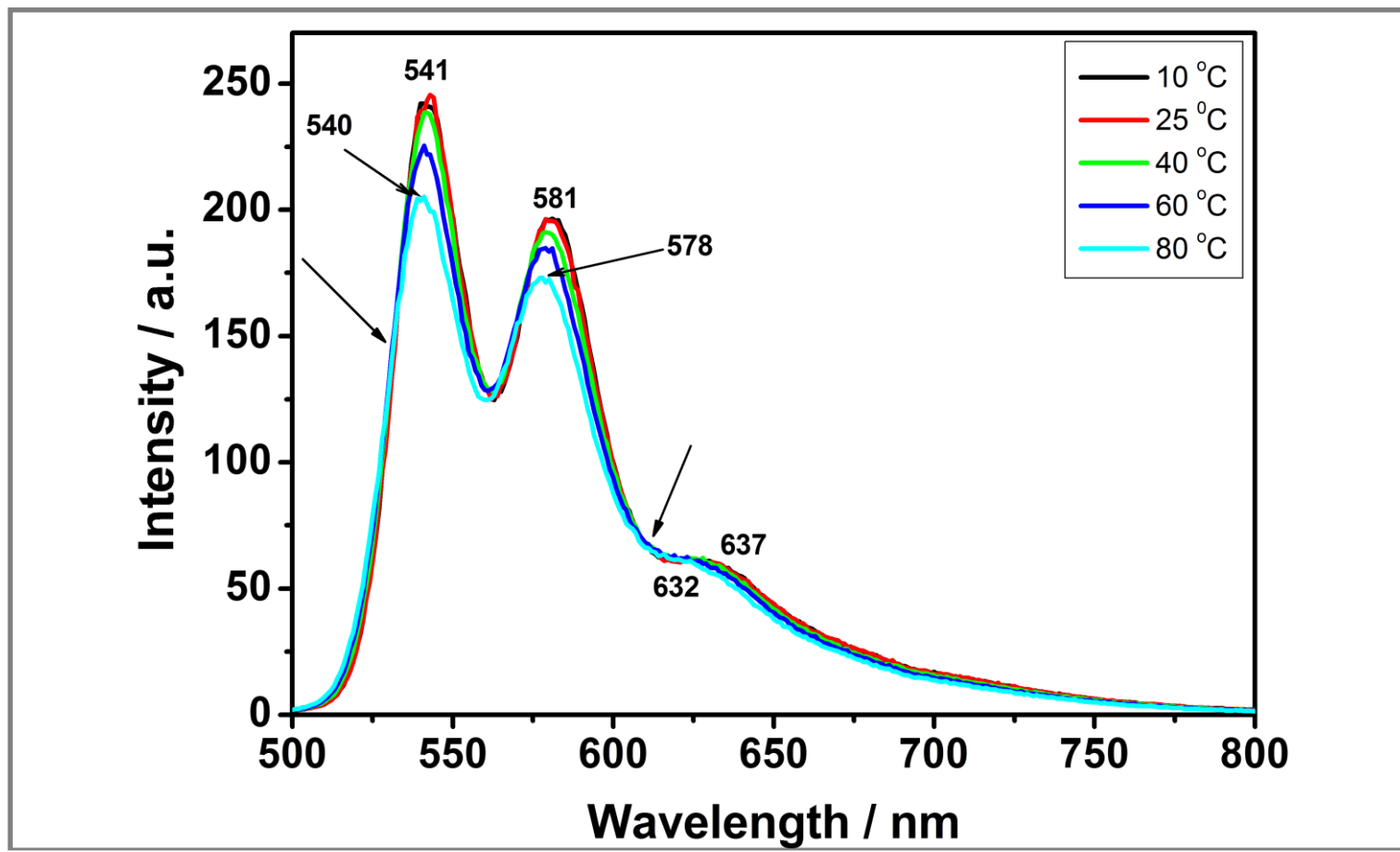
Figure 4.38: Temperature-dependent emission spectra of N-(2-aminohexanoic acid)-N'-(1-phenyl-ethylamine)-3,4,9,10 perylenebis (dicarboximide) (LPPDI) in NMP.
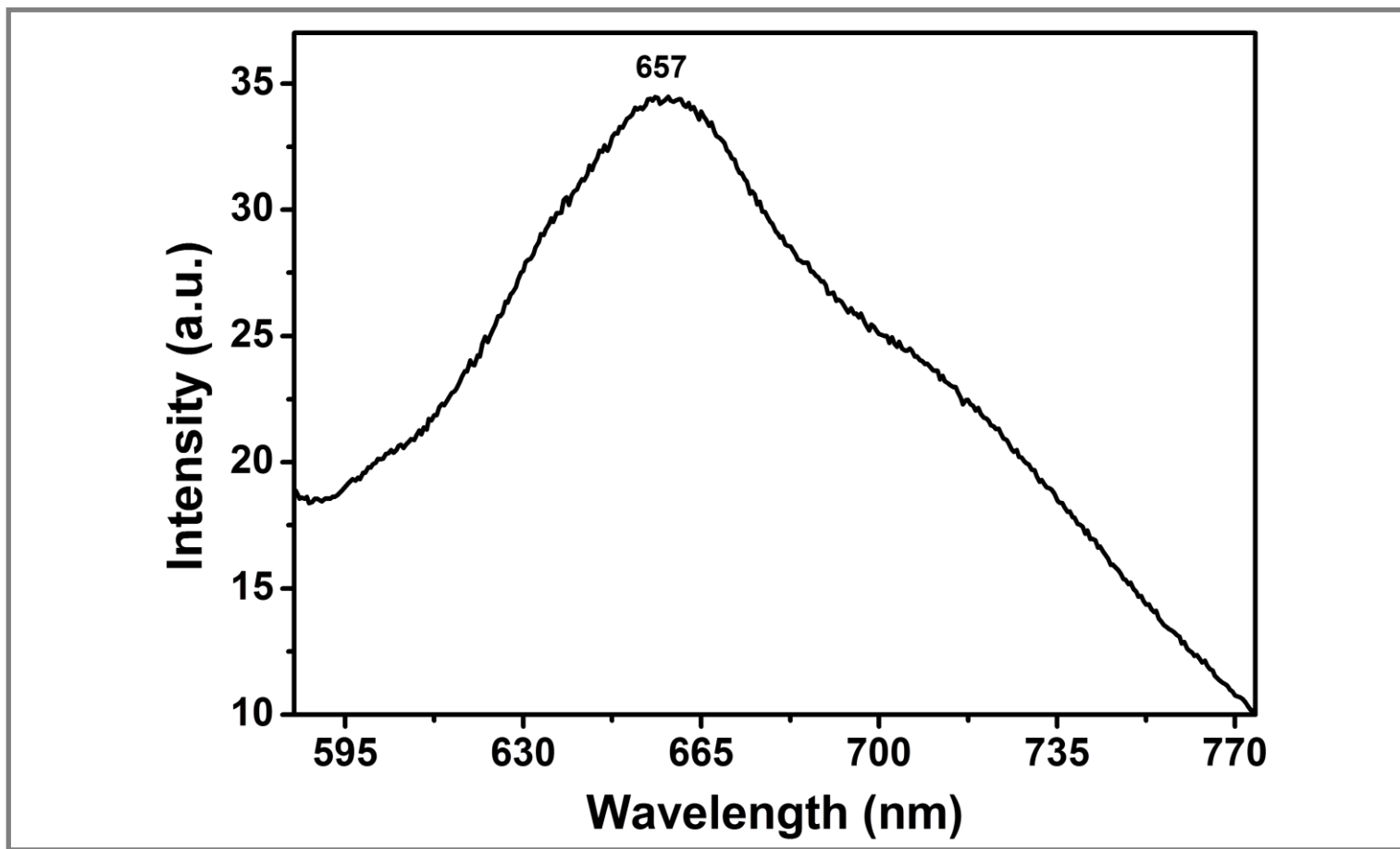
Figure 4.39: Solid-state emission spectrum of N-(2-aminohexanoic acid)-N'-(1-phenyl-ethylamine)-3,4,9,10 perylenebis(dicarboximide) (LPPDI).
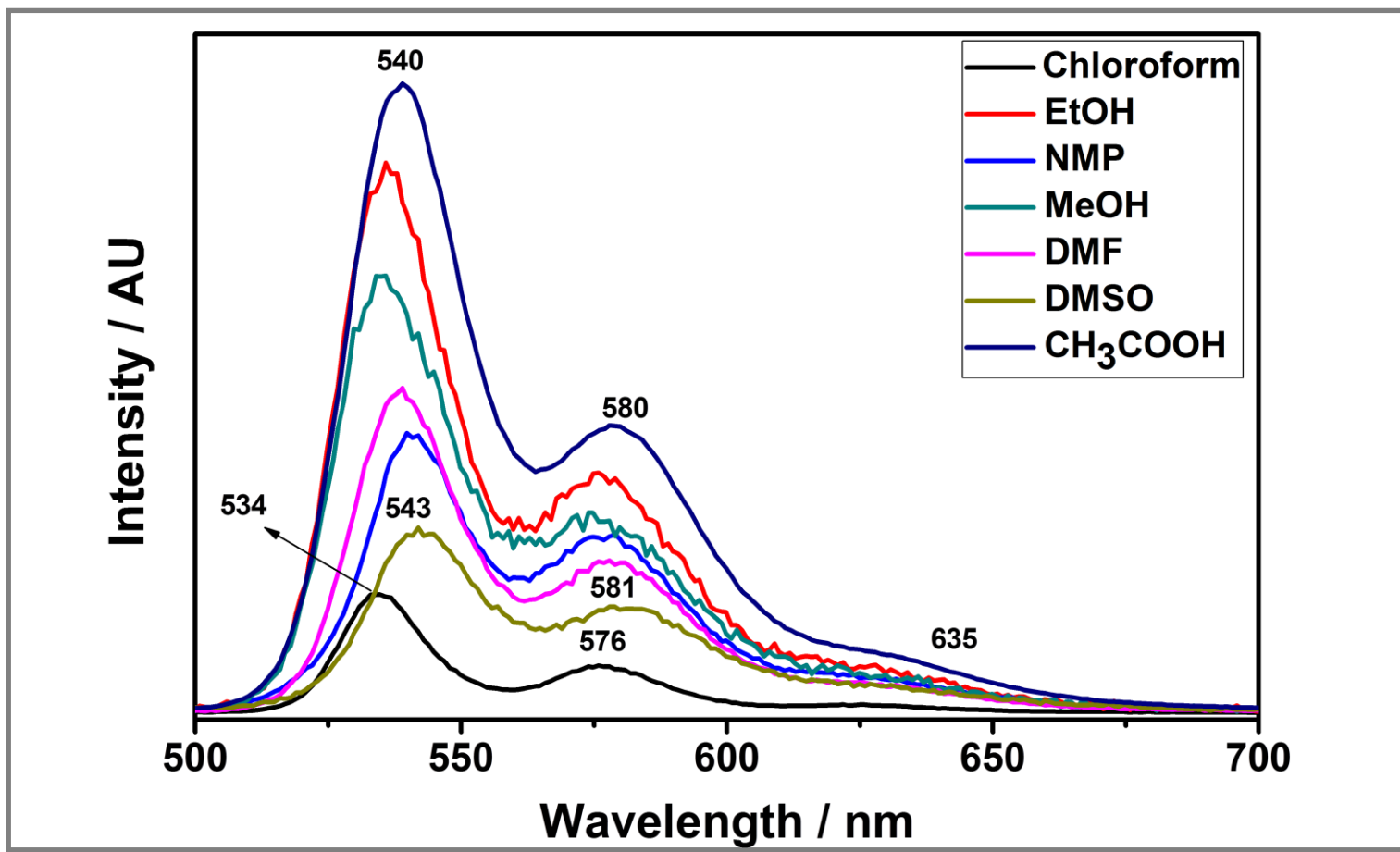
Figure 4.40: Emission spectra of N-(2-hydroxy-4-benzoic acid)-N'-(4-hydroxyphenyl)-3,4,9,10 perylenebis (dicarboximide) (BPDI) in different solvents.
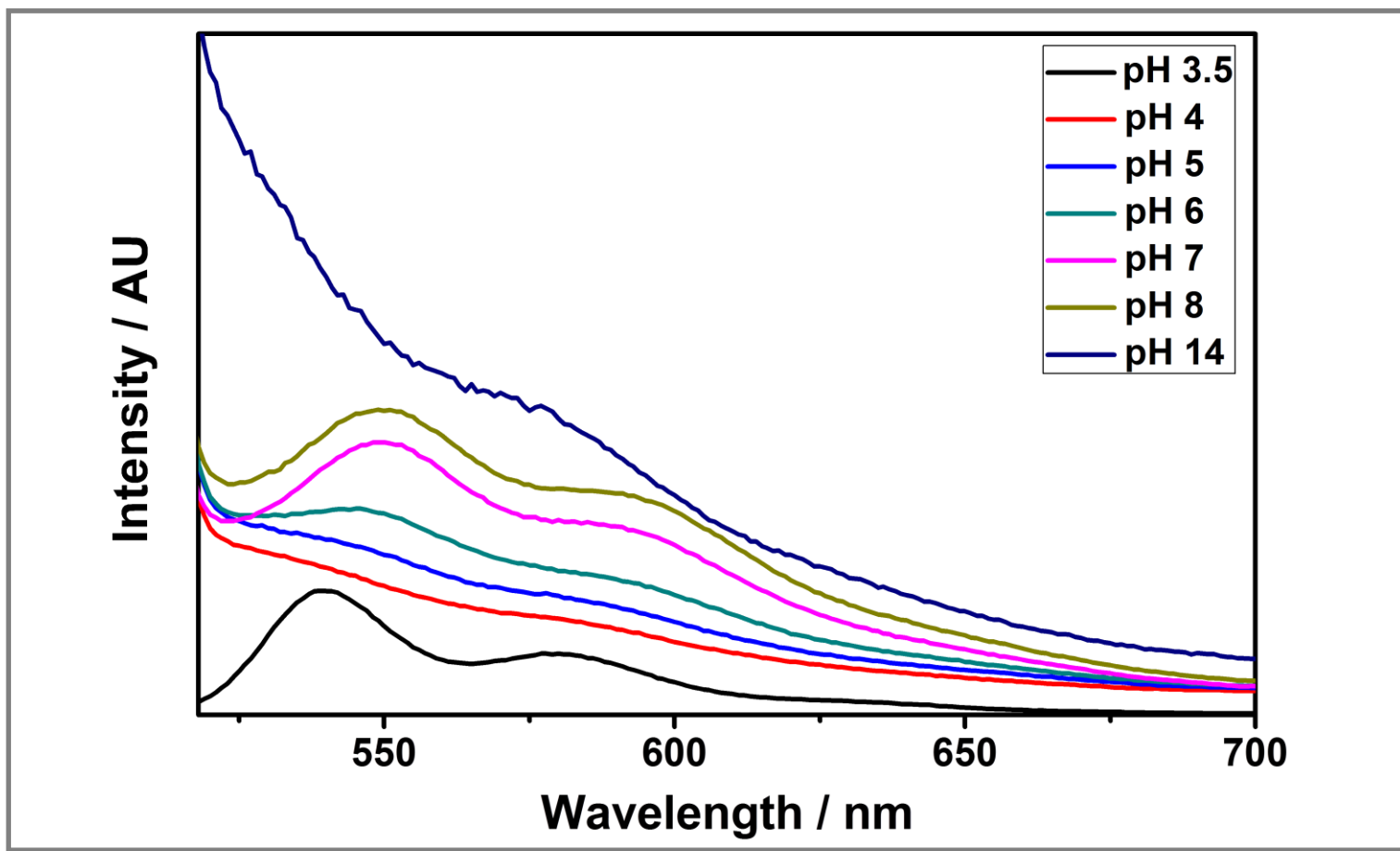
Figure 4.41: Emission spectra of N-(2-hydroxy-4-benzoic acid)-N'-(4-hydroxyphenyl)-3,4,9,10 perylenebis (dicarboximide) (BPDI) at different pH values.
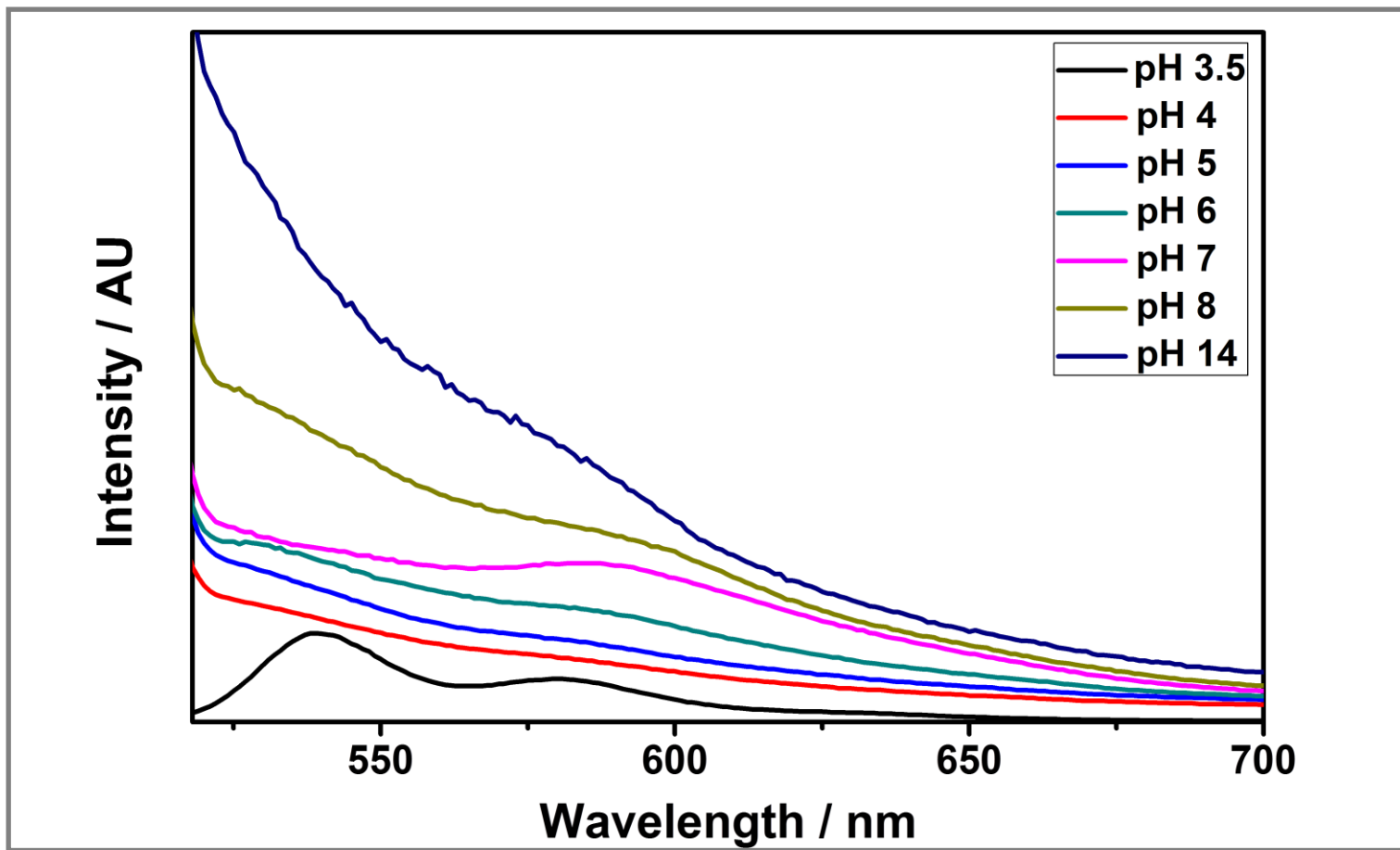
Figure 4.42: Emission spectra of N-(2-hydroxy-4-benzoic acid)-N'-(4-hydroxyphenyl)-3,4,9,10 perylenebis (dicarboximide) (BPDI) at different pH values after filtration with 0.2 μm filter.
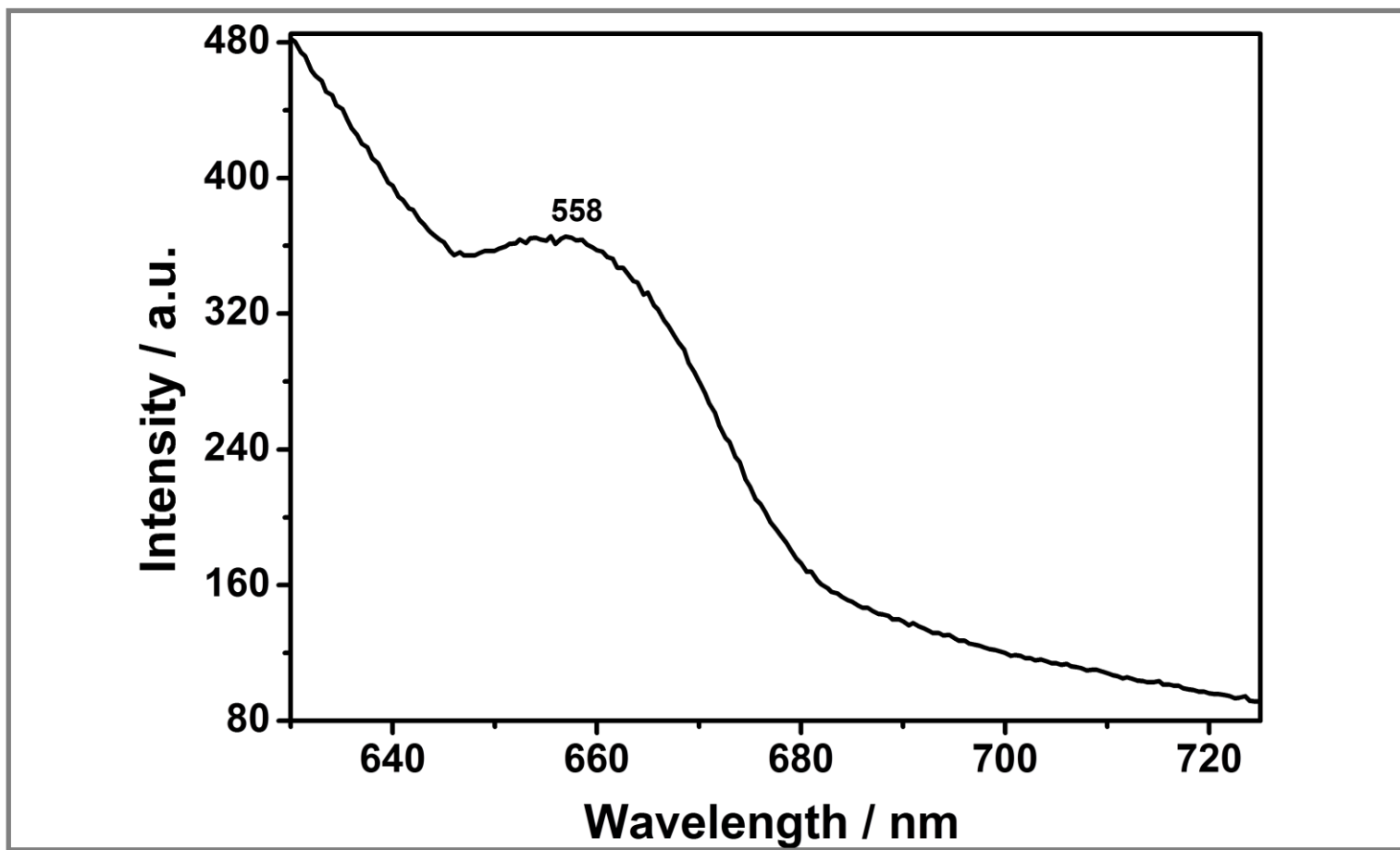
Figure 4.43: Solid-state emission spectrum of N-(2-hydroxy-4-benzoic acid)-N'-(4-hydroxyphenyl)-3,4,9,10 perylenebis (dicarboximide) (BPDI).
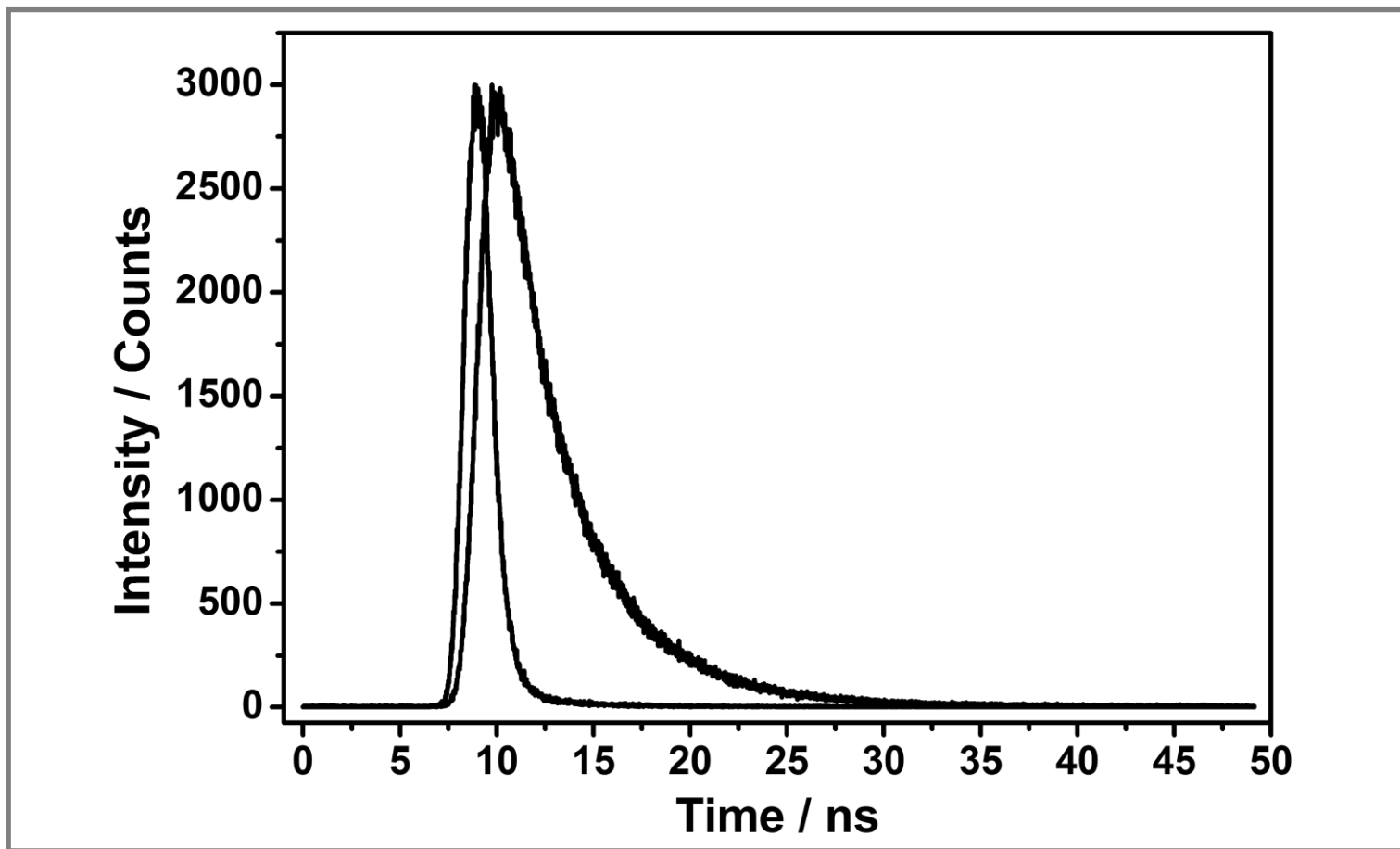
Figure 4.44: Fluorescence decay curve of 10^{-5} M of N-(2-aminohexanoic acid)-3,4,9,10 perylenetetracarboxylic-3,4-anhydride-9,10 imide (LPMI) ($\lambda_{excit.}$= 530 nm and λ_{em}= 580 nm) in DMF.
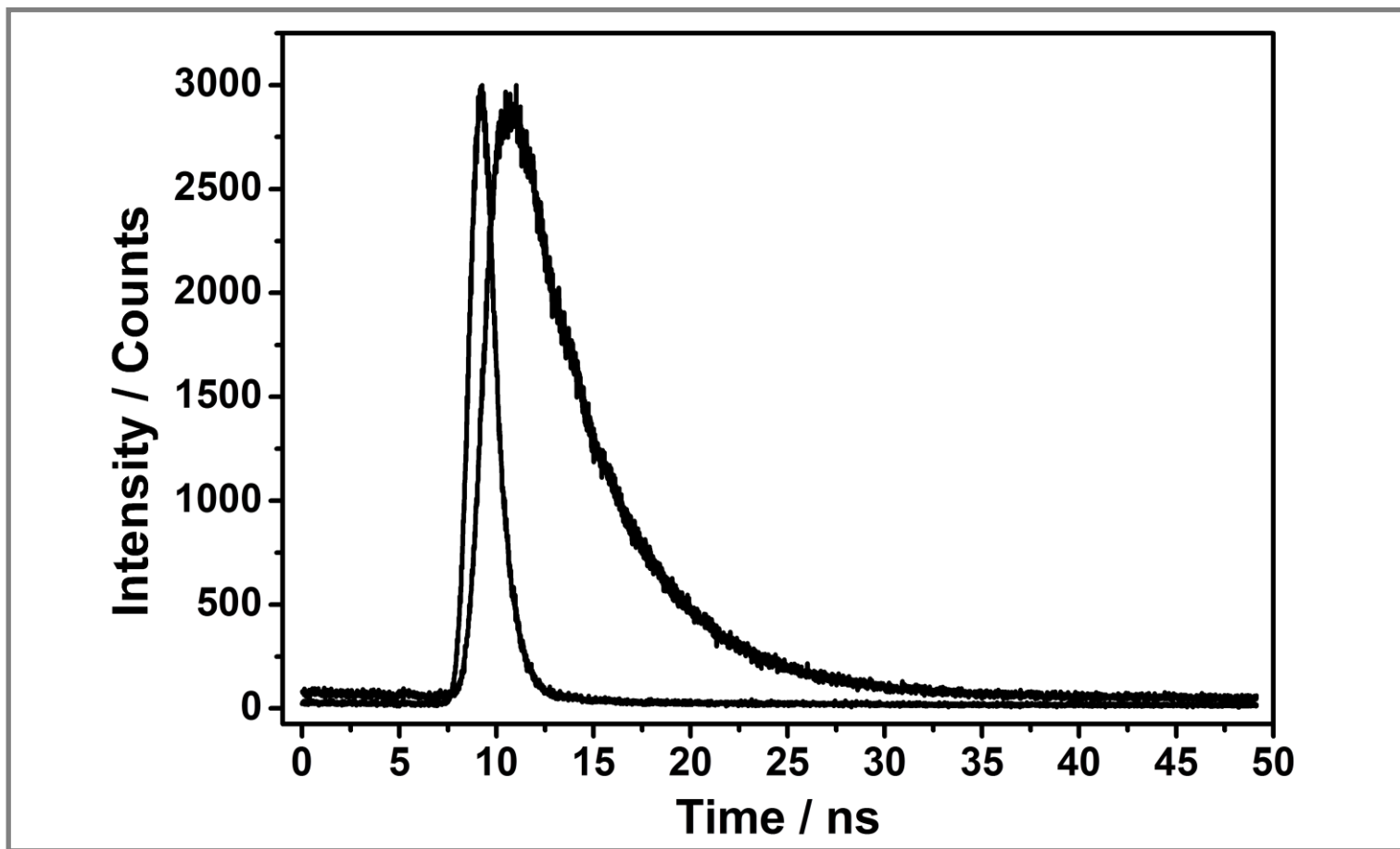
Figure 4.45: Fluorescence decay curve of 10^{-5} M of N, N'-bis(2-aminohexanoic acid)-3,4,9,10 perylenebis(dicarboximide) (LPDI) ($\lambda_{excit.}$= 530 nm and λ_{em}= 580 nm) in DMF.
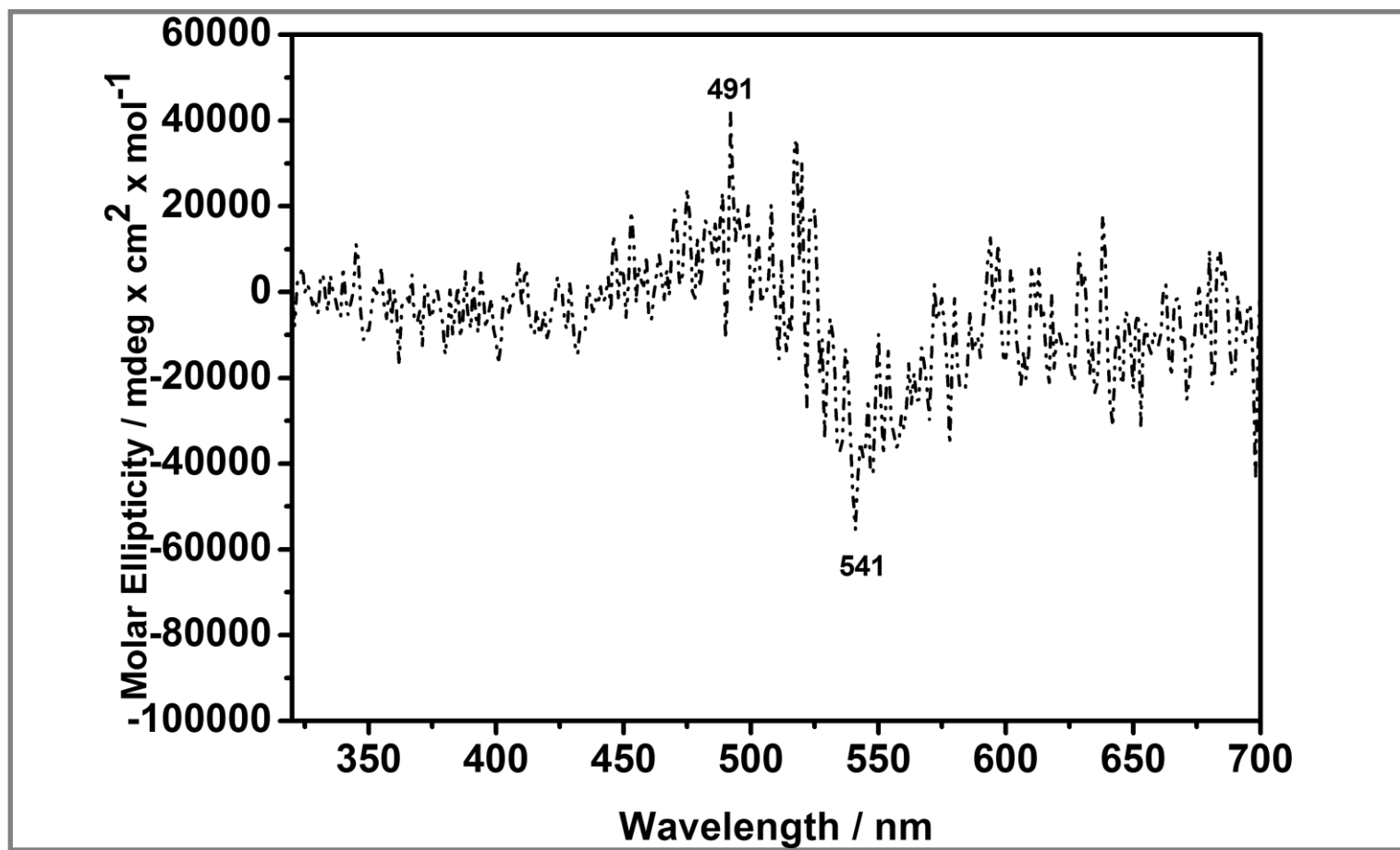
Figure 4.46: CD spectrum of N-(2-aminohexanoic acid)-3,4,9,10 perylenetetracarboxylic-3,4-anhydride-9,10 imide (LPMI) in trifluoroacetic acid, cell path length, 0.2 cm.
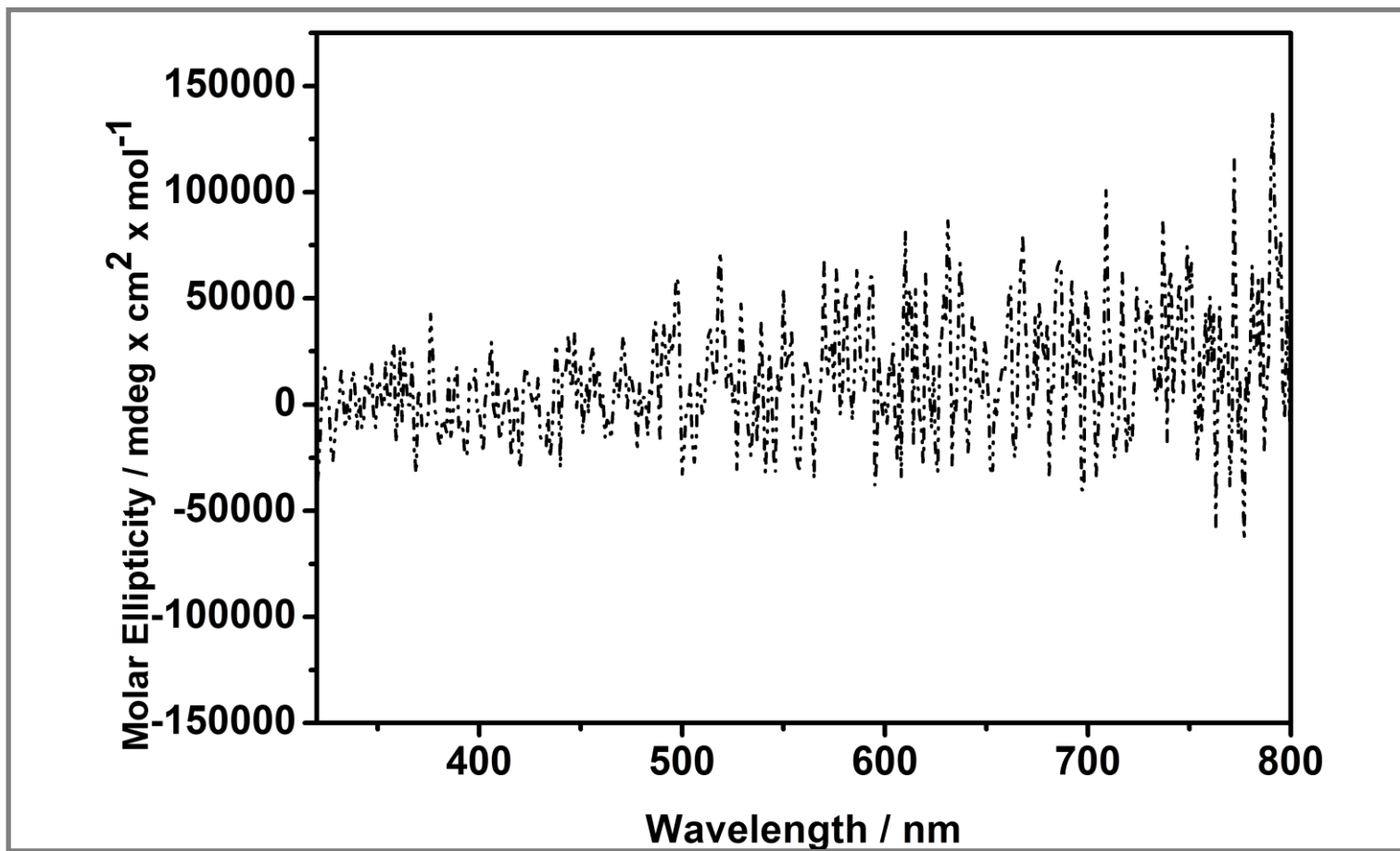
Figure 4.47: CD spectrum of N, N'-bis(2-aminohexanoic acid)-3,4,9,10 perylenebis(dicarboximide) (LPDI) in trifluoroacetic acid, cell path length, 0.2 cm.
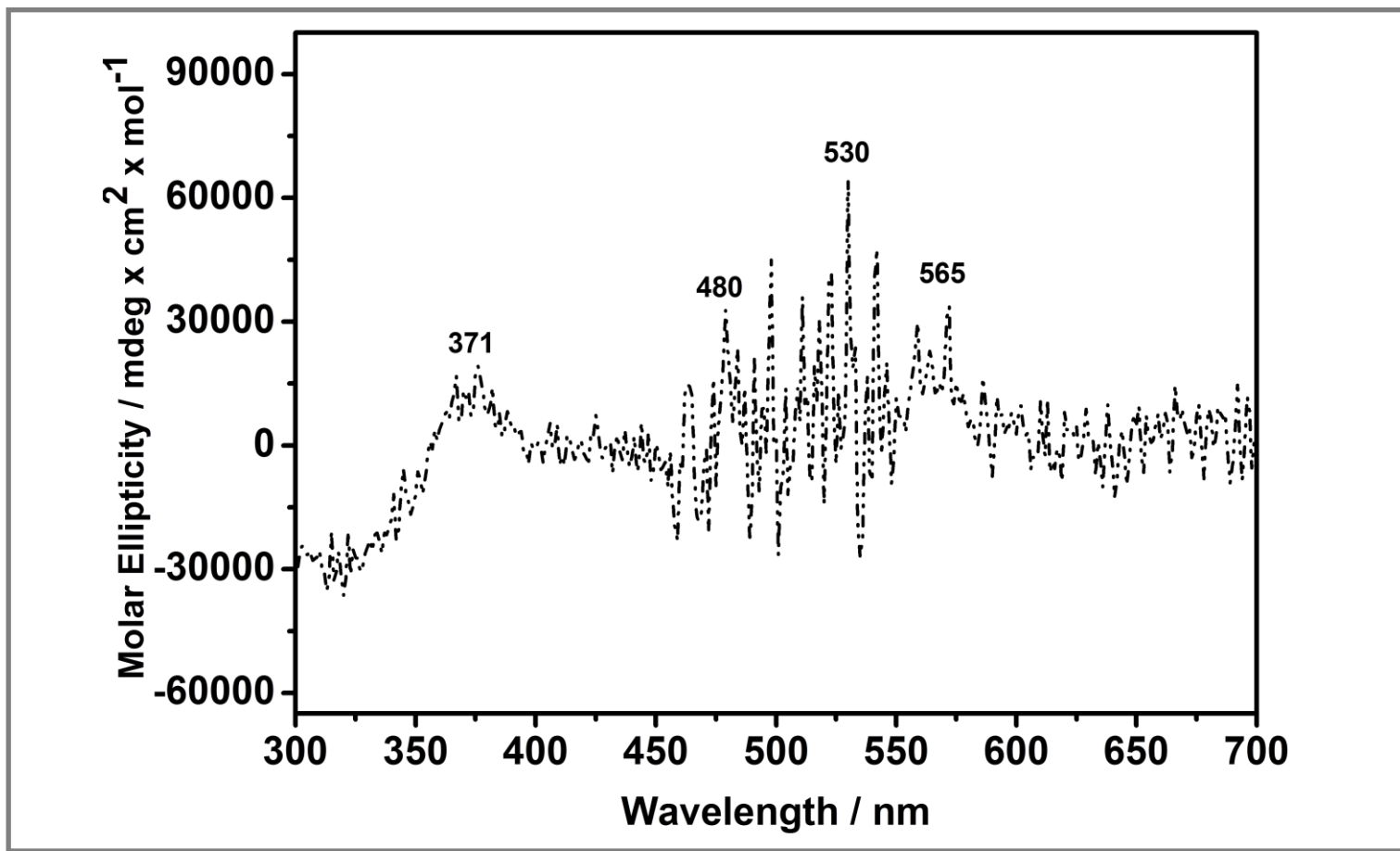
Figure 4.48: CD spectrum of N-(2-aminohexanoic acid)-N'-(1-phenyl-ethylamine)-3,4,9,10 perylenebis (dicarboximide) (LPPDI) in trifluoroacetic acid, cell path length, 0.2 cm.
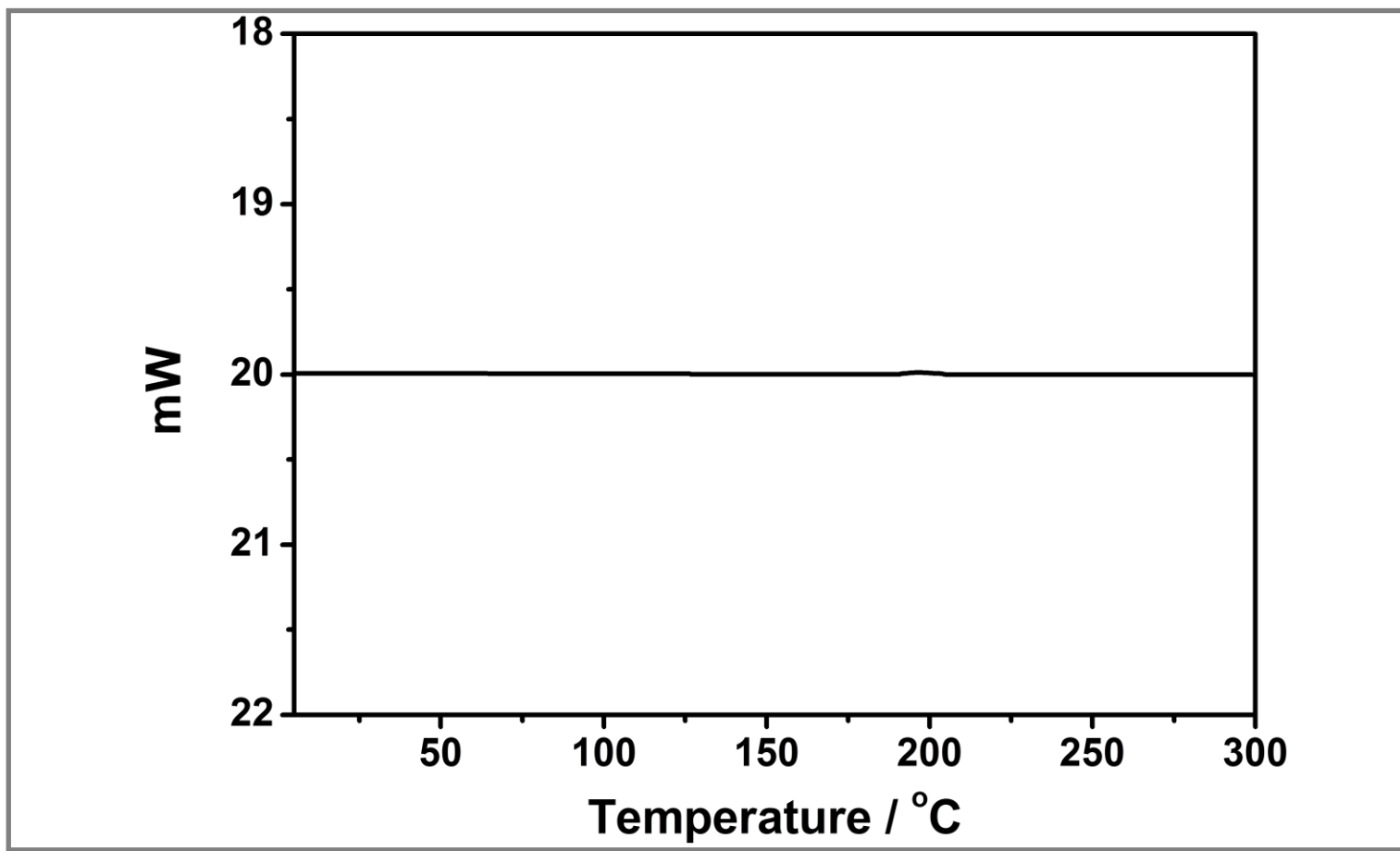
Figure 4.49: DSC thermogram of N-(2-aminohexanoic acid)-3,4,9,10 perylenetetracarboxylic-3,4-anhydride-9,10 imide (LPMI) at a heating rate of 10 K min^{-1}.
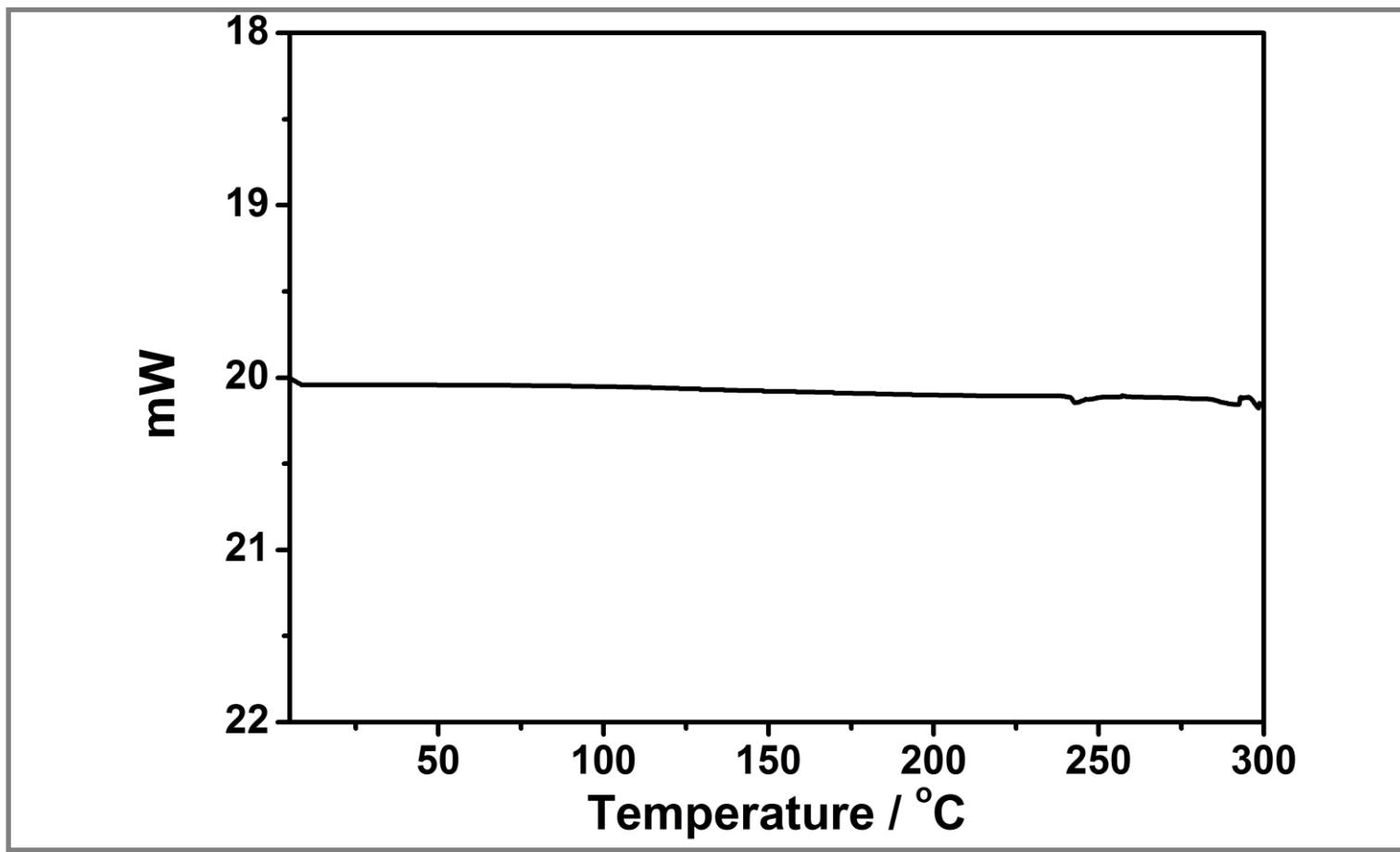
Figure 4.50: DSC thermogram of N, N'-bis(2-aminohexanoic acid)-3,4,9,10 perylenebis(dicarboximide) (LPDI) at a heating rate of 10 K min^{-1}.
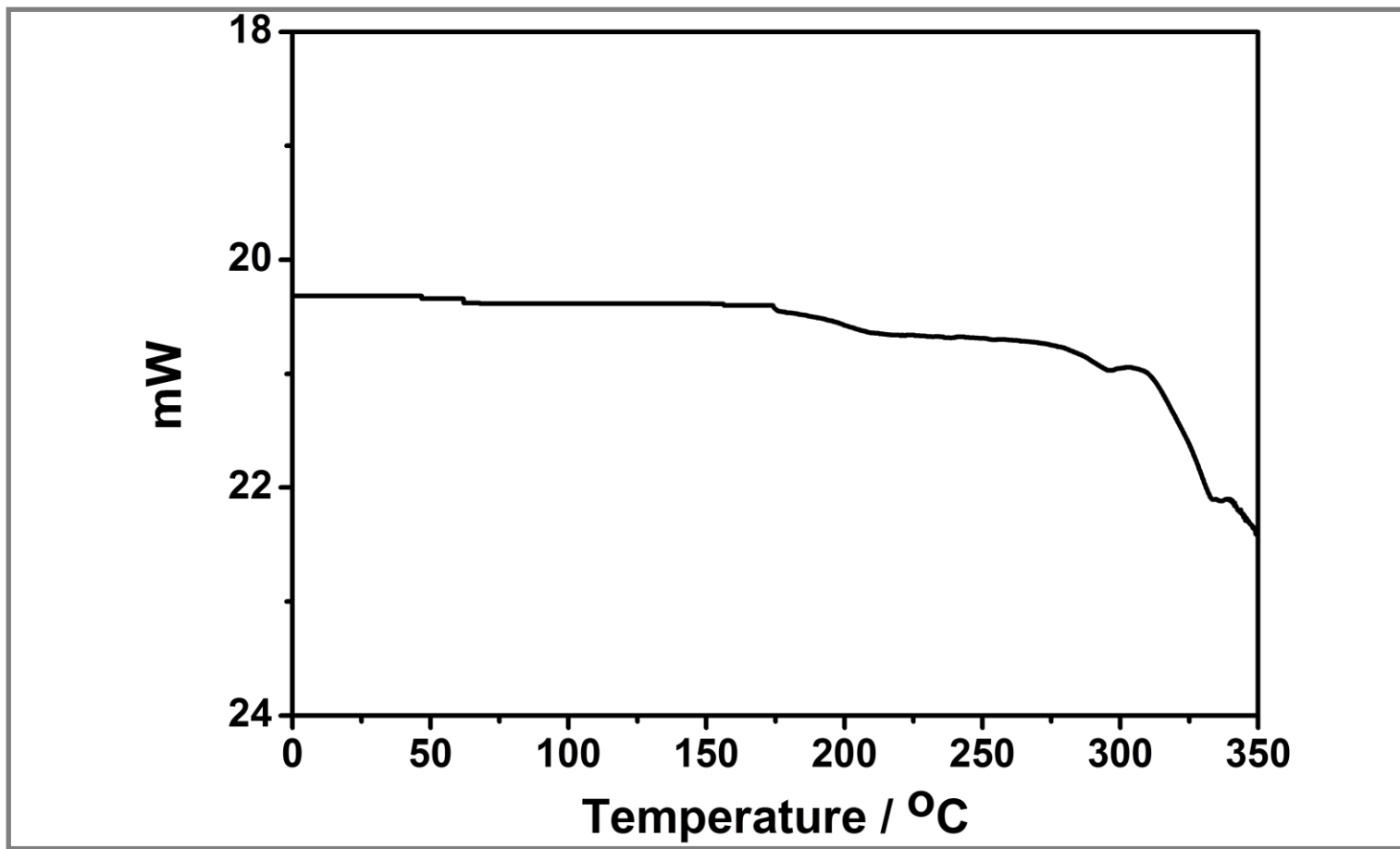
Figure 4.51: DSC thermogram of N-(2-aminohexanoic acid)-N'-(1-phenyl-ethylamine)-3,4,9,10 perylenebis (dicarboximide) (LPPDI) at a heating rate of 10 K min^{-1}.
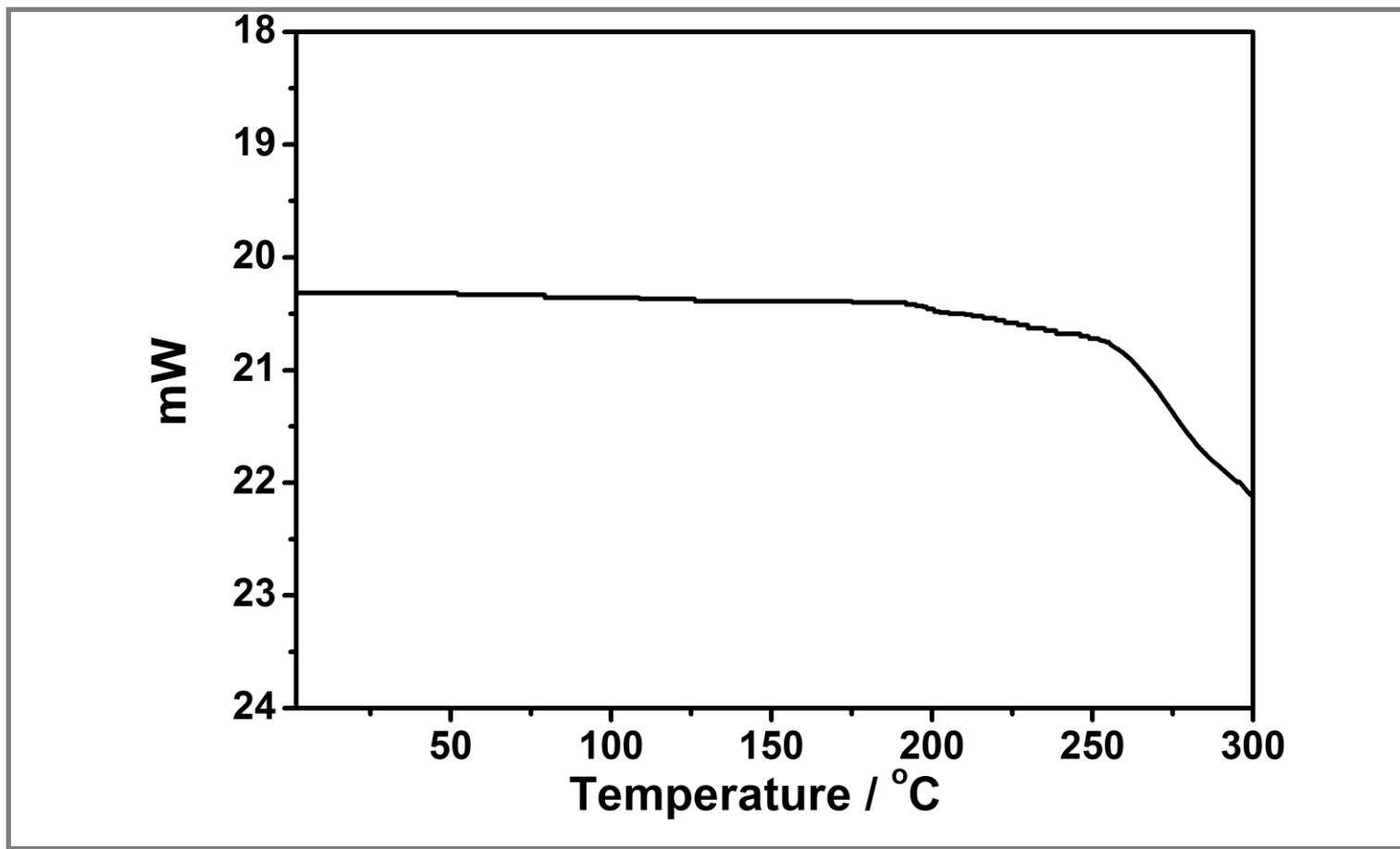
Figure 4.52: DSC thermogram of N-(2-hydroxy-4-benzoic acid)-N'-(4-hydroxyphenyl)-3,4,9,10 perylenebis (dicarboximide) (BPDI) at a heating rate of 10 K min^{-1}.
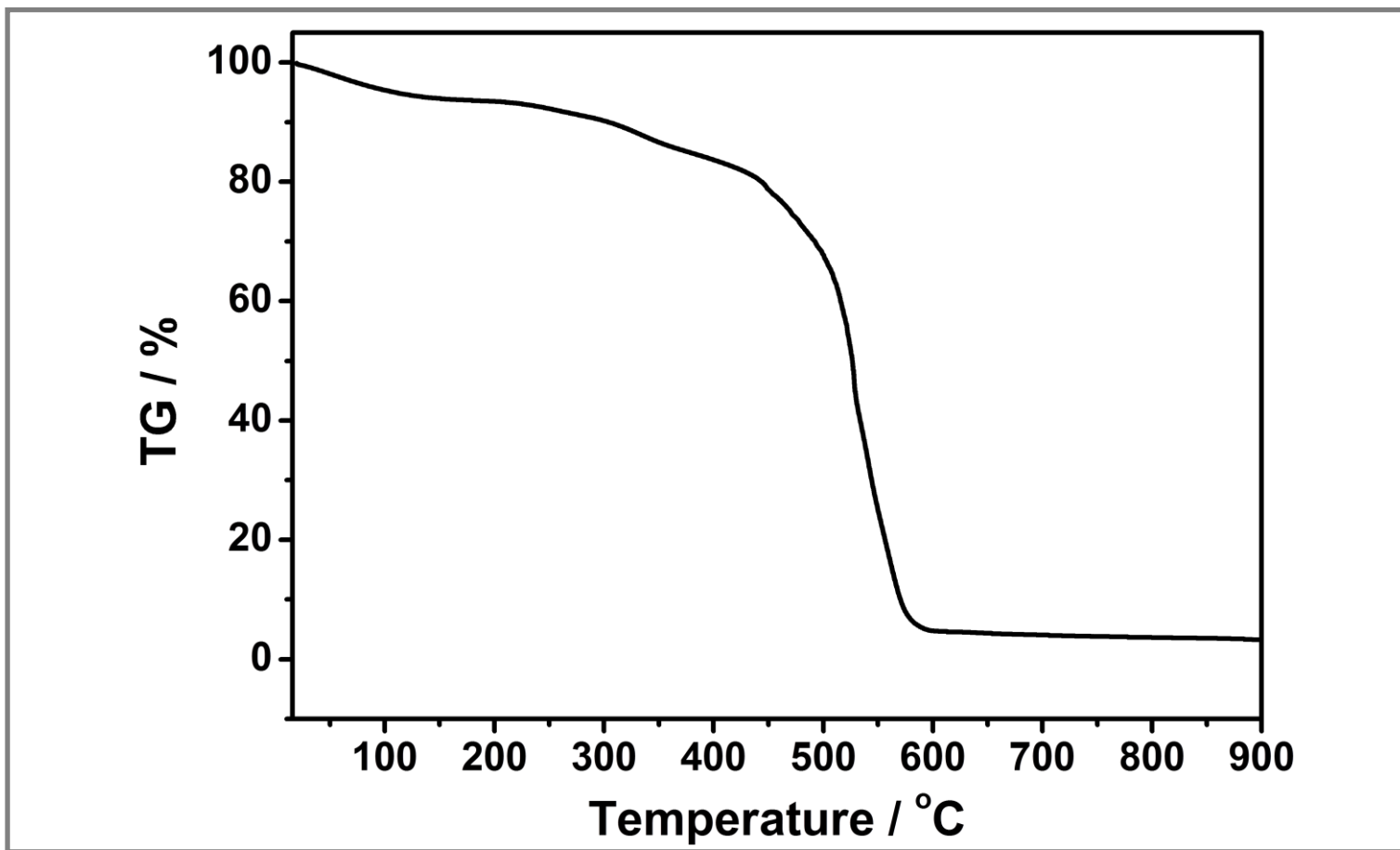
Figure 4.53: TGA curve of N-(2-aminohexanoic acid)-3,4,9,10 perylenetetracarboxylic-3,4-anhydride-9,10 imide (LPMI) at a heating rate of 5 K min^{-1}.
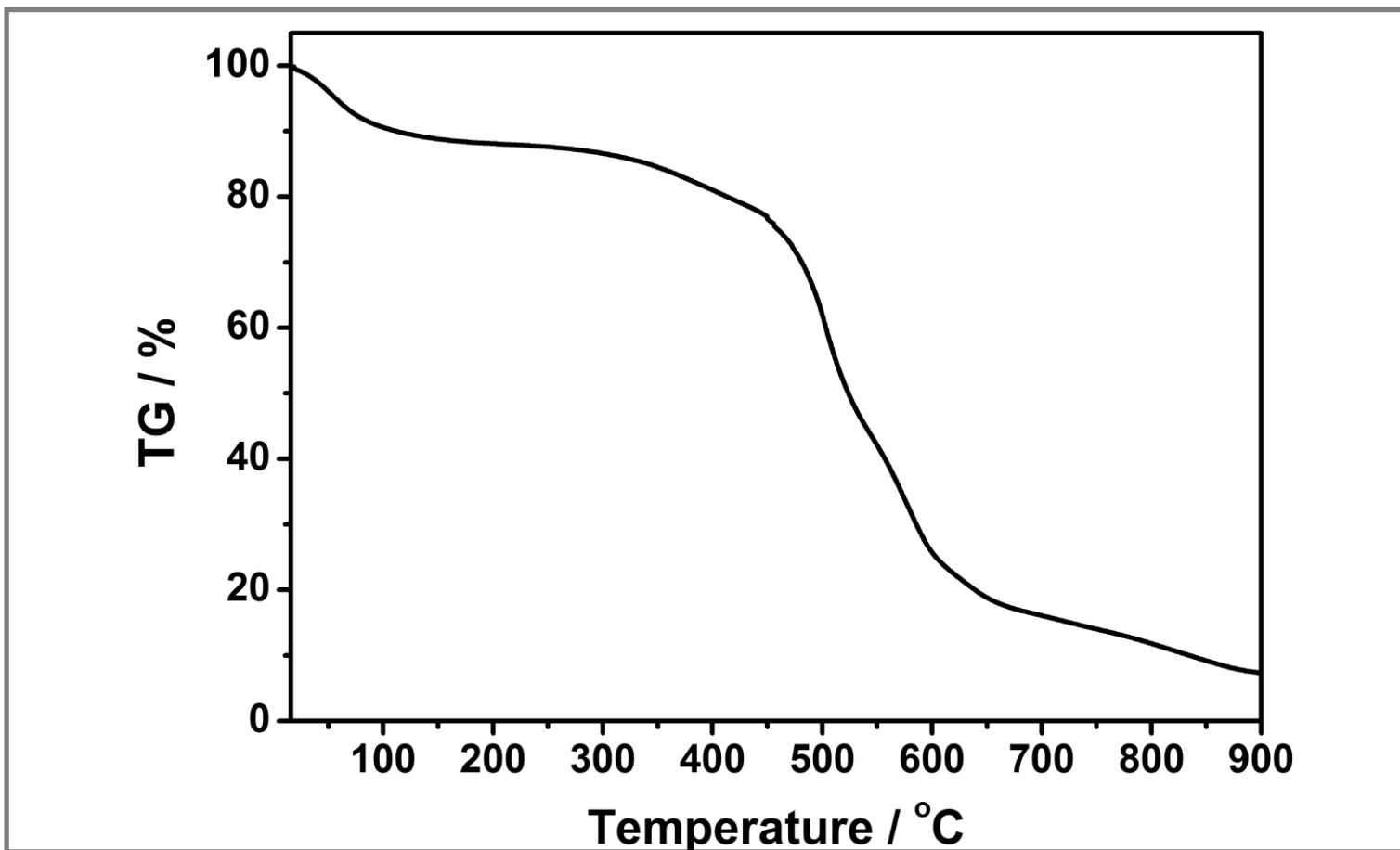
Figure 4.54 TGA curve of N, N'-bis(2-aminohexanoic acid)-3,4,9,10 perylenebis(dicarboximide) (LPDI) at a heating rate of 5 K min^{-1}.
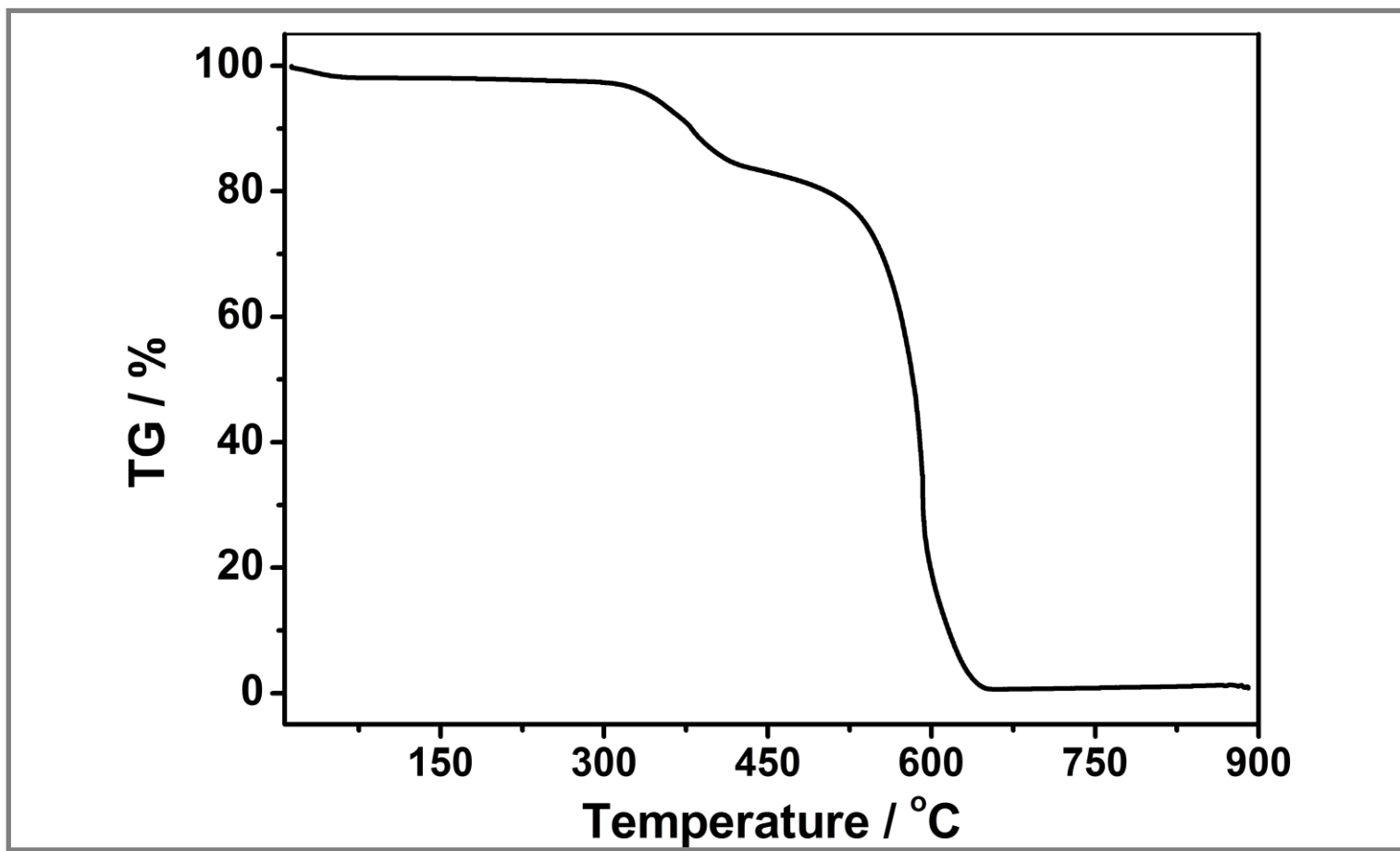
Figure 4.55: TGA curve of N-(2-aminohexanoic acid)-N'-(1-phenyl-ethylamine)-3,4,9,10 perylenebis (dicarboximide) (LPPDI) at a heating rate of 5 K min^{-1}.
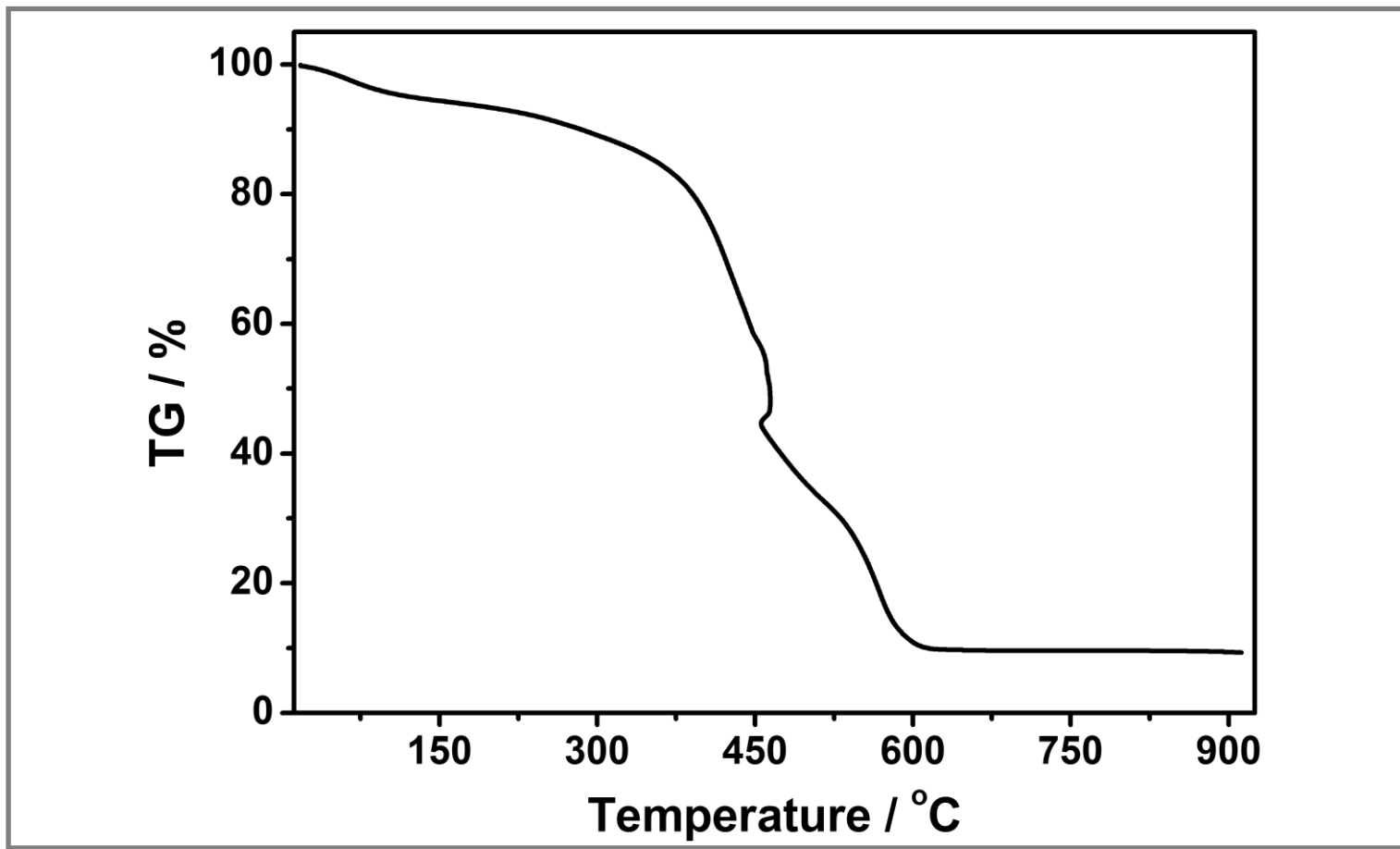
Figure 4.56: TGA curve of N-(2-hydroxy-4-benzoic acid)-N'-(4-hydroxyphenyl)-3,4,9,10 perylenebis (dicarboximide) (BPDI) at a heating rate of 5 K min^{-1}.
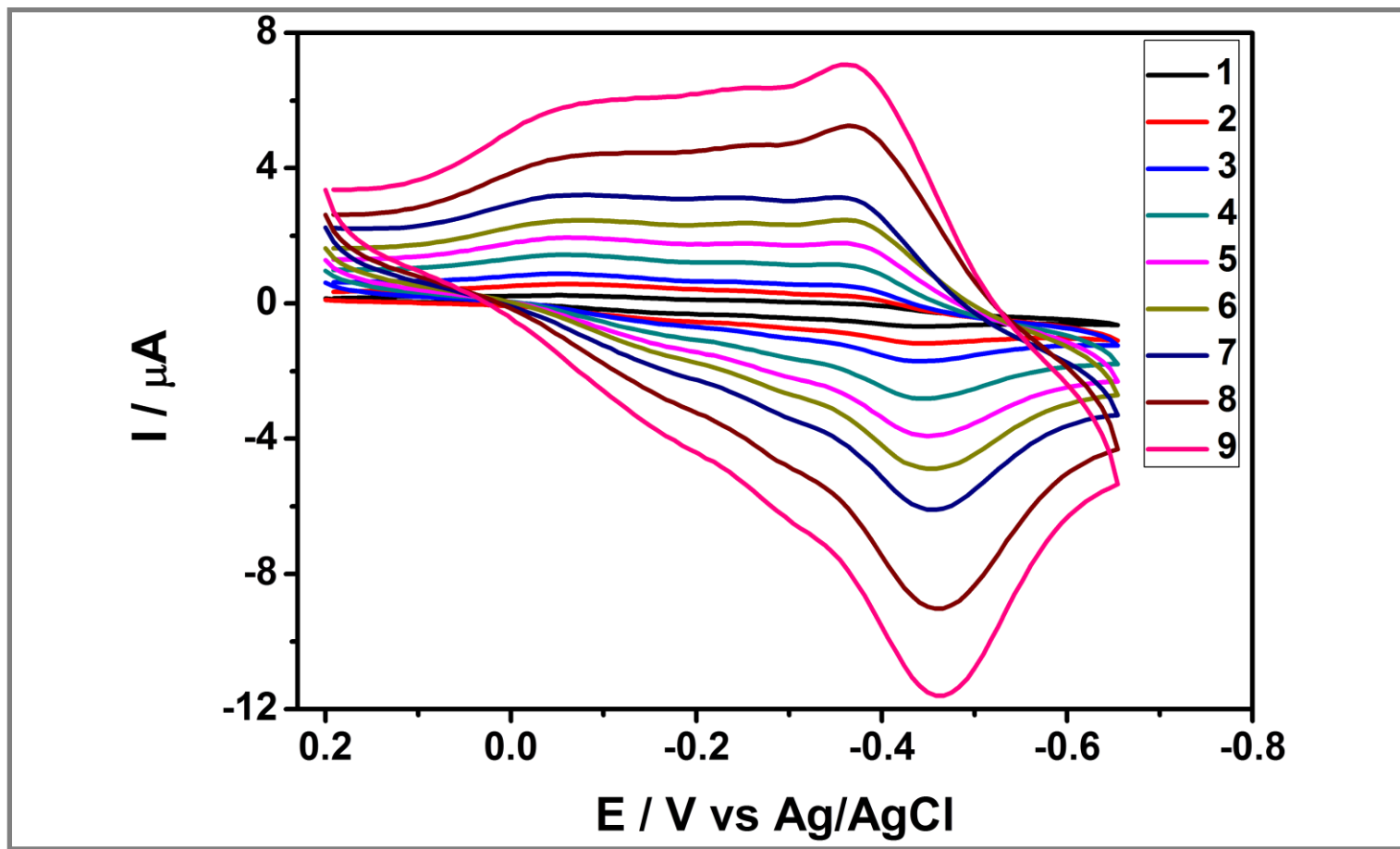
Figure 4.57: Cyclic voltammograms of N-(2-aminohexanoic acid)-3,4,9,10 perylenetetracarboxylic-3,4-anhydride-9,10 imide (LPMI) in DMF at different scan rates (mV s^{-1}): 1 (20), 2 (50), 3 (100), 4 (200), 5 (300), 6 (400), 7 (500), 8 (750), 9 (1000), supporting electrolyte: NaBF$_4$, at 25 ^{o}C.
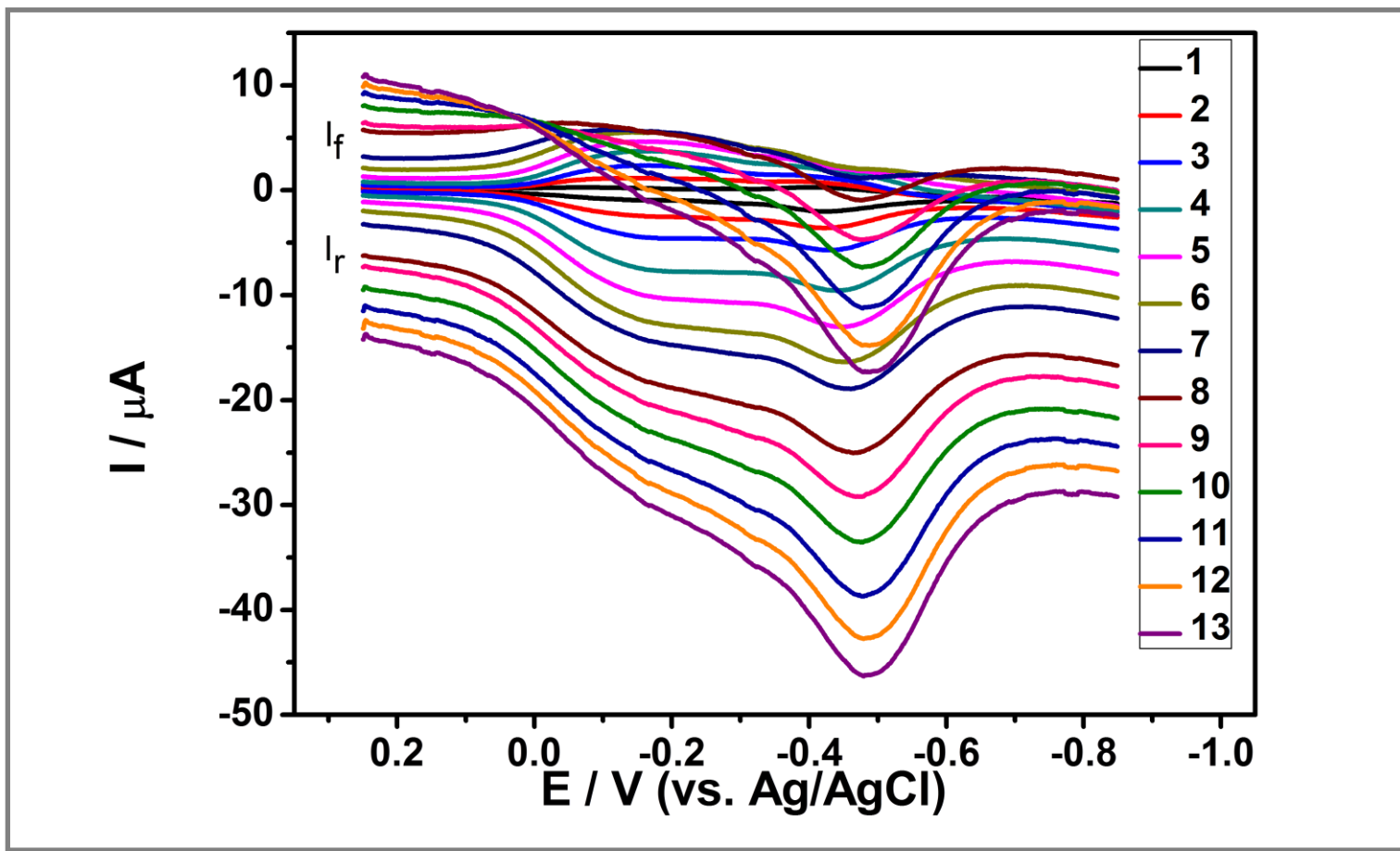
Figure 4.58: Square-wave voltammograms of N-(2-aminohexanoic acid)-3,4,9,10 perylenetetracarboxylic-3,4-anhydride-9,10 imide (LPMI) in DMF at different frequencies (Hz): 1 (20), 2 (50), 3 (100), 4 (200), 5 (300), 6 (400), 7 (500), 8 (750), 9 (1000), 10 (1250), 11 (1500), 12 (1750), 13 (2000), supporting electrolyte:NaBF$_4$, at 25 ^{o}C.
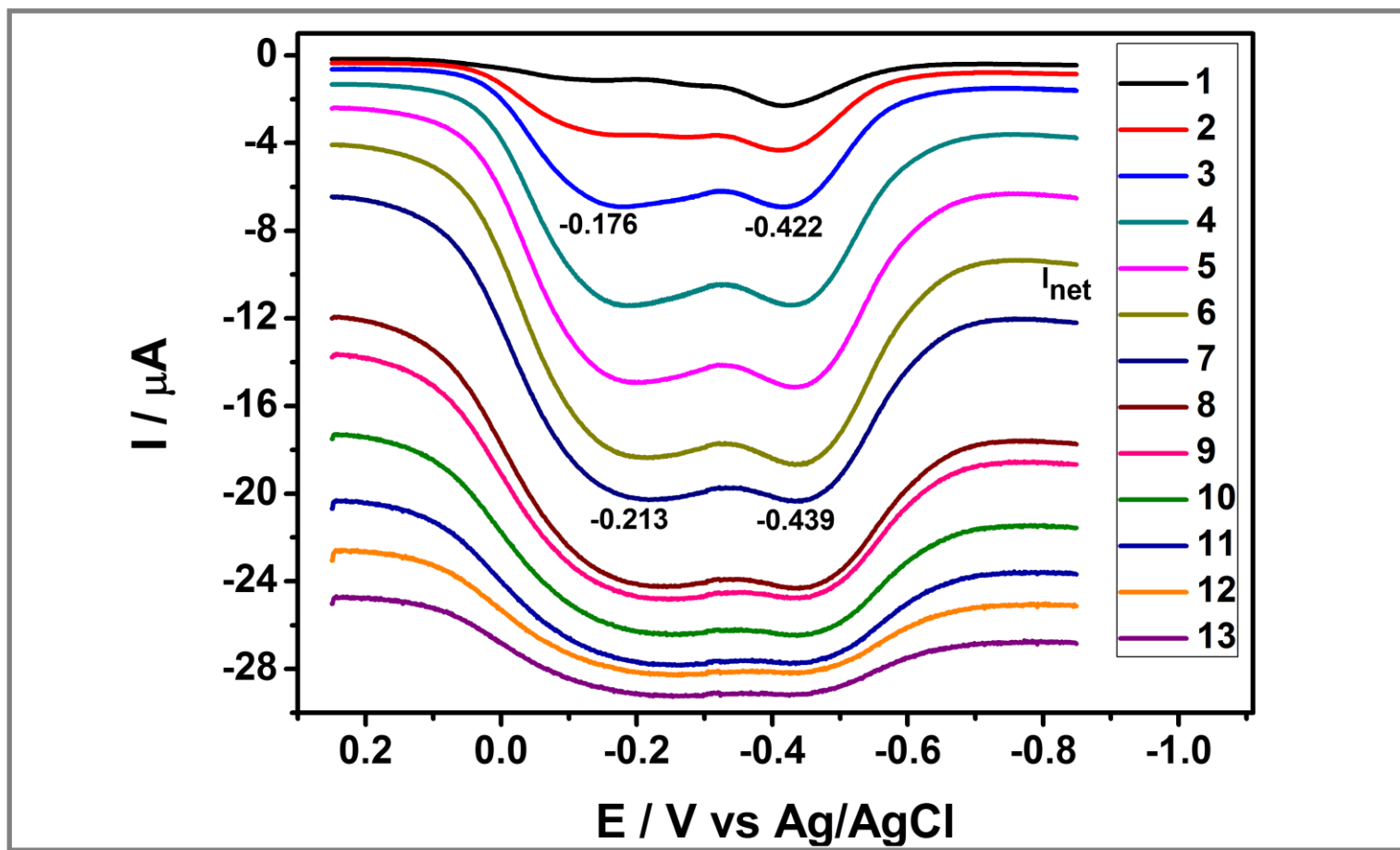
Figure 4.59: Square-wave voltammograms (I_{net}) of N-(2-aminohexanoic acid)-3,4,9,10 perylenetetracarboxylic-3,4-anhydride-9,10 imide (LPMI) in DMF at different frequencies (Hz): 1 (20), 2 (50), 3 (100), 4 (200), 5 (300), 6 (400), 7 (500), 8 (750), 9 (1000), 10 (1250), 11 (1500), 12 (1750), 13 (2000), supporting electrolyte:NaBF$_4$, at 25 ^{o}C.
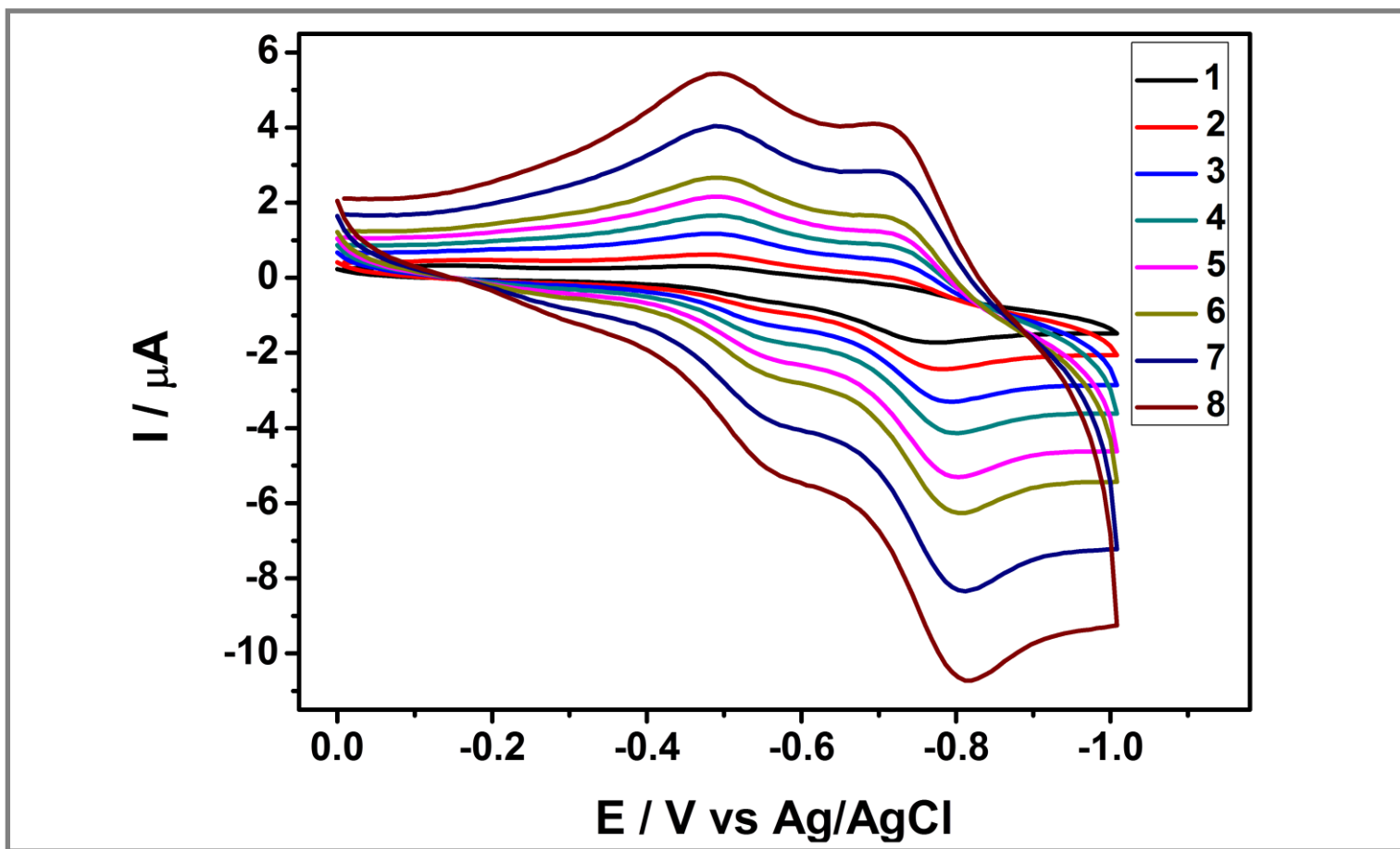
Figure 4.60: Cyclic voltammograms of N, N'-bis(2-aminohexanoic acid)-3,4,9,10 perylenebis(dicarboximide) (LPDI) in DMF at different scan rates (mV s^{-1}): 1 (50), 2 (100), 3 (200), 4 (300), 5 (400), 6 (500), 7 (750), 8 (1000), supporting electrolyte: NaBF$_4$, at 25 ^{o}C.
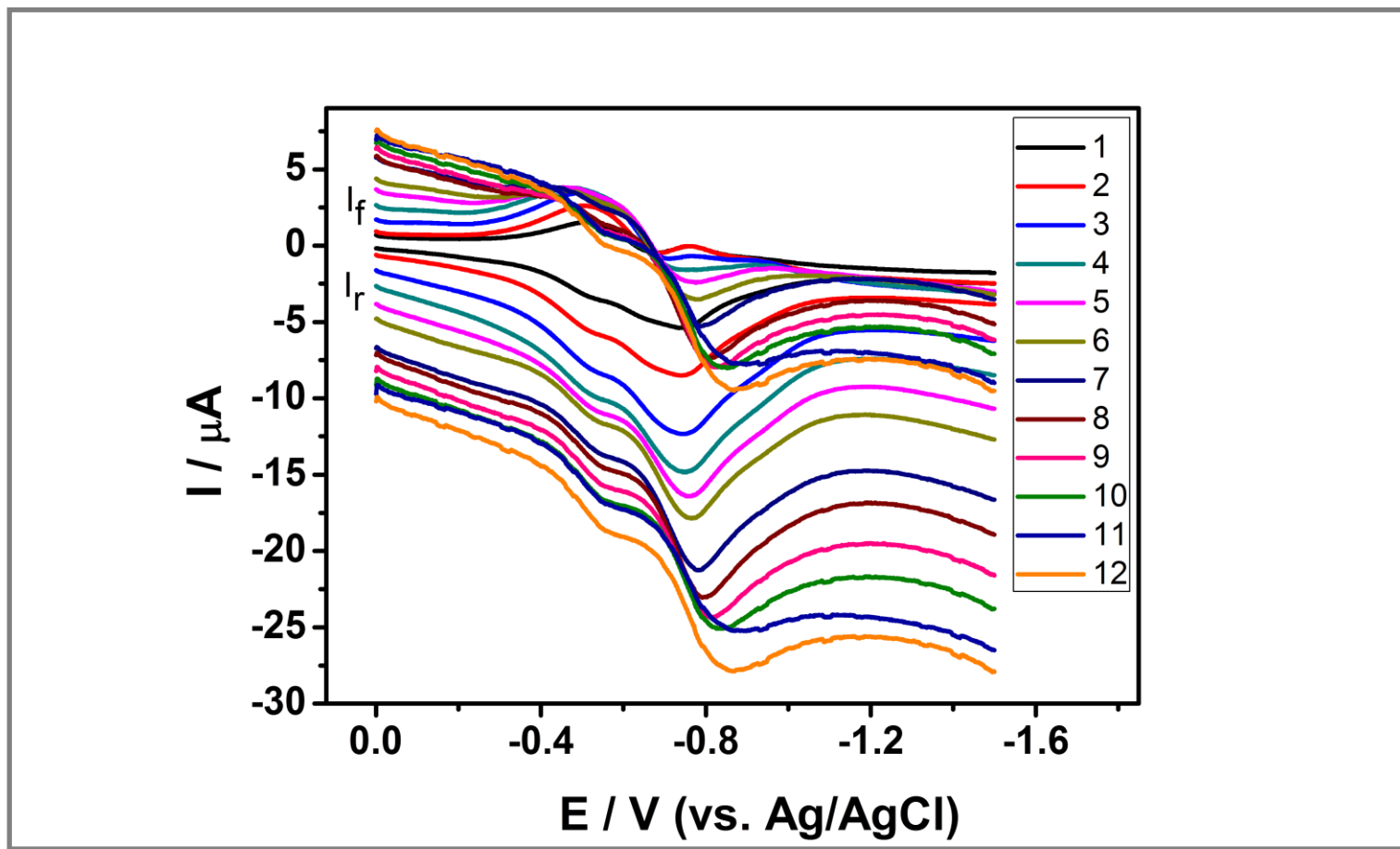
Figure 4.61: Square-wave voltammograms of N, N'-bis(2-aminohexanoic acid)-3,4,9,10 perylenebis(dicarboximide) (LPDI) in DMF at different frequencies (Hz): 1 (50), 2 (100), 3 (200), 4 (300), 5 (400), 6 (500), 7 (750), 8 (1000), 9 (1250), 10 (1500), 11 (1750), 12 (2000), supporting electrolyte: $NaBF_4$, at 25 ^{o}C.
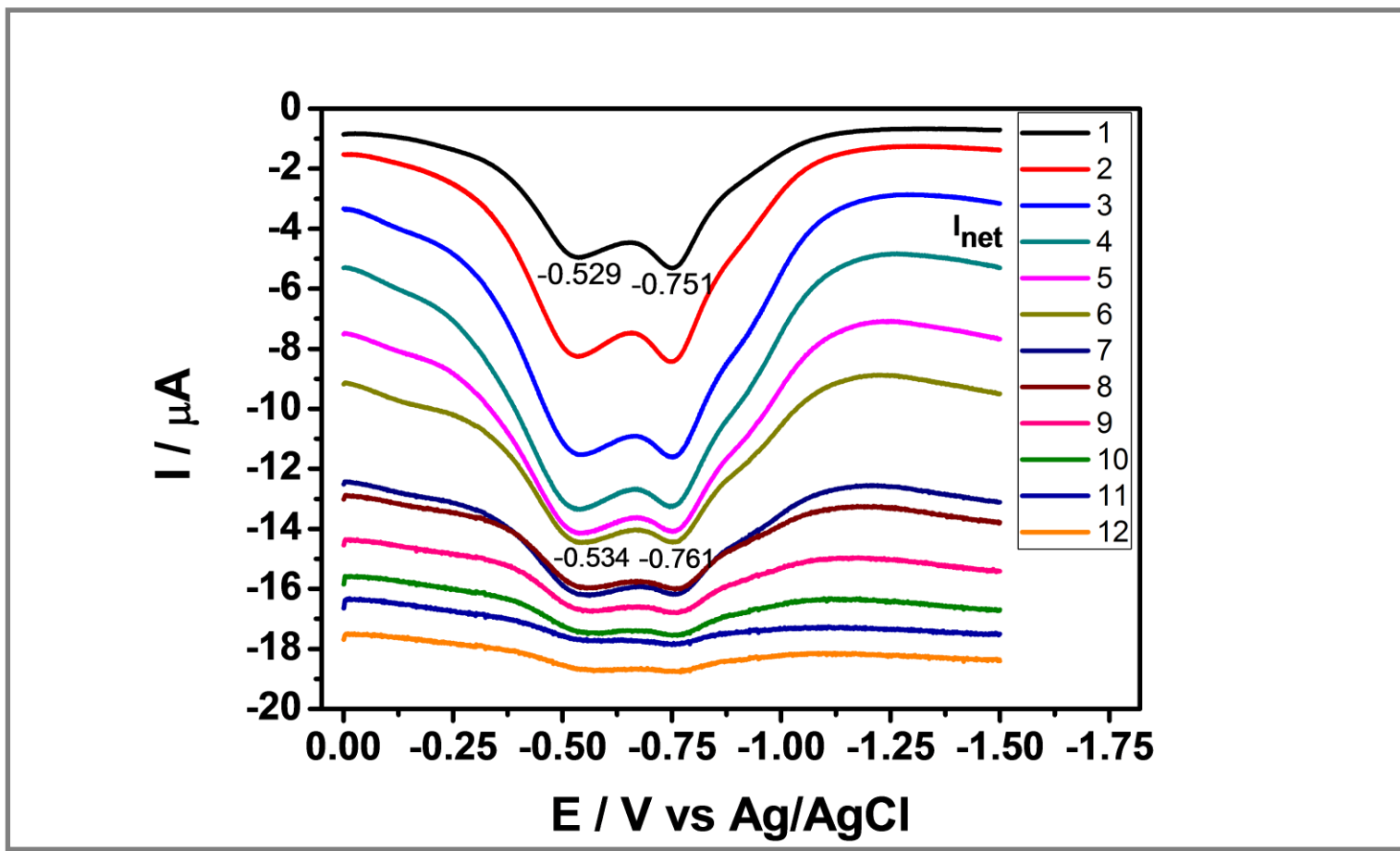
Figure 4.62: Square-wave voltammograms (I$_{net}$) of N, N'-bis(2-aminohexanoic acid)-3,4,9,10 perylenebis(dicarboximide) (LPDI) in DMF at different frequencies (Hz): 1 (50), 2 (100), 3 (200), 4 (300), 5 (400), 6 (500), 7 (750), 8 (1000), 9 (1250), 10 (1500), 11 (1750), 12 (2000), supporting electrolyte: NaBF$_4$, at 25 ^{o}C.
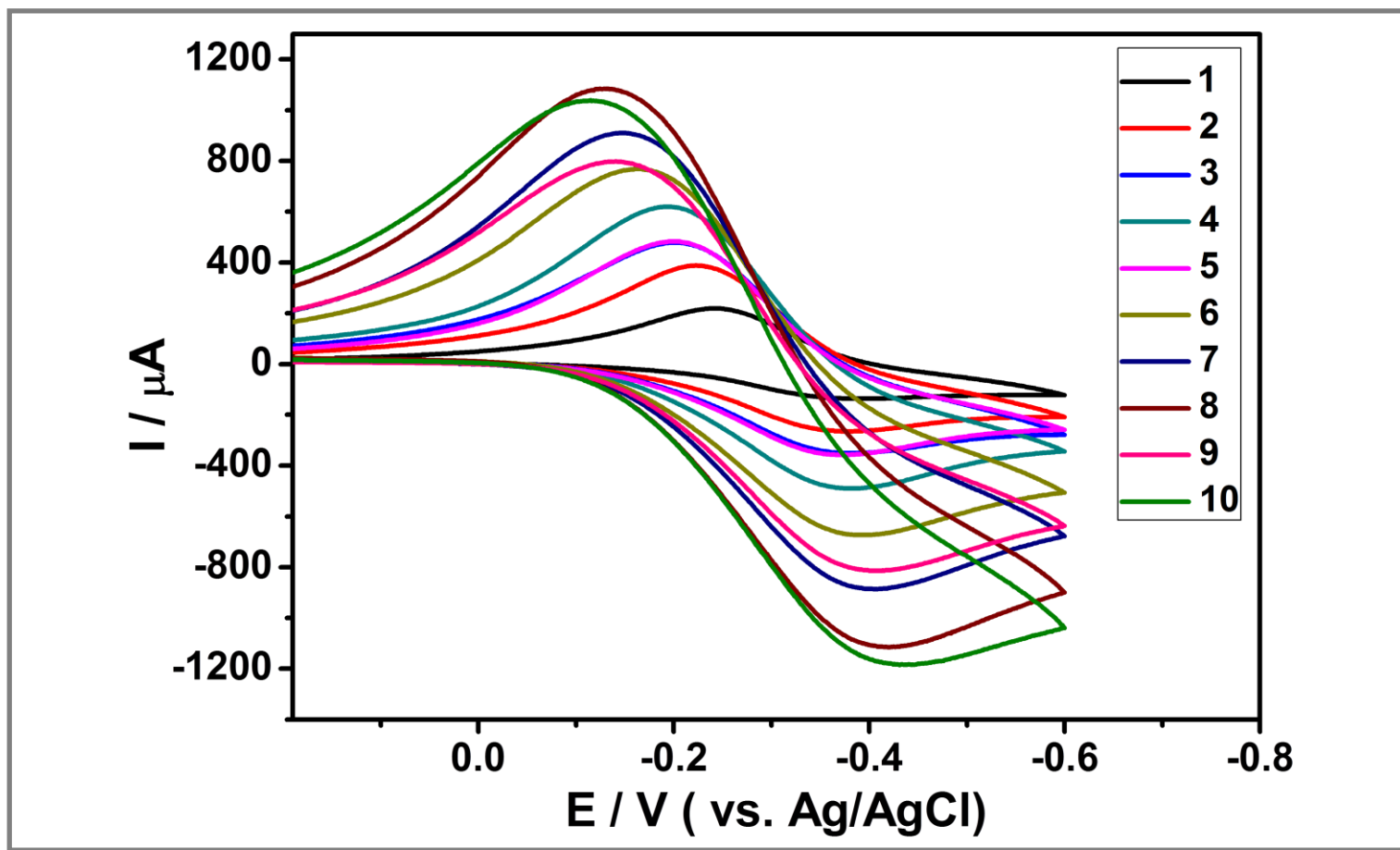
Figure 4.63: Solid-state cyclic voltammograms of N-(2-aminohexanoic acid)-3,4,9,10 perylenetetracarboxylic-3,4-anhydride-9,10 imide (LPMI) at different scan rates (mV s^{-1}): 1 (10), 2 (25), 3 (50), 4 (75), 5 (100), 6 (200), 7 (300), 8 (500), 9 (750), 10 (1000), supporting electrolyte: HCl, at 25 ^{o}C.
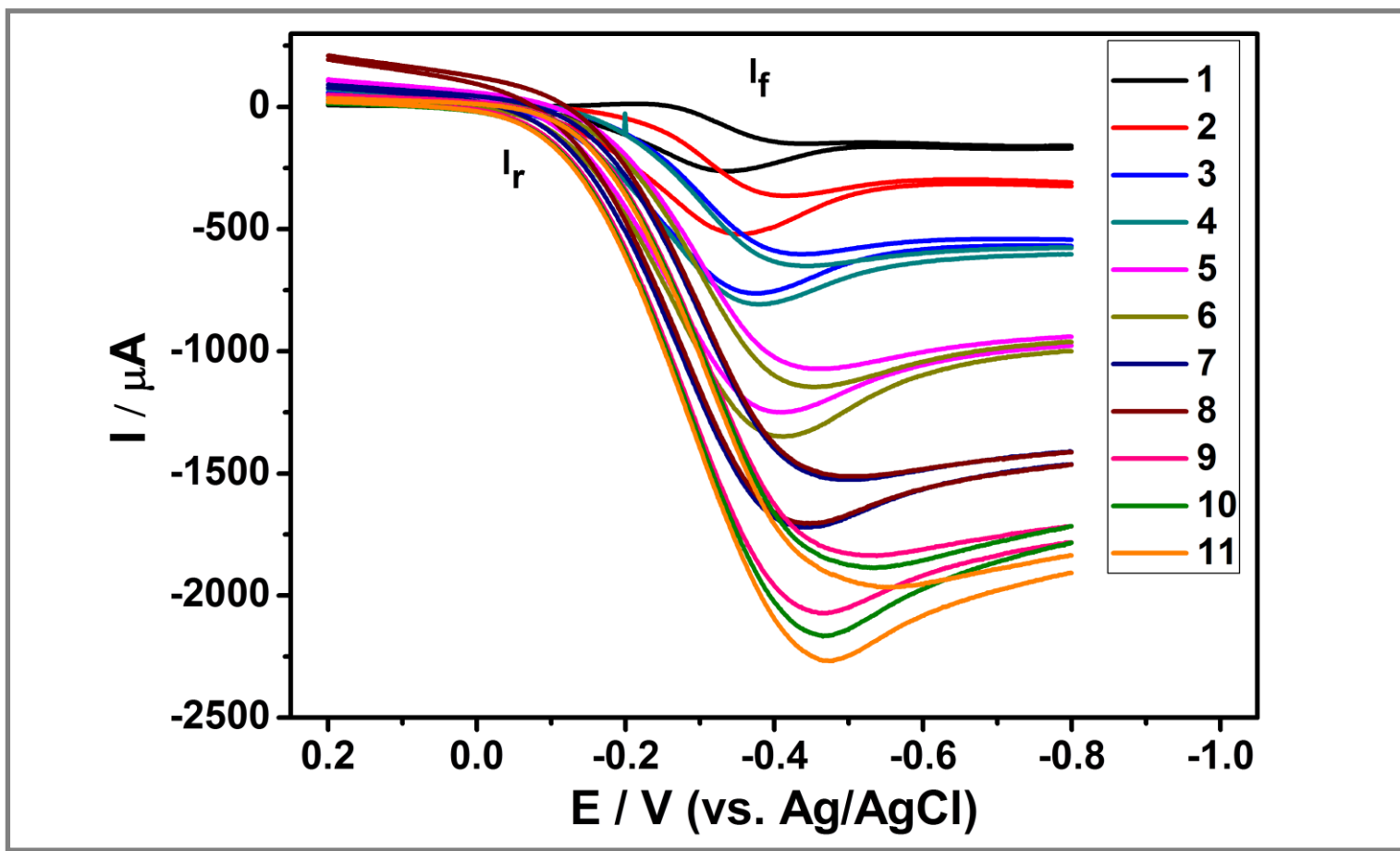
Figure 4.64: Solid-state square-wave voltammograms of N-(2-aminohexanoic acid)-3,4,9,10 perylenetetracarboxylic-3,4-anhydride-9,10 imide (LPMI) at different frequencies (Hz): 1 (10), 2 (50), 3 (75), 4 (100), 5 (300), 6 (500), 7 (750), 8 (1000), 9 (1500), 10 (1750), 11 (2000), supporting electrolyte: HCl, at 25 ^{o}C.
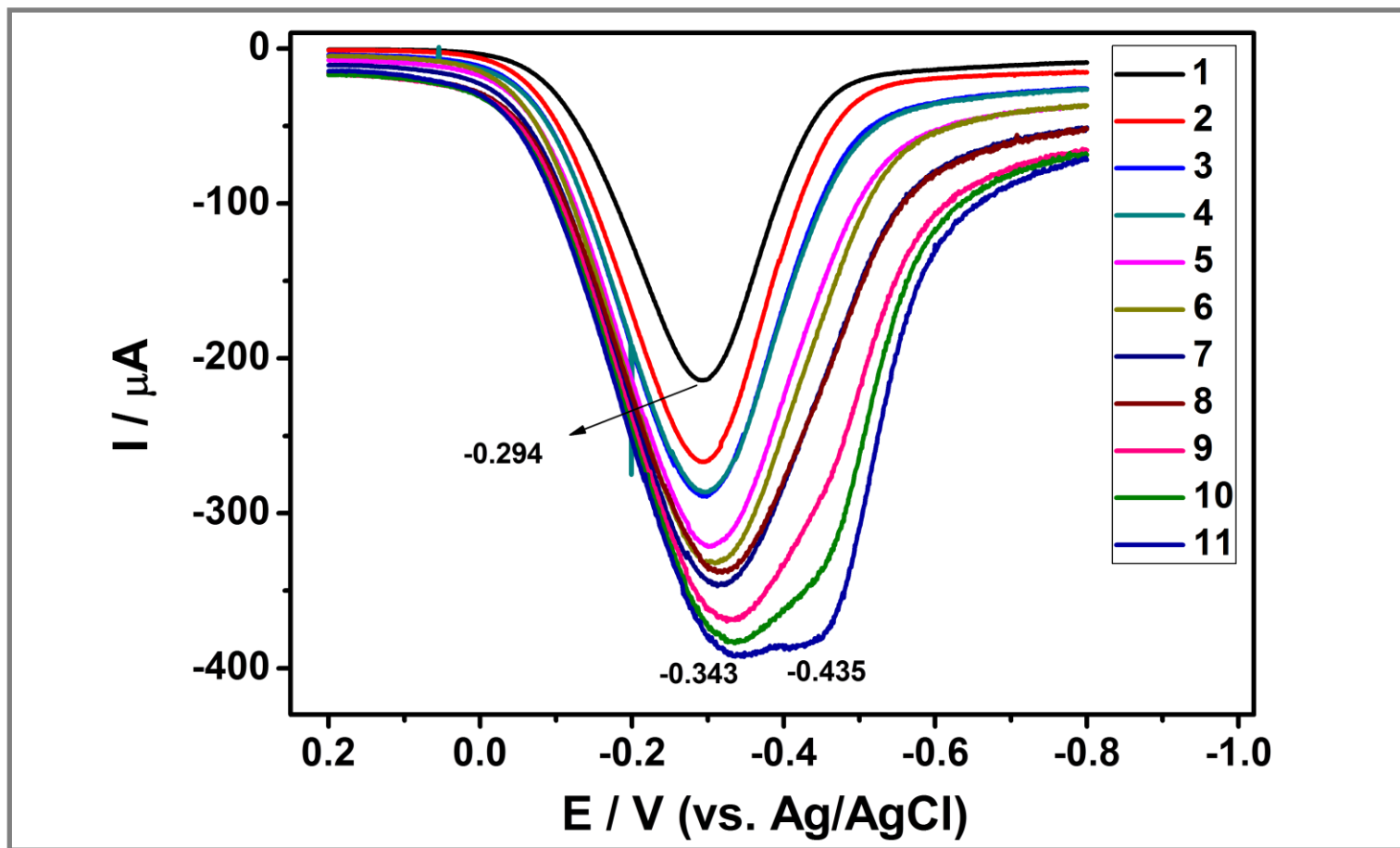
Figure 4.65: Solid-state square-wave voltammograms (I_{net}) of N-(2-aminohexanoic acid)-3,4,9,10 perylenetetracarboxylic-3,4-anhydride-9,10 imide (LPMI) at different frequencies (Hz): 1 (10), 2 (50), 3 (75), 4 (100), 5 (300), 6 (500), 7 (750), 8 (1000), 9 (1500), 10 (1750), 11 (2000), supporting electrolyte: HCl, at 25 ^{o}C.
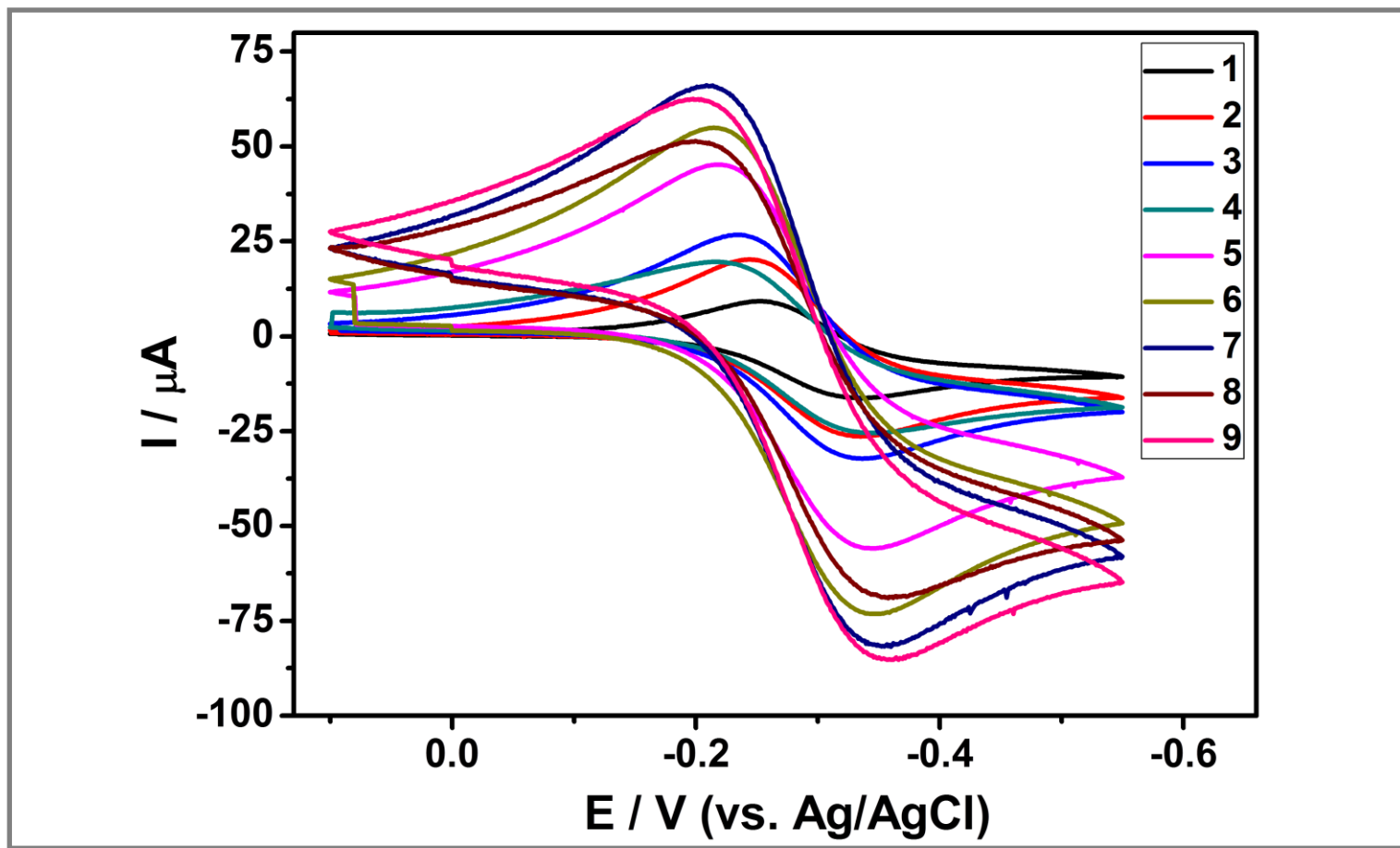
Figure 4.66: Solid-state cyclic voltammograms of N, N'-bis(2-aminohexanoic acid)-3,4,9,10 perylenebis(dicarboximide) (LPDI) at different scan rates (mV s^{-1}): 1 (10), 2 (25), 3 (50), 4 (100), 5 (200), 6 (300), 7 (500), 8 (750), 9 (1000), supporting electrolyte: HCl, at 25 ^{o}C.
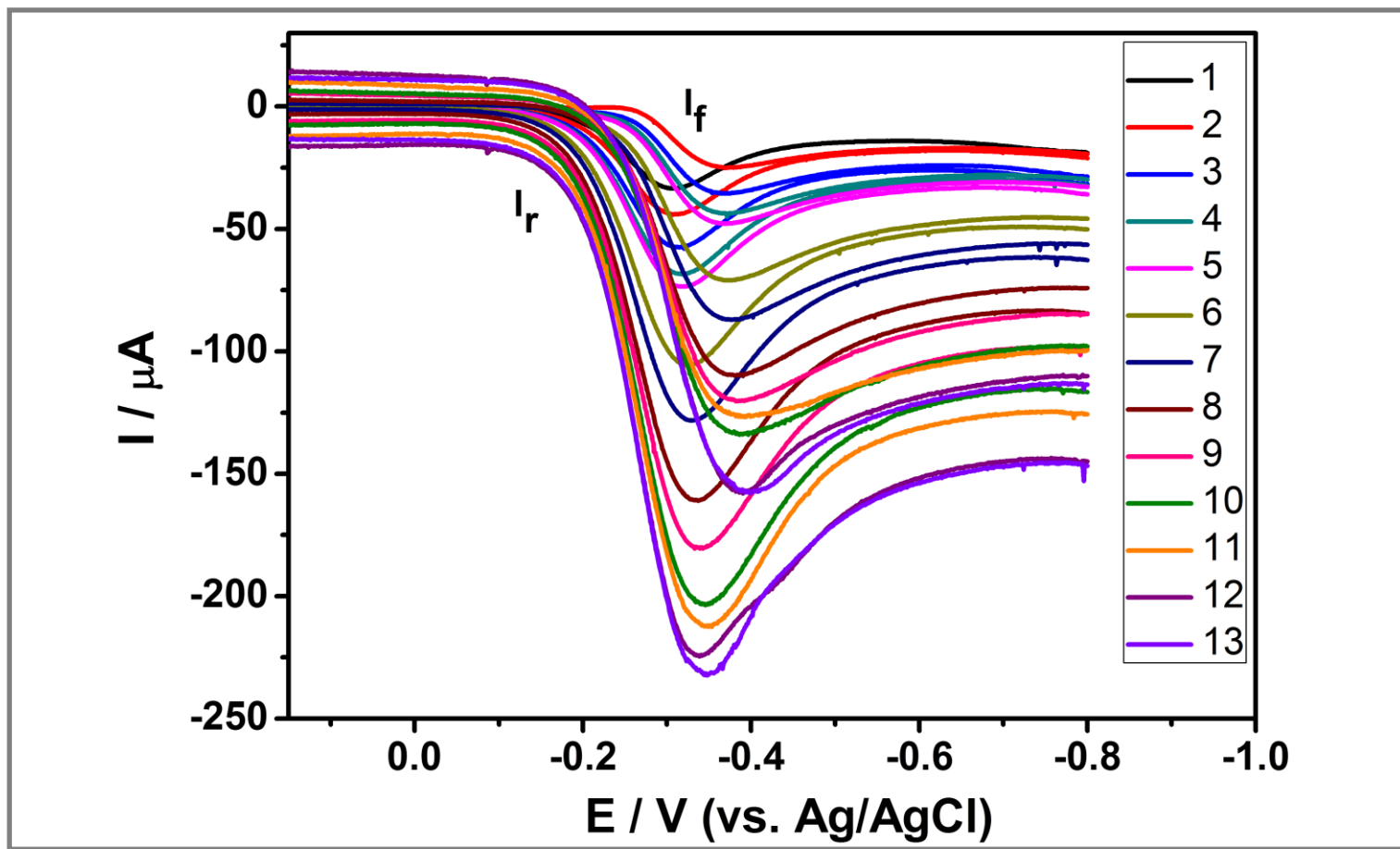
Figure 4.67: Solid-state square-wave voltammograms of N, N'-bis(2-aminohexanoic acid)-3,4,9,10 perylenebis(dicarboximide) (LPDI) at different frequencies (Hz): 1 (10), 2 (20), 3 (50), 4 (75), 5 (100), 6 (200), 7 (300), 8 (500), 9 (750), 10 (1000), 11 (1500), 12 (1750), 13 (2000), supporting electrolyte: HCl, at 25 ^{o}C.
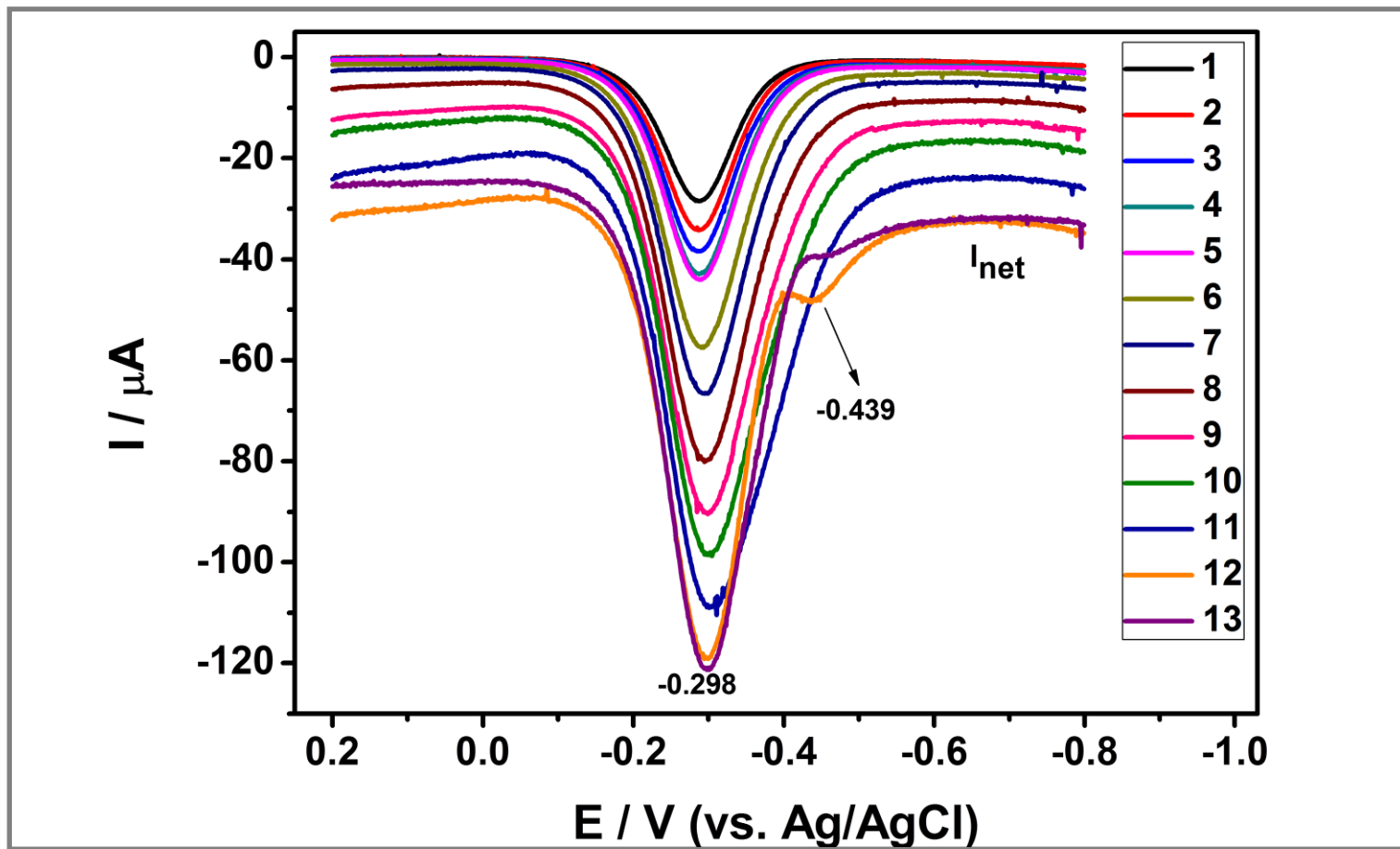
Figure 4.68: Solid-state square-wave voltammograms (I_net) of N, N'-bis(2-aminohexanoic acid)-3,4,9,10 perylenebis(dicarboximide) (LPDI) at different frequencies (Hz): 1 (10), 2 (20), 3 (50), 4 (75), 5 (100), 6 (200), 7 (300), 8 (500), 9 (750), 10 (1000), 11 (1500), 12 (1750), 13 (2000), supporting electrolyte: HCl, at 25 ^{o}C.
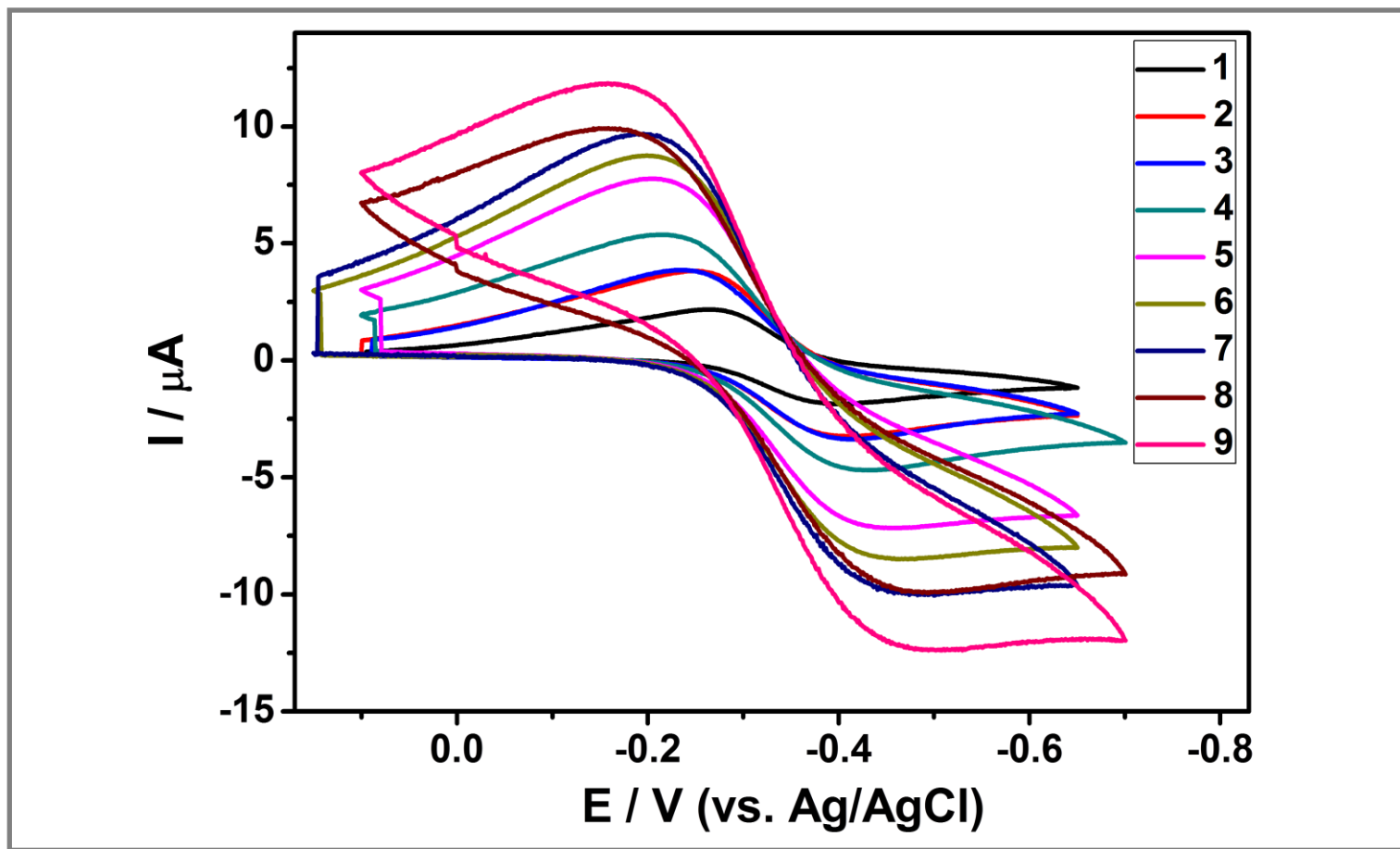
Figure 4.69: Solid-state cyclic voltammograms of N-(2-aminohexanoic acid)-N'-(1-phenyl-ethylamine)-3,4,9,10 perylenebis (dicarboximide) (LPPDI) at different scan rates (mV s^{-1}): 1 (10), 2 (25), 3 (50), 4 (100), 5 (200), 6 (300), 7 (500), 8 (750), 9 (1000), supporting electrolyte: HCl, at 25 ^{o}C.
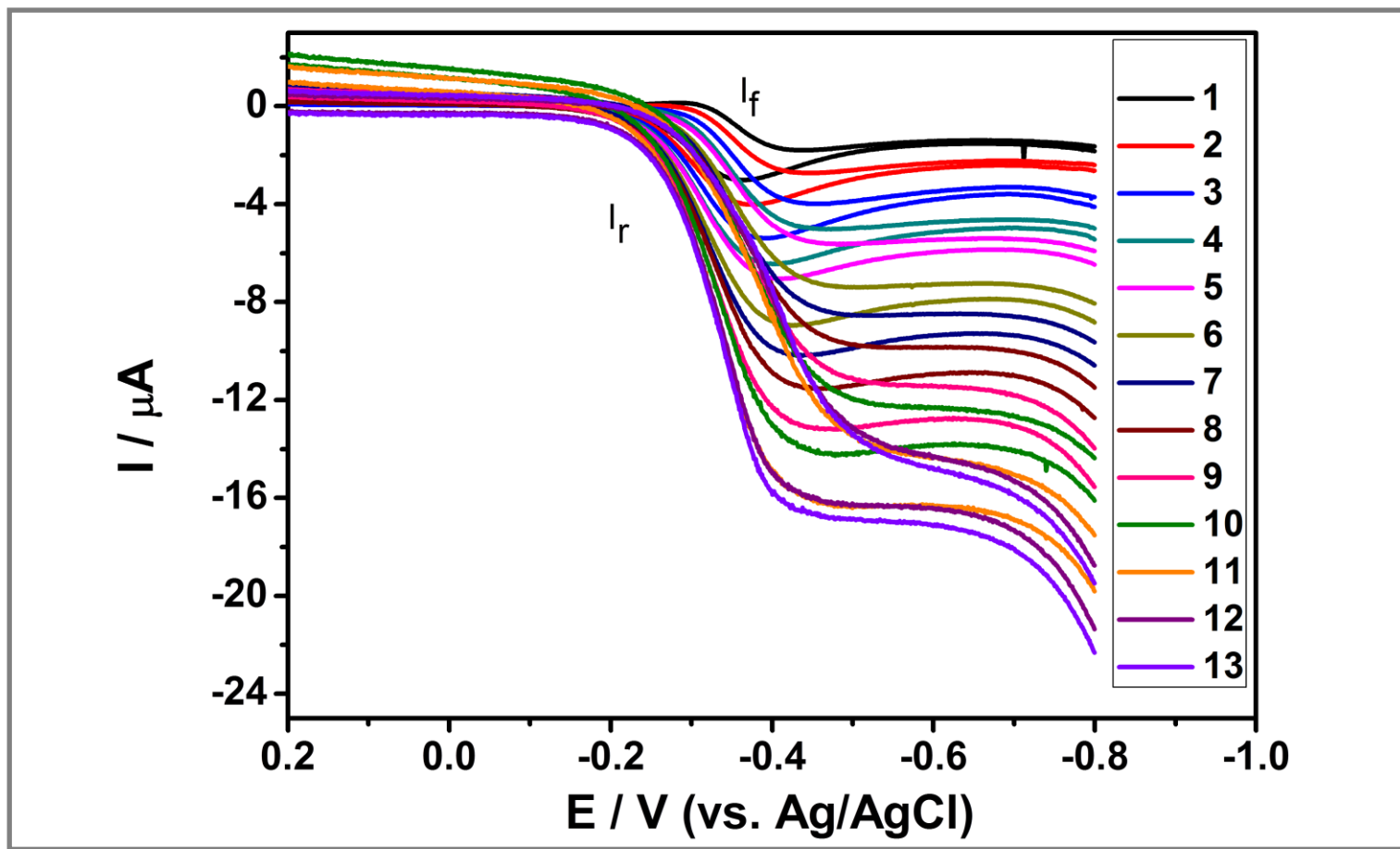
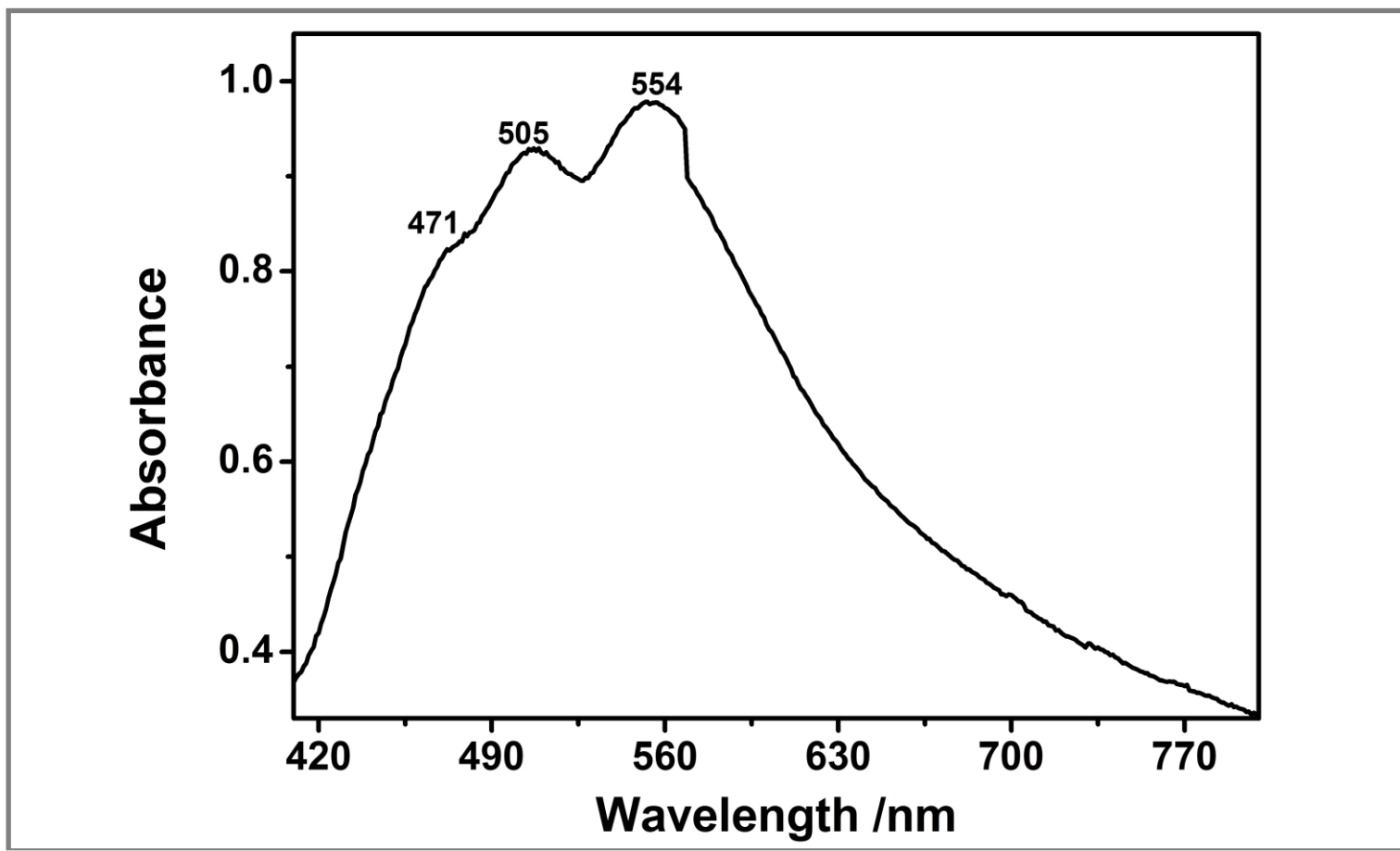Figure 4.70: Solid-state square-wave voltammograms of N-(2-aminohexanoic acid)-N'-(1-phenyl-ethylamine)-3,4,9,10 perylenebis (dicarboximide) (LPPDI) at different frequencies (Hz): 1 (10), 2 (20), 3 (50), 4 (75), 5 (100), 6 (200), 7 (300), 8 (500), 9 (750), 10 (1000), 11 (1500), 12 (1750), 13 (2000), supporting electrolyte: HCl, at 25 ^{o}C.
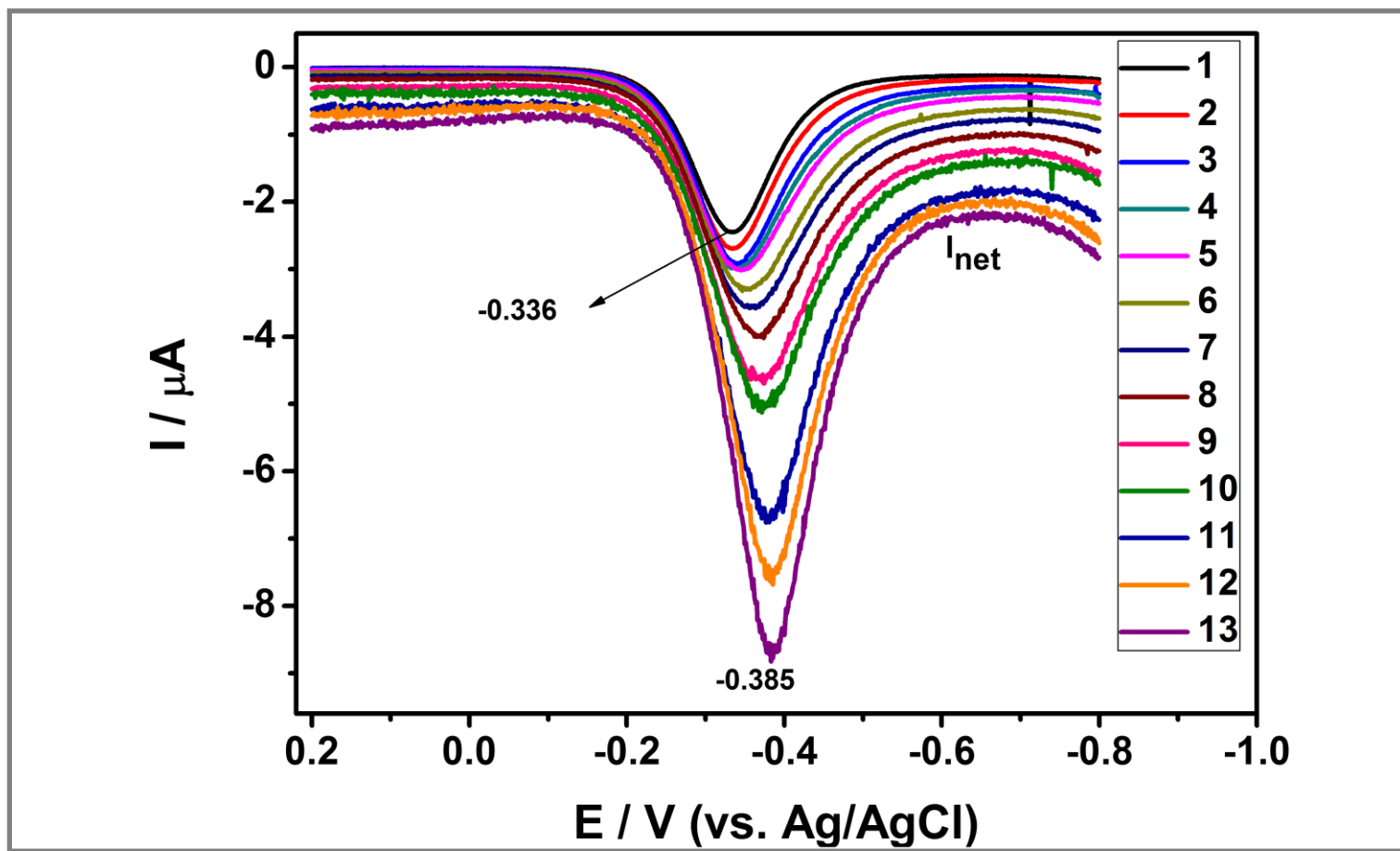
Figure 4.71: Solid-state square-wave voltammograms ($_{Inet}$) of N-(2-aminohexanoic acid)-N'-(1-phenyl-ethylamine)-3,4,9,10 perylenebis (dicarboximide) (LPPDI) at different frequencies (Hz): 1 (10), 2 (20), 3 (50), 4 (75), 5 (100), 6 (200), 7 (300), 8 (500), 9 (750), 10 (1000), 11 (1500), 12 (1750), 13 (2000), supporting electrolyte: HCl, at 25 ^{o}C.
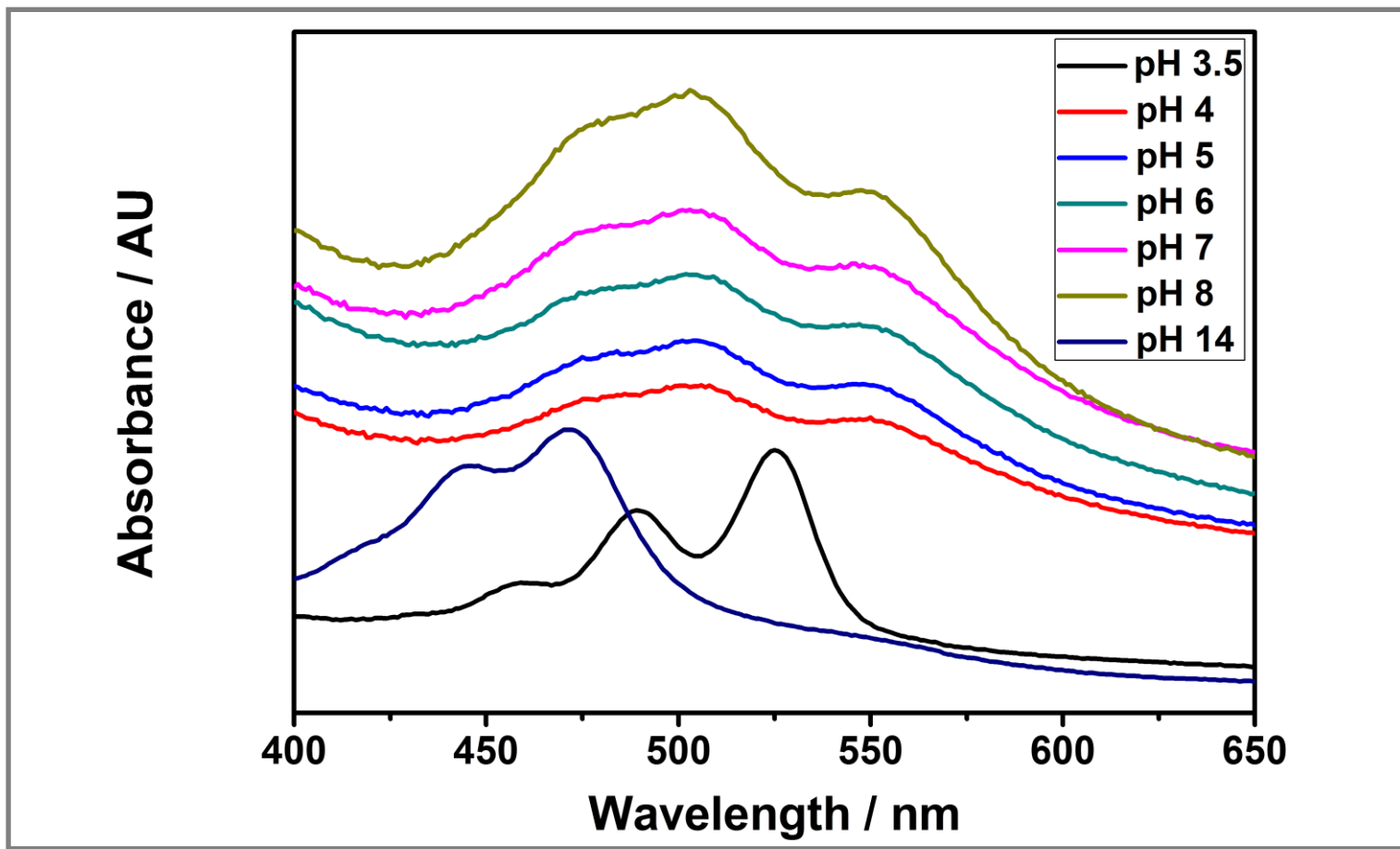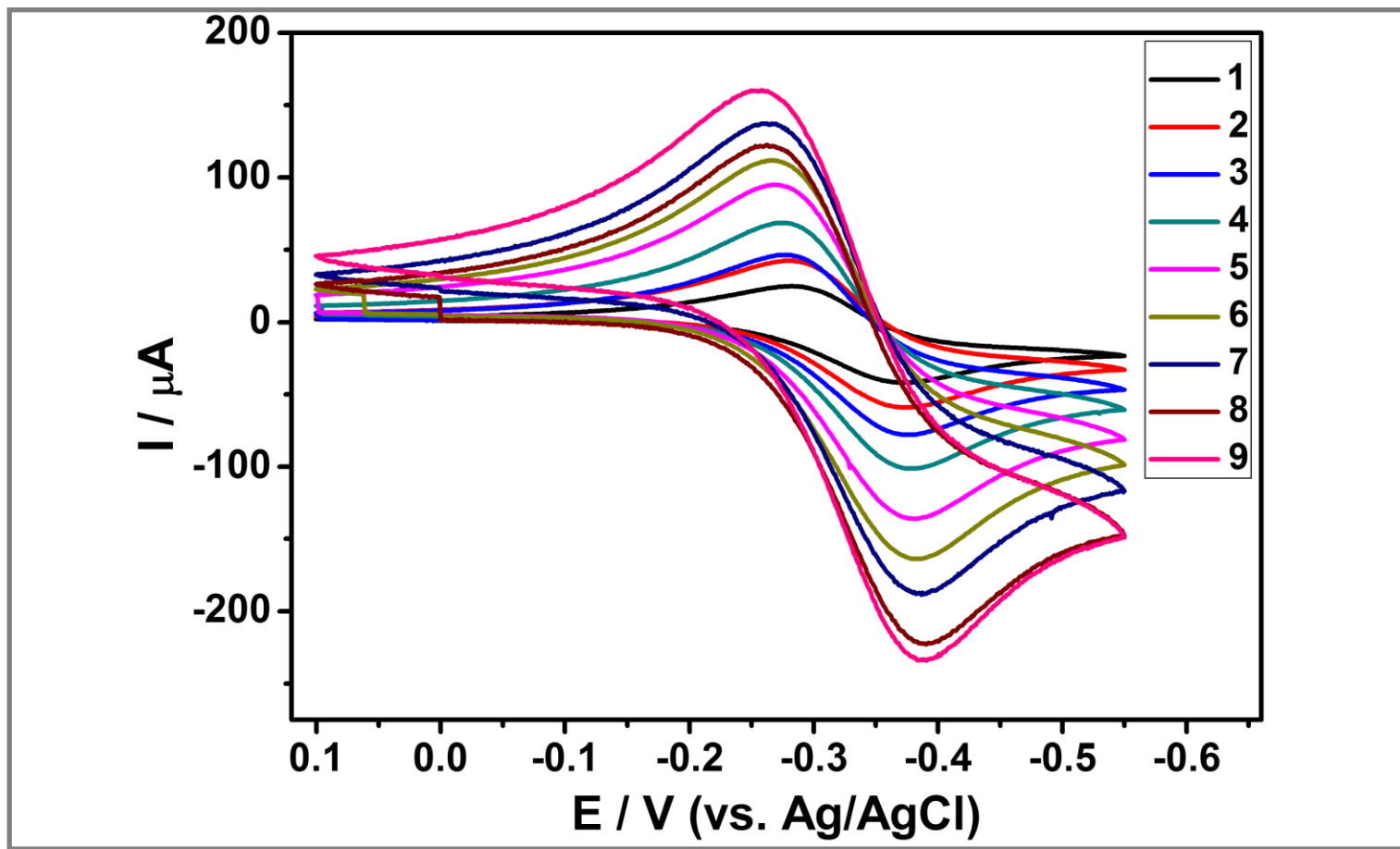
Figure 4.72: Solid-state cyclic voltammograms of N-(2-hydroxy-4-benzoic acid)-N'-(4-hydroxyphenyl)-3,4,9,10 perylenebis (dicarboximide) (BPDI) at different scan rates (mV s^{-1}): 1 (10), 2 (25), 3 (50), 4 (100), 5 (200), 6 (300), 7 (500), 8 (750), 9 (1000), supporting electrolyte: HCl, at 25 ^{o}C.

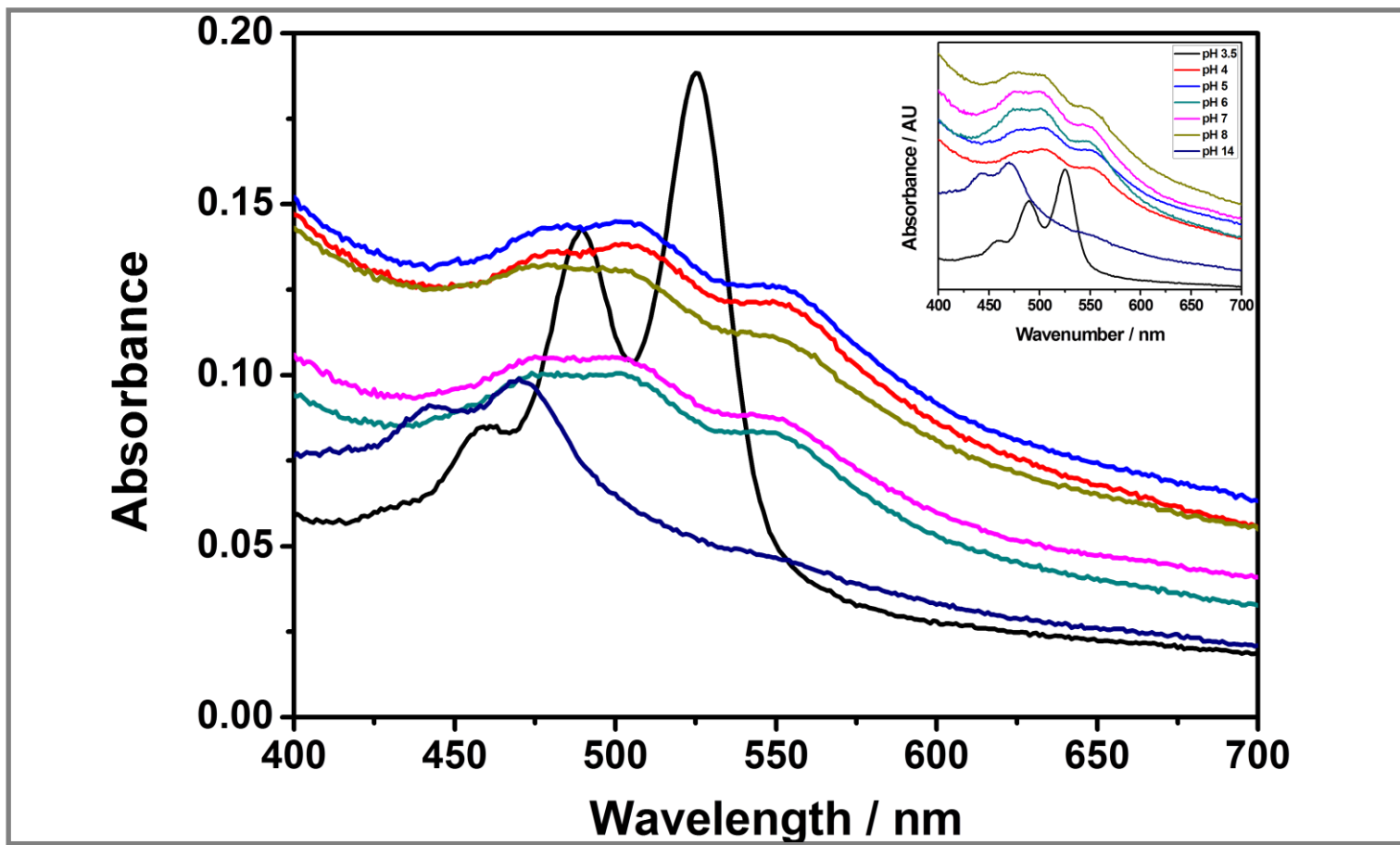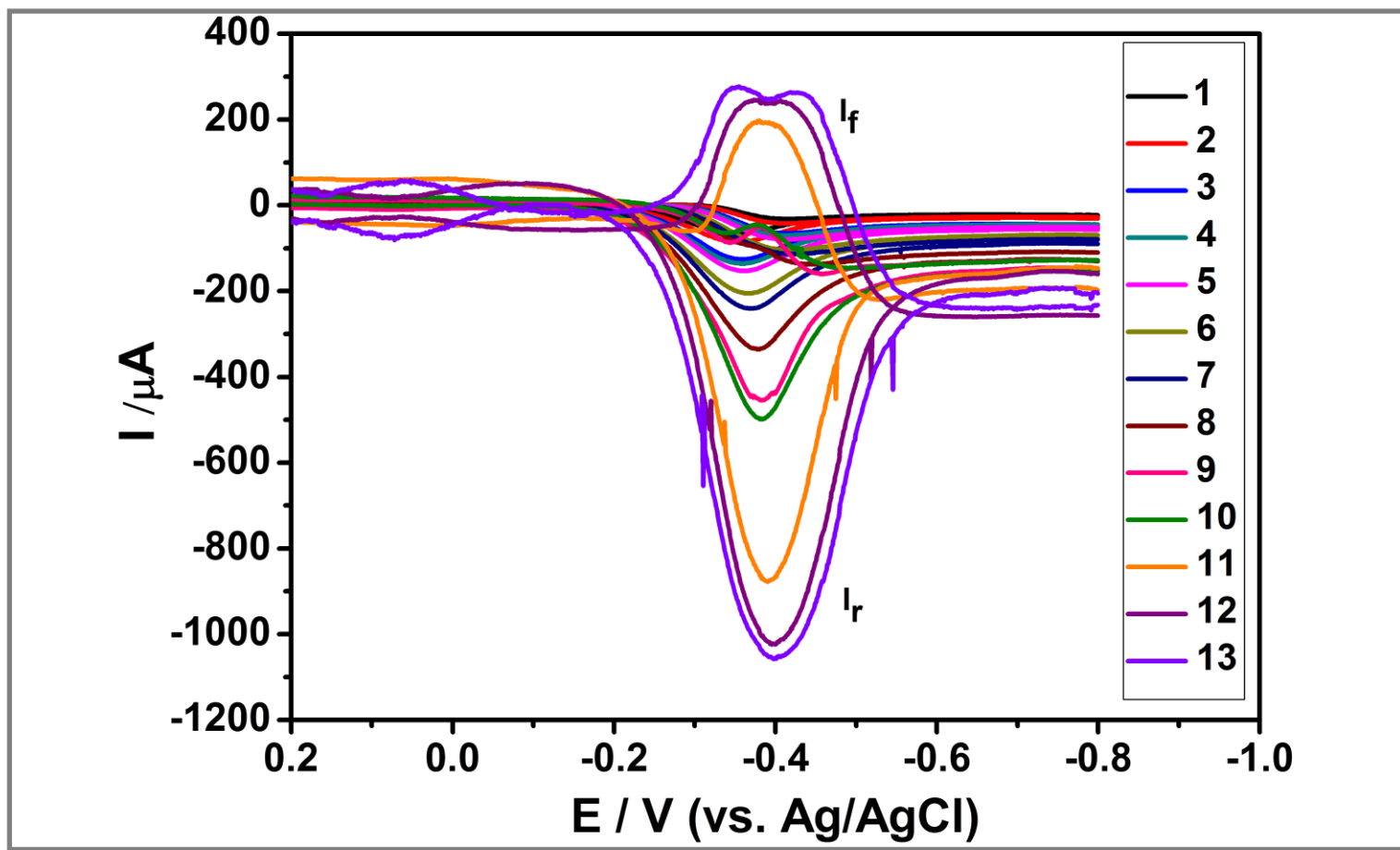Figure 4.73: Solid-state square-wave voltammograms of N-(2-hydroxy-4-benzoic acid)-N'-(4-hydroxyphenyl)-3,4,9,10 perylenebis (dicarboximide) (BPDI) at different frequencies (Hz): 1 (10), 2 (20), 3 (50), 4 (75), 5 (100), 6 (200), 7 (300), 8 (500), 9 (750), 10 (1000), 11 (1500), 12 (1750), 13 (2000), supporting electrolyte: HCl, at 25 ^{o}C.
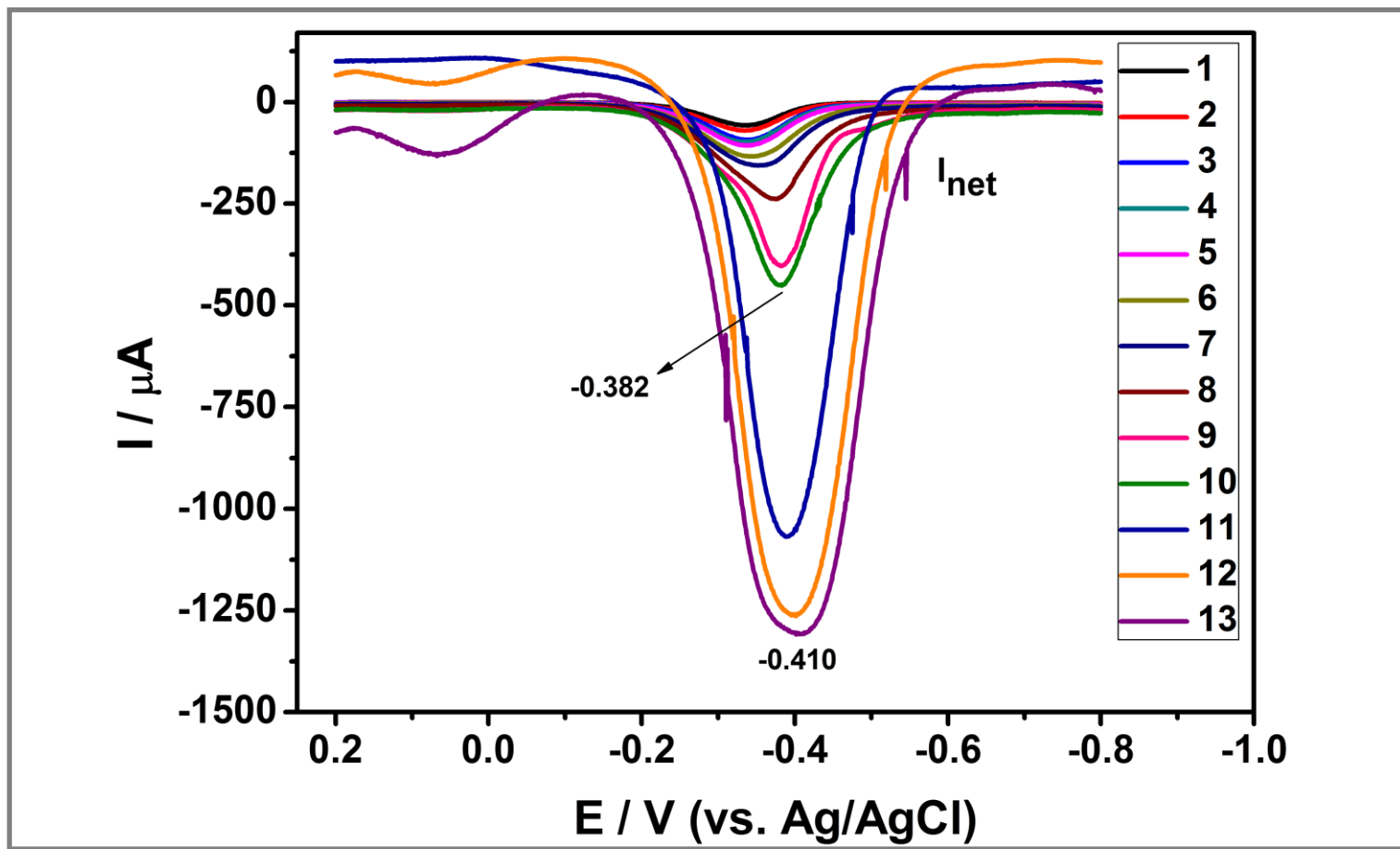
Figure 4.74: Solid-state square-wave voltammograms (I$_{net}$)of N-(2-hydroxy-4-benzoic acid)-N'-(4-hydroxyphenyl)-3,4,9,10 perylenebis (dicarboximide) (BPDI) at different frequencies (Hz): 1 (10), 2 (20), 3 (50), 4 (75), 5 (100), 6 (200), 7 (300), 8 (500), 9 (750), 10 (1000), 11 (1500), 12 (1750), 13 (2000), supporting electrolyte: HCl, at 25 ^{o}C.

Chapter 5

RESULTS and DISCUSSION

5.1 Synthesis and Characterization

Chiral symmetrical and unsymmetrically substituted perylene diimides have been prepared following the synthetic routes presented in Scheme 3.1. The synthesis of perylene tetracarboxylic diimides (PTCDIs) takes the advantages of the fact that the two nitrogen positions at the imides of PTCDI are nodes in the π-orbital wavefunction, providing enormous options for modifying the structures of the two side-chains. Symmetrical perylene diimide was synthesized via condensation of perylene 3,4,9,10-tetracarboxylic dianhydride with L-lysine in the mixture of high boiling point solvents; m-cresol and isoquinoline. In case of unsymmetrically substituted perylene diimides, syntheses were accomplished in three steps according to methods mentioned elsewhere [47]. In order to construct supramolecular structures of PTCDI containing multifunctional moieties (e.g., electron donor for charge separation, hydrophilic-side-chain for enhanced layer-by-layer stacking), it is generally required to make the monoimide as precursor to synthesize PTCDIs for further steps [57]. Therefore, as a first step, perylene-3,4,9,10-tetracarboxylic acid monoanhydride monopotassium carboxylate was prepared. Then N-alkyl(aryl)-3,4,9,10-perylene tetracarboxylic monoanhydride monoimide was synthesized as the key intermediate. Finally, the desired unsymmetrical perylene dyes; BPPDI and LPPDI were achieved via condensation of corresponding amines with N-alkyl(aryl)-

3,4,9,10-perylene tetracarboxylic monoanhydride monoimide in the presence of m-cresol and isoquinoline as solvent mixture. All of the synthesized compounds have been characterized by ^{1}HNMR, ^{13}CNMR, IR and elemental analyses. The results nicely supported the predicted chemical structures of the desired compounds.

The solubility properties of LPMI-LPDI, LPPDI and OHPMI-BPDI are exhibited in Tables 5.1, 5.2 and 5.3, respectively. It was clearly observed that solubility of monoimides was lower than their corresponding imides due to intermolecular interactions affected by the rigidity and symmetry. The presence of secondary carbon atoms next to nitrogen atoms was expected to force the phenyl substituents out of the plane of the molecule and thereby hamper to face-to-face π-π stacking of the BPDI and LPPDI leading to enhanced solubility. However, BPDI is only partly soluble in limited number of solvents most probably due to strong hydrogen bonding interactions. LPPDI, unsymmetrically substituted chiral perylene diimide with two chiral centers showed a relatively higher solubility in a variety of the solvents as the sterically hindered chiral substituent decreased the short π-π contacts of the chromophore to a certain extend. Moreover, LPPDI exhibited a higher solubility in dipolar protic solvents due to absence of hydrogen bonding interactions. The effect of hydrogen-bonding interactions on solubility was observed on LPDI with two long aliphatic carbon chain substitutents where a higher solubility was expected.

Table 5.1: Solubility properties of LPMI and LPDI

	Solubility[a]/Colour			
	LPMI		LPDI	
CH$_3$COOH	+ -	pale yellow-orange	+ -	pale pink
CF$_3$COOH	+ -	orange	+ -	dark pink
m-cresol	+ -	pink	+ -	dark pink
pyridine	-		+ -	pink
NMP	-		+ -	pale pink-orange
DMF	+ -	pale pink-orange	+ -	pale pink-orange
DMAc	-		+ -	pink
DMSO	+ -	pale pink	+ -	pink
H$_2$SO$_4$	+ -	dark red-blue	+ -	dark violet

- insoluble at RT; NMP: N-methylpyrolidinone; DMF: dimethylformamide; DMAc: N,N-dimethylacetamide; DMSO: dimethyl sulfoxide. [a] 0.1 mg in 1.0 mL of solvent. + soluble; + - partially soluble.

Table 5.2: Solubility properties of LPPDI

	Solubility[a] / color	
Toluene	+ -	pale pink
Chloroform	+ -	fluorescent pale orange
TCE	+ -	fluorescent orange
CH_3COOH	+ -	pale pink
CF_3COOH	+ -	cherry red
m-cresol	+ -	cherry-red
H_2SO_4	+ -	dark blue/violet
THF	+ -	pale orange
DCM	+ -	pale orange
Pyridine	+ -	fluorescent orange
Acetone	+ -	pale orange
NMP	+ -	brown orange
DMF	+ -	pale orange
DMAc	+ -	fluorescent pale pink-orange
DMSO	+ -	pink

TCE: 1,1,2,2 tetracloroethane; DCM: dichloromethane;
NMP: N-methylpyrolidinone; DMF: dimethylformamide;
DMAc: Dimethylformacetamide; DMSO: dimethyl sulfoxide.
[a] 0.1 mg in 1.0 mL of solvent. + soluble; + - partially soluble.

Table 5.3: Solubility properties of BPDI

	Solubility[a] / Colour		
	OH-PMI[58]	BPDI	
CH₃COOH	-	+ -	dark pink-orange
CF₃COOH	-	+ -	dark red
Chloroform	-	+ -	pale pink
Pyridine	-	+ -	pink
EtOH	-	+ -	pale pink
NMP	+ red	+ -	pink
MeOH	-	+ -	pale pink
DMF	+ red	+ -	pink
DMSO	+ red	+ -	pink

- insoluble at RT; NMP: N-methylpyrolidinone; DMF: dimethylformamide; DMSO: dimethyl sulfoxide. [a] 0.1 mg in 1.0 mL of solvent. + soluble; + - partially soluble.

All of the IR spectra were consistent with the assigned structures representing the various functional groups existing (Figures 4.3-4.6). All of the 4 compounds exhibited strong intermolecular hydrogen bonding which is characterized by a broad, irregular shapeless band between $\sim$ 3500-1700 cm^{-1} regions. The IR spectrum of LPMI showed characteristic absorption bands at 3442 cm^{-1} (overlapping of N-H and O-H stretch); 2925, 2850 cm^{-1} (aliphatic C-H stretch), 1766, 1725 cm^{-1} (anhydride C=O stretch); 1690, 1655 cm^{-1} (imide C=O); 1593 cm^{-1} (aromatic C=C stretch); 1556 cm^{-1} (N-H bend); 1444, 1400, 1320 cm^{-1} (C-N stretch); 1244 cm^{-1} (aliphatic C-O stretch); 1125, 1015, 858, 806, 731 cm^{-1} (Aromatic C-H bend). The IR spectrum of

LPDI and LPPDI exhibited characteristic bands where absorption bands of anhydride carbonyl stretching bands (1766 and 1725 cm^{-1}) of LPMI had disappeared and were replaced by N-imides carbonyl stretching bands (1696 and 1654 cm^{-1}) for both LPDI and LPPDI. The aliphatic C-O stretching band at 1244 cm^{-1} (LPMI) had shifted to 1242 cm^{-1} and 1251 cm^{-1} in the IR spectra of LPDI and LPPDI, respectively. The IR spectrum of BPDI presented characteristic absorption bands at 3340 cm^{-1} (O-H stretch); 3062 cm^{-1} (aromatic C-H stretch); 1693, 1658 cm^{-1} (imide C=O), 1593 (aAr C=C stretch); 1174, 1126, 966, 810, 743 cm^{-1} (Ar C-H bend). In addition, the absence of aliphatic C-H, anhydride carbonyl bands and N-H bend peaks in the spectra supported the structure. Other infrared bands of all compounds were very similar.

5.2 Absorption and Fluorescence Properties

The UV-vis absorption and emission spectra of 1x10^{-5} mol L^{-1} solutions of LPMI, LPDI, LPPDI and BPDI in different solvents are given in Figures 4.18, 4.21-4.24,4.29,4.32,4.35-4.38 and 4.40. The maximum absorption wavelengths $\lambda_{abs\ max}$ (nm), stoke shifts (nm), ratios of absorption intensities $A^{0\to0}/A^{0\to1}$ and singlet energes Es (kcal mol^{-1}) of LPMI, LPDI, LPPDI and BPDI in different solvents have been exhibited in Tables 5.4 and 5.5. Moroever, the maximum absorption wavelengths $\lambda_{abs\ max}$ (nm), stoke shifts (nm) and ratios of absorption intensities $A^{0\to0}/A^{0\to1}$ of LPMI, LPDI and BPDI in different pH values (3.5-14) are presented in Table 5.6. The absorbance is significantly dependent on the solubility of the compound and the polarity of the solvent. In polar protic and aprotic solvents, The chiral perylene monoimide, LPMI UV-vis spectra (Figure 4.15) show absorption bands between 400 and 550 nm for the S$_0$─S$_1$ transition of the perylene chromophore, with a well resolved vibronic structure that can be attributed

to breathing vibrations of the perylene skeleton which strongly couples with S_0-S_1 transition polarized along the long axis of molecules. In DMF, LPMI exhibited 3 characteristic absorption bands with increasing intensity at higher wavelengths (450 nm, 485 nm, and 520 nm) and this property is consistent with the literature data [59]. In trifluoroacetic acid and DMSO, absorption is red-shifted (2-8 nm) and is blue-shifted in acetic acid, sulfuric acid (2 nm) and in m-cresol (35 nm). It is mentioned that changes in the absorption ratio between the $0{\rightarrow}0$ and $0{\rightarrow}1$ transition indicate aggregation which can be quantified from the absorption ratios: while monomeric perylene diimides (PDIs) exhibit normal Franck Condon progression with $A^{0{\rightarrow}0}/A^{0{\rightarrow}1}$ ≈ 1.6, aggregated PDIs display an inverted intensity distribution among their vibronic states states with $A^{0{\rightarrow}0}/A^{0{\rightarrow}}$≤0.7 [28] (Table 5.4).Similarly, corresponding chiral symmetrical, LPDI in exhibited 3 characteristic absorption bands in polar protic and dipolar aprotic solvents UV spectra. (Figure 4.18) In dipolar aprotic solvents such as pyridine, NMP, DMF, DMAc, and DMSO, three bands at around 523 nm, 487 nm and 457 nm are observed respectively with slight shifting. Considering $A^{0{\rightarrow}0}/A^{0{\rightarrow}1}$ values in Table 5.6, LPDI is only weakly aggregated in these solvents. However in case of hydrogen bonding ability solvents such as acetic acid (525 nm, 490nm, 458 nm), trifuoroacetic acid (534 nm, 498 nm, 466 nm), m-cresol (550 nm, 510 nm, 473 nm) and sulphuric acid (597 nm, 554 nm, 510), there is a trend of red shifting in absorption spectra with increasing solvent polarity where the $A^{0{\rightarrow}0}/A^{0{\rightarrow}1}$ values are 1.11, 1.11, 1.19 and 1.54 respectively implying that LPDI is very weakly aggregated and not at all in H_2SO_4. Differently from the other spectra, new bands positioning at around 378 nm in trifluoroacetic acid, 374 in m-cresol and 402 nm in sulphuric acid were observed, most probably due to the electronic S_0-S_2 transition with a dipole moment perpendicular to the long axis of the molecule. The absorption spectra of

chiral perylene diimide, LPPDI in nonpolar, polar protic and dipolar aprotic solvents are represented in Figures 4.21-4.23. In non-polar solvents such as chloroform and TCE, LPPDI exhibits 2 characteristic peaks (in the range of 450-550 nm) and a shoulder at around 456 nm which respectively refer to 0-0, 0-1 and 0-2, vibronic components of the first π-π* transition. As depicted in Table 5.5, the $A^{0\to0}/A^{0\to1}$ ratios of chloroform and TCE are 1.24 and 1.20 respectively which shows that it is very weakly aggregated in these solvents. In another nonpolar solvent; toluene, LPPDI exhibits 2 slightly blue-shifted peaks (3-7 nm) at 524, 488 and a shoulder at 456 nm which respond to 0-0, 0-1 and 0-2 electronic transitions respectively. In addition, a new unstructured band centred at around 620 nm was observed. This new band could be attributed to aggregation effect. As shown in Table 5.5, a ratio of $A^{0\to0}/A^{0\to1} = 1.24$ was achieved which also showed that LPPDI was slightly aggregated in toluene. In case of polar protic solvents; such as acetic acid, LPPDI showed 2 peaks at 526, 490 nm and a shoulder at 460 nm which respectively refer to 0-0, 0-1 and 0-2 vibronic components of the first π-π* transition. However, the ratio of $A^{0\to0}/A^{0\to1}$ as 0.97 suggests an intermediate case showing both aggregated as well as monomeric molecules. In trifluoroacetic acid, LPDDI showed 2 peaks at 538, 499 nm and a shoulder at 468 nm which are assigned to vibronic $0\to0$, $0\to1$ and $0\to2$ progressions of the electronic $S_0\to S_1$ transition respectively. In addition, a new band positioning around 376 nm which is attributed to the electronic $S_0\to S_2$ transition with a transition dipole moment perpendicular to the long axis of the molecule has appeared [42]. The reversal intensity between the 0-0 and 0-1 transitions could be attributed to exactly face to face stacked dimer of LPPDI. In m-cresol, 2 peaks at 551, 510 nm and a shoulder at 476 nm existed where red shifted peaks at 599, 544,

Table 5.4: Maximum absorption wavelengths $\lambda_{abs\ max}$ (nm), Stoke shifts (nm), Ratios of absorption intensities $A^{0\rightarrow0}/A^{0\rightarrow1}$ and singlet energes Es (kcal mol^{-1}) of LPMI, LPDI and BPDI in different solvents.

Solvents	$\lambda_{abs}^{0\rightarrow0}$ (nm)			$\Delta\lambda$ (nm)			$A^{0\rightarrow0}/A^{0\rightarrow1}$			E_s (kcal mol^{-1})		
	LPMI	LPDI	BPDI	LPMI	LPDI	BPDI	LPMI	LPDI	BPDI	LPMI	LPDI	BPDI
CH$_3$COOH	519	525	525	14	13	15	1.36	1.11	1.32	55.1	54.5	54.5
CF$_3$COOH	528	535	-	21	20	-	1.22	1.11	-	54.2	53.5	-
m-cresol	545	550	-	-	-	-	1.30	1.19	-	52.5	52.0	-
Pyridine	-	529	-	-	9	-	-	1.10	-	-	54.1	-
Ethanol	-	-	524	-	-	12	-	-	1.32	-	-	54.6
NMP	-	525	526	-	12	15	-	1.11	1.51	-	54.5	54.4
Methanol	-	-	523	-	-	13	-	-	1.30	-	-	54.7
DMF	520	523	525	13	10	13	1.10	1.14	1.50	55.0	54.7	54.5
*	545	552	556	118	109	2	0.91	0.97	1.05	58.3	57.0	51.4
DMAc	-	524	-	-	10	-	1.07	1.07	-	-	54.6	-
DMSO	521	526	527	12	12	15	1.12	1.09	1.45	54.9	54.4	54.3
H$_2$SO$_4$	581	596	-	46	38	-	1.29	1.54	-	49.2	48.0	-

* in solid state

Table 5.5: Maximum absorption wavelengths $\lambda_{abs\ max}$ (nm), maximum emission wavelengths $\lambda_{em\ max}$ (nm), Stoke shifts (nm), Ratios of absorption intensities $A^{0\to0}/A^{0\to1}$ and singlet energes E_s (kcal mol^{-1}) of LPPDI in different solvents.

Solvents	$\lambda_{abs.max}$ (nm)	$\lambda_{em.max}$ (nm)	Stoke shift (nm)	$A^{0\to0}/A^{0\to1}$	E_s (kcal mol^{-1})
Toluene	456, 488, *524*, 620	535, 577, 628	11	1.24	54.6
Chloroform	459, 491, *528*	536, 577, 626	8	1.20	54.2
∗	470, 508, *555*	658	103	1.06	51.5
TCE	463, 493, *531*	542, 582, 630	11	1.1	53.9
CH$_3$COOH	460, 490, *526*	539, 579, 632	13	0.97	54.2
CF$_3$COOH	376, 468, 499, *538*	552, 591, 645	14	0.93	51.9
m-cresol	376, 476, 510, *551*	-	-	1.19	51.7
H$_2$SO$_4$	406, 512, 544, *599*	634, 687	35	1.61	47.6
THF	453, 487, *521*	531, 570, 618	10	1.08	54.9
DCM	455, 490, *527*	534, 575, 623	7	1.21	54.1
Pyridine	464, 493, *532*	541, 584, 632	9	0.86	53.6
Acetone	461, 490, *526*	541, 580, 632	15	1.11	54.2
NMP	463, 493, *529*	539, 581, 631	10	0.82	53.9
DMF	461, 490, *527*	536, 577, 629	9	0.84	54.1
DMAc	461, 490, *527*	536, 577, 629	9	0.78	54.1
DMSO	464, 493, *530*	540, 581, 633	10	0.81	53.8

*in solid state; **bold** and *italics* wavalengths are absorption wavelength of 0-0 transitions and used for $A^{0\to0}/A^{0\to1}$.

and a red shifted shoulder at 512 nm were observed in H_2SO_4. New absorption bands positioning around 376 nm in m-cresol and 406 nm in H_2SO_4 were observed, most probably due to the electronic $S_0 \rightarrow S_2$ transition with a transition dipole moment perpendicular to the long axis of the molecule just like in the case of trifluoroacetic acid. Normally, an exactly face to face stacked dimer of PDI will give absorption with an intensity of 0-0 transition smaller than that of 0-1 transition. In both of the solvents spectra, any reversal intensity between the 0-0 and 0-1 transitions was not observed. This suggests either a slipped face to face stacked structure for the molecular self-assembly or the existence of large portion of non-aggregated LPPDI molecules in solution due to low stability of the molecular self-assembly [29]. It is noteworthy that in trifluoroacetic acid and sulphuric acid absorption spectra of LPDI, the intensity of high energy vibronic band observed around 376 nm increased and red shifted upon solvent polarity and proticity. This could be attributed to the probable protonation interaction of the proton-donor solvent with amine. Moreover, referring to Figure 4.36 in hydrogen-bonding ability solvents, red shifted absoption spectra appeared with increasing solvent polarity as well. In dipolar aprotic solvents such as THF, DCM and acetone the ratios of $A^{0 \rightarrow 0}/A^{0 \rightarrow 1}$ = 1.08, 1.21 and 1.11, respectively implied the existence of weak aggregation. In the rest of the solvents such as pyridine, NMP, DMF, DMAc, and DMSO, LPPDI showed two absorption peaks at around 532, 493 and a shoulder at around 464 nm which correspond to vibronic 0-0, 0-1, 0-2 progressions of the electronic $S_0 \rightarrow S_1$ transition, respectively. In all of these solvents there was an intensity reversal between 0-0 and 0-1 transitions where the ratios of $A^{0 \rightarrow 0}/A^{0 \rightarrow 1}$ = 0.86, 0.82, 0.84, 0.78 and 0.81 for pyridine, NMP, DMF, DMAc and DMSO, respectively which suggested LPPDI was strongly aggregated, the most in DMAc. Referring to Figure (4.37), both red-shifted and blue shifted

absorption peaks were observed independently of increasing solvent polarity. The absorption spectra of unsymmetrical BPDI in nonpolar, polar protic and dipolar aprotic solvents are represented in Figure 4.25. Characteristically three absorption bands have been observed in UV spectra of the compound BPDI in nonpolar, polar protic and dipolar aprotic solvents. In DMF and MeOH, three bands at 523 nm, 490 nm and 458 nm, respectively appeared. Absorption is slightly red shifted (1-4) in NMP, EtOH (524 nm, 489 nm, 458 nm), acetic acid (525 nm, 489, 457 nm), chloroform and DMSO (527 nm, 491 nm, 459 nm). Referring to Table 5.4, $A^{0\rightarrow0}/A^{0\rightarrow1}$ values in the range of 1.30-1.51 showed that BPDI is not aggregated at all in any of the investigated solvents.

Emission spectra of LPMI, LPDI, LPPDI and BPDI taken at $\lambda_{exc} = 485$ nm are depicted in Figures 4.29, 4.32, 4.35-4.38 and 4.40. The fluorescence spectra of LPMI closely match the absorption spectra (mirror symmetrical) with small Stokes shifts; 14, 13 and 12 nm only in acetic acid, DMF and DMSO respectively (Table 5.4). The solvent independency of the Stokes shift indicates that there is no appreciable change between the dipole moments of ground and excited states. As expected, it was the dominance of rigidity and planarity giving rise to small shifts and greater absorption. In case of trifluoroacetic acid and sulfuric acid, emission spectra displayed excimer like emissions which were usually observed for π interacting molecules in solution, with higher Stokes shifts; 21 and 46 respectively, showing the presence of a relatively large amount of non-radiative energy lost. In addition, considering the shape and the broadening of emission spectrum LPMI (broader FWHM) in trifluoroacetic acid indicated aggregated emission besides the excimer emission in the excited state. It is mentioned that in J-aggregates, absorption is allowed to the

146

bottom area of the exciton band, absorption is red-shifted, and they show high intense fluorescence [60]. Since emission spectrum of LPMI is red-shifted in trifluoroacetic acid and it fluoresces intensely (Figure 5.1), it might show a tendency to J-type aggregation. In sulphuric acid, an excimer like emission was observed at 627 nm. In m-cresol, a heavily quenched fluorescence was observed which can be explained by an electron-transfer process from the m-cresol-donor to the perylene-acceptor chromophore due to formation of an intermolecular O-H…N hydrogen bonding interaction between m-cresol molecule and the NH_2 group of compound LPMI. Similarly emission spectra of LPDI closely match the absorption spectra (mirror symmetrical) with small Stokes shifts; 9, 12, 10, 10 and 12 nm in pyridine, NMP, DMF, DMAc and DMSO. Similar discussions mentioned above are valid here as well. Moreover, heavily quenched m-cresol fluorescence spectrum was also observed in LPDI due to same reasons. In sulphuric acid emission spectrum of LPDI, a broad red shifted peak is observed at 634 nm together with a shoulder like emission at 684 nm. Most probably the monomeric emission comes from trace of non-face-to-face stacked LPDI in solution and the excimer's emission has been overlapped with the monomeric PDI's emission [26].
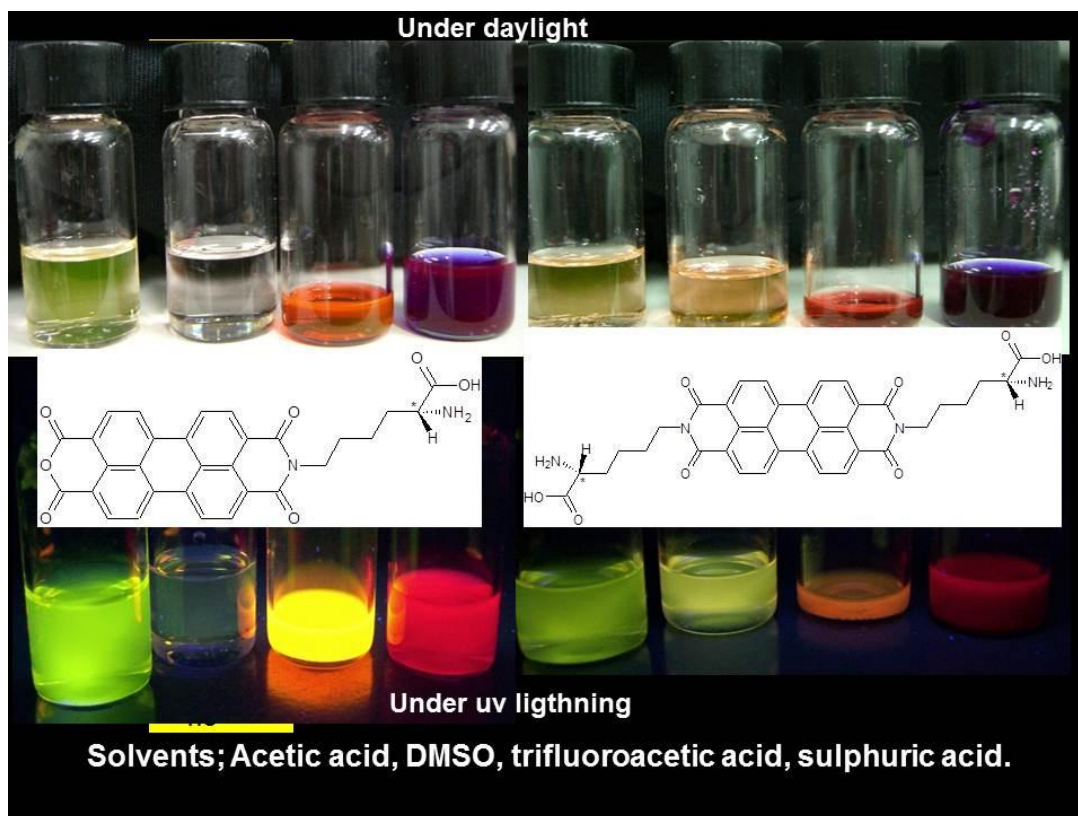
Figure 5.1: Picture of LPMI and LPDI in acetic acid, DMSO, trifuoroacetic acid and suphuric acid both in day light and UV lightning.

Referring the Picture 5.1, LPMI fluoresces intensely in hydrogen bonding ability solvents like acetic acid, trifluoroacetic acid and sulphuric acid when exposed to UV light. Where the corresponding chiral symmetrical LPDI exhibit fluorescence at low intensity under the same conditions which may be attributed to the higher degree of hydrogen bonding interaction between LPDI molecules that may cause quenching. In emission spectra of LPPDI in nonpolar solvents, there existed 3 characteristic mirror image emission bands (toluene: 535, 577, 628 nm; chloroform: 536, 577, 626; TCE: 542, 582, 630) corresponding to 0-0, 1-0 and 2-0 electronic transitions, respectively. A small Stoke shift in the range of 8-11 nm is observed. It is worth noting that any excimer or excimer-like peaks was not observed which proposed to similar intermolecular interaction of LPPDI in ground state and excited state. In polar protic

solvents, LPPDI behaved in a similar manner as LPDI exhibited in polar protic solvents. In the emission spectra of LPPDI in all dipolar protic solvents, blue-shifted and red-shifted peaks were observed not correlating with solvent polarity. A Stoke shift in the range 7-15 nm was observed emphasizing the similarity between ground S_0 and excites S_1. Fluorescence properties of LPPDI in NMP upon heating (from 10 ^oC to 80 ^oC) have been investigated as well. It can be inferred from Figure 4.33 that emission maxima are blue shifted (1-5 nm) and decreased in emission intensity with increasing temperature. This optical difference could be attributed to conformational transition of the conjugated backbone and to aggregation. Due to blue shifting, LPPMI showed a tendency to H type aggregates upon increasing temperature. It is noted that the existence of an isosbestic point over a certain range of temperature in the fluorescence spectra of a compound is accepted when it emits from the monomer as well as the excimer state. In other words, when there is an overlap between the monomer and excimer spectra, an isosbestic point is observed in the fluorescence spectra within a certain range of temperature [61]. In Figure 4.33 two isosbestic points supplying the conditions are observed at 533 and 611 nm.

The emission spectra of LPMI, LPDI, LPPDI and BPDI were taken at λ_{exc}=485 nm and the relative fluorescence quantum yields of LPMI and LPDI were determined in acetic acid, DMF, DMSO while of LPPDI in DMF and BPDI in DMSO with the standard solution of N,N′-didodecyl-3,4,9,10-perylenebis (dicarboximide) in chloroform. The fluorescence quantum yields of compounds were measured and presented in Table 4.1. There was a trend of decreasing quantum yield with increasing polarity for both compounds. Compounds LPMI has given higher quantum yields compared to compound LPDI except for DMF due to relatively

higher degree of aggregation (Table 5.5 for $A^{0\rightarrow 0}/A^{0\rightarrow 1}$). It is well known that generally perylene derivatives have high quantum yields, almost unity. In the present study, relatively low fluorescence quantum yields in the studied solvents could be attributed to the re-absorption of emitted photons and self-quenching due to intra and intermolecular hydrogen bonding interactions.

Absorption and emission properties of LPMI, LPDI and BPDI at pH 3.5, 4, 5, 6, 7, 8 and 14 have been studied where λ_{exc} = 485 (Figures 4.16, 4.19, 4.26, 4.30, 4.33 and 4.41). a pH range from 3.5 to 14 has been scanned for LPI and BDI. Since LPMI is not soluble at pH 14, its scanned pH range is 3.5-8. At pH 3.5, LPMI exhibited 3 characteristics peaks with increasing intensity at 519 nm, 484 and 454 nm, respectively. In the range of pH 4-6, absorption bands become broader and there is an intensity reversal between 0-0 and $0\rightarrow 1$ transitions and the $A^{0\rightarrow 0}/A^{0\rightarrow 1}$ is around 0.66 (Table 5.6) implying that compound LPMI is strongly aggregated. At pH 6 the beginning of charge transfer is observed. At pH 7 and 8, excellent charge transfer peaks at 501 nm and 499 nm appeared, respectively. The lowest energy absorption band of LPMI at pH 3.5 is blue-shifted by about 20 nm in comparison with that at pH 8. Hence, compound LPMI shows chromogenic behavior in different pH values by changing the color of aqueous solution from yellow-orange at pH 3.5 to pink at higher pHs, which can be detected with naked eye [62]. In the emission spectra of LPMI, two characteristic peaks were obtained at 533 nm and 572 nm for pH 3.5 and at 544 and 586 nm for pH 4 and 5. In the emission spectrum of pH 6, excimer (588 nm) has just started. At pH 7 and 8, there are excimer peaks appearing 592. In absorption spectrum of LPDI at pH 3, 3 characteristic bands at 525 nm, 490 nm and 458 nm were observed. In the pH range of 4-14, charge transfer complexes were

observed with red-shifted absorption maxima (32-27 nm) where they have a $A^{0\rightarrow0}/A^{0\rightarrow1}$ of ~ 0.8 impyling that the compound was aggregated. Interestingly, in emission spectrum of LPDI, two characteristic peaks were observed pH 3.5, 4, 5 and 6. At pH 7, 8, excimer like peaks at 586 nm and 550 nm and 586 and 543 nm, respectively. At pH 14, an excimer peak at 568 nm appeared. It can be concluded that, intermolecular interactions of LPDI are different in ground and excited state at pH 4, 5, and 6. In case of BPDI, all the solutions prepared at different pH media were percolated through a 0.2 μm filter and absorption and emission spectra before and after filtration were presented in Figures 4.26, 4.27, 4.41 and 4.42, respectively. Any remarkable difference was not observed in absorption spectra. 3 characteristics bands at pH 3.5 and pH 14 were observed at 525 nm, 489 nm, 412 nm and 489 nm, 470 nm and 412 nm, respectively. At pH 4, 5, 6, 7 and 8 charge transfer complexes appeared at around 550 nm. In emission spectra of filtered and non-filtered solutions, only difference was observed in the spectrum at pH 7 and 8. At pH 3.5 two characteristic emission bands were observed at 540 nm and 580 nm. Emission was heavily quenched in the rest of the spectra of pH media most probably due to photoinduced electron transfer.

Table 5.4: Absorption wavelengths $\lambda_{abs(0\to0)}$, Stokes Shift $\Delta\lambda$ (nm), absorption ratios $A^{0\to0}/A^{0\to1}$ of BPDI, LPMI and LPDI at different pH values

pH	λ_{max}			$\Delta\lambda$			$A^{0\to0}/A^{0\to1}$		
	LPMI	LPDI	BPDI	LPMI	LPDI	BPDI	LPMI	LPDI	BPDI
3.5	519	524	525	14	15	14	1.36	1.11	1.33
4	552	551	552	-8	-4	-	0.68	0.81	0.87
5	554	550	552	-9	-3	-	0.66	0.78	0.87
6	550	546	551	-4	0	-	0.67	0.85	0.82
7	502	548	551	9	0	39	1.05	0.78	0.82
8	499	550	549	92	-7	43	0.09	0.06	0.85
14	-	491	470	-	76	113	-	0.83	1.07

Absorption spectra of all compounds in solid state are shown in Figures 4.17, 4.20, 4.24 and 4.28. It is worth noting that the absorption spectra of the compounds LPMI and LPDI in solid state have different characteristics than those in solution. Two absorption peaks at 545 nm and 491 nm and three broad peaks at 552, 502 and 464 nm with $A^{0\to0}/A^{0\to1}$ values of 0.91 and 0.97 for LPMI and LPDI respectively. These values represent an intermediate case indicating both aggregated as well as monomeric molecules [28]. Interestingly, solid state absorption spectra of LPPDI and BPDI were very similar to those in solution in terms of spectral shape where three clearly resolved peaks at 470, 508 and 555 nm for LPPDI and at 477, 512 and 556 nm for BPDI. The three resolved bands have been attributed to weakly interacting π-stacks in solid state. In solid state, LPPDI and BPDI have $A^{0\to0}/A^{0\to1}$ values of 1.06 and 1.05, respectively which imply an intermediate case indicating both aggregated as well as monomeric molecules probably due to intermolecular π-π stacking and hydrogen bonding interactions. The attractive high fluorescence of perylene dyes in solution is strongly

quenched by π-stacking in solid state. Strong fluorescence in the solid state could be achieved successfully with the elimination of this self-quenching. In literature, the importance of preparation of solid state fluorescent materials was emphasized [63]. Solid state emission of all compound have been taken successfully. The four compounds; LPMI, LPDI, LPPDI and BPDI have shown excimer-like emission in red light (λ_{em}= 663, 661, 668 and 658 nm, respectively) which was very similar to the excimer-like emissions as usually observed for weakly interacting π-stacked perylene molecules in solution. The rather red shifted and excimer-like emissions in solid state indicate that the light emitting species are dominantly intermolecular in nature, originating from aggregates and excimers. Moreover, large Stoke shifts of 118, 109 103 and 102 nm were obtained for LPMI, LPDI, LPPDI and BPDI, respectively. It suggested excited state relaxation in the solid state to lower energy state where larger inter-perylene interaction took place [64].

Maximum absorption wavelengths λ_{max} (nm), extinction coefficients ε_{max} (1 mol^{-1} cm^1), oscillator strength f, fluorescence quantum yield Φ_f (λ_{exc} = 485 nm), radiative lifetimes τ_0 (ns), fluorescence lifetimes τ_f (ns), fluorescence rate constants k_f (10^8 s^{-1}), rate constants of radiationless deactivation k_d (10^8 s^{-1}), and optical activities $[\alpha]_D^{20}$ of LPMI and LPDI in DMF are given in Table 5.7. Moreover, experimental fluorescence lifetimes for BPDI and LPPDI have been observed as 3.0 ns and 2.8 ns, respectively while it was 2.9 ns for LPMI and 3.9 ns for LPDI Fluorescence lifetimes of the compounds were measured in argon-saturated solutions. The technique of time correlated single photon counting was used to record fluorescence lifetimes of the compounds. The decay curve was multi-exponential and analysed by using standard method of iterative reconcolution and

nonlinear least square fitting method (λ_{exc}= 530 nm, Figures 4.36 and 4.37). The quality of calculated fits was judged using statistical parameters, the reduced χ^2 value and the residual data. The experimental radiative lifetimes, fluorescence lifetimes, fluorescence rate constants, and rate constants of radiationless deactivation were in good agreement with literature data [47].

The specific optical rotation ($[\alpha]_D^{20}$, alpha) values of LPMI, LPDI and LPPDI were measured at 20 ^{o}C (LPMI: c = 0.0188 mg mL^{-1} in H$_2$SO$_4$; LPDI: c = 0.0188 mg mL^{-1} in H$_2$SO$_4$; LPPDI: c = 0.02 mg mL^{-1} in DMF) as +1191.5, +201.7 and -1647.5, respectively. The higher optical activities of LPMI and LPPDI compared to LPDI and N,N'bis-((S)-(─)-1-phenylethyl)-3,4,9,10-perylenebis(dicarboximide) [59] could be attributed to asymmetric molecule. The n-π^* transitions due to hydrogen bonding interactions are electrically forbidden but magnetically permitted therefore in the asymmetric molecule such a transition can have very low absorption of light but high optical activity. Figures 4.38-4.40 show the CD spectra of LPMI, LPDI and LPPDI in trifluoroacetic acids, respectively. Figure 4.36 exhibited a weak positive CD band at 491 nm and a weak negative weak band at 541 nm. No detectable bands could be observed for LPDI (Figure 4.39) probably due to aggregates in solution at room temperature. Figure 4.40 showed a weak positive CD band at 371 nm however the remaining bands at 480 nm, 530 and 565 nm were very pallid probably due to weak intermolecular aggregation and self-assembly. Furthermore, the exciton coupling taking place between perylene and the phenyl π-π^* transitions had given rise to very pallid signals in the region of 400-500 nm probably due to the large energy difference between the two transitions and/or the unfavourable arrangement between the two transition diploes which are almost coplanar [65].

5.3 Thermal Stability

The thermal behaviors of all compounds were investigated by DSC (heating rate 10 K min^{-1}, Figures 4.41-4.44) and TGA (heating 5 K min^{-1}, Figures 4.45-4.47). None of compounds exhibited any glass transition temperatures in the DSC run. The curves showed high starting decomposition temperatures (T_d) for all of the compounds. BPDI, LPMI, LPDI and LPPDI were stable up to 361 ^{o}C, 387 ^{o}C, 356 ^{o}C and 415 ^{o}C, respectively. For compound BPDI, a rapid weight loss of 19 % took place between 361 ^{o}C and 394 ^{o}C. When BPDI was heated to 900 ^{o}C, 90 % of the initial weight was lost and 10 % char yield was left behind. In case of LPMI, a rapid weight loss of 19 % initial weight occurred between 387 ^{o}C and 443 ^{o}C. When LPMI was heated to 620 ^{o}C, 86 % of the initial weight was lost rapidly and 14 % char yield was observed. For compound LPDI, a rapid weight loss of 15 % of initial weight occurred between 356 ^{o}C and 457 ^{o}C. When LPDI was heated to 900 ^{o}C, 87 % of the initial weight was lost rapidly and 13 % char yield was observed. For LPPDI, a rapid weight loss of 15.3 % initial weight occurred between 315 ^{o}C and 425 ^{o}C. When LPPDI was heated to 640 ^{o}C, 99.3 % of the initial weight was lost rapidly and 0.7 % char yield was observed. While LPPDI showed the highest initial decomposition temperature such as 415 ^{o}C, at elevated temperature, LPDI showed best thermal stability compared to its corresponding chiral monoimide and chiral unsymmetrical diimide most probably due to intermolecular forces and symmetry of the structure.

155

5.4 Electrochemistry

The electrochemical characterization of LPMI and LPDI have been investigated in detail using cyclic and square wave voltammetries in DMF containing 0.05 NaBF$_4$ as a supporting electrolyte. Solid state cyclic and square wave voltammetries have been applied for LPMI, LPDI, LPPDI and BPDI where the supporting electrolyte was 1 M HCl. All of the results have been summarized and presented in Tables 4.3-4.13. All of the measured redox potentials, HOMO (highest occupied molecular orbital)/LUMO (Lowest unoccupied molecular orbital) and band gap energy E$_g$ values calculated from those data have been tabulated in Tables 4.3, 4.4 and 4. 7. LPMI undergoes three reversible one-electron reductions, the first of which is the reduction of the neutral compound to radical anion (LPMI$^-$), the second reduction could be attributed to the formation of dianion (LPMI^{2-}) and the third reduction correspond to the formation of trianion (LPMI^{3-}). Whereas LPDI undergoes two reversible one-electron reductions, first of which is the reduction to radical anion (LPDI$^-$) and the second reduction refers to formation of dianion (LPDI^2). Referring to Figure 4.57, cyclic voltammogram of LPMI has shown three reversible one-electron reductions at -0.112 V, -0.270 V and -0.401 V (vs. Ag/AgCl, scan rate: 100 mV s^{-1}) with peak potential separation ΔE$_g$ values of 108 mV, 55 mV and 80 mV, respectively in DMF (Table 4.3). Two reversible one-electron reductions at -0.514 V, and -0.752 V (vs. Ag/AgCl, scan rate: 100 mV s^{-1}) with ΔE$_g$ values of 72 mV and 52 mV, respectively in cyclic voltammogram of LPDI in DMF (Figure 4.60, Table 4.3). Notable E$_{1/2}$ shifting towards high negative potentials in the corresponding chiral symmetrical diimide (LPDI) indicate a more difficult reduction most probably due to the intermolecular forces, rigidity and symmetry of the structure. In square

156

wave voltammogram of LPMI in DMF, three reversible reduction potentials were obtained at -0.167 V, -0.270 V and -0.409 V (vs. Ag/AgCl, frequency: 50 Hz). Two reduction potentials at -0.533 V and -0.751 V (vs. Ag/AgCl, frequency: 50 Hz) were observed for square wave voltammogram of LPDI in DMF. As a result, similarity of cyclic and square wave results for each compound showed that they are in good agreement in DMF.

In order to calculate the absolute energies of LUMO level of LPMI and LPDI with respect to vacuum level, the redox data have been standardized to the ferrocene/ferricenium couple which is an absolute value of − 4.8 eV. While the LUMO energies of LPMI and LPDI in DMF were calculated from cyclic voltammograms, as -3.988 eV and -3.586 eV, respectively, the optical band gap E_g values were estimated as 2.385 eV for LPMI and 2.250 eV for LPDI where E_g was achieved from the edge of the electronic absorption band with $E_g = hc/\lambda$ (h = 6.626 x 10^{-34} js, c = 3 x 10^{10} cm s^{-1}, 1 ev = 1.602 x 10^{-19} j). Accordingly, HOMO energies of LPMI and LPDI were obtained as -6.373 eV and -5.836 e V, respectively.

In order to investigate the solid state electrochemical properties of LPMI, LPDI, LPPDI and BPDI, the voltammetry of immobilized microparticles was applied. This technique is a simple and powerful tool for the characterization of the thermodynamics and elucidation of the redox mechanisms of electroactive species which have poor solubility in water [66-72]. The basic principle of the voltammetry of immobilized microparticles consists of mechanical attachment of the substance on the surface of the working electrode (paraffin impregnated graphite electrode, i.e., PIGE), and immersion of the modified electrode in an aqueous electrolyte solution. If

the substance is electroactive, and if its product is insoluble in water, for reasons of neutrality, ions must be exchanged with the solution. In case of a reduction, either anions, if available, must leave the solid, or cations must be transferred from the solution into the solid phase. The processes of coupled electron and ion transfer occur simultaneously and give rise to a single voltammetric response. All of the voltammetric measurements have been repeated several times and values of the reduction potentials have been found to be reproducible within ± 3 mV.

The solid state cyclic voltammograms of 4 compounds exhibited one reversible reduction waves, implying the formation of anions (LPMI⁻, LPDI⁻, LPPDI⁻ and BPDI⁻) at -0.288 V, -0.282 V, -0.324 V and -0.327 V (vs. Ag/AgCl, scan rate 100 mV $^{-1}$) with peak potential separation, ΔE_p values of 169 mV, 126 mV, 215 mV and 104 mV for LPMI, LPDI, LPPDI and BPDI respectively. Similarly, reversible reduction potentials have been observed in square wave voltammograms of LPMI, LPDI, LPPDI and BPDI at -0.294 V, -0.288 V, -0.345 V and -0.336 V (vs. Ag/AgCl, frequency: 50 Hz for all), respectively showing that cyclic and square wave voltammetric results were in good agreement in solid state.

The LUMO energies of LPMI, LPDI, LPPDI and BPDI in solid state and the former two in DMF have been calculated from cyclic voltammograms as -4.242 eV, -4.248 eV, -4.206 eV, -3.988 eV and -3.586 eV, respectively. The optical band gap, E_g values were estimated as 2.385 eV for LPMI and 2.250 eV for LPDI in DMF and 1.890 eV, 1.737 eV, 1.696 eV and 1.896 eV for LPMI, LPDI, LPPDI and BPDI, respectively in solid state. Accordingly, HOMO energies of LPMI, LPDI, LPPDI and BPDI in solid state were calculated as -6.133 eV, -5.985 eV, -5.903 eV and -6.099 eV, respectively where -6.373 eV for LPMI and -5.836 eV for LPDI in DMF were

obtained (Scheme 5.1). The remarkably smaller LUMO and E_g values were observed at the solid state characterization of LPMI and LPDI when compared with those obtained in solution state.
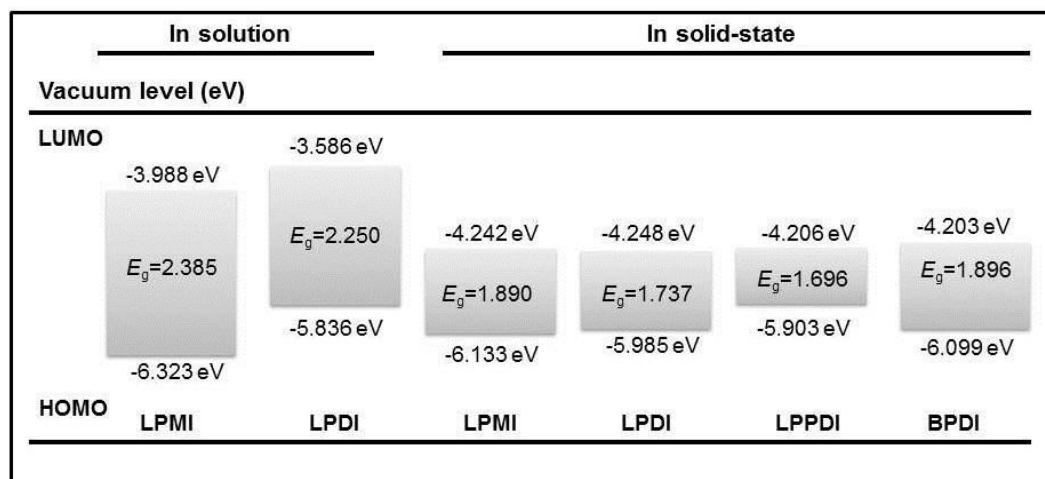
Scheme 5.1: Schematic energy diagram of LPMI, LPDI, LPPDI and BPDI.

Chapter 6

CONCLUSION

In the current study, a novel chiral perylene monoimide (LPMI), its corresponding symmetrical (LPDI) and unsymmetrically subsituted chiral diimides (LPPDI) and another unsymmetrically substituted perylene diimide (BPDI) for have been synthesized successfully. Their characterization has been carried out in detail and their chiral, amphiphilic, photophysical, thermal and electrochemical properties have been investigated extensively as well. The synthesized compounds exhibited partial solubility in a variety of common organic solvents due to intermolecular hydrogen bonding interaction occurred related with the substituents. In UV spectra of LPDI and LPPDI showed new bands positioning at around 378 nm in trifluoroacetic acid, 374 in m-cresol and 402 nm in sulphuric acid, most probably due to the electronic S_0-S_2 transition with a dipole moment perpendicular to the long axis of the molecule. Heavily quenched fluorescence spectra in m-cresol were obtained for LPMI, LPDI and LPPDI. In the emission spectra of LPPDI in NMP, two isosbestic points at 533 and 611 nm were observed between the temperature interval 10 ^{o}C-80 ^{o}C confirming the existence of overlapped monomer and excimer emissions. In solid state, the four compounds; LPMI, LPDI, LPPDI and BPDI have shown excimer-like emission in red light (λ_{em}= 663, 661, 668 and 658 nm, respectively) which was very similar to the excimer-like emissions as usually observed for weakly interacting π-stacked perylene

molecules in solution. The rather red shifted and excimer-like emissions in solid state indicate that the light emitting species are dominantly intermolecular in nature, originating from aggregates and excimers. Moreover, large Stoke shifts of 118, 109 103 and 102 nm were obtained for LPMI, LPDI, LPPDI and BPDI, respectively. It suggested excited state relaxation in the solid state to lower energy state where larger inter-perylene interaction took place. Huge optical activities were determined as +1191.5 for LPMI and -1647.5 for LPDI which is attributed to asymmetric molecule. CD bands obtained were weak probably due to weak intermolecular aggregation and self-assembly. LPMI, LPDI, LPPDI and BPDI showed high thermal stabilities; (T_d; 361 ^{o}C, 387 ^{o}C, 356 ^{o}C and 415 ^{o}C, respectively). The electrochemical properties of four compounds were investigated from dilute solution to solid state. Cyclic voltammogram of LPMI in DMF has shown three reversible one-electron reductions at -0.112 V, -0.270 V and -0.401 V (vs. Ag/AgCl, scan rate: 100 mV s^{-1}) while two reversible one-electron reductions at -0.514 V, and -0.752 V (vs. Ag/AgCl, scan rate: 100 mV s^{-1}) were observed in cyclic voltammogram of LPDI. Remarkable $E_{1/2}$ shifting towards high negative potentials in the corresponding chiral symmetrical diimide (LPDI) indicates a more difficult reduction most probably due to the intermolecular forces, rigidity and symmetry of the structure. Similar square wave results for each compound were obtained showing that they are in good agreement in DMF. The solid state cyclic voltammograms of 4 compounds exhibited one one-electron reduction waves, implying the formation of anion. Cyclic and square wave voltammetric results were also in good agreement in solid state.

The novel chiral perylene dyes have great potentials for chirooptical switches, solid state lighting technology, dye sensitized solar cell and photomedicine.

REFERENCES

1. 'A vision for photovoltaic technology for 2030 and beyond' preliminary report by the photovoltaic technology research advisory council (PV-TRAC), 2005.

2. Bernede, J. C., Organic Photovoltaic Cells: History, Principle and Techniques. *J. Chil. Chem. Soc.,* 53 (2008) 1549-1564.

3. Bonaccorso, F., Debundling and Selective Enrichment of SWNTS for Applications in Dye-sensitized Solar Cells. *International Journal of Photoenergy,* 2010 (2010) 1-14.

4. Wang, X., Liu, D., and Li, J., Organic photovoltaic materials and thin-film solar cells. *Front. Chem. China*, 5 (2010) 45–60.

5. Meng, S and Kaxiras E., Electron and Hole Dynamics in Dye-Sensitized Solar Cells: Influencing Factors and Systematic Trends. *Nano Lett*, 10 (2010) 1238-1247.

6. Calandra, P., Calogero, G., Sinopoli, A., and Gucciardi, P., G., Metal Nanoparticles and Carbon-Based Nanostructures as Advanced Materials for Cathode Application in Dye-Sensitized Solar Cells. *International Journal of Photoenergy,* 2010 (2010) 1-15.

7. Gratzel, M., Dye-sensitized solar cells. *Journal of Photochemistry and Photobiology C: Photochemistry Reviews* 4 (2003) 145–153.

8. Calogero, G. and Marco, G., D, Red Sicilian orange and purple eggplant fruits as natural sensitizers for dye-sensitized solar cells. *Solar Energy Materials & Solar Cells* 92 (2008) 1341-1346.

9. Kong, F. T., Dai, S.Y., Wang, K. J., Review of Recent Progress in Dye-Sensitized Solar Cells. *Advances in OptoElectronics,* 2007 (2007)1-13.

10. Campbell, W. M., Burrell, A, K., Officer, D. L., and Jolley, K. W., Porphyrins as light harvesters in the dye-sensitized TiO_2 solar cell. *Coordination Chemistry Reviews* 248 (2004), 1363-1379.

11. Wang, S., Li, Y., Du, C., Shi, Z., Xiao, S., Zhu, D., Gao, E., and Cai, S., Dye sensitization of nanocrystalline TiO_2 by perylene derivatives. *Synthetic Metals* 128 (2002) 299-304.

12. Lee, D. H., Lee, M. J., Song H. M., Song, B. J., Seo, K. D., Pastore, M., Anselmi, C., Fantacci, S., F. D., Nazeeruddin, M. K., Graetzel, M. and Kim, H. K., Organic dyes incorporating low-band-gap chromophores based on π-extended benzothiadiazole for dye-sensitized solar cells. *Dyes and Pigments* 91 (2011) 192-198.

13. Klaus Petrisch, PhD thesis "Organic Solar Cell Architecture", July 2000.

14. Xue, C., Chen, M. and Jin, S., Synthesis and characterization of the first soluble nonracemic chiral main-chain perylene tetracarboxylic diimide polymers. *Dyes and Pigments 49* (2008) 5314-5321.

15. Tiwari, G. N. and Dubey, S. (2010) Fundamentals of Photovoltaic Modules and Their Applications, RSC publishing.

16. Kalyanasundaram, K. and Gratzel M., Applications of functionalized transition metal complexes in photonic and optoelectronic devices. *Coordination Chemistry Reviews* 177 (1998) 347-414.

17. Zhao, Y., Zhai, J., He, J., Chen, X., Chen, X., Chen, L., Zhang, L., Tian, Y., Jiang, L., and Zhu, D., High-Performance All-Solid-State Dye-Sensitized Solar Cells Utilizing Imidazolium-Type Ionic Crystal as Charge Transfer Layer. *Chem Mater* 20 (2008) 6022-6028.

18. Midya, A., Xie, Z., Yang, J. X., Chen, Z. K., Blackwood, D. J., Wang, J., Adams, S. and Loh, K. P., A new class of solid state ionic conductors for application in all solid state dye sensitized solar cells. *Chem. Commun*., 46 (2010) 2091-2093.

19. Yong, Z. Wei, C., Jin, Z., Xianling, S., Qingguo, S., Tianxin, W., Fenglian, B., Lei, J., Daoben, Z., Solid-state dye-sensitized photovoltaic device with newly designed small organic molecule as hole-conductor. *Chemical Physics Letters* 445 (2007) 259-264.

20. Bach, U., Lupo, D., Comte, P., Moser, J. E., Weissörtel, F., Salbeck, J., Spreitzer, H. and Gratzel, M., Solid-state dye-sensitized mesoporous TiO$_2$ solar cells with high photon-to-electron conversion efficiencies. *Nature* 395 (1998) 583-585.

21. Mende, L. S. and Gratzel M., TiO$_2$ pore-filling and its effect on the efficiency of solid-state dye-sensitized solar cells. *Thin Solid Films* 500 (2006) 296-301.

22. Fraas, L. and Partain, L. 2010, Solar Cells and Their Applications, Wiley

23. Diebold U., The surface science of titanium dioxide. *Surface Science Reports* 48 (2003) 53-229.

24. Nunzi, J. M., Organic photovoltaic materials and devices. *C. R. Physique* 3 (2002) 523-542.

25. Li, C., Schoneboom, J., Liu, Z., Pschirer, N. G., Erk, P., Herrmann, A. and Mullen, K., Rainbow Perylene Monoimides: Easy Control of Optical Properties. *Chem. Eur. J.* 15 (2009) 878 – 884.

26. Chen, Y.; Kong, Y.; Wang, Y.; Ma, P.; Bao, M.; Li, X. Supramolecular self-assembly study of a flexible peryleneteracarboxylic diimide dimer in *Langmuir and Langmuir-Blodgett films. Journal of Colloid and Interface Science* 330 (2009) 421-427.

27. Wrobel, D. and Graja, A. Photoinduced electron transfer in fullerene-organic chromophore systems. *Coordination Chemisty Reviews*, 2011, in press.

28. Schmidt, C. D.; Bottcher, C.; Hirsch, A. Chiral water-soluble perylenediimides. *European Journal of Organic Chemistry 2009* (2009) 5337-5349.

29. Xue, L.; Wang, Y.; Chen, Y.; Li X. Aggregation of wedge-shaped perylenetetracarboxylic diimide with a different number of hydrophobic long alkyl chains. *Journal of Colloid and Interface Science* 350 (2010) 523-529.

30. Langhals, H. and Jona, W. The Synthesis of Perylenebisimide Monocarboxylic Acids. *Eur. J. Org. Chem.* 29 (1998) 847-851.

31. Zhang, Y., Xu, Z., Cai, L., Lai, G., Qiu, H. and Shen, Y. Highly soluble perylene tetracarboxylic diimides and tetrathiafulvalene–perylene tetracarboxylic diimide–tetrathiafulvalene triads. *Journal of Photochemistry and Photobiology A: Chemistry* 200 (2008) 334-345.

32. Fan, L., and Xu, Y. and Tian, H. 1,6-Disubstituted perylene bisimides: concise synthesis and characterization as near-infrared fluorescent dyes. *Tetrahedron Letters* 46 (2005) 4443-4447.

33. Ilhan, F., Tyson, D., S., Stasko, D., J., Kirschbaum, K. and Meador, M., A. Twisted, Z-Shaped Perylene Bisimide. J. AM. CHEM. SOC. 128 (2006) 702-703.

34. Yang, X. G., Yuan, H., Yuan, H., Zhao, Q. L., Yang, Q. and Chen, X. H. Self-assembly constructed by perylene bisimide derivatives bearing complementary hydrogen-bonding moieties. *J. Cent. South Univ. Technol.* 16 (2009) 206-211.

35. Jancy, B., and Asha, S. K. Hydrogen-Bonding-Induced Conformational Change from J to H Aggregate in Novel Highly Fluorescent Liquid-Crystalline Perylenebisimides. *Chem. Mater.* 20 (2008) 169-181.

36. http://www.dstuns.iitm.ac.in/teaching.../H-%20and%20J-%20Aggregates.pdf, 2011.

37. Ghosh, S., Li, X. Q., Stepanenko, V. and Wurthner, F. Control of H- and J-type pi stacking by peripheral alkyl chains and self-sorting phenomena in perylene bisimide homo- and heteroaggregates. *Chem Euro J* 14 (2008) 11343-11357.

38. Jancy, B.; Asha, S. K. Hydrogen-bonding-induced conformational change from J to H aggregate in novel highly fluorescent liquid-crystalline perylenediimides. *Chemistry of Materials* 20 (2008) 20, 169-181.

39. Steiner, T. The Hydrogen Bond in the Solid State. *Angew. Chem. Int. Ed.* 41 (2002) 48-76.

40. Wurthner, F., Hanke, B., Lysetska, M., Lambright, G. and Harms, G. S. Gelation of a highly fluorescent urea-functionalized perylene bisimide dye. *Organic Letters* 7 (2005) 967-970.

41. Yang, X.; Xiaohe, X.; Ji, H. F. Solvent effect on the self-assembled structure of an amphiphile perylene diimide derivative. *Journal of Physical Chemistry B* 112 (2008) 7196-7202.

42. Xu, S.; Sun, J.; Song, G.; Zhang, W.; Zhan, C. An expected solvent effect on the self-assembly of a 1,7-bis-pyridinoyl perylene diimide amphiphile. *Journal of Colloid and Interface Science* 349 (2010) 142-147.

43. Sun, R.; Xue, C.; Owak, M.; Peetz, R. M.; Jin, S. Facile synthesis of chiral unsymmetric perylene tetracarboxylic diimides involving α-amino acids. *Tetrahedron Letters* 48 (2007) 6696-6699.

44. Huang, Y.; Hu, J.; Kuang, W.; Wei, Z.; Faul, C. F. J. Modulating helicity through amphiphilicity-tuning supramolecular interactions for the controlled assembly of perylenes. *Chemical Communications* 47 (2011) 5554-5556.

45. Aigner, D., Borisov, S. M. and Klimant, I. New fluorescent perylene bisimide indicators—a platform for broadband pH optodes. *Anal Bioanal Chem* 400 (2011) 2475–2485.

46. Rybtchinski, B., Sinks, L. E. and Wasielewski, M. R. Photoinduced Electron Transfer in Self-Assembled Dimers of 3-Fold Symmetric Donor−Acceptor Molecules Based on Perylene-3,4:9,10-bis(dicarboximide). *J. Phys. Chem. A*, 108 (2004) 7497-7505.

47. Pasaogullari, Nur., Icil, H. and Demuth, M. Symmetrical and unsymmetrical perylene diimides: Their synthesis, photophysical and electrochemical properties. *Dyes and Pigments*, 69 (2006) 118-127.

48. Troster, H. Untersuchungen zur Protonierung von Perylen-3,4,9,10-tetracarbonsäurealkalisalzen. *Dyes and Pigment* 4 (1983) 171-177.

49. Rempel, S. P. N. Quantum yield calculations for strongly absorbing chromophores. *J Fluorescence* 16 (2006) 483-485.

50. http://www.nanotechnologies.com, 2011.

51. Williams, A. T. R., Winfield, S. A. and Miller, J. N. Relative fluorescence quantum yields using a computer-controlled luminescence spectrometer *Analyst* 108 (1983) 1067-1071.

52. Turro, N. J. (1965) Molecular Photochemistry, W. A. Benjamin, Inc, New York.

53. http://www.cryst.bbk.ac.uk, 2011.

54. Bard A. J., Faulkner L. R. (1980) Electrochemical Methods, Fundamentals and Applications, Wiley & Sons Inc, New York.

55. Bredas J. L., Silbey R., Boudreaux D. S., Chance R. R. Chain-length dependence of electronic and electrochemical properties of conjugated systems: Polyacetylene, Polyphenylene, Polythiophene, and Polypyrrole. *Journal of American Chemical Society*, 105 (1983) 6555-6559.

56. Peng Z., Bao Z., Galvin M. E. Polymers with bipolar carrier transport abilities for light emitting diodes. *Chemistry of Materials*, 10 (1998) 2086-2090.

57. Huang, H., Che, Y.and Zang, L. Direct synthesis of highly pure perylene tetracarboxylic monoimide. *Tetrahedron Letters*, 51 (2010) 6651-6653.

58. Asir, S., Demir, S. A. and Icil, H. The synthesis of novel, unsymmetrically substituted, chiral naphthalene and perylene diimides: Photophysical, electrochemical, chiroptical and intramolecular charge transfer properties. *Dyes and Pigments,* 84 (2010) 1-13.

59. Amiralaei, S.; Uzun, D.; Icil, H. Chiral substituent containing perylene monoanhydride monoimide and its highly soluble symmetrical diimide: synthesis, photophysics and electrochemistry from dilute solution to solid state. *Photochemical & Photobiological Sciences* 7 (2008) 936-947.

60. Johansson, M. K. and Cook, R. M. Intramolecular Dimers: A New Design Strategy for Fluorescence-Quenched Probes. *Chem. Eur. J.* 9 (2003) 3466 3471.

61. Hamilton, T. D. S.; Naqvi, K. R. Isosbestic points in emission spectra. *Chemical Physics Letters* 2 (1968) 374-378.

62. Qina, W., Baruaha, M., Borggraevea W. M. D. and Boens, N., Photophysical properties of an on/off fluorescent pH indicator excitable with visible light based on a borondipyrromethene-linked phenol. *Journal of Photochemistry and Photobiology A: Chemistry* 183(2006)190-197.

63. Chen, Z., Baumeister, U., Tschierske, C. and Wurthner F. Effect of Core Twisting on Self-Assembly and Optical Properties of Perylene Bisimide Dyes in Solution and Columnar Liquid Crystalline Phases. *Chem. Eur. J.* 13 (2007) 450-465.

64. Tsumatori, H.; Nakashima, T.; Yuasa, J.; Kawai, T. Enhanced circularly polarized emission of chiral dimer of π-conjugated perylene in opaque film. *Synthetic Metals* 158 (2009) 952–954.

65. Pucci, A.; Donati, F.; Nazzi, S.; Barretta, G. U.; Pescitelli, G.; Bari, L.D.; Ruggeri, G. Association phenomena of a chiral perylene derivative in solution and in poly(ethylene) dispersion. *Reactive & Functional Polymers* 70 (2010) 951-960.

66. Kahlert H., Retter U., Lohse H., Siegler K., Scholz F. On the determination of the diffusion coefficients of electrons and potassium ions in copper (II) hexacyanoferrate (II) composite electrodes. *Journal of Physical Chemistry B* 102 (1998) 8757-8765.

67. Lovric M., Scholz F. A model for the coupled transport of ions and electrons in redox conductive microcrystals**.** *Journal of Solid State Electrochemistry* 3 (1999) 172-175.

68. Lovric M., Hermes M., Scholz F. Solid state electrochemical reactions in systems with miscibility gaps. *Journal of Solid State Electrochemistry* 4 (2000) 394-401.

69. Schroder U., Scholz F., The Solid state electrochemistry of metal octacyanomolybdates, octacyanotungstates, and hexacyanoferrates Explained on the basis of dissolution and reprecipitation reactions, their lattice structures and crystallinities. *Inorganic Chemistry* 39 (2000) 1006-1015.

70. Hermes M., Lovric M., Hartl M., Retter U., Scholz F. On the electrochemically driven formation of bilayered systems of solid Prussian-blue-type metal hexacyanoferrates: A model for Prussian blue ï cadmium hexacyanoferrate supported by finite difference simulations. *Journal of Electroanalytical Chemistry* 501 (2001) 193-204.

71. Widmann A., Kahlert H., Petrovic-Prelevic I., Wulff H., Yakhmi J. V., Bagkar N., Scholz F. The structure, insertion electrochemistry and magnetic properties of a new type of substitutional solid solutions of copper, nickel and iron hexacyano-ferrates/hexacyanocobaltates. *Inorganic Chemistry* 41 (2002) 5706-5715.

72. Grygar T., Marken F., Schroder U., Scholz F. The electrochemical analysis of solids. *Collection of Czechoslovak Chemical Communications* 67 (2002) 163-208.

Home Adress: Haci Ali Sitesi I,
D Block, No. 12, Famagusta,
TRNC.
Phone: +90 392 630 21 36
Fax: +90 392 365 16 04
E-mail: hurmus.refiker@emu.edu.tr

Personal Information

Name& Surname: Hürmüs Refiker

Marital status: Single

Nationality: Turkish Cypriot

Date of Birth: 24/04/1980

Place of Birth: Nicosia, Cyprus.

Education

1991 – 1994   Bayraktar Türk Maarif Koleji, Nicosia, Cyprus.

1994 – 1997   Türk Maarif Koleji, Nicosia, Cyprus.
                    (9 GCE O-levels, 4 with Grade A and 5 with Grade B)

1997 – 2002 Feb. BS in Chemistry Education, Chemistry Education Department,
                    Middle East Technical University, Ankara, Turkey.

2002 – 2005   MSc in Analytical Chemistry, Chemistry Department, Middle East
                    Technical University, Ankara, Turkey.

2005 – 2011   PhD in Organic Chemistry-Photochemistry, Chemistry Department,
                    Eastern   Mediterranean University, Famagusta, North Cyprus.

Work Experience

- Practice teaching for three months at Atatürk Anadolu Lisesi, Ankara
  (February 2000).

- One-month summer practice as a volunteer in Devlet Laboratuvarı, in Food
  Analysis Section (June 2000).

- Research Assistant, Chemistry Department, Eastern Mediterranean
  University (2005-2011).

Teaching experience

Attended to Chem 101/General Chemistry (for engineering students) lab and tutorial sessions
(2005-2011).

Skills:

- **Language,** Turkish (native), English (fluent), German (intermediate).

- **Computer**, Microsoft applications.

- **Technical and specialized skills,** experienced in the use of the following instruments:
  High Performance Liquid Chromatography (HPLC)
  Gas Chromatography (GC)
  Flame Atomic Absorption Spectrometer (FAAS)
  UV-VIS
  Fluorescence Spectrometer
  IR

- **Research Interest,** Solid-phase extraction, preconcentration, trace analysis, photoorganic chemistry, synthesis of functional dyes to be used as sensitizers in dye-sensitized solar cells (DSSC), synthesis of chiral dyes to be used in DNA-binding for biological applications.

List of publications

MSc Thesis

Hürmüs Refiker, "Preconcentration of Some Precious Metals Using DEBT Impregnated Resin", *Middle East Technical University*, Ankara, Turkey, August 2005.

1. **Three modified activated carbons by different ligands for the solid phase extraction of copper and lead.**

   M. Ghaedi, F. Ahmadi, Z. Tavakoli, M. Montazerozohori, A. Khanmohammadi and M. Soylak.

   Journal of Hazardous Materials, 152, 3 (2008) 1248-1255.

2. A multi-element solid-phase extraction method for trace metals determination in environmental samples on Amberlite XAD-2000.

Volkan Numan Bulut, Ali Gundogdu, Celal Duran, Hasan Basri Senturk, Mustafa Soylak, Latif Elci and Mehmet Tufekci.

Journal of Hazardous Materials, 146, 1-2 (2007) 155-163.

(SCI, SCI-expanded Journals)

2- Hürmüs Refiker, M. Merdivan, R. S. Aygün, "Solid-phase Extraction of Silver in Geological Samples and Its Determination by FAAS", *Separation Science and Technology*, 43 (2008) 179-191.

Cited by:

1-   **1- Determination of Available Cadmium and Lead in Soil by Flame Atomic Absorption Spectrometry after Cloud Point Extraction**
Huayun Han a, Yayun Xu a & Cong Zhang.
Communications in Soil Science and Plant Analysis 42 (2011) **14** 1739-1751.

2- A novel method for the determination of trace copper in cereals by dispersive liquid–liquid microextraction based on solidification offloating organic drop coupled with flame atomic absorption spectrometry
Chun XiaWu,QiuHuaWu,ChunWang,ZhiWang.
Chinese Chemical Letters 22 (2011) **4** 473-476.

3- Carbon Nanotubes-Loaded Silica Gel for Preconcentration of Trace Silver with   Detection by Flame Atomic Absorption Spectrometry
YU Hong-Mei, SUN Wei, CHEN Ming-Li, TIAN Yong, WANG Jian-Hua,
Chinese Journal of Analytical Chemistry, 38 (2010) **12** 1721–1726.

4- Determination of Trace Silver in Water Samples by On-line Solid Phase Oxide Collection-Flame Atomic Adsorption Spectrometry

Yu HM, Zhu XH, Chen ML, et al.

Chemical Journal of Chinese Univeristies-Chinese 31(2010) **10** 1949-1954

5- Protein-based electrochemical biosensor for detection of silver (I) ions

Krizkova S, Huska D, Beklova M, et al.

Environmental Toxicology and Chemistry 29 (2010) **3** 492-496

6- Multi-element coprecipitation for separation and enrichment of heavy metal

ions for their flame atomic absorption spectrometric determinations

Mustafa Tuzen, Mustafa Soylak,

Journal of Hazardous Materials 162 (2009) 724–729.

7- A preconcentration system for determination of copper and nickel in water and food samples employing flame atomic absorption spectrometry.

Mustafa Tuzen, Mustafa Soylak, Demirhan Citak, Hadla S. Ferreira, Maria G.A. Korn, Marcos A. Bezerra,

Journal of Hazardous Materials 162 (2009) 1041–1045.

8- Simultaneous preconcentration of Co(II), Ni(II), Cu(II), and Cd(II) from

environmental samples on Amberlite XAD-2000 column and determination by FAAS

Celal Duran,, Hasan Basri Senturk, Latif Elci , Mustafa Soylak, Mehmet Tufekci,

Journal of Hazardous Materials 162 (2009) 292–299.

9- Atomic spectrometry update. Environmental analysis

Owen T. Butler, Jennifer M. Cook, Christine M. Davidson, Chris F. Harrington, Douglas L. Miles,

Journal of Analytical Atomic Spectrometry 24 (2009)131-177.

10- **Carrier element-free coprecipitation with 3-phenly-4-o-hydroxybenzylidenamino-4,5-dihydro-1,2,4-triazole-5-one for separation/preconcentration of Cr(III), Fe(III), Pb(II) and Zn(II) from aqueous solutions.**

Celal Duran, Volkan N. Bulut, Ali Gundogdu, Duygu Ozdes, Nuri Yildirim, Mustafa Soylak, H. Basri Senturk, Latif Elci,

Journal of Hazardous Materials, 167 (2009) 294-299.

11- **Multi-element coprecipitation for separation and enrichment of heavy metal ions for their flame atomic absorption spectrometric determinations.**

Mustafa Tuzen, Mustafa Soylak,

Journal of Hazardous Materials, 162 (2009) 724-729.

12- **Cloud point extraction and flame atomic absorption spectrometry combination for copper (II) ion in environmental and biological samples.**

Ardeshir Shokrollahi, Mehrorang Ghaedi, Omid Hossaini, Narges Khanjari, Mustafa Soylak,

Journal of Hazardous Materials, 160, (2008) 435-440.

13. **Coprecipitation of Ni^{2+}, Cd^{2+} and Pb^{2+} for preconcentration in environmental samples prior to flame atomic absorption spectrometric determinations.**

Mustafa Soylak, Ayse Kars and Ibrahim Narin,

Journal of Hazardous Materials, 159, (2008), 435-439.

3- Hürmüs Refiker, Huriye İcil, ''Amphiphilic and chiral unsymmetrical perylene dye for solid-state dye-sensitized solar cells''(accepted), *Turkish Journal of Chemistry*.

4- Hürmüs Refiker, Huriye Icil, "The synthesis of α-amino acid bearing perylene monoimide and its diimide: Their photophysical, electrochemical and pH responsive properties" (submitted), *Dyes and Pigments*.

Proceedings

Usama Alshana, **H.Refiker**, S.Tuncel. R.S.Aygün, Separation and Quantitation of Some Platinum Group Elements by HPLC. "4th Aegean Analytical Chemistry Days, Aydin, Turkey (2004), pp. 557-559.

International Congress Presentations:

1-H. Refiker, Huriye Icil,

"Functional Perylene Dyes Potentially Anchoring To TiO$_2$ Electrodes", The David G. Whitten Symposium, Albuquerque, New Mexico, USA (August 19-20, 2010).

2-Hurmus Refiker, H. Icil,

"Spectral Studies of Carboxyl Group Containing Perylene Monoanydride Monoimide and Diimides in Different pH Media", XXIV International Conference on Photochemistry, Toledo, Spain (July 2009).

3-H. Refiker, Huriye Icil,

"Carboxyl Group Containing Perylene Dyes for Efficient Dye-Sensitized Solar Cells", 23rd European Photovoltaic Solar Energy Conference at the Feria Valencia in Spain, (September 2008).

4-Hurmus Refiker, H. Icil,

"Solid-State Fluorescence Studies of Newly Synthesized N-(2-hydroxy-4-benzoic acid)-N'-(4-hydroxyphenyl)-3,4,9,10 perylenebis(dicarboximide) and N-(1-Dehydroabietyl)-N'-(4-hydroxyphenyl)-3,4,9,10 perylenebis(dicarboximide) toward Organic Solar Cells Applications", International Conference on Organic Chemistry, Erzurum, Turkey, (2007).

5-Hurmus Refiker, M. Merdivan, R. S. Aygun,

"Solid-phase Extraction of Silver in Geological Samples and its Determination by FAAS", 30th International Symposium on High Performance Liquid Phase Separation and Related Techniques, San Francisco, CA, USA, (2006).

6-Hurmus Refiker, U. Alshana, M. Merdivan and R. S. Aygun,

"Preconcentration of Some Precious Metals Using N,N-diethyl-N'-benzoylthiourea Impregntaed Resin'', 4th Aegean Analytical Chemistry Days, Aydın, Turkey, (2004).

7-Usama Alshana, **H. Refiker**, S. Tuncel and R. S. Aygun,
"Separation and Quantitation of Some Platinum Group Metals by High Performance Liquid Chromatography'', 4th Aegean Analytical Chemistry Days, Aydın, Turkey, (2004).

National Congress Presentations:

1-Hurmus Refiker, M. Merdivan, R. Sezer Aygun,

"Striking Selectivity of DEBT for Preconcentration of Gold in Ore Sample from Lefke", XXII. National Chemistry Congress, Famagusta, North Cyprus (October 2008).

2-Hurmus Refiker, H. Icil,

"Synthesis and characterization of symmetrical perylene diimide with polyamine; its potential interactions with G-quadruplex DNA", XXII. National Chemistry Congress, Famagusta, North Cyprus (October 2008).

3-H. Refiker, Huriye Icil,

"Potential chiroptical and pH responsive switches; the synthesis and the characterization of perylene monoanhydride monoimide with α-amino acid", XXII. National Chemistry Congress, Famagusta, North Cyprus (October 2008).

Refereeing:

1- Journal of Hazardous Materials, 2008

Reviewer acknowledgement list of Journal of Hazardous Materials.

Journal of Hazardous Materials, 162, 1 (2009) 540-574.

2- International Symposium on energy Engineering, Economics and Policy: EEEP 2009

3- International Symposium on energy Engineering, Economics and Policy: EEEP 2010

4- International Symposium on energy Engineering, Economics and Policy: EEEP 2011

Scholar: Researcher in Research Project, TUBİTAK, (2010-2012, TBAG-110T201), Turkey.

Memberships:

Turkish Chemical Society

ARBİS

European Photochemistry Association

Organizations:

XXIInd National Chemistry Congress, 6-10 October 2008, Eastern Mediterranean University, Famagusta, North Cyprus, Organizing Secretariat.